Advanced passivity-based control for hybrid power systems : application to hybrid electric vehicles and microgrids

Suyao Kong

To cite this version:

Suyao Kong. Advanced passivity-based control for hybrid power systems : application to hybrid electric vehicles and microgrids. Electric power. Université Bourgogne Franche-Comté, 2020. English. NNT : 2020UBFCD006 . tel-03681001

HAL Id: tel-03681001

https://theses.hal.science/tel-03681001

Submitted on 30 May 2022

UBFC
UNIVERSITÉ
BOURGOGNE FRANCHE-COMTÉ

UFC
UNIVERSITÉ
DE FRANCHE-COMTÉ

THÈSE DE DOCTORAT DE L'ÉTABLISSEMENT UNIVERSITÉ BOURGOGNE FRANCHE-COMTÉ

PRÉPARÉE À L'UNIVERSITÉ DE FRANCHE-COMTÉ

École doctorale n°37

Sciences Pour l'Ingénieur et Microtechniques

Doctorat de Génie Electrique

par

Suyao KONG

Commande passive avancée de systèmes hybrides - application aux véhicules hybrides électriques et micro-réseaux

Thèse présentée et soutenue à Belfort, le 29 mai 2020

Composition du Jury :

Emmanuel GODOY	Professeur à CentraleSupélec	Rapporteur
Franck PLESTAN	Professeur à l'Ecole Centrale de Nantes	Rapporteur
Ionela PRODAN	Maître de Conférences à Grenoble INP	Examinatrice
Marie-Cécile PÉRA	Professeur à l'Université Bourgogne Franche-Comté - UFC	Examinatrice
Serge PIERFEDERICI	Professeur à l'Université de Lorraine	Examinateur
Mohamed BECHERIF	Maître de Conférences HDR à l'Université Bourgogne Franche-Comté - UTBM	Examinateur
Mickaël HILAIRET	Professeur à l'Université Bourgogne Franche-Comté - UFC	Directeur de thèse
Robin ROCHE	Maître de Conférences HDR à l'Université Bourgogne Franche-Comté - UTBM	Co-encadrant de thèse

N°

THÈSE DE DOCTORAT DE L'ÉTABLISSEMENT UNIVERSITÉ BOURGOGNE FRANCHE-COMTÉ

PRÉPARÉE À L'UNIVERSITÉ DE FRANCHE-COMTÉ

École doctorale n°37
Sciences Pour l'Ingénieur et Microtechniques

Doctorat de Génie Electrique

par

Suyao KONG

Advanced Passivity-Based Control for hybrid power systems - application to hybrid electric vehicles and microgrids

Thèse présentée et soutenue à Belfort, le 29 mai 2020

Composition du Jury :

EMMANUEL GODOY	Professeur à CentraleSupélec	Rapporteur
FRANCK PLESTAN	Professeur à l'Ecole Centrale de Nantes	Rapporteur
IONELA PRODAN	Maître de Conférences à Grenoble INP	Examinatrice
MARIE-CÉCILE PÉRA	Professeur à l'Université Bourgogne Franche-Comté - UFC	Examinatrice
SERGE PIERFEDERICI	Professeur à l'Université de Lorraine	Examinateur
MOHAMED BECHERIF	Maître de Conférences HDR à l'Université Bourgogne Franche-Comté - UTBM	Examinateur
MICKAËL HILAIRET	Professeur à l'Université Bourgogne Franche-Comté - UFC	Directeur de thèse
ROBIN ROCHE	Maître de Conférences HDR à l'Université Bourgogne Franche-Comté - UTBM	Co-encadrant de thèse

N°

SPIM
école doctorale **sciences pour l'ingénieur et microtechniques**

Titre : Advanced Passivity-Based Control for hybrid power systems - application to hybrid electric vehicles and microgrids

Mots-clés : Système hybride à base de pile à combustible, commande passive, méthodologie IDA-PBC, plate-forme HIL, plate-forme PHIL

Résumé :

Un système hybride à base de pile à combustible (PàC) est une solution efficace pour faire face aux problèmes de pollution atmosphérique et de pénurie des combustibles fossiles. Cette thèse se concentre sur la conception de la commande pour les systèmes d'alimentation hybrides à base de PàC, et appliquée à deux applications : le véhicule électrique et le centre de données alimenté par un micro-réseau.

Tout d'abord, cette thèse propose une commande basée sur la passivité pour un système hybride PàC/supercondensateurs (SCs). Cette commande a été conçue via la méthode de conception IDA-PBC (Interconnection and Damping Assignment - Passivity Based Control), afin de résoudre le problème de coordination des convertisseurs. L'état de charge des SCs ainsi que toutes les limitations sont intégrés directement dans la loi de commande. Un banc d'essais PHIL (Power Hardware-in-the-loop) est utilisé pour la validation. Ensuite, un filtre de Kalman étendu (EKF) est combiné avec la commande proposée, pour prévoir l'état de santé (SoH) de la pile à combustible. Enfin, un banc d'essais HIL (Hardware-in-the-loop) basé sur un FPGA INTEL / ALTERA est conçu afin de valider le fonctionnement des algorithmes en temps réel pour un véhicule commercial.

Pour l'application à un micro-réseau, une commande passive est proposée pour un système hybride comprenant des panneaux photovoltaïques, une PàC, des SCs et un électrolyseur. La faisabilité de cette commande est validée par les résultats expérimentaux sur un banc d'essai PHIL. Ce travail est intégré au projet ANR DATAZERO.

La nouveauté principale de cette commande est qu'elle intègre certaines contraintes de composants directement dans la loi de commande, en préservant la stabilité de l'ensemble du système, en boucle fermée.

Title: Advanced Passivity-Based Control for hybrid power systems - application to hybrid electric vehicles and microgrids

Keywords: Fuel cell hybrid system, passivity-based control, IDA-PBC methodology, hardware-in-the-loop platform, power hardware-in-the-loop platform

Abstract:

A Fuel cell (FC) hybrid power system is a promising solution to deal with the atmospheric pollution and fossil fuels shortage problems. This thesis focuses on the controller design for FC hybrid power systems, towards two applications: the hybrid electrical vehicle and the microgrid-powered datacenter.

Firstly, this thesis proposes an advanced passivity-based control for a FC/super-capacitors (SCs) hybrid system. In order to solve the converters coordination problem, a controller designed using the design method Interconnection and Damping Assignment - Passivity-Based Control (IDA-PBC) is applied, which considers the state-of-charge of the SCs as well as voltage and current limitations. The proposed controller is validated on a Power Hardware-in-the-loop (PHIL) platform. Then an Extended Kalman Filter (EKF) is applied to forecast the State-of-Health (SoH) of the fuel cell and is combined with the proposed controller. Finally, a Hardware-in-the-loop (HIL) platform based on an INTEL/ALTERA FPGA is designed in order to validate the real-time operation of the algorithms for a specific case study with a commercial vehicle.

For microgrid applications, a passivity-based controller for a hybrid power supply system for a green datacenter is proposed, including photovoltaic panels, a fuel cell, SCs and an electrolyzer. The feasibility of this non-linear controller is proven by the simulation results and experimental validation on a PHIL test bench. This work is integrated into the ANR DATAZERO project.

The main novelty of the proposed controller is that it integrates some component constraints directly into the controller equations, while the locally asymptotic stability of the whole closed-loop system is preserved.

UBFC
UNIVERSITÉ BOURGOGNE FRANCHE-COMTÉ

Université Bourgogne Franche-Comté
32, avenue de l'Observatoire
25000 Besançon, France

ACKNOWLEDGMENTS

This thesis is supported by the China Scholarship Council and part of this work is participated into the national project DATAZERO. This research has been done in the research federation FCLAB, with the ”Systèmes Electriques Hybrides, Actionneurs Electriques, Systèmes Piles à Combustible” (SHARPAC) team of the department Energy in the research institute “Franche-Comté Electronics Mechanics Thermal Science and Optics - Sciences and Technologies” (FEMTO-ST Institute).

It is my great pleasure to extend my thanks to those who helped and supported me during this thesis. In the first place, I would like to give the most sincere thanks to Prof. Mickaël HILAIRET and Dr. Robin ROCHE, who have supervised this thesis with continuous guidance, encouragement and responsibility. Thanks to their insightful advice and constructive comments all along with the research work, I progressed and learned a lot.

I would like to express my deepest gratitude and respect to Prof. Emmanuel GODOY and Prof. Franck PLESTAN, for their precious suggestions on the manuscript. Profuse thanks go equally to members of my thesis jury Prof. Marie-Cécile PÉRA, Dr. Inoela PRODAN, Prof. Serge PIERFEDERICI and Dr. Mohanmed BECHERIF, for their profound insights and comments.

I would also thank my colleagues : Elodie, Meiling, Neigel, Haidar, Hugo, Dan, Rania, Hanqing, Hailong, Huan, Bei, Pièrre, Berk and other colleagues in FCLab, we have a lot of good memories during past three years. Special thanks to Laurence, Violaine and Bruno, for theirs administration helps.

I am also grateful to the partners in the project DATAZERO, with whom I had an excellent experience in the project.

Finally, I would like to express my special thanks to my parents, my friends and my boyfriend for their supports and regards.

CONTENTS

I

CONTEXT AND STATE-OF-THE-ART

1

GENERAL INTRODUCTION

1.1/ MOTIVATION AND OBJECTIVES

1.1.1/ CONTEXT

Over the past two centuries, the global energy consumption has increased with a significant growth. The growing requirement for electricity has also led to an increase in energy-related carbon dioxide (CO_2) emissions, which is a strong cause of climate change [1]. As reported by the International Energy Agency (IEA) - global energy-related CO_2 emissions rose by 1.7 % in 2018 to reach a historic high of 33.1 Gt CO_2, the fastest for seven years (see Fig. 1.1) [2]. A regional summary of energy-related CO_2 of 2018 is shown in Tab. 1.1 : China, India, and the United States accounted for 85 % of the net increase in emissions, while emissions declined for Germany, Japan, Mexico, France and the United Kingdom [2].

The Exponential Climate Action Roadmap report pointed out that further actions are needed to reach net zero emissions by 2050 [3]. It is recommended by the Intergovernmental Panel on Climate Change (IPCC) that we have to restrict warming to no more than 1.5°C above pre-industrial levels, and currently, the planet has already warmed by about 1°C on average [4].

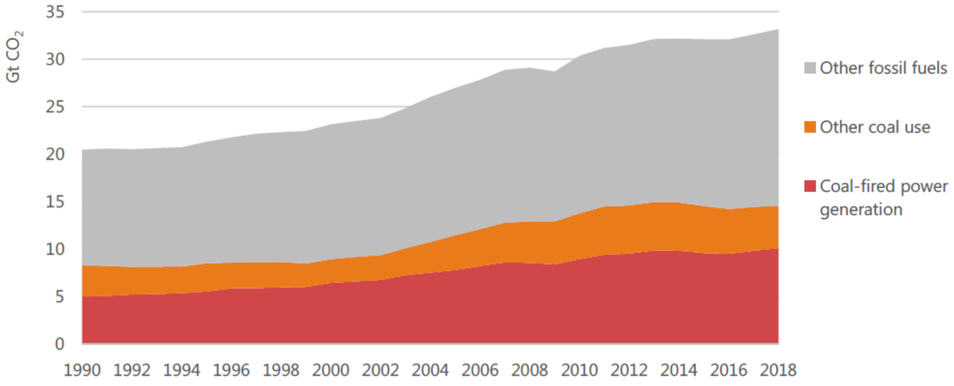

FIGURE 1.1 – Global energy-related CO_2 emissions [2]

Region	**Total CO_2 emissions (Mt CO_2) in 2018**	**Growth Rate (%) for 2017-2018**
United States	4 888	3.1 %
China	9 481	2.5 %
India	2 299	4.8 %
Europe	3 956	-1.3 %
Rest of the World	11 249	1.1 %
World	33 143	1.7 %

TABLE 1.1 – Regional summary of energy-related CO_2 emissions [2]

Transportation, information and communication technology (ICT) are two sectors that have great responsibility on the global CO_2 emission. A study of the U.S. Energy Information Administration (EIA) shows that the transportation sector accounts for almost 55 % of the world's total energy consumption and 30.9 % of CO_2 emissions in 2014 [5]. In order to reduce CO_2 emissions in the transportation sector and reduce the environmental impact, electric vehicles (EVs) are attracting attention. Compared to gas or oil powered vehicles, EVs can help maintain a clean and healthy environment, and can also reduce the operating cost of vehicles [6].

According to some researches, ICT can be responsible for up to 23 % of the global greenhouse gas emissions in 2030 [7]. As a part of the ICT category, datacenters are increasingly polluting since their consumption of electricity is growing rapidly. Datacenters will use around up to 13 % of global electricity in 2030, compared to 1 % in 2010 [7].

Therefore, zero-emission vehicles and zero-emission datacenters are required, in addition to other measures. There is a strong trend of using renewable energy in vehicles [8] as well as in datacenters [9, 10].

1.1.2/ TOWARD HYBRID ELECTRIC VEHICLES

Currently, renewable energy only accounts for a very small part in the transportation sector. As shown in Fig. 1.2 [11], in 2016, only 4 % of the energy consumption is powered by renewable energy, where energy is mostly provided by biofuels. Electrification with renewable power generation has only a share of about 1 %, which is extremely limited.

According to the renewable energy road map analysis by IRENA (REmap), by 2050, renewable electricity will provide 37 % of the total energy consumption in the transportation sector. It will reduce 80 % of the annual transport emissions (in 2016) to just 2.4 Gt CO_2, due to a combination of low-carbon approaches [11].

The vehicles that use only electrical power are called all-electric vehicles (AEV), which are divided into three types : battery electric vehicles (BEV), fuel cell electric vehicles (FCEV), and fuel cell hybrid electric vehicles (FCHEV). A FCHEV uses a fuel cell as the main energy source and a battery or super capacitor as energy storage. Since BEVs are limited in speed and distance and fuel cells are not suitable for abrupt changes in power demand, FCHEV research has led to successful commercial fuel cell vehicles [6]. Some new models of FCHEV are available for sale in the United States, such as the Honda Clarity and Toyota Mirai in 2019, as well as the Hyundai Nexo and Hyundai Nexo Blue in

2020 [12].

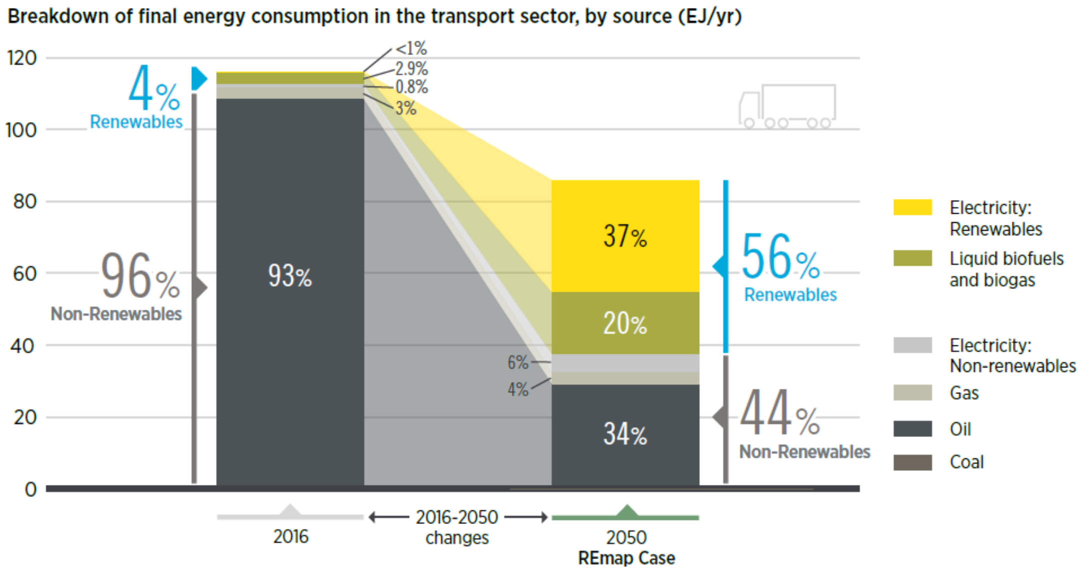

FIGURE 1.2 – Energy consumption in the transport sector [11]

In order to ensure efficient and smooth operation of a FCHEV, many issues need to be considered. One of the objectives in this thesis is to solve the coordination problem between the converters that are associated with each energy source, while ensuring the stability of the hybrid power system. The novelty of the proposed controller lies in the integration of elements' constraints into the controller while considering the aging of the FC.

1.1.3/ TOWARD MICROGRIDS FOR DATACENTERS - DATAZERO PROJECT

Over the past few years, energy efficiency in datacenters has improved but the amount of electricity needed for operating cloud services is growing with the size of the infrastructure and the user demands. With renewable energies, some new solutions can be proposed for solving this issue. A datacenter powered by renewable energy with zero emission is called green datacenter. Nowadays, a green datacenter is not only a concept but a reality. In the past two years, both Google and Apple have achieved 100 % renewable-powered datacenters. Facebook has announced that it will achieve 100 % by 2020, and Microsoft plans to run 60 % of its datacenters with renewable power by 2020 [13].

However, theses green datacenters are powered by purchased renewable energy [14], and there are more challenges to realize a microgrid-powered green datacenter. Reliability is one of the most important issues for the datacenter electricity supply system, since the IT elements need to be powered without interruption. Therefore, the main challenge of the green datacenter is nevertheless to match high availability of IT (Information Technologies) services, avoiding unnecessary redundancies, under the constraints of intermittent nature of renewable electrical energy supply. The FCLAB research federation (CNRS) and FEMTO-ST Institute are working on those topics, in the framework of a French national research project named DATAZERO [15], funded by the National Research Agency

(ANR). Several ways to solve the intermittency problem of renewable energies are proposed, such as the job scheduling that increases the flexibility of the IT load and the long (seasonal) storage of electricity using the hydrogen-energy vector.

The objectives of project DATAZERO can be seen as follows :
- Designing and operating a zero-emission green datacenter, powered by 100 % renewable energies such as solar energy, wind energy and hydrogen to meet the consumption of the datacenter.
- Integration of real-time simulation and Power Hardware-in-the-loop (PHIL) which combines virtual and physical elements.

The framework of the DATAZERO project is shown in Fig. 1.3. The IT Decision Module (ITDM) realizes an effective tasks scheduling on the IT servers while the Power Decision Module (PDM) aims at power dispatching among different sources of energy. The Negotiation Module (NM) is an optimization module between the ITDM and PDM, in order to find an agreement between IT power consumption and electrical production.

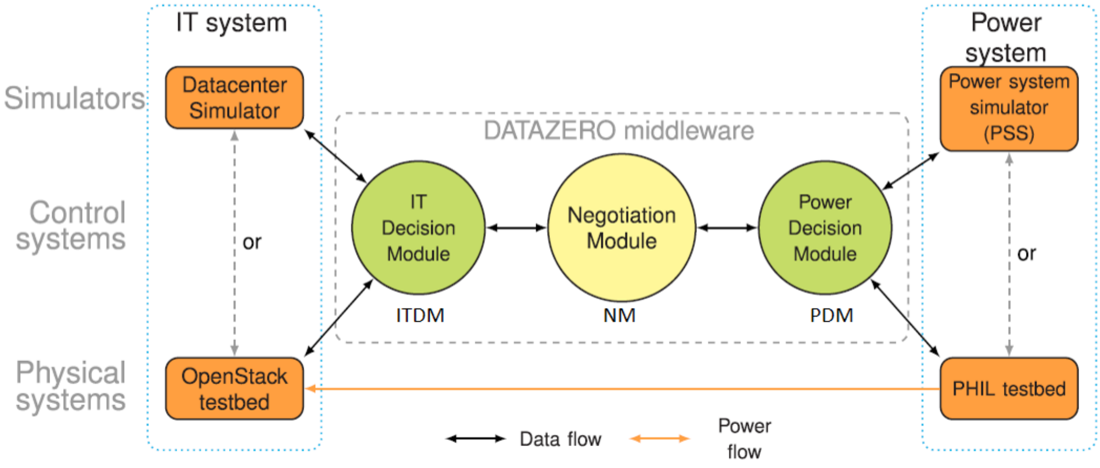

FIGURE 1.3 – Framework of DATAZERO [16]

The contributions of this thesis to the DATAZERO project are divided into two parts : firstly, the design of a passivity-based controller for the microgrid ; secondly, the software set-up and the integration of a real-time controller on the PHIL testbed, which enables a real-time simulation for the decision of PDM.

1.2/ OUTLINE OF THESIS

The manuscript is structured into six chapters, as shown in Fig. 1.4. As presented in the motivations, the contributions of this thesis focus on the control of a hybrid power system, which is applied for two aspects : a hybrid electric vehicle and a microgrid supplying datacenter.

Chapter 2 describes the state-of-the-art and related works of hybrid power systems and controller design. The power sources as well as energy storage system are presented, then the topologies of HEV and microgrids are introduced. A brief introduction of linear and nonlinear controller design methodologies as well as their applications are presented. Then a detailed theoretical introduction of applied passivity-based control and a literature review of related works toward HEV and microgrids are presented.

Chapter 3 introduces two test benches that are applied for experimental controller validation in this thesis : a hardware-in-the-loop (HIL) platform and a power hardware-in-the-loop (PHIL) platform. The hardware and software parts on these two platforms are presented. An application of the PHIL test bench for the project DATAZERO is also introduced.

Chapter 4 proposes an advanced passivity-based control for a fuel cell/super-capacitor hybrid system, which considers the components constraints while ensuring the stability of the system. A control strategy for a dissipative resistance load was also integrated into the proposed controller, in order to protect the system from over-voltage. Finally, experimental validation is realized on the PHIL test bench.

Chapter 5 describes an aging-tolerant passivity-based control, which combines the controller proposed in Chapter 4 with an aging estimation algorithm of the fuel cell. An Extended Kalman Filter (EKF) is applied to forecast the State-of-Health (SoH) of the fuel cell ; then the maximum current that the fuel cell can deliver can be calculated and be considered in the controller. Finally, an application of the proposed controller on a commercial vehicle model is tested on the HIL test bench.

Chapter 6 proposes a passivity-based control for a DC microgrid consisting of photovoltaic panels, a fuel cell, an electrolyzer and super-capacitors, which represents the hybrid power supply system of a green datacenter. This work contributes to the DATAZERO project. The proposed real-time controller is integrated into the PHIL DC microgrid test bench and is experimentally validated.

Lastly, in chapter 7, the contributions of this work are summarized, and the possible future works and perspectives are proposed.

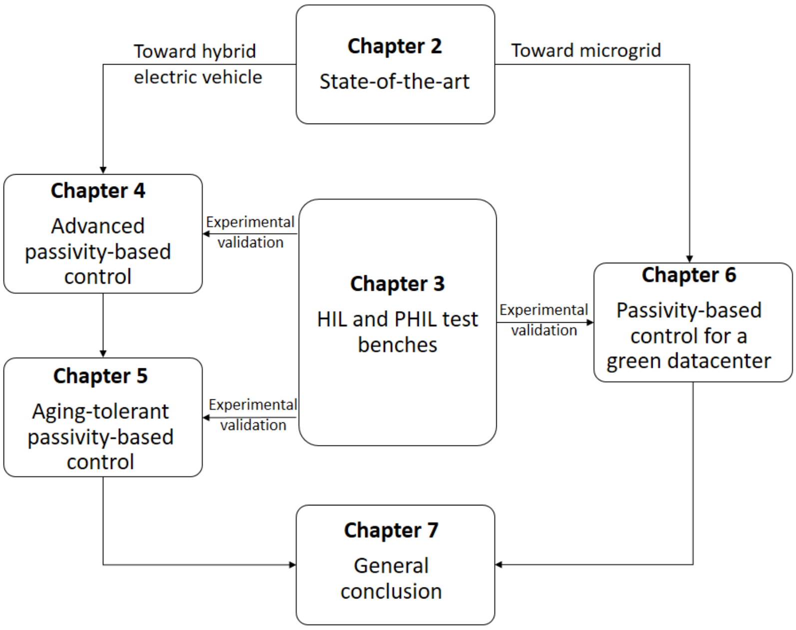

FIGURE 1.4 – Diagram of the thesis structure

2

STATE-OF-THE-ART OF HYBRID POWER SYSTEMS AND CONTROLLER DESIGN

2.1/ INTRODUCTION

A state-of-the-art of the studied hybrid power systems is introduced in this chapter, with two aspects : the hybrid electrical vehicle and the microgrid. Section 2.2 presents the hybrid power system components as well as the topologies of FCHEV and microgrids ; section 2.3 introduces several commonly-used linear and nonlinear controller design methodologies and theirs applications ; the applied nonlinear controller based on passivity-based control of this thesis is introduced by section 2.4 ; finally, the conclusion is presented in section 2.5.

2.2/ HYBRID POWER SYSTEM COMPONENTS

2.2.1/ PHOTOVOLTAIC SYSTEM

Solar power is a clean energy technology, as it does not cause the environmental disruptions (i.e., the problem of hydroelectric energy) and does not have a waste storage problem (i.e., the problem of nuclear energy) [9]. Nowadays, solar energy is widely used all over the world and according to the International Energy Agency (IEA), the global PV capacity exceeds 500 GW [17].

In photovoltaic technology, the solar cell can be described as a device that produces direct current and power fluctuating with the flux of sunlight. A PV module, also called a PV panel, is made of solar cells in series. A PV array is a complete power generating unit, which is an ensemble of PV panels in series and in parallel. The relationship of photovoltaic cell, module (panel) and array can be expressed by Fig. 2.1.

The production of PV depends on the weather conditions such as solar irradiance, air temperature, cloud variation, wind speed, relative humidity, etc. [18]. Since these meteorological variables are uncertain [19], the penetration of such systems in the actual power system is a challenge [20]. Therefore, in order to meet the uncertainty of PV generation, some researches proposed methods for forecasting the output power of PV [21, 22, 23], which requires a great deal of data and calculation. Another solution is to associate PV with a storage system, such as a battery, super-capacitors (SCs) or energy storage in the form of hydrogen.

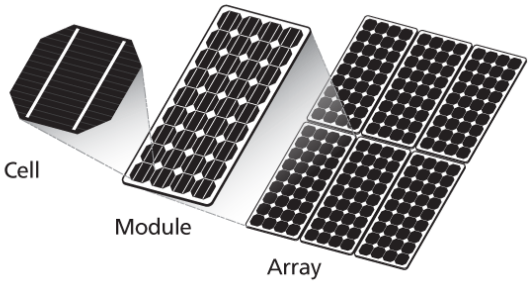

FIGURE 2.1 – PV cell, module (panel) and array [24]

2.2.2/ HYDROGEN ENERGY STORAGE SYSTEM

A fuel cell (FC) is an electrical device that converts chemical energy from a fuel (hydrogen) into electricity through a chemical reaction. A FC consists of an anode, a cathode and an electrolyte to realize the exchange of ions between the anode and the cathode. The operation principle of the fuel cell is presented in Fig. 2.2, the reaction is shown by (2.1) :

$$2H_2 + O_2 \rightarrow 2H_2O \tag{2.1}$$

After the chemical reactions at the anode (2.2) and the cathode (2.3), no gasses are emitted from the fuel cell since only water and heat are produced [25].

$$\begin{aligned} 2H_2 &\rightarrow 4H^+ + 4e^- && (2.2)\\ O_2 + 4H^+ + 4e^- &\rightarrow 2H_2O && (2.3) \end{aligned}$$

Among the various types of FC systems, Proton Exchange Membrane Fuel Cells (PEMFCs) have been found to be especially suitable for hybrid energy systems because of their high energy density, low operating temperature, small size and quick start-up [26].

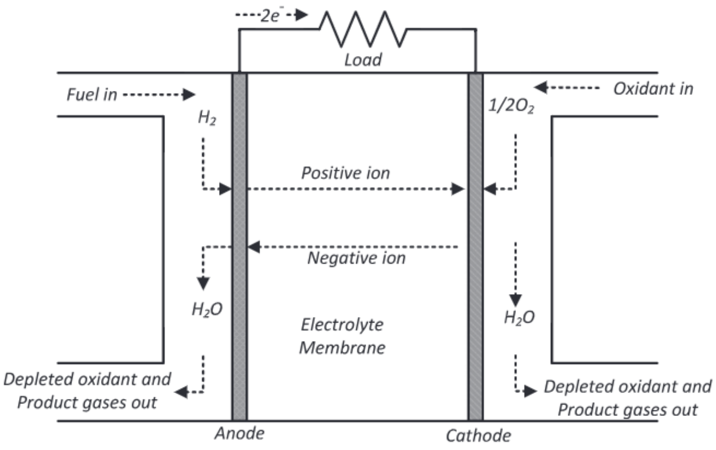

FIGURE 2.2 – Fuel cell diagram [27]

A water electrolyzer (EL) has an opposite reaction of a FC (see (2.4)), that can produce the hydrogen for FC.

$$2H_2O \rightarrow 2H_2 + O_2 \tag{2.4}$$

PEM water electrolyzers are considered as a feasible alternative for hydrogen generation from renewable energy sources [28]. Fig. 2.3 presents the diagram of a PEM electrolytic cell, with the chemical reaction at the anode (2.5) and the cathode (2.6).

$$2H_2O \rightarrow 4H^+ + 4e^- + O_2 \tag{2.5}$$

$$4H^+ + 4e^- \rightarrow 2H_2 \tag{2.6}$$

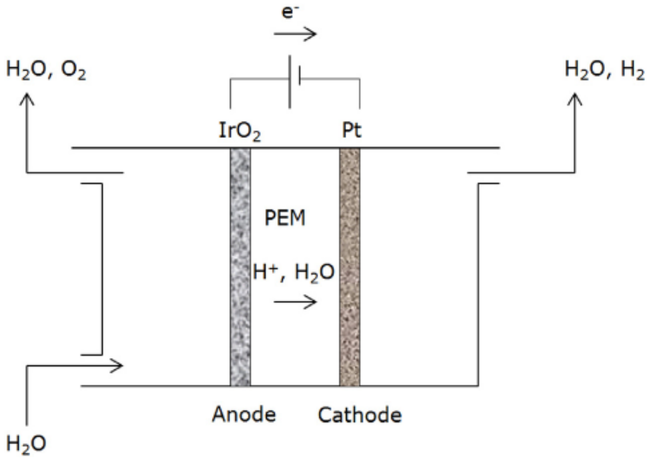

FIGURE 2.3 – Electrolyzer diagram [29]

A Hydrogen Energy Storage System (HESS) consists of a FC, a water electrolyzer and hydrogen storage tanks. Fig. 2.4 presents a typical HESS associated with a PV generator where the electrolyzer is supplied by the PV with DC voltage. In general, the extra energy in a power system is used by the electrolyzer to produce hydrogen, and is stored in the hydrogen tanks for use by the fuel cell when necessary [30].

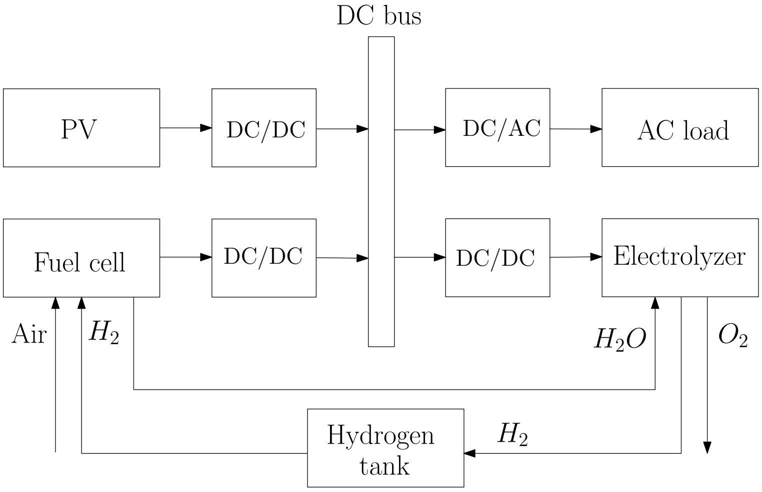

FIGURE 2.4 – HESS with PV generation

2.2.3/ BATTERIES AND SUPER-CAPACITORS

A battery (BT) is a storage device which consists of one or more electrochemical cells that convert the stored chemical energy into electrical energy. There are different types of batteries available for hybrid systems, such as lead acid batteries, nickel batteries, ZEBRA batteries, lithium batteries and metal air batteries. Among these types of batteries, lead acid battery is the cheapest and the most commonly used battery in hybrid systems [31]. In a lead acid battery, the positive plate is made with lead peroxide and the negative plate is made with soft sponge lead, which are dipped in dilute Sulphuric acid (electrolyte) to produce electricity [31].

A super-capacitor (SC) is a high-capacity electrochemical capacitor with high power density [32]. Depending on current research and development trends, SCs are used in various applications as a replacement for batteries for their high power density, high efficiency (>90 %) and high operating temperature range [6]. SCs can be divided into three major classes : Electrochemical Double Layer Capacitor (EDLC), pseudocapacitors and hybrid capacitors. For most of the applications, EDLC is most commonly used due to its low price and higher power density [33].

In a hybrid system, the power sources are divided into two parts : Main Energy Source (MES) and Rechargeable Energy Storage System (RESS) [34]. The MES is a source with high energy supply capability to provide most of the demanded energy, and the RESS is a source with high power capability and reversibility facility to provide transient power. Fig. 2.5 shows the power density and energy density of different sources. The fuel cell and the battery have a significantly higher energy density than the SCs, but they have low power density. Therefore, the FC and BT are appropriate as MES [6]. On the contrary, the SCs have very high power density and also very high discharge rate for 1 ms to 1 s with low energy density, which means that SCs can supply high power, but only over a short duration. These characteristics make them suitable to be applied as RESS [6]. Although the electrolytic capacitors have the highest power density, they cannot be used as energy sources due to their low energy density.

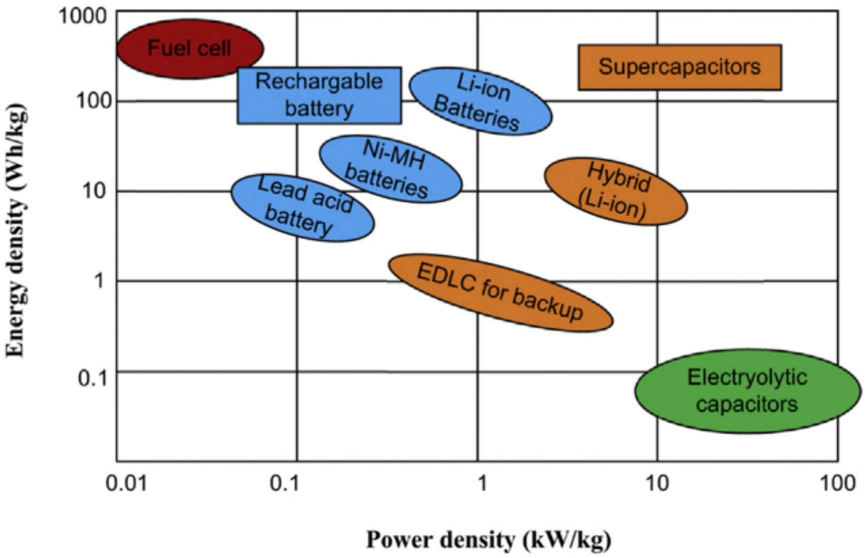

FIGURE 2.5 – Power density and energy density [31]

2.2.4/ POWER ELECTRONIC ARCHITECTURE

2.2.4.1/ TOPOLOGIES OF FCHEV

In the domain of FCHEV, the application of BTs or SCs as auxiliary power sources of FCHEV or the hybridization of these two devices as a hybrid energy storage system are well studied in many researches. A multiple-stage power conversion consists of DC-DC conversion and DC-AC conversion. The power sources with low DC voltage are converted into high voltage on the DC bus, then converted by inverters to supply AC loads [6]. Fig. 2.6 shows some typical typologies.

In the first topology (T_1), no converter is applied, the FC and the storage devices are connected directly to the DC bus. This structure is less used because we cannot control the sources. Therefore, some researches have applied the structure with one more converter on the FC (T_2) [35, 36, 37, 38] or the storage device (T_3) [39, 40], where the DC bus voltage is variable in order to control the power source without any converter. T_4 is more popular in the researches because of the flexibility in controlling both the fuel cell power and the power from the storage device. This structure requires strict control on both source converters, in order to meet the demanded power while keeping the DC bus voltage around the reference value. Many control strategies are proposed for FC/BT systems [41, 42, 43, 44, 45] or FC/SCs systems [46, 47, 48, 49, 50, 51, 52].

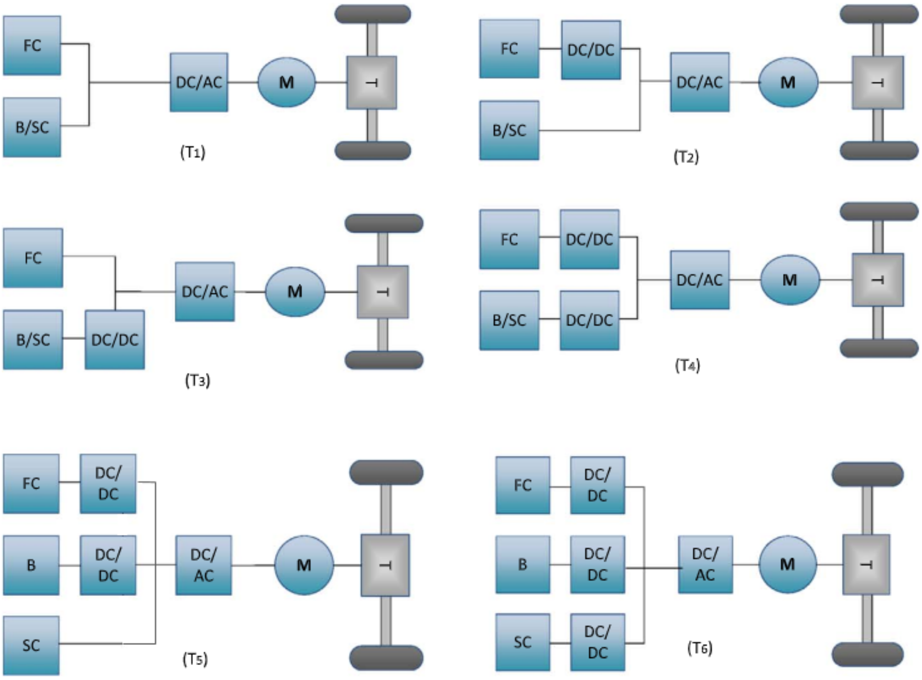

FIGURE 2.6 – Topologies of FCHEV [6, 53]

In some researches, both the battery and the SCs are applied, with topologies T_5 [54, 55, 56, 57, 58] or T_6 [59, 60, 61, 62, 63, 64]. These topologies benefit from the power handling capabilities the SCs as well as the energy storage capacity of the battery, which provides both high power density and high energy density. For example, in [58], the SCs are applied for supplying the energy required to achieve the DC link voltage regulation while the batteries are controlled as the power source that supplies energy to the SCs to keep them at a given state-of-charge (SoC). The FC is obviously the main energy source of the system that supplies energy to the batteries to keep them charged. However, the drawbacks of these two topologies are the complexity, cost, weight and volume. More topologies are reported in [65].

Among these topologies, the chosen structure for this thesis is T_4, which provides flexibility on control of the DC bus voltage and less complexity in practical applications.

2.2.4.2/ TOPOLOGIES OF MICROGRID

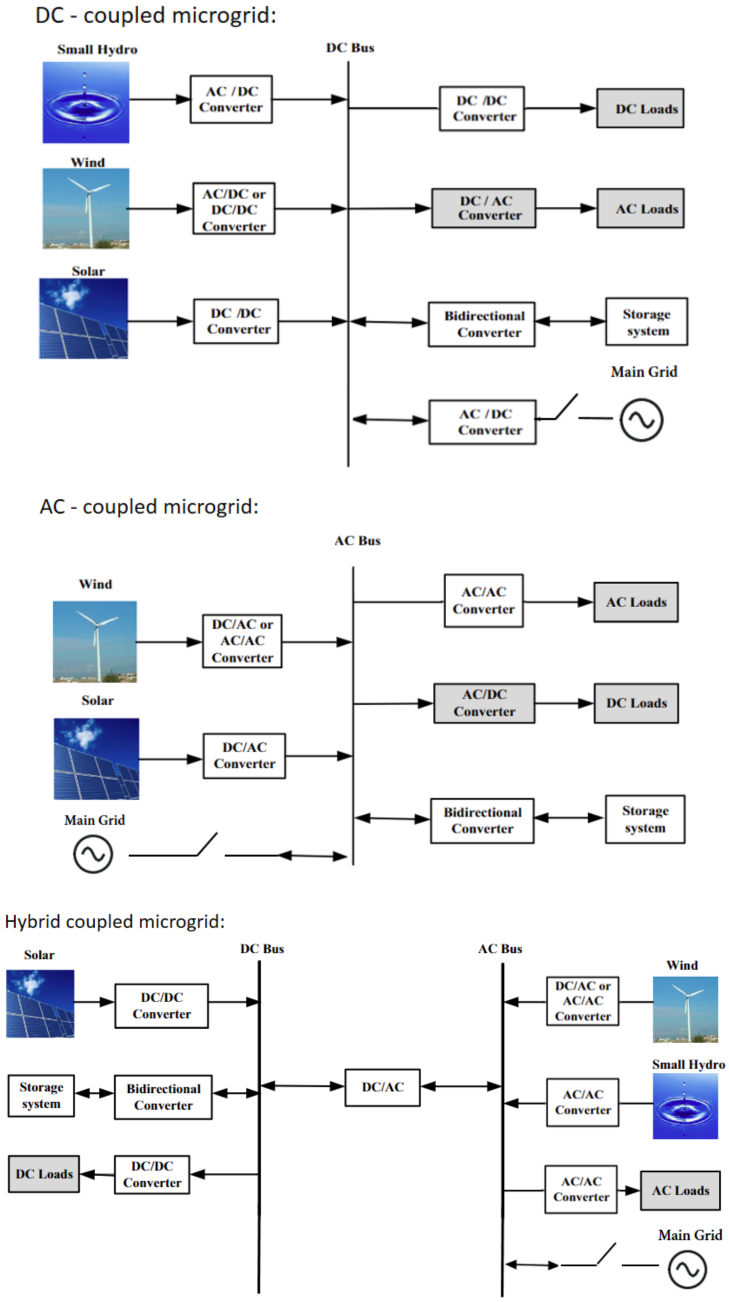

Figure 2.7 – Topologies of microgrid [66]

A microgrid is a controllable system as a basic element of future smart grids. It is a distributed energy system, which provides power to a particular area by employing generators and loads [67]. Microgrids can be operated in two modes : grid-connected mode and isolated mode. They can provide customers with a reliable and secure source of energy as well as prepare the grid for a prompt response to faults [68].

There are three types of topologies for microgrid : DC-coupled, AC-coupled and a hybrid configuration utilizing both DC and AC. An example for each of the topologies is shown in Fig. 2.7 [66]. In a DC-coupled microgrid, the generating components as well as the load are connected to the DC bus via DC/DC or DC/AC converters, which is widely applied in many researches [69, 70, 71]. This structure enables a fairly simple configuration, as synchronization is not required for integration of the various energy sources [72]. In an AC-coupled system, all the components are connected to an AC bus, while synchronization may be required with higher conversion losses [73]. This structure is applied in [74, 75, 76]. A hybrid DC/AC-coupled configuration involves both DC and AC bus as [66], several researches have studied this structure [77, 78, 79]. However, these systems are naturally more complex in terms of control and energy management [72].

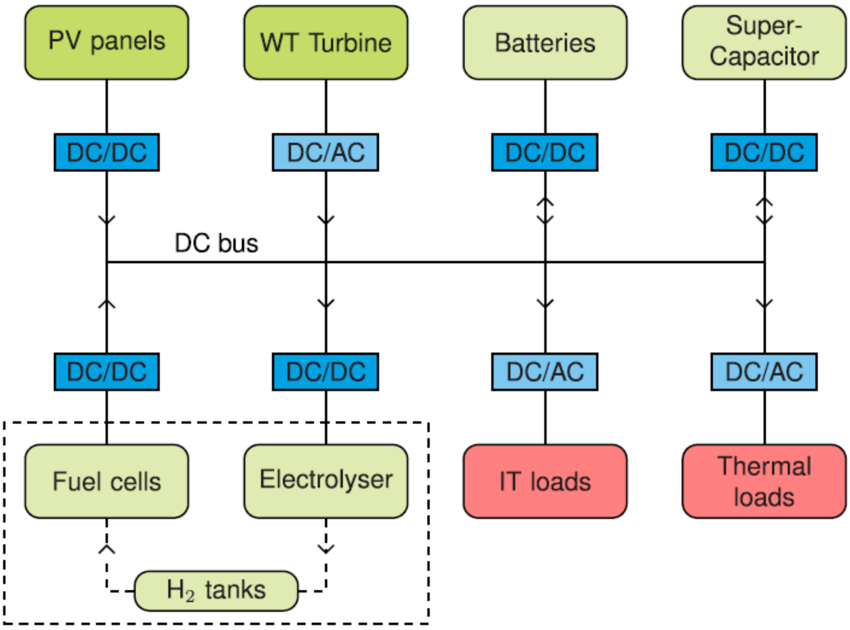

FIGURE 2.8 – DC microgrid supplying the datacenter loads [16]

Compared to an AC-coupled microgrid, the DC microgrid has higher controllability and reliability, since it does not need to track phase and frequency [80]. Therefore, in the DATAZERO project, the applied topology is chosen as a DC microgrid for its low energy conversion links, higher system efficiency, and lower line losses [81]. Solar and wind energy are applied as the green power sources. Since PV and wind turbine (WT) generation are uncertain, batteries, SCs and a HESS are associated as storage units. Fig. 2.8 presents the system composed of multiple distributed power, energy storage devices, as well as local loads, all of them connected to the same DC bus.

2.3/ CONTROLLER DESIGN METHODOLOGIES

2.3.1/ INTRODUCTION

Control, robustness, stability, efficiency, and optimization of distributed generation systems remain an essential area of research, where the stabilization of the DC bus is an important issue in power electronic applications [82]. The DC bus voltage is influenced by the changing current and voltage of electrical elements, while it needs to be stabilized at a reference value. In order to solve this control problem, linear controllers are generally applied. These traditional methods are usually based on a linearized model of the power converter and proportional – integral (PI), integral – proportional (IP) or proportional – integral – derivative (PID) feedback. The classical linear model predictive control (MPC) is also applied in many researches [59, 60].

Due to the nonlinearity of the switching model of the hybrid power plant, it is natural to apply nonlinear control strategies without requiring a linear approximation [82]. Studies of some nonlinear controllers for nonlinear systems have been proposed, such as rule-based control [83], flatness based control [84], sliding mode control [85], passivity-based control [86], etc. These controllers are classified in Fig. 2.9. Several widely-used linear and nonlinear controllers are introduced in this section. The passivity-based control is introduced in details in section 2.4, since this is the methodology that is applied in this thesis.

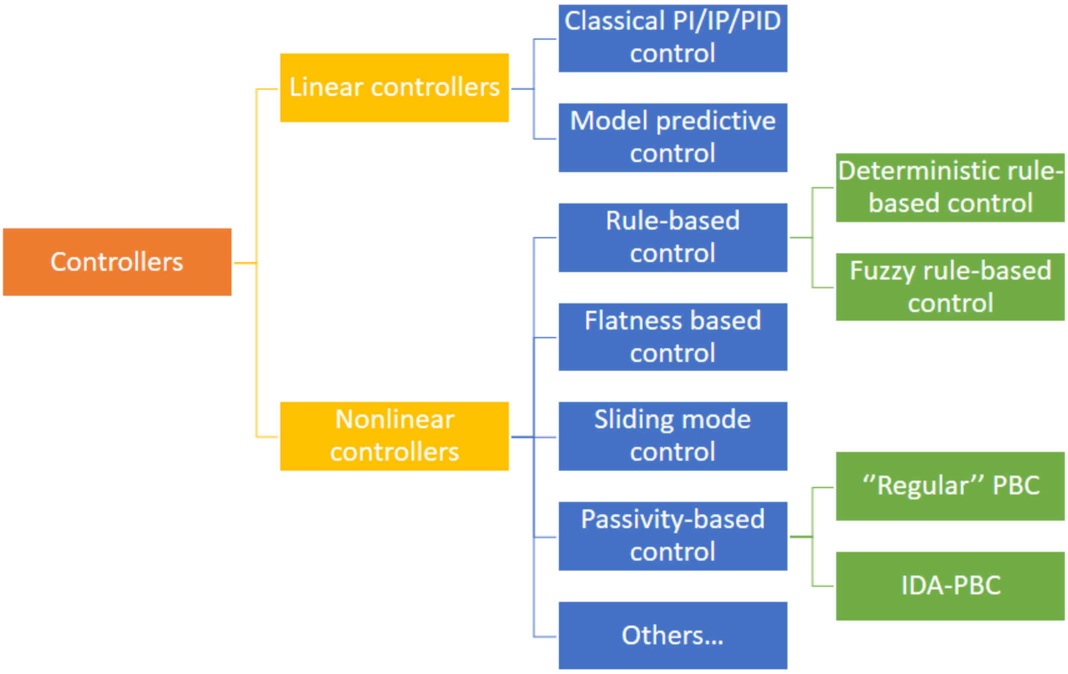

FIGURE 2.9 – Linear and nonlinear controllers

2.3.2/ LINEAR CONTROLLERS

2.3.2.1/ CLASSICAL PI/IP/PID CONTROL

The controllers that are implemented based on linear control algorithms such as PI, IP and PID controllers are widely used in feedback control of industrial applications, for their advantages of clear functionality, applicability, and ease of use [87].

Some researches have proposed this kind of linear controller for hybrid power systems [38, 88, 89]. A frequency-based distribution for FC/SCs hybrid electric vehicles is for example proposed in [90], using PI and PID controllers. Researches in [91] designed two PID controllers in order to calculate the battery current and fuel cell current, according to the error on the battery SoC and current. A linear controller using PI regulators for a FC/SCs hybrid power plant is proposed in [92], where the DC bus regulation is realized by the SCs converter and the FC converter is driven to maintain the SCs bank at a given SoC. Similar controllers are applied in [58] for a FC/BT/SCs hybrid power system, where the regulation of the SCs current is contained inside the PI control for the DC bus voltage.

2.3.2.2/ MODEL PREDICTIVE CONTROL

Classical linear MPC is an advanced methodology that relies on dynamic models of the system, in order to control the system while satisfying a set of constraints. The basic structure of MPC is shown in Fig. 2.10, where the future plant outputs are predicted by a model, based on past and current values and on the proposed optimal future control actions that consider the cost function as well as the constraints [93]. There are many types of MPC, where two types are often applied in the literature : online MPC and offline MPC. Online MPC uses an online optimisation, which is limited with long computing and response time. Offline MPC is also called Explicit Model Predictive Control (eMPC), and uses an offline optimisation to realize time-consuming and complex computations [94].

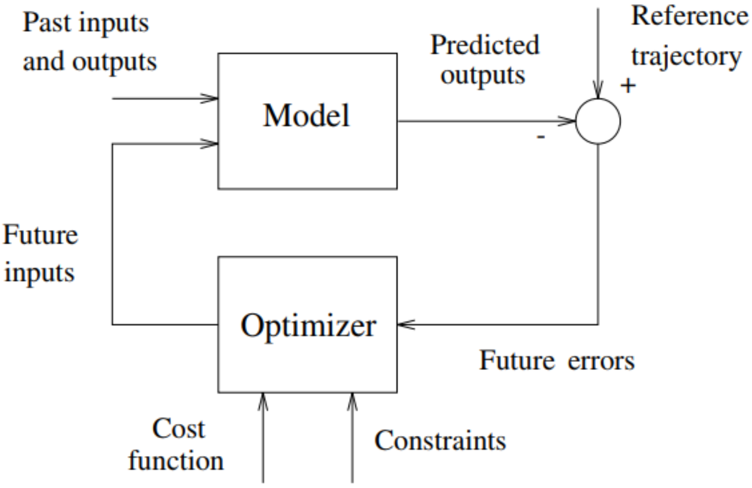

FIGURE 2.10 – Basic structure of MPC [93]

MPC has been applied in many researches [95, 96, 97, 98]. A MPC-based controller was proposed in [99], and is applied to a plug-in hybrid electric vehicle. The proposed controller can promote fuel economy, of which the robustness was verified by three typical driving cycles. In [100], a MPC-based method is proposed to control a microgrid for power balance and bus voltage regulation and is validated using a HIL experiment.

However, these linear controllers require of a linear model while the hybrid power systems are nonlinear. In many researches, the IP controllers are applied to design the current loops while the voltage loops are designed by nonlinear methodologies [62, 101]. In this thesis, the passivity-based nonlinear theory is applied to design the voltage loops and IP controllers are applied for current loops, which is detailed in section 3.2.4 of Chapter 3.

2.3.3/ NONLINEAR CONTROLLERS

2.3.3.1/ RULE-BASED CONTROL

Rule-based control (RBC) is widely used in power electronic systems, and can be divided into deterministic rule-based control and fuzzy rule-based control. Deterministic rule-based controllers are simple controllers that control the split of power requirement among different power sources, which relies on several rules designed according to the designer's experience under different situations.

In [102], an operating mode control is proposed for a FC/SCs vehicle, where the controller was designed by 5 operation modes to limit the dynamic power change rate of the FC. In [103], a similar controller based on the operating mode control was applied for a FCHV.

A rule-based energy management strategy is proposed in [104] for parallel hybrid SCs/BT vehicles, where the SCs are discharged when the required power from energy storage is above a threshold, meaning that the driver needs a boost of power for a period of time. In [105], a distributed energy management system is developed for a hybrid power source system based on a rule-based power distribution strategy, which has better rationality in terms of fuel economy and dynamic properties.

An optimal load sharing strategy for a PV/FC/BT/SCs system is proposed in [106]. The fuel cell is used to complement the intermittent output of the PV source while battery storage is used to compensate for part of the temporary peak demand which the PV and fuel cell cannot meet. SCs are used to meet the narrow and repeated transient charging and discharging in order to ensure longer battery life. The supervisory control is effected within a rule-based power flow management center to keep the DC bus voltage at the nominal voltage.

Deterministic rule-based strategy is simple and can easily be applied in reality, and it is also applied in [107, 108]. Many researches focus on fuzzy rule-based control based on fuzzy logic methodology, which can compute accurate outputs from imprecise inputs [109]. Fig. 2.11 shows the block diagram of the fuzzy logic controller.

This methodology is applied in many researches [110, 111, 112]. A fuzzy control based controller is proposed in [113] for a grid-connected PV/PEMFC/BT hybrid distributed generation system, which realizes the control of power electronic DC/DC and DC/AC converters. In [56], a fuzzy logic-based energy management strategy is proposed for a FCHEV, with validity of dynamic properties and fuel economy. An optimal online power management strategy is developed in [114] using machine learning and fuzzy logic in order to minimize energy sources power losses. In [115], a fuzzy logic-based decision system is applied in a FC/SCs hybrid electric vehicle, where the performance and robustness of the proposed controller are tested on two different driving cycles. An experimental validation of a fuzzy logic controller on a mobile laboratory is presented in [116], and the proposed controller has good performance in energy management of hybrid electrical vehicles.

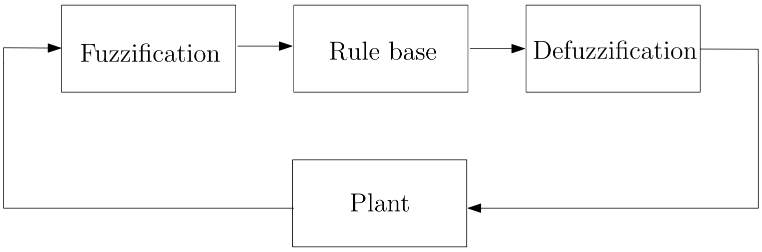

FIGURE 2.11 – Block diagram of fuzzy logic controller

2.3.3.2/ SLIDING MODE CONTROL

Sliding mode control (SMC) is a quick and powerful variable structure approach that governs nonlinear systems via a predefined switch sliding surface, which is widely used in hybrid power system control due to its flexible form and robustness [117]. This technique consists of two stages : firstly, a sliding surface is designed according to some performance criterion ; secondly, a discontinuous controller is designed to enforce system state in this manifold which is equivalent to a stability problem [118, 119].

SMC has been widely used in the domain of hybrid electric vehicles [85, 120, 121, 122, 123] as well as microgrids [124]. Two controllers based on MPC are designed in [125], for a HEV application : conventional SMC was applied for controlling the converter voltage and the SCs current while adaptive-gain second order SMC was used to control the FC current and the servomotor speed. In [126], the inner current control loop for a hybrid energy storage system was designed by SMC, where the performance on the system transient response to different loads and boundary conditions are verified.

This methodology has also been applied in the air-feed system of PEMFC, with experimental validations [127, 128, 129, 130]. This controller was also applied for switching power converters in [131] and for switched reluctance machine in [132].

2.3.3.3/ OTHER NONLINEAR CONTROLLERS

Flatness based control (FBC) is an effective nonlinear model-based control that can estimate the trajectory of a system in a straightforward manner using the trajectory of flat outputs [133]. This method can be applied for stabilization problems, DC bus voltage regulation as well as energy management [134], and has been applied for controlling hybrid power systems in many researches [82, 133, 135, 136] as well.

There are also many nonlinear methodologies such as adaptive control [137, 138], Lure-Lyapunov theory [139], Lyapunov-based nonlinear control [140, 125, 141, 142], nonlinear state-space approaches [143], nonlinear robust control by state feedback exact linearization [144], regular controllers or optimization algorithms [145], which are typically used in controller design.

2.3.4/ SUMMARY AND COMPARISON

A summary of advantages and disadvantages of introduced control strategies is presented in Tab. 2.1. Compared to linear controllers, nonlinear controllers are more suitable for hybrid power systems according to the nonlinearity of the system model. For the presented nonlinear controllers, most of them have a theoretically challenging problem : the system stability has not been proven theoretically. Therefore, in this thesis, passivity-based control (PBC) is applied for its theoretical demonstration of stability [146]. The controller is designed using the interconnection and damping assignment passivity-based control (IDA-PBC) method that was proposed in [146], where the local asymptotic stability of the closed-loop system was proven. The passivity-based control theory and the IDA-PBC methodology are introduced in the next section.

Control strategies	**Advantages**	**Disadvantages**
PI/IP/PID control	Clear functionality, applicability, and ease of use	Requirement of strict parameter configuration
MPC	Flexible constraint handling capabilities, integration of constraints	Requirement of dynamic linear models of the system
RBC	Rapid and easy to understand	Relies on designer's experience
SMC	Stabilization of uncertain non-linear systems and Theoretical demonstration of stability	High frequency oscillations
FBC	Robustness during perturbations, highly achievable on trajectory tracking	Low response speed
PBC	Theoretical demonstration of stability	Requirement of good acknowledgements of system parameter, or application of an integral term for unknown parameters

TABLE 2.1 – Summary of advantages and disadvantages of control strategies

2.4/ PASSIVITY-BASED CONTROL

2.4.1/ INTRODUCTION

Passivity is a fundamental property of dynamic systems which may be roughly defined in terms of energy dissipation and transformation. Based on the energy-balance equation, a passive system cannot store more energy than it is supplied to by some “source”, with the difference being the dissipated energy [147]. Passivity-based control (PBC) is a generic name to define a nonlinear controller design methodology that stabilizes the system by rendering the closed-loop system passive.

There are two large groups of PBC : ”regular” PBC and the second class of PBC. In the ”regular” PBC, the designer chooses the storage function, and then designs the controller that makes the storage function non-increasing [148]. The standard Lyapunov method that controls physical system described by Euler-Lagrange (EL) equations of motion, can be classified in this group, which is detailed in [149]. However, as shown in [146], for applications that require the modification of kinetic energy, the closed-loop system is no longer an EL system and the given storage function does not have the interpretation of total energy. As a result, these designs carry out an inversion of the system along the reference trajectories that not only destroys the Lagrangian structure but also imposes an unnatural stable invertibility requirement to the system [148].

Conversely, in the second class of PBC, the storage function is not fixed, but a desired structure of the closed-loop system is selected by the designer such as Lagrangian or Port-Controlled Hamiltonian (PCH). The most notable example of this approach is the IDA-PBC method that controls systems described by PCH, and is introduced in the following.

2.4.2/ PORT-CONTROLLED HAMILTONIAN SYSTEMS

PCH systems are represented by a form that confines energy balancing, which provides a clear identification of the structural properties of the system through the damping and the interconnection matrices [150]. The PCH form is presented as follows :

$$\dot{x} = [\mathcal{J}(x) - \mathcal{R}(x)]\nabla H(x) + g(x)u \tag{2.7}$$

$$y = g^T(x)\nabla H(x) \tag{2.8}$$

where the gradient of the energy function is :

$$\nabla H(x) = \begin{bmatrix} \frac{\partial H}{\partial x_1}(x) & \frac{\partial H}{\partial x_2}(x) & \dots & \frac{\partial H}{\partial x_n}(x) \end{bmatrix}^T$$

where x are the state variables, u and y are the port power variables that are conjugated (e.g. currents and voltages), $\mathcal{J}(x) = -\mathcal{J}^T(x)$ is a skew-symmetric matrix of dimension $n \times n$ representing the interconnections between states, and $\mathcal{R}(x) = \mathcal{R}^T(x) \geq 0$ is a positive semi-definite symmetric matrix representing the natural damping of the system.

2.4.3/ IDA-PBC METHODOLOGY

The objective of IDA-PBC is to find a static state-feedback control $u(x) = \beta(x)$ such that the closed-loop dynamics is a PCH system with the interconnection and the dissipation of the form :

$$\dot{x} = [\mathcal{J}_d(x) - \mathcal{R}_d(x)]\nabla H_d \tag{2.9}$$

where $H_d(x)$ is the natural energy function of the system, $J_d(x)$ is a skew-symmetric matrix of dimension $n \times n$ representing the interconnections between states, and $R_d(x)$ is a positive semi-definite symmetric matrix representing the natural damping of the system.

Considering a non-linear system :

$$\begin{aligned} \dot{x} &= f(x) + g(x)u; \quad x \in \Re^n; u \in \Re^m \\ y &= h(x); \quad y \in \Re^m \end{aligned}$$

To rewrite the system in the form of (2.9), the first step is to rewrite the nonlinear system to PCH form in (2.7) and (2.8).

We assume that there are matrices $\mathcal{J}_d(x) = -\mathcal{J}_d^T(x)$, $\mathcal{R}_d(x) = \mathcal{R}_d^T(x) \geq 0$ and a function $H_d(x) : \Re^n \longrightarrow \Re$ so that the closed-loop system with control variable u

$$u = \left[g^T(x)g(x)\right]^{-1} g^T(x)\left\{\left[\mathcal{J}_d(x) - \mathcal{R}_d(x)\right]\nabla H_d - f(x)\right\}$$

takes the PCH form

$$\dot{x} = [\mathcal{J}_d(x) - \mathcal{R}_d(x)]\nabla H_d \tag{2.10}$$

$H_d(x)$ is such that $x^* = \mathrm{argmin}_{x\in\Re^n}(\mathrm{H_d(x)})$ with $x^* \in \Re^n$ the local equilibrium to be stabilized. The system is asymptotically stable if x^* is an isolated minimum of $H_d(x)$ and if the largest invariant set under the closed-loop dynamics (2.10) contained in $\left\{x \in \Re^n \mid [\nabla H_d]^T \mathcal{R}_d(x)\nabla H_d = 0\right\}$ equals x^* [101].

The stability of x^* is established noting that, along the trajectories of (2.10), we have

$$\dot{H}_d = -[\nabla H_d]^T \mathcal{R}_d(x)\nabla H_d \leq 0, \qquad H_d(x = x^*) = \dot{H}_d(x = x^*) = 0$$

Hence, $H_d(x)$ is qualified as a Lyapunov function and the closed-loop system is asymptotically stable, according to La Salle's invariance principle [151].

2.4.4/ LITERATURE REVIEW OF PBC ON HYBRID POWER SYSTEM APPLICATION

2.4.4.1/ TOWARD HYBRID ELECTRIC VEHICLES

Since PBC is a powerful nonlinear technique with a theoretical proof of stability, it is widely used in the domain of hybrid vehicles. An IDA-PBC controller for a FC/SCs hybrid vehicle is proposed in [101], where a load resistance estimator as well as an integral action on the load current are proposed. Finally, a comparison of the IDA-PBC controller and the PI controller is presented. Although the DC bus voltage is well controlled with the PI controller due to greater SCs current, the FC supplies a smoother current with the IDA-PBC controller, which enables the FC to have a longer life time [101]. Also, the proposed passivity-based controller ensures a locally asymptotic stability of the whole closed-loop system, while that is not demonstrated for PI controllers. Another advantage of the IDA-PBC controller is that it has less tuning parameters than the PI controller, which makes the implementation of the IDA-PBC on a real-time system easier. A similar IDA-PBC is designed in [150], where the chosen storage function is different from the one in [101].

Fault-tolerant PBC is proposed in many researches, by combining PBC with other algorithms. An energy management strategy based on passivity-based control using fuzzy logic estimation is proposed for a FC/SCs vehicle in [46], where the fuzzy estimation is capable to determine the desired current of SC according to the SCs SoC and the FC remaining hydrogen quantity.

In [152], a controller using IDA-PBC for a FCHEV with FC/SC/BT is designed with a 8th-order state space equation and the control law is proposed by controlling the duty cycle of the FC, SCs and battery. Faults of the FC are also taken into account by integrating a fault rate into the current equation. The battery current equilibrium trajectory is based on the SoC and the fault of the fuel cell, and it also supplies energy during the FC start-up.

The IDA-PBC controller is designed for a FC/SCs hybrid vehicle in [153]. The multi-phase asynchronous motors driven by rotor flux with minimization of non-sequential components are applied in this research, which increases the reliability of the system in the event of a fault.

2.4.4.2/ TOWARD MICROGRIDS

In order to maintain the bus voltage and to avoid a loop flow current that is caused by the voltage difference between converters and loads, a control strategy is necessary [80] in a microgrid. Several controllers for PV/wind hybrid system are introduced in [154], including PBC.

Since Euler-Lagrange modeling is widely used to present the energy changes on multi-physical hybrid systems, the ”regular” PBC methodology is applied to offer satisfying performance by shaping these energy exchanges in nonlinear systems [149]. In [155], a passivity-based controller with feedback decomposition is implemented for a wind generator, and a passivity-based sliding mode control for the PV panels is also proposed. An application of PBC for a street lighting system is introduced in [156], where the system is powered by a photovoltaic solar panel hybridized with a battery.

As a new type of PBC, IDA-PBC is also applied in the domain of microgrids. In [157], two controllers based on classical Euler-Lagrange PBC as well as IDA-PBC are designed for a PV/battery microgrid ; the results show that EL-PBC has a lower overshoot and a shorter settling time than the IDA-PBC while the steady-state error of IDA-PBC is zero, but there is considerable error for EL-PBC.

In the research of [158], a robust controller based on the IDA-PBC methodology for ensuring high voltage quality of a standalone microgrid is proposed. In [159], IDA-PBC is applied for the device-level controller design for hybrid energy storage systems. An IDA-PBC controller for superconducting magnetic energy storage systems which can support active and reactive power in power distribution system is proposed in [160]. In [161], an innovative IDA-PBC with multi-equilibrium states for controlling a hybrid distributed generation system is presented. It is proven that the proposed IDA-PBC controller can optimally balance power flow distribution in the hybrid system and ensure the stability of the hybrid system in different operating modes. A similar system was also studied in [162], where a full-order IDA-PBC energy control strategy has been proposed.

2.5/ CONCLUSION

This chapter introduced a state-of-the-art about hybrid power systems and controller design, which is divided into two aspects : hybrid electrical vehicles and microgrids. Several electrical components as well as the hybrid power system architecture were presented. Based on this analysis, the parallel FC/SCs FCHEV structure with two converters and the DC-coupled microgrid were chosen for the research in this thesis.

Also, an introduction of the linear and nonlinear controller design methodologies was presented, including the IDA-PBC methodology, which is the controller used in this thesis. All these controllers are based on the same principle, i.e., to decide the power and energy sharing between the sources. However, a perfect coordination of the sources is rarely studied in normal conditions, and even more during abnormal working conditions, such as with power limitations due to aging phenomena or current limitations of the FC or SCs. Therefore, an advanced controller based on IDA-PBC methodology is proposed in this thesis, where the limitations of the components are integrated directly into the controller.

II

EXPERIMENTAL SETUP

3

PHIL AND HIL TEST BENCHES

3.1/ INTRODUCTION

Experimental validations are necessary to demonstrate the performance of controllers. However, the validation using physical experiments in controllable and real time operating conditions is usually expensive. It can also be ineffective, unstable, restricted in regulation and limited in scale [163, 164]. To meet the increasing safety requirements of electronic control systems, experimental testing methods become ineffective in revealing potential safety issues and covering critical test cases [165].

As a consequence, real-time simulation can be applied to validate the controllers, which conjoins software and hardware testing. In the fields of power systems, hardware-in-the-loop (HIL) and power hardware-in-the-loop (PHIL) have been widely used because of the following distinctive features :

- Reduction of the risk of experiments,
- Cost-effective testing,
- Verification of models and methodologies with full efficacy,
- Enable scaleup and validation.

HIL involves only signal exchange which means that there is only signal coupling between the hardware and the virtual system. PHIL is an extension of HIL, which involves real power devices, with virtual exchanges at real power between software and the actual hardware through a power interface.

HIL and PHIL simulation have been applied in many researches [166, 167, 168], for the design, analysis, and testing of electrical power system controllers as well as the simulation of hybrid power system operation. These two methods of real-time simulation could be applied to a system development life cycle, for the design and verification of a proposed project. Fig. 3.1 shows the diagram of the systems engineering process represented by a V-model [169]. It involves the procedures of the early project definition as well as the integration and validation tests, which ensure nothing is done unnecessarily and everything necessary is accomplished.

In this work, the proposed controller was firstly integrated into a dSPACE MicroLabBox on the PHIL test bench discussed in Chapter 4, with real power devices. The PHIL test provides the system dynamic, real-time performance in laboratory environment, which is a step for the detailed design of the controller (see Fig. 3.1). In order to test the feasibility of the controller in industrial practice, the controller was then implemented into a Field Programmable Gate Array (FPGA) board on the HIL platform, using C programming and the hardware description language VHDL. This step enables the integration test and verification of the controller that is indicated in Fig. 3.1.

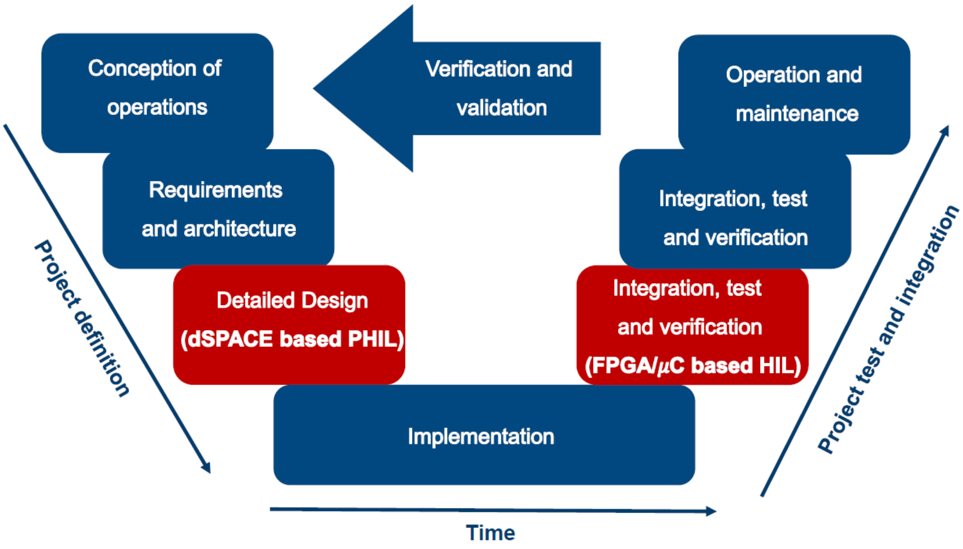

FIGURE 3.1 – The V-model of the systems engineering process [169]

In this section, a PHIL test bench as well as a HIL test bench are introduced. Firstly, the PHIL test bench is detailed in section 3.2, where the hardware construction is realized in [170]. In this work, the main contribution on the PHIL test bench is the software part, which includes the models in Matlab/Simulink (see Appendix A) as well as the real-time controllers (see section 3.2.5). Finally, as part of the ANR project DATAZERO for green datacenter, the communication between the PHIL platform and remote controller is established in JAVA, which enables to integrate the long-term energy management decision. The experimental test results with a rule-based controller connected to the remote controller are provided in section 3.2.6. In this thesis, the PHIL platform was used to validate the proposed advanced passivity-based controller (see Chapter 4) for a vehicle, as well as the IDA-PBC controller for a green data center (see Chapter 6).

Then, an existing HIL platform which was introduced in [171] is described in 3.3 and updated for the needs of this work. The proposed controller as well as the system emulator are integrated into the HIL platform, in order to validate the application of the aging-tolerant passivity-based controller on a commercial vehicle, for industrial practice (see Chapter 5).

3.2/ POWER HARDWARE-IN-THE-LOOP TEST BENCH

3.2.1/ OVERVIEW

A PHIL simulation system consists of three parts : software, hardware and their interface that provides digital and analog input/output (I/O) signals [172]. In our platform, the emulated system is implemented with the Matlab/Simulink tools and uploaded to a dSPACE MicroLabBox. Fig. 3.2 describes the test bench formed by the following components :

- A host PC,
- A dSPACE MicroLabBox,
- A measurement and acquisition card and pulse width modulation (PWM) generation card,
- PV panels and their converter (boost),
- SCs and lead-acid batteries for energy storage,
- Bi-directional converters for the SCs and batteries,
- An electronic load to emulate the load as well as the electrolyzer,
- A power supply to emulate the FC.

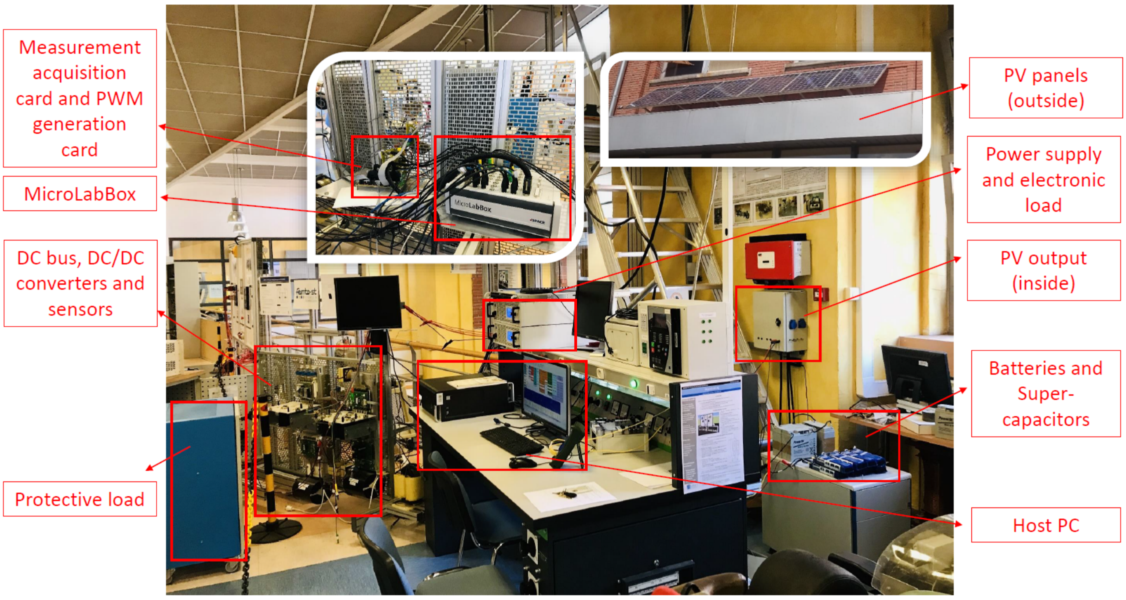

FIGURE 3.2 – PHIL platform

3.2.2/ ELECTRICAL DEVICES CHARACTERISTICS

The PV array consists of six PHOTOWATT PW1650-24V PV modules, which are connected in 2x1 serial-parallel connection in three separate groups, as shown in Fig. 3.3. Based on the system requirements (voltage limit) of the test bench, the DC bus voltage should not exceed 100 V, only one group (two PV modules) is connected to the test bench.

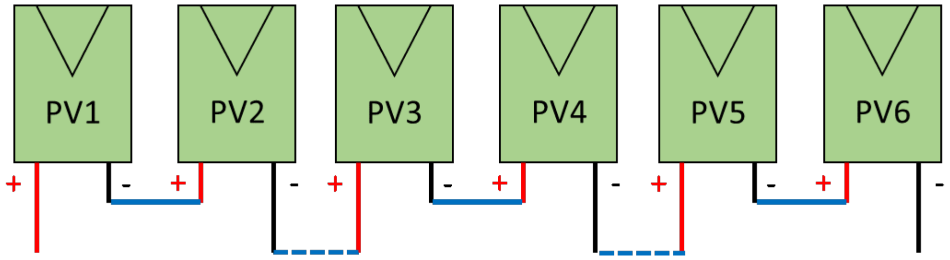

FIGURE 3.3 – Electrical connection of the PV modules

Since the DC bus voltage is set to 70 V, the sizing of the energy storage is configured based on the desired power and the voltage level of each element. The Maxwell BPAK0058-

E015 SCs are applied to this platform, with four in series and two in parallel. Also, three Powerfit S312/18 G5 type lead-acid batteries in series are installed.

PV module characteristics PW1650-24V	
Power (at MPP)	165 [W]
Voltage (at MPP)	34.4 [V]
Current (at MPP)	4.8 [A]
Voltage (open circuit)	43.2 [V]
Current (short circuit)	5.1 [A]
Characteristics of the SCs Maxwell BPAK0058-E015	
Capacitance	58 [F]
Voltage Rating	15 [V]
Characteristics of the lead-acid battery S312/18 G5	
Capacity	18 [Ah]
Voltage Rating	12 [V]
Weight	5.8 [kg]
Characteristics of the electronic load EA-ELR 9080-510	
Voltage Adjustment Range	0 - 80 [V]
Current Adjustment Range	0 - 510 [A]
Power Adjustment Range	0 - 10.5 [kW]
Weight	31 [kg]
Characteristics of the power supply EA-PSI 9080-340	
Voltage Adjustment Range	0 - 80 [V]
Current Adjustment Range	0 - 340 [A]
Power Adjustment Range	0 - 10 [kW]
Weight	20 [kg]
Characteristics of the DC bus	
Cell capacity	3300 [μF]
Number of cells in parallel	6
Maximum voltage	100 [V]
Total capacity	19.8 [mF]
Characteristics of the converters	
FC inductance L_{fc}	100 [mH]
SCs inductance L_{sc}	100 [mH]
Batteries inductance L_{bat}	100 [mH]
PV inductance L_{pv}	100 [mH]

TABLE 3.1 – PHIL hardware parameters

The power supply EA-PSI 9080-340 and the electrical load EA-ELR 9080-510 are connected directly to the DC bus, for emulating the hydrogen system (fuel cell, electrolyzer and hydrogen tank) that are not integrated with real devices. Moreover, the electronic load is also used to emulate the load power consumption.

Two bi-directional converters are connected to the DC bus for the connection of batteries and SCs by boosting up the voltage output of these electrical resources. The bi-directional converter is capable of providing two-way power flow between the DC bus and the electrical resources (for example : charging/discharging the batteries). A boost converter is connected to the DC bus for boosting up the voltage output of the PV panels. The boost converter is only capable of providing one-way power flow from the PV array to the DC bus.

In the test bench, the DC bus is designed by connecting capacitors in parallel. The total capacity of the DC bus is 19.8 mF with a maximum voltage of 100 V. Thus, the operating voltage is always kept under 100 V in all cases. Finally, the parameters of each element are shown in Tab. 3.1.

3.2.3/ TEST BENCH CONNECTION

In Fig. 3.4, the electrical connections of the equipment are presented in details. The PV panels are connected to the boost converter while the SCs and batteries are connected to the bi-directional converters. As seen in the figure, the electronic load and the power supply are directly connected to the DC bus. The electronic load is used for emulating the electrolyzer with its converter as well as the load (vehicle, datacenter, etc.). The power supply is used for emulating the fuel cell with its converter. An introduction of the HESS emulator can be found in Appendix A.3.

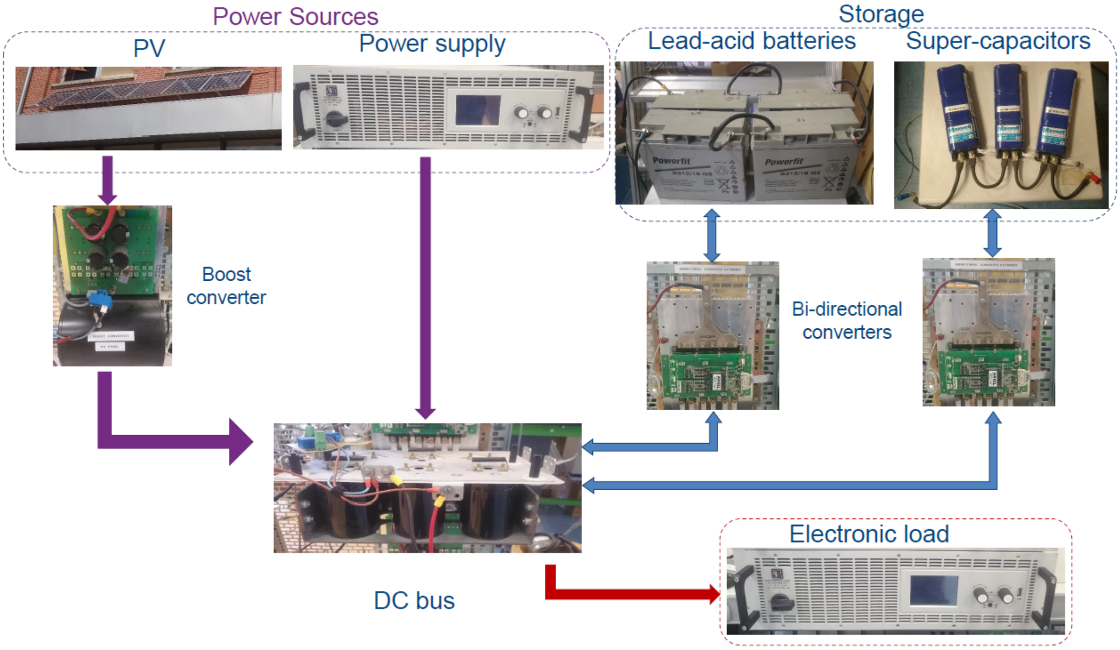

FIGURE 3.4 – Power devices of the PHIL platform

To be able to gather the required power output from these two elements, current and voltage sensors are connected. The current of SCs, battery, and PV (i_{pv},i_{sc},i_{bat}) are measured by current sensors LEM HAS 50-S while the voltages (v_{bus},v_{pv},v_{sc},v_{bat}) are measured by the voltage sensor LEM LV 25-P. These sensors are designed based on the Hall effect measuring principle. On the other hand, the power supply and electronic load are directly connected to the DC bus without using any converter and sensor. Measurements are taken from the device using analog inputs.

In this test bench, the outputs of the sensors are connected to the analog inputs of the MicroLabBox to gather current/voltage measurements of the electrical components. The duty cycle of each converter is sent via a PWM signal, and the requested current/voltage values of the power supply and the electronic load are sent via analog output (DAC). The connection between the Host PC and the MicroLabBox is done via the university ethernet network.

The MicroLabBox not only serves as an interface between software and hardware, but also operates as a real-time emulator. Firstly, the real-time applications are modeled and compiled on Matlab software using the dSPACE toolbox, and then loaded to the MicroLabBox microprocessor board and finally displayed on the human-machine interface (HMI) in ControlDesk (see Appendix B). There are two boards in the MictroLabBox, the real-time controller algorithm runs on the DS1202 board, which operates as a real time processor. The DS1302 board is connected with the connector panel which provides an I/O interface for generating and measuring real-time signals with analog I/O and digital I/O.

There are three steps to realize the real-time control of the system. Firstly, the current (i_{pv},i_{sc},i_{bat}) and voltage (v_b,v_{pv},v_{sc},v_{bat}) measurements are received from the analog inputs of the MicroLabBox, and converted to digital signals. An acquisition card is used in order to receive these measurement signals and send them to the ADC ports of the MicroLabBox after conversion. Then the processor on the DS1202 board computes the reference current of each element with the energy management algorithm. The duty cycle of the PWMs are computed by the IP current loops and sent via the the digital I/O to generate the PWM signal. Finally, the PWM signal is sent to the converter driver (ARCAL E+3P) via an interface card in order to control the output current to its reference. Also, the PWM can be activated/deactivated via the digital I/O channel. Differently, the FC reference current is converted to analog signals and sent to the power supply via the DAC output, as well as for the eletrolyzer reference current.

3.2.4/ IP CONTROLLER OF THE CURRENT LOOP

In order to control the current flowing in or out of the SCs with respect to the reference current set by the energy management strategy, an IP controller of the SCs current loop is designed.

Fig. 3.5 presents the structure of the IP controller. This controller has the integral part in the feed forward path and the proportional part in the feedback path. Compared to a PI controller, the advantage of the IP controller is that it can reduce the high peak overshoot [173]. The non-linear system state space model of the SCs current is :

$$\frac{d}{dt} i_{sc} = \frac{-(1-\alpha_1)v_b + v_{sc}}{L_{sc}} \tag{3.1}$$

where α_1 is the duty cycle of the PWM control, L_{sc} is the inductance of the converter. The modeling is detailed in section 4.2.3.

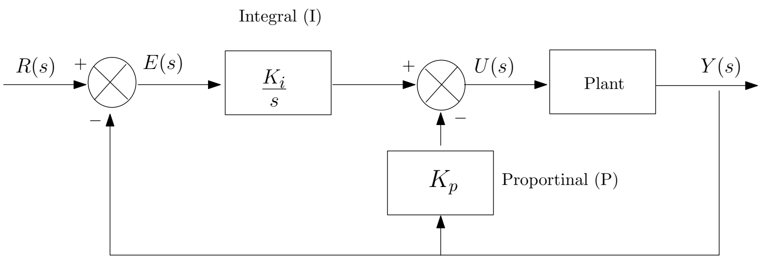

FIGURE 3.5 – Block diagram of IP controller

The first step of IP controller design is the linearization : setting $-(1-\alpha_1)v_b + v_{sc} = \tilde{V}$, we have

$$\begin{aligned} \frac{d}{dt} i_{sc} &= \frac{\tilde{V}}{L_{sc}} && (3.2) \\ \alpha_1 &= 1 + \frac{\tilde{V} - v_{sc}}{v_b} && (3.3) \end{aligned}$$

The IP controller in continuous time is :

$$\tilde{V} = \frac{K_{i-i_{sc}}}{s}(i_{sc}^* - i_{sc}) - K_{p-i_{sc}} i_{sc} \tag{3.4}$$

The structure of the IP controller can be seen in Fig. 3.6 :

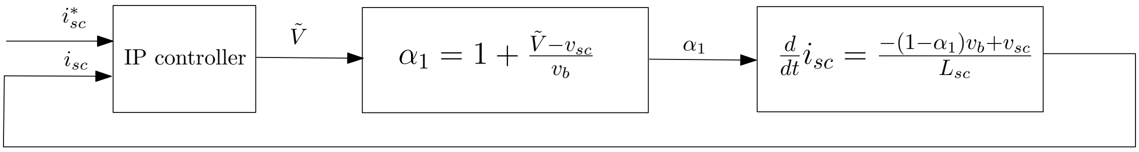

FIGURE 3.6 – IP controller

In order to determine parameters $K_{p-i_{sc}}$ and $K_{i-i_{sc}}$, we have :

$$\frac{i_{sc}}{i_{sc}^*} = \frac{1}{1 + \frac{K_{p-i_{sc}}}{K_{i-i_{sc}}} s + \frac{L_{sc}}{K_{i-i_{sc}}} s^2} \tag{3.5}$$

It is known that the transfer function of a 2nd order system can be written as :

$$\frac{i_{sc}}{i_{sc}^*} = \frac{1}{1 + \frac{2\xi}{\omega_n} s + \frac{1}{\omega_n^2} s^2} \tag{3.6}$$

where ξ is the damping ratio, ω_n is the natural (or resonant) frequency of the system. By matching equations (3.5) and (3.6), $K_{p-i_{sc}}$ and $K_{i-i_{sc}}$ can be determined from the system parameters :

$$\begin{aligned} K_{i-i_{sc}} &= L_{sc} \omega_n^2 && (3.7) \\ K_{p-i_{sc}} &= 2\xi L_{sc} \omega_n && (3.8) \end{aligned}$$

Then the controller needs to be discretized in order to implement it with a real-time processor in the MicroLabBox. With a Tustin approximation, the IP controller with an anti-windup feedback is :

$$\begin{aligned} \tilde{V}[k] &= -K_{p-i_{sc}} i_{sc}[k] + I[k] && (3.9) \\ I[k] &= I[k-1] + \frac{T_{ei}}{2} K_{i-i_{sc}} (\tilde{i}[k-1] + \tilde{i}[k]) + \tilde{V}_{out}[k-1] - \tilde{V}[k-1] && (3.10) \end{aligned}$$

where $\tilde{i} = i_{sc}^{*} - i_{sc}$, $\tilde{V}_{out}$ is the output of the saturation, which ensures the duty cycle between 0.02 and 0.98, in order to protect the MOSFETs in the converters. According to (3.3), the upper and lower limits of this dynamic saturation function are :

$$\begin{aligned} \tilde{V}_{min} &= v_{sc} + (\alpha_{1_{min}} - 1)\, v_b = v_{sc} - 0.98 v_b && (3.11) \\ \tilde{V}_{max} &= v_{sc} + (\alpha_{1_{max}} - 1)\, v_b = v_{sc} - 0.02 v_b && (3.12) \end{aligned}$$

With the same procedure, the IP controller of the battery current can be designed as follows :

$$\begin{aligned} \tilde{V}[k] &= -K_{p-i_{bat}} i_{bat}[k] + I[k] && (3.13) \\ I[k] &= I[k-1] + \frac{T_{ei}}{2} K_{i-i_{bat}} (\tilde{i}[k-1] + \tilde{i}[k]) + \tilde{V}_{out}[k-1] - \tilde{V}[k-1] && (3.14) \end{aligned}$$

where $\tilde{i} = i_{bat}^{*} - i_{bat}$, $\tilde{V}_{out}$ is the output of the saturation, with the upper and lower limits :

$$\begin{aligned} \tilde{V}_{min} &= v_{bat} - 0.98 v_b && (3.15) \\ \tilde{V}_{max} &= v_{bat} - 0.02 v_b && (3.16) \end{aligned}$$

The natural frequency ω_n is determined by the choice of the response time t_R (at 95 %) and the damping ratio ξ :

$$\omega_n = \frac{4.8}{t_R}\ (for\, \xi = 1) \qquad (3.17)$$

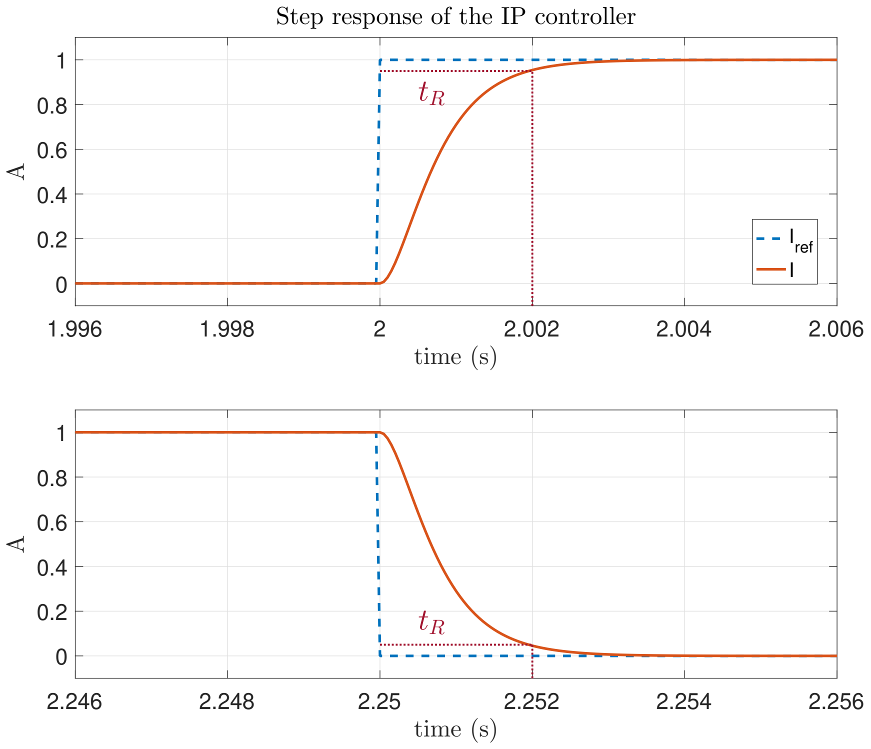

FIGURE 3.7 – Simulation result for a step response

In this work, t_R is determined as 40 times the sampling time Ts (50 μs), which is 0.002 s. Fig. 3.7 shows the step response of the IP controller, with $\xi = 1$. The output current follows the reference value with a response time of about 0.002 s, which corresponds to the theoretical configuration.

3.2.5/ RULE-BASED CONTROL AND REMOTE CONTROL CONNECTION

The test bench can work at two modes : the isolated mode and the connected mode. For the isolated mode, the DC microgrid test bench is controlled only by the local controller that is integrated on the PHIL system. In the connected mode, the microgrid is controlled by both the local controller and the remote controller, which means that the local controller receives the long-term energy management decision from the remote controller and considers it in the real-time control.

Two real-time controllers are proposed for the PHIL test-bench : a rule-based controller and a passivity-based controller. The rule-based control is a basic method which is applied to test the whole system and enables to connect with the PDM (see section 2.3.3.1). The passivity-based control is a high performance controller, which has been presented in section 2.4. It realizes the stability of the system automatically with a smooth response from the FC side. However, the connection between the PBC and the PDM has not been established yet. As a part of the DATAZERO project, the rule-based control is firstly applied in order to test the function of the system as well as the remote controller connection. In Chapter 5, the operation of the passivity-based controller in isolated mode is presented.

3.2.5.1/ ISOLATED MODE

The rule-based controller is proposed at first in isolated mode, in order to test the operation of the whole system. The main idea of this controller is that the battery serves as the primary storage source with PV as the main source and the HESS acts as a secondary, longer term storage. A load cycle is emulated by the electrical load. If the PV production is higher than the load demand power, the battery is first charged and then the EL is activated if the battery is fully charged ; otherwise, if the PV production is lower than the load power, the battery discharges first and then if the battery SoC is low, the FC is activated.

3.2.5.2/ CONNECTED MODE

The optimization results for this commitment (or scheduling) generally assign control decisions for long-term operation such as hours. However, in real time, the long-term decisions may create unbalances between actual generation and consumption due to environmental conditions (i.e., solar radiation uncertainty). In such cases, the mismatch between generation and consumption should be addressed really fast in real time to ensure system stability. Therefore, the short-term control algorithm, which uses the determined power output values of the remote controller, alters the determined amounts based on a set of rules.

The open-source messaging software ActiveMQ [174] is applied as the message bridge between the remote controller and the PHIL test bench. As shown in Fig. 3.8, the data transfer between the remote control and PHIL is realized using different message formats. The transformation of the data format is realized by a bridge program in Matlab and a receiver program in Java.

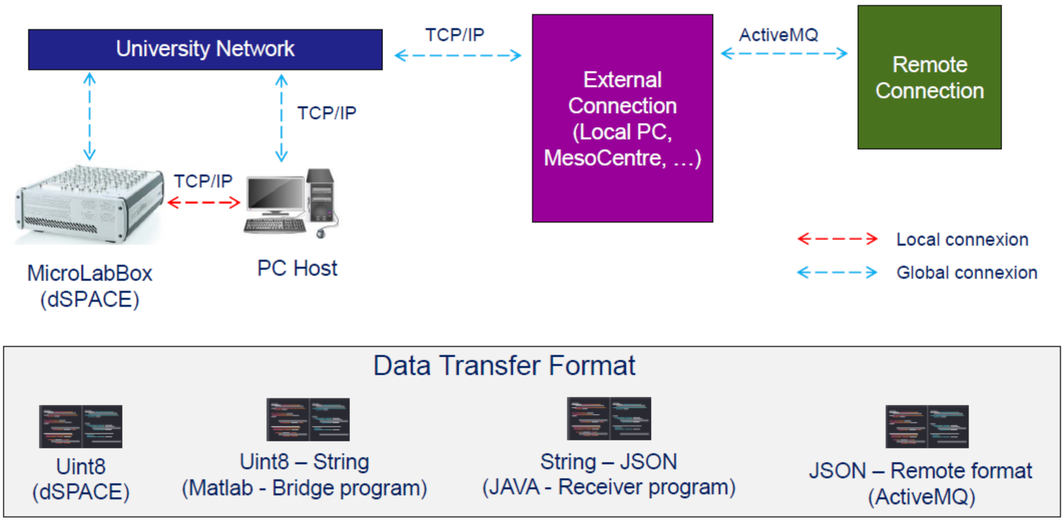

FIGURE 3.8 – Remote connection of the test bench

When the system is connected with the remote controller, the real-time controller needs to consider the remote controller commitments for each electrical resource received from ActiveMQ. The power of each element follows the remote commitment and is adapted by the real-time controller based on the rules listed in section 3.2.5.1, according to the real-time conditions (i.e., PV production, stabilization).

3.2.6/ EXPERIMENTAL TEST WITH RULE-BASED CONTROL

3.2.6.1/ ISOLATED MODE

The experimental results of the rule-based controller in isolated mode are shown in Fig. 3.9. In reality, for the PHIL short-term test, the battery will be charged at the reference SoC level during the start procedure (see Appendix A.2), the HESS system will not be used since the battery SoC level will not change a lot in such a short period. That is the reason why, from the power curves in Fig. 3.9, the FC and EL power are always zero while the battery supplies the energy that the PV cannot afford and is charged by the extra energy (from 195 s to 200 s). From the voltage curves in Fig. 3.9, we observe that the DC bus voltage is stabilized at the reference value (70 V) using the battery. The battery reference current is determined by the rule-based controller and then the duty cycle for the PWM control is calculated by the IP current loop, which is shown by the duty cycle display. The duty cycle of the PV current is also presented in this part, and is determined by the MPPT algorithm through PWM control. Since the HESS system is not used in this test, the setting current of the electrical load is determined only by the load cycle emulator while the setting current is 0 for the power supply (FC emulator).

Ic...	Name	Value	Raster	Platform	Unit
🟥	I_V_load_set/p_load	69.6872	HostService	Platform	
🟪	MATLAB Function/Pel_display	0	HostService	Platform	
🟨	MATLAB Function/Pfc_display	0	HostService	Platform	
🟩	P_Bat/Out1	-83.3716	HostService	Platform	

I...	Name	Value	Raster	Platform
🟩	V_Battery3/Out1	36.5923	HostService	Platfor
🟥	V_bus/Out1	69.6872	HostService	Platfor
🟧	V_PV/Out1	59.389	HostService	Platfor

I...	Name	Value	Raster	Platform	Unit
🟩	I_Battery/O...	-2.27839	HostService	Platform	
🟧	I_PV/Out1	3.1879	HostService	Platform	
☒	I_SC/Out1	---	HostService	Platform	
🟥	I_V_load_s...	1	HostService	Platform	

I...	Name	Value	Raster	Platform
🟩	duty_cycle_bat/Out1	0.422999	HostService	Platfor
☒	Duty_cycle_el/Out1	---	HostService	Platfor
☒	Duty_cycle_fc/Out1	---	HostService	Platfor
🟧	Duty_cycle_pv1/Out1	0.264	HostService	Platfor

FIGURE 3.9 – Experimental result of rule-based controller in isolated mode

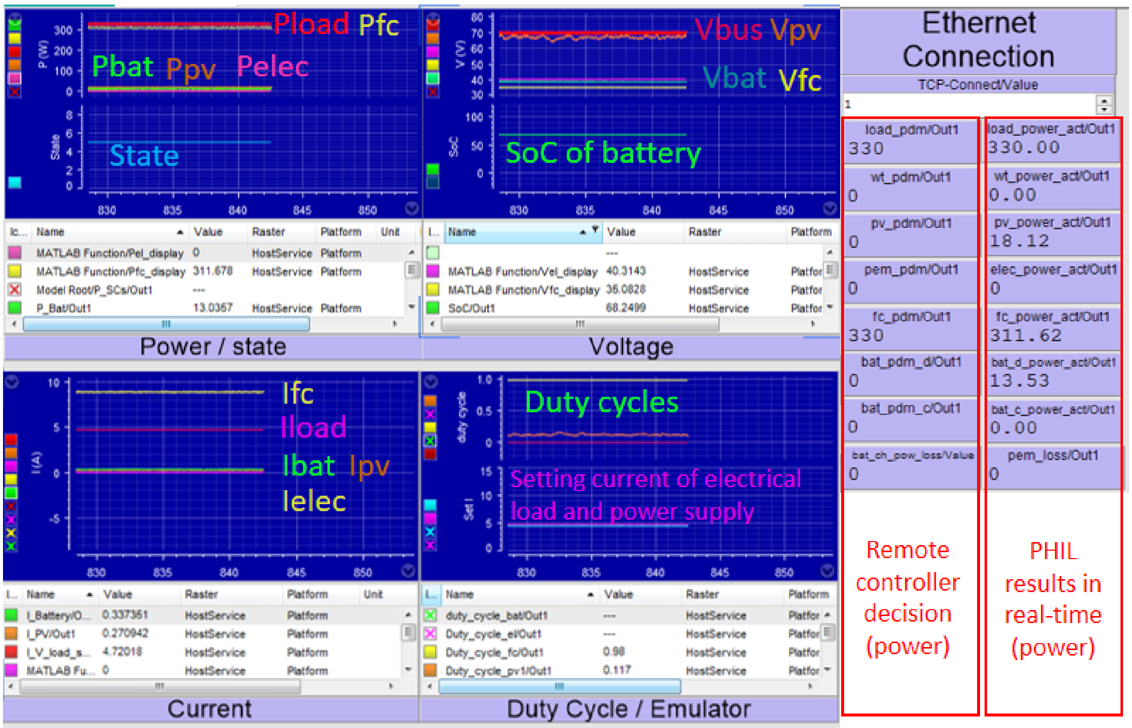

Ic...	Name	Value	Raster	Platform	Unit
🟪	MATLAB Function/Pel_display	0	HostService	Platform	
🟨	MATLAB Function/Pfc_display	311.678	HostService	Platform	
☒	Model Root/P_SCs/Out1	---			
🟩	P_Bat/Out1	13.0357	HostService	Platform	

I...	Name	Value	Raster	Platform
☐		---		
🟪	MATLAB Function/Vel_display	40.3143	HostService	Platfor
🟨	MATLAB Function/Vfc_display	35.0828	HostService	Platfor
🟩	SoC/Out1	68.2499	HostService	Platfor

I...	Name	Value	Raster	Platform	Unit
🟩	I_Battery/O...	0.337351	HostService	Platform	
🟧	I_PV/Out1	0.270942	HostService	Platform	
🟥	I_V_load_s...	4.72018	HostService	Platform	
🟪	MATLAB Fu...	0	HostService	Platform	

I...	Name	Value	Raster	Platform
☒	duty_cycle_bat/Out1	---	HostService	Platfor
☒	Duty_cycle_el/Out1	---	HostService	Platfor
🟨	Duty_cycle_fc/Out1	0.98	HostService	Platfor
🟧	Duty_cycle_pv1/Out1	0.117	HostService	Platfor

TCP-Connect/Value
1

load_pdm/Out1 330	load_power_act/Out1 330.00
wt_pdm/Out1 0	wt_power_act/Out1 0.00
pv_pdm/Out1 0	pv_power_act/Out1 18.12
pem_pdm/Out1 0	elec_power_act/Out1 0
fc_pdm/Out1 330	fc_power_act/Out1 311.62
bat_pdm_d/Out1 0	bat_d_power_act/Out1 13.53
bat_pdm_c/Out1 0	bat_c_power_act/Out1 0.00
bat_ch_pow_loss/Value 0	pem_loss/Out1 0

FIGURE 3.10 – Experimental results of the rule-based controller in connected mode

3.2.6.2/ CONNECTED MODE

The connection between the PHIL test bench and the remote controller (PDM) is established via ActiveMQ. The test case is realized using the information from the PDM. After the communication is established between the remote controller and the PHIL test bench, the PDM commitments are received. Fig. 3.10 shows the real-time curves of each equipment as well as the remote commitments. Using the received commitments (Load : 330 W, PV : 0 W, Bat : 0 W, FC : 330 W, EL : 0 W, Loss : 0 W), the power consumption of the datacenter is emulated by the electrical load and the short term control algorithm determines the output values of battery and hydrogen sources using the actual PV power outputs (Total Load : 330 W, PV : 18.12 W, Battery : 13.53 W, FC : 311.62 W, EL : 0 W). In the real system, the generation of PV system is more than the expected power generation (0 W). That is the reason why the FC generates less power than the commitment. The difference between the real production and the consumption is mainly caused by the real system losses of about 13 W, which are supplied by the batteries. These losses may be caused by the converter losses or cable losses. Also, we can see that the DC bus voltage is stable around its reference value by the batteries, which means that the stability of the system is maintained.

3.3/ HARDWARE-IN-THE-LOOP TEST BENCH

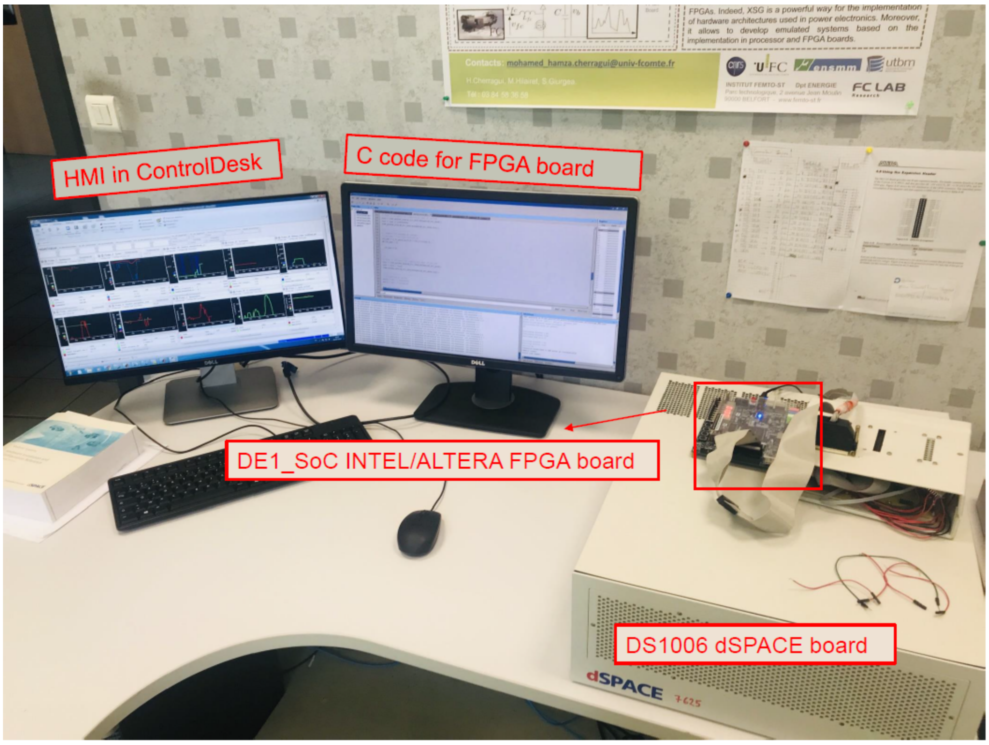

FIGURE 3.11 – Hardware-in-the-loop platform

Although PHIL is an extension of HIL, the controller also needs to be validated by a HIL test. Firstly, there are constraints on the real power devices. For example, in this work, to further validate the real-time operation of the proposed passivity-based control and prognostic algorithm, with an application on a commercial vehicle (see Chapter 5), the DC bus voltage needs to be kept around 550 V while the maximum voltage of the DC bus of the PHIL platform is 100 V. Therefore, an implementation and experiment were conducted using a HIL platform, as shown in Fig. 3.11. Secondly, on the applied HIL platform, the energy management algorithm was implemented on a System On Chip (SoC) FPGA board, which is a FPGA/μC board. Unlike the dSPACE devices, the SoC board is a real controller board that has been generally used in industrial practice. Therefore, as shown in the V-model diagram in Fig. 3.1, an SoC-based HIL test could be the next step after the PHIL test on a dSPACE board.

The test bench consists of two parts : a SoC FPGA board (DE1_SoC INTEL/ALTERA Field Programmable Gate Array) for the control and dSPACE boards for the emulation of the system. On the host PC, the Matlab/Simulink programs are downloaded into the dSPACE boards and a HMI in ControlDesk plots the collected data of the emulator. The same host PC is used to program the SoC FPGA and to collect some data.

In this section, the introduction of the hardware can be seen in section 3.3.1 while the presentation of the software part is detailed in section 3.3.2.

3.3.1/ HARDWARE INTRODUCTION

The equipment under test is a control board based on a DE1_SoC INTEL/ALTERA FPGA board, where the algorithms are implemented in a NIOS II microcontroller. An aging-tolerant passivity-based control is integrated into the HIL platform, in order to validate the application on a FC/SCs hybrid vehicle. The fuel cell State-of-Health (SoH) is estimated by an Extended Kalman Filter (EKF) while the energy management is realized by the IDA-PBC controller. Fig. 3.12 shows the structure of the HIL platform based on two equipment, i.e., dSPACE boards to emulate the hybrid system and communicate with the controller, and the DE1_SoC board for the implementation of the controller and EKF algorithms.

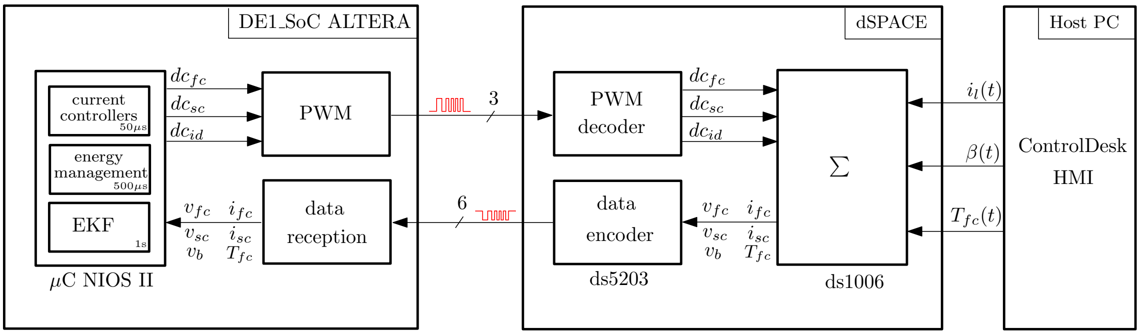

FIGURE 3.12 – Hardware-in-the-loop scheme

On the DS1006 dSPACE board, the model of the hybrid system is computed every 50 μs with a Runge-Kutta algorithm. The designer can modify the load profile, FC temperature and speed of degradation ($\beta(t)$) of the FC.

All the data necessary for the control and SoH estimation are sent to the ALTERA board with 32 bit serial ports (in 32Q14 format, i.e., 14 fractional bits) to emulate CAN converters. The data encoders are implemented in a VHDL black box from XSG (Xilinx System Generator). The 3 PWM signals generated by the ALTERA FPGA are decoded in the

DS5203 dSPACE board to retrieve the duty cycles of the 3 converters.

The DE1_SoC ALTERA FPGA board is composed of 3 blocks : 3 PWMs, 6 data decoders and a NIOS II microcontroller. The algorithms are executed in 3 Interrupt Service Routines (ISR), based on 3 timers configured with a sampling time equal to 50 μs for the current loops and PWMs, 500 μs for the energy management, and 1 s for the EKF algorithm. Timer 0 for the current loop control uses a timeout pulse of one clock cycle in order to reset the PWM counter and therefore synchronize the ISR and PWM signals.

The 3 ISRs for the current loops, energy management, and EKF algorithm use vectorized interrupts in order to manage the interrupts priorities. The computation times of the ISRs are respectively equal to 7.20 μs, 9.84 μs and 117 μs, as shown in Fig. 3.13.

The implementation of the proposed IDA-PBC does not introduce additional difficulty compared to regular controllers [101]. The only requirement is that the sampling time of the outer power management control loop must be less than 5 ms [175], in order to have a stable closed loop system. That is the reason why a value equal to 500 μs is selected for energy management.

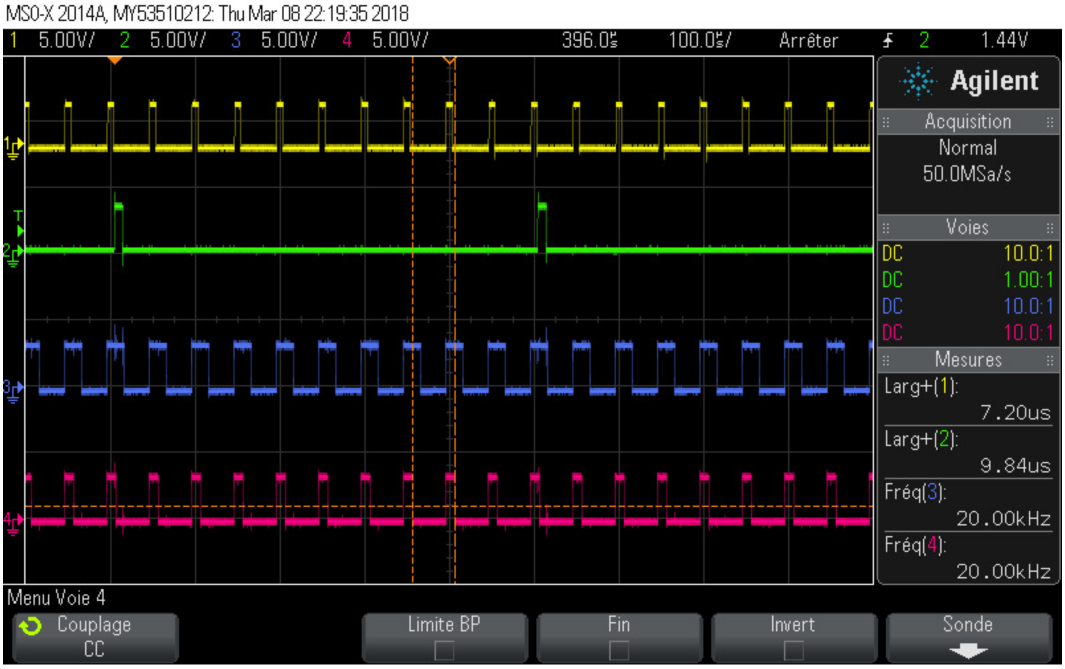

MSO-X 2014A, MY53510212: Thu Mar 08 22:19:35 2018

1 5.00V/ 2 5.00V/ 3 5.00V/ 4 5.00V/ 396.0µs 100.0µs/ Arrêter ⨍ 2 1.44V

Acquisition
Normal
50.0MSa/s

Voies
DC 10.0:1
DC 1.00:1
DC 10.0:1
DC 10.0:1

Mesures
Larg+(1): 7.20us
Larg+(2): 9.84us
Fréq(3): 20.00kHz
Fréq(4): 20.00kHz

Menu Voie 4
Couplage CC

FIGURE 3.13 – HIL scheme : 1) computation time of Timer 0 (for current loop), 2) computation time of Timer1 (for energy management), 3) FC PWM, 4) SCs PWM

3.3.2/ SOFTWARE INTRODUCTION

Fig. 3.14 presents the Simulink models of the HIL platform, with a simplified diagram that represents the role of each part. In this system, the controller was firstly implemented into the dSPACE boards for simple tests through zones 1 and 2, and then validated into the SoC FPGA by changing the state of the switches (blue circles). In the last situation, the duty cycles come from the DS5203 dSPACE board (zone 6) to the emulated system (zone 3) by blocks in zone 4. Similarly, data computed into the emulated system is sent to the DS5203 dSPACE board (zone 6) by blocks in zone 5.

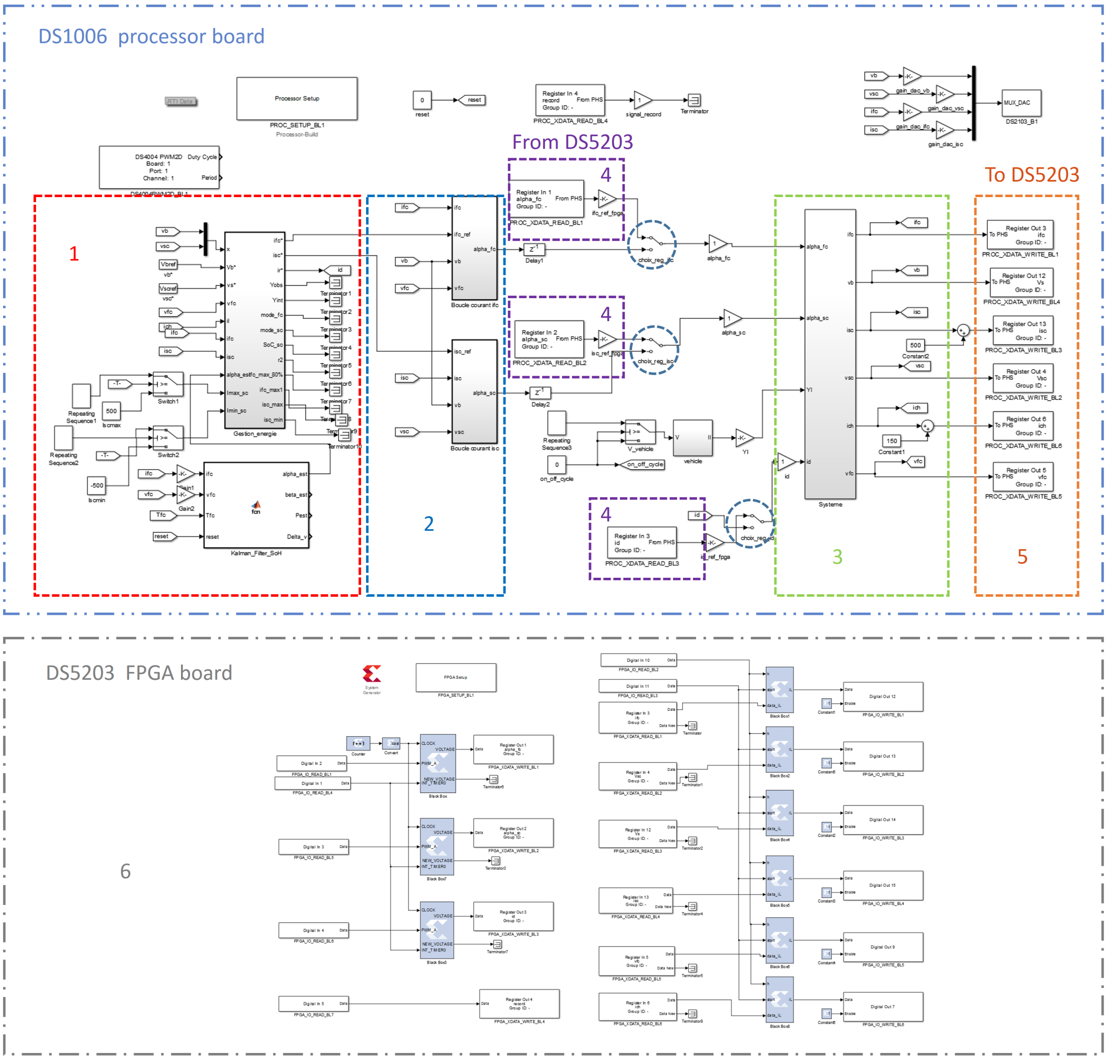

FIGURE 3.14 – Models in Matlab/Simulink

A HMI is established in ControlDesk, as shown in Fig. C.2 of Appendix C, where the reset and system settings can be changed. Currents, voltages and other signals of the emulated system are displayed in the HMI and all the data can be stored in .mat format to be plotted in Matlab. The control algorithms are integrated into the SoC FPGA board by C codes, using the Intel FPGA Monitor Program shown in Fig. C.1 of Appendix C. Some data of the controller is also displayed in the terminal.

The design and the configuration of the HIL platform is realised and detailed in [171]. In Chapter 5, the proposed controller is implemented into the FPGA board by C programming, in order to demonstrate the feasibility of the controller.

3.4/ CONCLUSION

In this section, two test benches were presented : the PHIL platform and the HIL platform, which will be used in the following chapters to validate the proposed controller in this thesis. In order to validate the operation of the hybrid system with the controller, the real-time simulation by PHIL is required. With real power exchanges in the system, the dynamic behavior of each element can be considered into the controller, as well as the validation of the control operation in real applications. In order to validate a controller algorithm in industrial practice, the HIL is usually applied.

An application of the PHIL platform for the green datacenter project DATAZERO was also presented in this chapter. A rule-based controller is integrated into the platform as the local real-time control while the long-term decision from the remote controller is considered into the local short-term controller.

In this thesis, an advanced passivity-based controller is firstly validated by the PHIL platform under a given scenario (Chapter 4). Then it is combined with an aging-tolerant algorithm and is validated by the HIL platform for vehicle application (Chapter 5). An passivity-based controller is also proposed for microgrid application and validated by the PHIL platform (Chapter 6).

III

CONTRIBUTION

4

ADVANCED PASSIVITY-BASED CONTROL FOR A FC/SCs HYBRID POWER SYSTEM

4.1/ INTRODUCTION

As presented in Chapter 1, using hydrogen and fuel cells is a promising way to deal with environmental problems and fossil fuels shortage. As electric and hybrid vehicles are becoming more and more popular, FCHEVs are also considered due to their fast recharge time, low weight and controllability. For several decades, FCHEVs have been developed with the goal of decreasing air pollution, oil dependence as well as greenhouse gases emissions.

In order to increase their lifetime, FCs must have slow power dynamics and a hybrid source system is, therefore necessary. Usually, in a FC hybrid system, the FC is the main power source and batteries or SCs are transient power sources. A FC is usually associated with SCs for their high dynamics, as batteries sometimes cannot sustain very high power charge and discharge conditions. Therefore, compared to a FC/BTs hybrid system, a FC/SCs source has better performance [176]. SCs are often considered as the best choice for fast power demands due to their ability to operate well at low temperatures, and are industrially manufactured [6].

In this chapter, an energy management strategy based on IDA-PBC for a FC/SCs hybrid system is proposed, which is a significant extension of previous work [101, 175]. This chapter is organized as follows : section 4.2 describes the hybrid system modeling ; in section 4.3, a general controller is designed for the hybrid system using the IDA-PBC methodology ; then an advanced passivity-based controller is detailed in section 4.4, by determining the control parameters of the general controller ; in section 4.5, the simulation results in different situations as well as a comparison with previous work are presented ; the experimental validation of the controller by a PHIL platform is introduced in section 4.6 ; finally, conclusions and discussions are drawn in section 4.7.

4.2/ HYBRID SYSTEM MODELING AND CONTROL STRUCTURE

4.2.1/ POWER ELECTRONIC ARCHITECTURE

In this work, a two-converter parallel structure of a FC/SCs system is studied, which could be applied in a hybrid FCV, as shown in Fig. 4.1. Here, the architecture of the power management control as well as the architecture of the power converters are represented.

Since the DC bus voltage is higher than the FC and SCs voltage, the FC is connected to the DC bus through a boost converter while SCs are connected with a reversible boost converter. In order to model generative and motor conditions, the load is modeled by a variable current source. Moreover, a controllable load is added to protect the system from DC bus over-voltage. In the case of current/voltage limitations of the SCs during a generative operation mode of the load, this additional dissipating resistance load is activated to dissipate the extra energy of the DC bus. Without this protection, the DC bus voltage can rise significantly and the dissipative charge is here to prevent such circumstances, such as in railway or automotive applications.

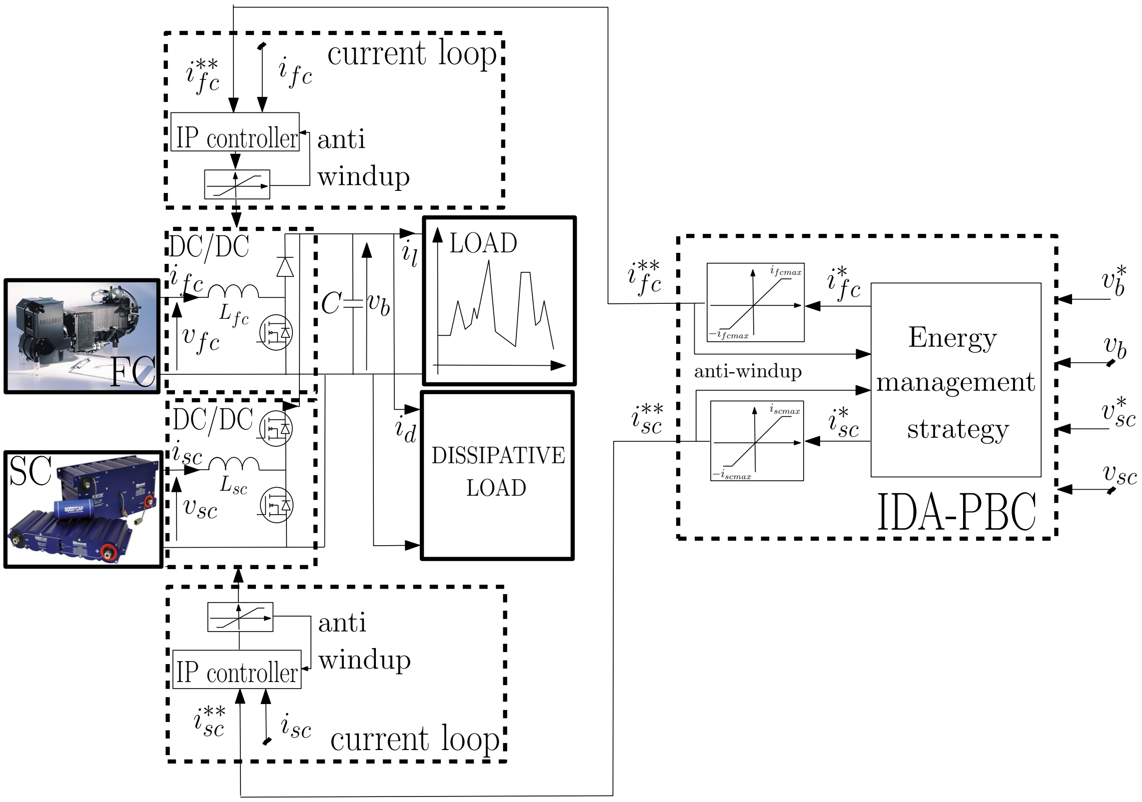

FIGURE 4.1 – Two-converter structure and control architecture

4.2.2/ FC AND BOOST CONVERTER MODEL

A static model of the fuel cell [177] is employed, where FC voltage v_{fc} is computed according to experimental stack current i_{fc} by a 5^{th} order polynomial function [101] as shown in Fig. 4.2 :

$$v_{fc}(t) = a_5 i_{fc}^5(t) + a_4 i_{fc}^4(t) + a_3 i_{fc}^3(t) + a_2 i_{fc}^2(t) + a_1 i_{fc}(t) + a_0 \tag{4.1}$$

where coefficients a_i ($i \in [0,5]$) were determined based on real current/voltage measurements on a Nexa Ballard FC (46 A/1200 W) [101], and are shown in Tab. 4.1.

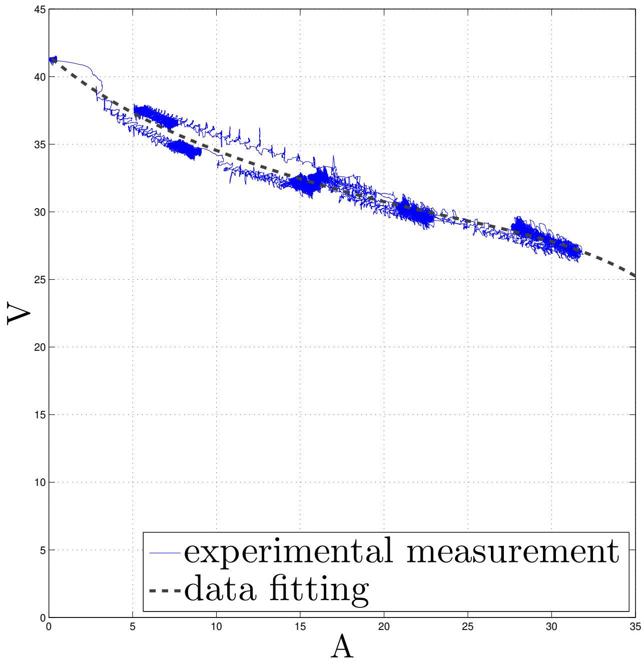

FIGURE 4.2 – V-I curve of fuel cell [101]

Parameter	Value
a_5	-8.8233 × 10^{-7}
a_4	7.3877 × 10^{-5}
a_3	-0.0026197
a_2	0.056074
a_1	-1.0618
a_0	41.524

TABLE 4.1 – FC parameters

The FC is associated with a boost converter, shown in Fig. 4.3. There are two states of the switch during a PWM period T_{PWM} : on-state and off-state. Therefore, the PWM period is divided into two parts by the duty cycle α_1, which is calculated by the IP current loop (see section 3.2.4). Fig. 4.4 shows a state space model of the boost converter, based on these two states. Finally, the boost converter can be described by an average model :

$$\frac{d}{dt} i_{fc}(t) = \frac{-(1-\alpha_1(t))\ v_b(t) + v_{fc}(t)}{L_{fc}} \tag{4.2}$$

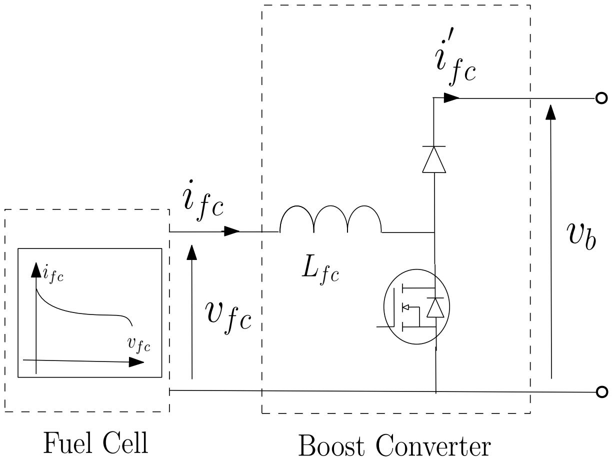

FIGURE 4.3 – FC and boost converter

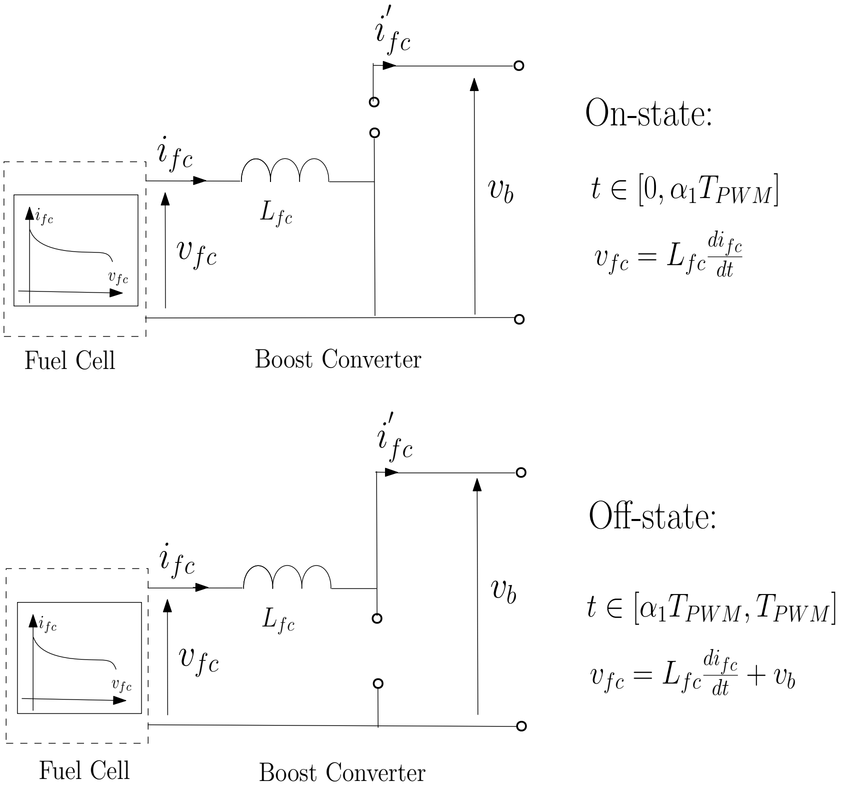

FIGURE 4.4 – State space model of the boost converter

4.2.3/ SCS AND BI-DIRECTIONAL CONVERTER MODEL

4.2.3.1/ SYSTEM MODEL

In the system, a simple RC equivalent circuit was applied for the modeling of the SCs, where the dynamic behavior of the SCs can be represented. The SCs are modeled as follows :

$$\begin{aligned}
\dot{q}_{scone}(t) &= -i_{scone}(t) && (4.3)\\
v_{scone}(t) &= \frac{1}{C_{scone}} q_{sc}(t) - R_{scone} i_{scone}(t) && (4.4)\\
v_{sc}(t) &= v_{scone}(t) Nsc_{ser} && (4.5)\\
i_{sc}(t) &= i_{scone}(t) Nsc_{par} && (4.6)
\end{aligned}$$

where $q_{scone}(t)$ is the charge in one SC, C_{scone} is the capacitance of one SC, $v_{scone}(t)$ and $i_{scone}(t)$ represent the voltage and current of one SC. The model is based on the parameters of the Maxwell BPAK0058-E015 supercapacitor, which is applied on the PHIL test bench, as shown in Tab. 4.2.

Parameters of SCs model	
Capacitance C_{scone}	58 [F]
Voltage Rating	15 [V]
Internal resistance R_{scone}	19 $[m\Omega]$
Number of SCs in series Nsc_{ser}	4
Number of SCs in parallel Nsc_{par}	2

TABLE 4.2 – SCs parameters

4.2.3.2/ CONTROLLER DESIGN

For the controller design, the internal resistance of the SCs is neglected, so that the SCs are modeled by an equivalent capacitor, as follows :

$$\frac{d}{dt} v_{sc}(t) = -\frac{i_{sc}(t)}{C_{sc}} \quad (4.7)$$

with 4 packs in series and 2 in parallel. The equivalent capacitance of the SCs is 29 F.

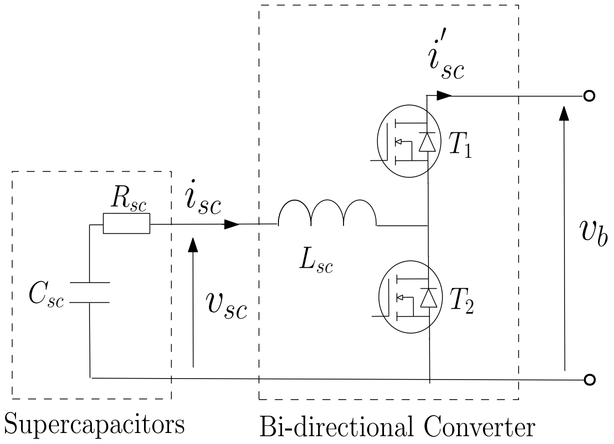

FIGURE 4.5 – SCs and the bi-directional converter

Since the SCs can be charged or discharged, they are connected with a reversible DC/DC converter that is shown in Fig. 4.5. An average model of the bi-directional converter is established with the same method as in section 4.2.2, and presented in Fig. 4.6. Then the bi-directional converter is expressed by the following state space average model :

$$\frac{d}{dt} i_{sc}(t) = \frac{-(1-\alpha_2(t))\, v_b(t) + v_{sc}(t)}{L_{sc}} \tag{4.8}$$

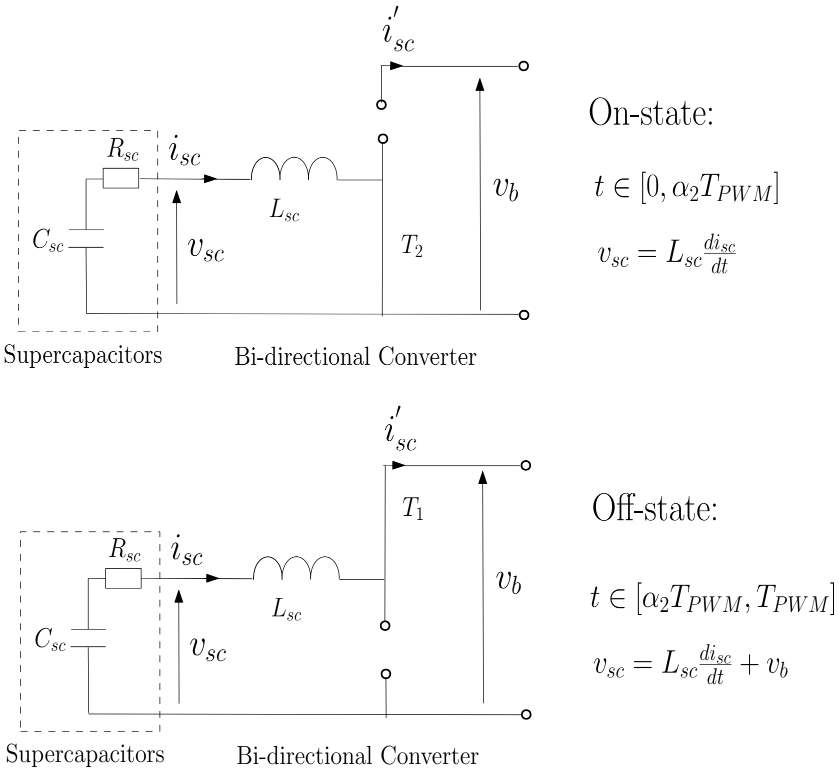

FIGURE 4.6 – State space model of the bi-directional converter

4.2.4/ HYBRID SYSTEM MODEL

According to sections 4.2.2 and 4.2.3, the complete hybrid system is represented by the following 4^{th} order non-linear state space model :

$$\frac{d}{dt} v_b(t) = \frac{(1-\alpha_1(t))\, i_{fc}(t) + (1-\alpha_2(t))\, i_{sc}(t) - i_l(t) - i_d(t)}{C} \tag{4.9}$$

$$\frac{d}{dt} v_{sc}(t) = -\frac{i_{sc}(t)}{C_{sc}} \tag{4.10}$$

$$\frac{d}{dt} i_{fc}(t) = \frac{-(1-\alpha_1(t))\, v_b(t) + v_{fc}(t)}{L_{fc}} \tag{4.11}$$

$$\frac{d}{dt} i_{sc}(t) = \frac{-(1-\alpha_2(t))\, v_b(t) + v_{sc}(t)}{L_{sc}} \tag{4.12}$$

with state space $x(t) = [v_b, v_{sc}, i_{fc}, i_{sc}]^T$, control inputs $u(t) = [\alpha_1, \alpha_2]^T$, and measurements $y(t) = x$, $i_l(t)$, $i_d(t)$ and $v_{fc}(t)$. $v_b(t)$ is the DC bus voltage, $v_{fc}(t)$, $v_{sc}(t)$ are the FC and SCs voltage, $i_{fc}(t)$, $i_{sc}(t)$ are the FC and SCs current, $i_l(t)$ is the DC current consumed by the load, $\alpha_{1,2}(t)$ are the duty cycles of the converters, and $i_d(t)$ represents the current consumed by the dissipative resistance load to protect the system.

The current control is mandatory for industrial applications, and is composed of two parts : two fast inner current control loops and two slower outer voltage loops. The first controllers are based on IP controllers, while the DC bus voltage and state-of-charge of the SCs are controlled by IDA-PBC.

Due to the fact that L_{fc} and L_{sc} are small compared to the other parameters, the system is called a singular perturbed system, because of the difference of time scale between the voltages and the currents. The same argument is used in [153]. In order to design the outer loop controller, the 4^{th} order non-linear state space model can be reduced to the 2^{nd} order, as follows :

$$\begin{aligned} \frac{d}{dt}v_b(t) &= \frac{1}{C}\left(\frac{v_{fc}(t)}{v_b(t)}\,i^*_{fc}(t) + \frac{v_{sc}(t)}{v_b(t)}\,i^*_{sc}(t) - i_l(t) - i^*_d(t)\right) && (4.13)\\ \frac{d}{dt}v_{sc}(t) &= -\frac{i^*_{sc}(t)}{C_{sc}} && (4.14)\end{aligned}$$

where $x_r(t) = [x_1, x_2]^T = [v_b, v_{sc}]^T$, control inputs $u_r = [i^*_{fc}, i^*_{sc}]^T$, and measurements $y_r = [v_b, v_{sc}]^T$ and $z_r = [i_{fc}, i_{sc}, v_{fc}]^T$.

4.3/ CONTROLLER DESIGN USING IDA-PBC

The aim of IDA-PBC is to assign the state point x_r to the desired equilibrium x^*_r. In this work, the objective of the controller is to keep the DC bus and SCs at the desired voltages v^*_b and v^*_{sc} :

$$\begin{aligned} x_r &= [x_1, x_2]^T = [v_b, v_{sc}]^T && (4.15)\\ x^*_r &= [v^*_b, v^*_{sc}] && (4.16)\end{aligned}$$

In this research, the energy function H_d is chosen as follows (as a Lyapunov function) :

$$H_d = \frac{1}{2}\,\tilde{x}_r^T\,Q\,\tilde{x}_r \tag{4.17}$$

where $\tilde{x}_r = x_r - x^*_r$ represents the error between the measurement x_r and the reference x^*_r, and $Q = \mathrm{diag(C, C_{sc})}$.

Then the PCH system can be expressed as follows, with the error of each state and the gradient of the desired closed-loop energy function :

$$\dot{\tilde{x}}_r = [\mathcal{J} - \mathcal{R}]\nabla H_d + A(u_r, x_r, x^*_r, z_r) \tag{4.18}$$

with

$$\begin{aligned} \mathcal{J} - \mathcal{R} &= \begin{bmatrix} 0 & 0 \\ 0 & 0 \end{bmatrix}, \quad \nabla H_d = \begin{bmatrix} C\,\tilde{v}_b \\ C_{sc}\,\tilde{v}_{sc} \end{bmatrix}\\ A^t &= \begin{bmatrix} \frac{1}{C}\left(\frac{v_{fc}}{v_b}\,i^*_{fc} + \frac{v_{sc}}{v_b}\,i^*_{sc} - i_l - i^*_d\right), -\frac{1}{C_{sc}}\,i^*_{sc} \end{bmatrix}\end{aligned}$$

We define $\mathcal{J}_d(x) = -\mathcal{J}^t_d(x)$ and $\mathcal{R}_d(x) = \mathcal{R}^t_d(x) \geq 0$, with the constraints of skew-symmetry and positive semi-definiteness as follows :

$$\mathcal{J}_d = \begin{bmatrix} 0 & J_{12} \\ -J_{12} & 0 \end{bmatrix}, \quad \mathcal{R}_d = \begin{bmatrix} r_1 & 0 \\ 0 & r_2 \end{bmatrix}$$

with

$$\dot{\tilde{x}}_r = [\mathcal{J}_d(x) - \mathcal{R}_d(x)]\nabla H_d \tag{4.19}$$

then the closed-loop system is asymptotically stable (for more explications, see [151]). Since the system is described in the IDA-PBC form (4.19) and the PCH form (4.18), these two equations need to be equal, and the matching equations are therefore established as follows :

$$\begin{aligned} -r_1 C\tilde{v}_b + J_{12} C_{sc}\tilde{v}_{sc} &= \frac{1}{C}\left(\frac{v_{fc}}{v_b}\, i^*_{fc} + \frac{v_{sc}}{v_b}\, i^*_{sc} - i_l - i^*_d\right) && (4.20) \\ -J_{12} C\tilde{v}_b - r_2 C_{sc}\tilde{v}_{sc} &= -\frac{1}{C_{sc}}\, i^*_{sc} && (4.21) \end{aligned}$$

This is the departure point for the design of general or specific controllers. Then the non-linear controller is determined by the equations (4.22) to (4.24). Here, an admittance estimator is applied to estimate the load and the stability of the whole system is proven in [101] :

$$\begin{aligned} \delta\dot{y} &= -y + i_l/v_b, \delta > 0 && (4.22) \\ i^*_{fc} &= \frac{v_b}{v_{fc}}\left(y v^*_b + i^*_d + C_{sc}\left(C J_{12} - \frac{v_{sc}}{v_b} C_{sc} r_2\right)\tilde{v}_{sc} - C\left(\frac{v_{sc}}{v_b} C_{sc} J_{12} + r_1 C\right)\tilde{v}_b\right) && (4.23) \\ i^*_{sc} &= C_{sc}\left(C J_{12}\,\tilde{v}_b + r_2 C_{sc}\,\tilde{v}_{sc}\right) && (4.24) \end{aligned}$$

4.4/ ADVANCED POWER MANAGEMENT STRATEGY

4.4.1/ OBJECTIVES

As an extension of the work in [101], the objective of the new strategy is to consider all the terms of the control strategy that have been ignored in previous work. The new controller is obtained from (4.22), (4.23) and (4.24), by involving a new control parameter γ and setting $J_{12} = -\frac{\gamma}{CC_{sc}}$, $\gamma > 0$, as follows :

$$\begin{aligned} \delta\dot{y} &= -y + i_l/v_b, \qquad \delta > 0 && (4.25) \\ i^*_{fc} &= \frac{v_b}{v_{fc}}\left(y v^*_b - \gamma\tilde{v}_{sc} - r_2\frac{v_{sc}}{v_b} C^2_{sc}\tilde{v}_{sc} + i^*_d + \left(\frac{v_{sc}}{v_b}\gamma - r_1 C^2\right)\tilde{v}_b\right), \qquad \gamma > 0 && (4.26) \\ i^*_{sc} &= -\gamma\,\tilde{v}_b + r_2 C^2_{sc}\tilde{v}_{sc} && (4.27) \end{aligned}$$

The challenge of this new controller is to determine the values of parameters r_1 and r_2 and the equation of dissipative load current i^*_d, while preserving the stability of the whole closed-loop system and ensuring the limiting constraints of the components.

4.4.2/ NORMAL OPERATION

In the case of normal operation of the FC and SCs (i.e., without limitation), the controller is determined with the following comments, for the same reasons as in [101] :

- In the situation of normal operation, the SCs voltage is within the range of $[v_{scl}, v_{sch}]$, where the SCs can work normally (see Fig. 4.7). There is no limitation of the FC and SCs currents, so the energy dissipation is not activated. Moreover, in order to protect the FC, the FC has to manage the voltage level of the SCs, without a direct action oo the DC bus voltage. Therefore, the term $(\frac{v_{sc}}{v_b}\gamma - r_1 C^2)\tilde{v}_b$ in (4.26) is set to zero, which leads to r_1 equal to L.

— According to the control method proposed in [52], the DC bus voltage is managed only by the SCs. Since there is no limitation for the SCs, the inner state of the SCs need not be considered, so that r_2 is set equal to zero in this situation.

— According to (4.25), the estimation of the unknown load $i_l(t)$ by the admittance estimator, which is equal to yv_b^*, is implemented into the computation of the FC reference current.

Based on the above analysis, the control is simplified to :

$$\delta\dot{y} = -y + i_l/v_b, \qquad \delta > 0 \tag{4.28}$$

$$i_{fc}^* = \frac{v_b}{v_{fc}}\left(yv_b^* - \gamma\,\tilde{v}_{sc}\right), \qquad \gamma > 0 \tag{4.29}$$

$$i_{sc}^* = -\gamma\,\tilde{v}_b \tag{4.30}$$

$$i_d^* = 0 \tag{4.31}$$

4.4.3/ SCS VOLTAGE LIMITATIONS

In practice, the SCs usually work within a range of state-of-charge, which depends on the SCs voltage. Therefore, the limitation [SoC$_{min}$,SoC$_{max}$] can be determined by the voltage level $[v_{scL}, v_{scH}]$. In the advanced controller, a dynamic saturation of the SCs current is designed, to implement constraints of the charge or discharge depending on the SCs voltage level. A specific saturation function is shown in Fig. 4.7, which represents these limitations [52]. Now, we propose to integrate this saturation function directly into the controller, so that the stability property of the passivity controller is preserved.

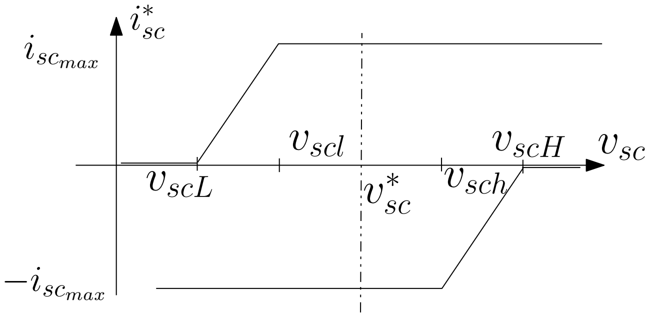

FIGURE 4.7 – Saturation functions of the reference current i_{sc}^*

According to (4.27), the SCs current can be limited by the term $(r_2 C_{sc}^2 \tilde{v}_{sc})$, witch depends on the voltage level, so that we can realize the dynamic saturation in Fig. 4.7 by defining parameter r_2. Fig. 4.8 shows the value of r_2, which should always be positive to respect the property of $\mathcal{R}_d(x)$ in (4.19). With this parameter in (4.27), the SCs current is limited according to the voltage level. Therefore, the SCs voltage is limited by this dynamic saturation of i_{sc}^*, which is determined by three limitation situations :

— When $v_{scL} < v_{sc} < v_{scl}$, the discharge of the SCs is limited by the term $(r_2 C_{sc}^2 \tilde{v}_{sc})$ in (4.27) during a discharge operation. With this saturation, there is also an acceleration of the SCs charge when the system is operating in generation mode (with $\tilde{v}_b < 0$).

- In contrary, when $v_{sch} < v_{sc} < v_{scH}$, we also set $r_2 > 0$ and the charge is also limited by the term $(r_2 C_{sc}^2 \tilde{v}_{sc})$. Also, the discharge is accelerated during a discharge operation (with $\tilde{v}_b < 0$).
- Otherwise ($v_{scl} \leq v_{sc} \leq v_{sch}$), r_2 is equal to zero, so that the controller is in normal operation as described in section 4.4.2 (i.e., with (4.28) to (4.31)).

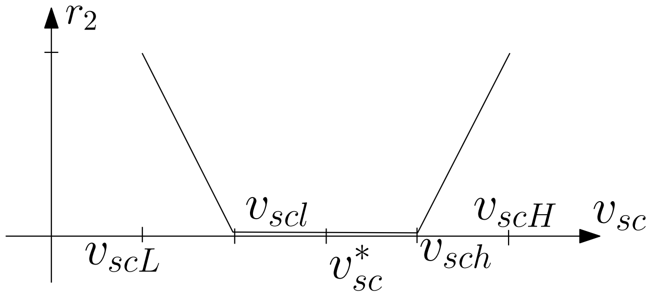

FIGURE 4.8 – Evolution of r_2 according to the SCs voltage

Therefore, v_{sc} is not supposed to be lower than v_{scL} or greater than v_{scH}. The SCs current should be zero when $v_{sc} = v_{scL}$ or $v_{sc} = v_{scH}$. Therefore the value of r_2 is calculated by setting $C_{sc}(CJ_{12}\,\tilde{v}_b + r_2 C_{sc}\,\tilde{v}_{sc}) = 0$, at these two voltage levels.

- At $v_{sc} = v_{scL}$:

$$r_2 = -\frac{CJ_{12}\,\tilde{v}_b}{C_{sc}\,\tilde{v}_{sc}} = -\frac{CJ_{12}}{C_{sc}\,(v_{scL} - v_{sc}^*)}\,\tilde{v}_b = -\sigma_L\,\tilde{v}_b \tag{4.32}$$

  with

$$\sigma_L = \frac{CJ_{12}}{C_{sc}\,(v_{scL} - v_{sc}^*)},\ \sigma_L > 0 \tag{4.33}$$

  where r_2 is equal to $-\sigma_L\,\tilde{v}_b$ when v_b is lower than v_b^* (generally during discharge mode) otherwise $\sigma_L\,\tilde{v}_b$ (generally during generative mode of the load), with $\sigma_L > 0$ so that r_2 is always positive to preserve the stability of the closed-loop system.

- At $v_{sc} = v_{scH}$:

$$r_2 = -\frac{CJ_{12}\,\tilde{v}_b}{C_{sc}\,\tilde{v}_{sc}} = -\frac{CJ_{12}}{C_{sc}\,(v_{scH} - v_{sc}^*)}\,\tilde{v}_b = \sigma_H\,\tilde{v}_b \tag{4.34}$$

  with

$$\sigma_H = -\frac{CJ_{12}}{C_{sc}\,(v_{scH} - v_{sc}^*)},\ \sigma_H > 0 \tag{4.35}$$

  where r_2 is equal to $-\sigma_H\,\tilde{v}_b$ when v_b is lower than v_b^* (generally during discharge mode) otherwise $\sigma_H\,\tilde{v}_b$ (generally during generative mode of the load), with $\sigma_L > 0$ so that r_2 is always positive.

According to the SCs voltage level, there are five different operation modes. The different values of r_2 of each operation mode are summarized as follows :

1. if $v_{scl} \leq v_{sc} \leq v_{sch}$: mode SCs 0 : normal operation, $r_2 = 0$ without limitation of SCs charge or discharge.
2. if $v_{sc} < v_{scl}$:
    1. mode SCs 1 : if $\tilde{v}_b < 0$, limit the discharge of the SCs gradually as a function of the SCs voltage, then $r_2 = -\sigma_L \tilde{v}_b \frac{v_{scl}-v_{sc}}{v_{scl}-v_{scL}}$, so that r_2 varies with v_b and v_{sc}. For the following cases, r_2 is also variable and is calculated as a function of v_b and v_{sc}.
    2. mode SCs 2 : if $\tilde{v}_b > 0$, increase the charge of the SCs compared to the previous control, then $r_2 = \sigma_L \tilde{v}_b \frac{v_{scl}-v_{sc}}{v_{scl}-v_{scL}}$.

3. if $v_{sc} > v_{sch}$:

   1. mode SCs 3 : if $\tilde{v}_b < 0$, increase the discharge of the SCs compared to the previous control, and to increase the convergence of v_b to v_b^*, then $r_2 = -\sigma_H \tilde{v}_b \frac{v_{sch}-v_{sc}}{v_{sch}-v_{scH}}$.

   2. mode SCs 4 : if $\tilde{v}_b > 0$, limit the charge of the SCs gradually as a function of the SCs voltage, then $r_2 = \sigma_H \tilde{v}_b \frac{v_{sch}-v_{sc}}{v_{sch}-v_{scH}}$.

The major theoretical remarks on the controller are as follows :

- Thanks to the term $(r_2 \frac{v_{sc}}{v_{fc}} C_{sc}^2 \tilde{v}_{sc})$ in (4.26), the FC current is naturally increased when the SCs current is limited (when the SCs voltage is lower than v_{scl} or greater than v_{sch}). This enables to counteract the non-injection of current in the DC bus by the SCs and consequently preserves the stability of the whole closed-loop system.
- During modes SCs 0 to 4, there is no extra energy to dissipate, which leads to $i_d^* = 0$.
- As mentioned in section 4.4.2, the FC does not control the DC bus voltage, in order to protect the FC system.
- The novelty of this new controller is that the term r_2 integrates an implicit saturation function of the SCs current while preserving the stability of the whole closed-loop system. In the previous work, this property was not guaranteed according to (4.28) to (4.30) and the *a posteriori* saturation function shown in Fig. 4.7 was implemented, so that the saturation was not considered into the control law, which may cause the instability.
- In addition, the new term r_2 enables a boost charge or discharge of the SCs when the required operating conditions are satisfied.

According to above analysis, the control law for the situation of SCs voltage limitation (mode SCs = 1, 2, 3 or 4) can be summarized as follows :

$$\delta \dot{y} = -y + i_l / v_b, \qquad \delta > 0 \tag{4.36}$$

$$i_{fc}^* = \frac{v_b}{v_{fc}} \left(y v_b^* - \gamma \tilde{v}_{sc} - r_2 \frac{v_{sc}}{v_b} C_{sc}^2 \tilde{v}_{sc} \right), \gamma > 0 \tag{4.37}$$

$$i_{sc}^* = -\gamma \tilde{v}_b + r_2 C_{sc}^2 \tilde{v}_{sc} \tag{4.38}$$

$$i_d^* = 0 \tag{4.39}$$

As mentioned in section 4.4.2 for normal operation (mode SCs 0), the control law is simplified with $r_2 = 0$.

4.4.4/ SCs CURRENT LIMITATIONS

The SCs should also be protected from over-current, so that the SCs reference current is limited within the range $[-i_{sc_{max}}, i_{sc_{max}}]$ (see Fig. 4.7). There are two situations for the SCs current limitation :

1. mode SCs 5 : The SCs reference current is limited to the maximum charging current $-i_{sc_{max}}$. So the dissipative load needs to be activated, which is detailed in section 4.4.6.

2. mode SCs 6 : The SCs reference current is limited to the maximum discharging current $i_{sc_{max}}$. It means that the SCs cannot afford the transient energy to stabilize the DC bus voltage at its reference value. Therefore, the sizing of the system is not suitable and needs to be changed.

Otherwise, there is a possible solution proposed with the controller (but not recommended), taking into account $\tilde{v}_b$ in the FC current equation using the last term of (4.26) so that the FC directly controls the DC bus voltage. Setting r_1 equal to $(\mu\frac{v_{sc}\gamma}{v_b C^2})$, with $\mu \geq 0$ leads to :

$$i^*_{fc} = \frac{v_b}{v_{fc}}\left(yv^*_b - \gamma\tilde{v}_{sc} - r_2\frac{v_{sc}}{v_b}C^2_{sc}\tilde{v}_{sc} + \frac{v_{sc}}{v_b}\gamma(1-\mu)\tilde{v}_b\right) \tag{4.40}$$

with $i^*_d = 0$.

4.4.5/ FC CURRENT LIMITATIONS

There are also two situations for the FC current limitation :

1. mode FC 7 : The FC reference current is limited to its maximum value ($i_{fc_{max}}$) if the FC current exceeds the maximum.
2. mode FC 8 : The FC current is saturated to 0 ($i_{fc_{min}}$). The extra energy on the DC bus should be dissipated, so the dissipatine load is activated according to (4.26), which is detailed in the next subsection.

4.4.6/ DISSIPATING RESISTANCE LOAD OPERATION

The energy dissipation is activated when the SCs or FC current is limited by the lower limit (i.e., mode SCs = 5 or mode FC = 8, see sections 4.4.4 and 4.4.5). In order to calculate the dissipating load current from (4.26), setting r_1 equal to $\mu\frac{v_{sc}\gamma}{v_b C^2}$, we have :

$$i^*_d \quad = \quad \frac{v_{fc}}{v_b}i^*_{fc} - yv^*_b + \gamma\tilde{v}_{sc} + r_2\frac{v_{sc}}{v_b}C^2_{sc}\tilde{v}_{sc} + \frac{v_{sc}}{v_b}\gamma\,(\mu-1)\,\tilde{v}_b \tag{4.41}$$

The choice of μ depends on the mode of SCs and FC, which is detailed in three different situations :

1. mode SCs = 5 and mode FC ≠ 8 :

   In this situation, the SCs current is limited to its maximum charging current $-i_{scmax}$, so that the SCs are not capable of stabilizing the DC bus voltage. The dissipative load needs to play the role of SCs. Since the FC current is not limited. i^*_{fc} is represented by (4.37), which leads to :

   $$i^*_d = \frac{v_{sc}}{v_b}\gamma\,(\mu-1)\,\tilde{v}_b \tag{4.42}$$

   Setting μ to $1 + \frac{i^{**}_{sc} - i^*_{sc}}{\gamma\tilde{v}_b}$ where i^{**}_{sc} is the output of the saturation function of the SCs current, i.e., $i^{**}_{sc} = -i_{sc_{max}}$, we then have :

   $$i^*_d = \frac{v_{sc}}{v_b}\,(i^{**}_{sc} - i^*_{sc}) \tag{4.43}$$

   i^*_d represents the SCs current that could not be absorbed, as seen from the DC bus.
2. mode SCs ≠ 5 and mode FC = 8 :

   In this situation, i^*_{fc} is limited at 0. Considering the energy efficiency, the extra energy needs to be stored firstly by the SCs and then consumed by the dissipative load if the SCs are not capable of it. Then there are two options in this situation :

- $v_{sc} < v_{sch}$: According to section 4.4.2, the SCs voltage is within the normal operation range, so that r_2 is set to 0 and the SCs are capable of consuming the extra energy. Therefore, the extra energy can be stored by the SCs. However, it is demonstrated that there is a steady state error in the DC bus voltage, which is equal to $\tilde{v}_b = -\frac{v_b i_l}{\gamma v_{sc}}$, from (4.14) and (4.27).

  An integral term is added without deteriorating the passivity properties [178] :

  $$i_{sc}^* = -\gamma \tilde{v}_b - x_c \tag{4.44}$$

  with $x_c = -\int k_i \tilde{v}_b dt$.
- $v_{sc} > v_{sch}$: Although the SCs are still capable of recharging from the DC bus for the purpose of stability, the SCs charging current is limited because of the voltage limitation. Thus, it is impossible to control the DC bus and SCs voltage at the same time. The dissipative load is activated to avoid instability on the DC bus and an integral term is added in order to remove the steady state error in the DC bus voltage. So we have :

  $$i_d^* = -yv_b^* + r_2 \frac{v_{sc}}{v_b} C_{sc}^2 \tilde{v}_{sc} - \frac{v_{sc}}{v_b} \gamma \tilde{v}_b + x_d \tag{4.45}$$

  with $x_d = -\int k_d \tilde{v}_b dt$, which leads μ be equal to $\frac{v_b}{v_{sc}\tilde{v}_b}\left(\frac{x_d}{\gamma} - \tilde{v}_{sc}\right)$.

3. mode SCs = 5 and mode FC = 8 :

In this situation, both SCs and FC currents are limited, i.e., $i_{sc}^{**} = -i_{sc_{max}}$, $i_{fc}^* = 0$, and $r_2 \geqslant 0$, so the extra energy is consumed by the dissipative resistance load. Based on (4.41) and the previous method, we set μ to $\left(1 + \frac{i_{sc}^{**} - i_{sc}^*}{\gamma \tilde{v}_b} + \frac{v_b}{v_{sc}\tilde{v}_b}\left(\frac{yv_b^*}{\gamma} - \tilde{v}_{sc}\right)\right)$, which leads to :

$$i_d^* = \frac{v_{sc}}{v_b}\left(i_{sc}^{**} - i_{sc}^*\right) + r_2 \frac{v_{sc}}{v_b} C_{sc}^2 \tilde{v}_{sc} \tag{4.46}$$

In summary, the role of this dissipation strategy is to keep the DC bus voltage around its reference level with as little impact as possible on the energy efficiency. With this dissipating resistance load operation, the stability is guaranteed, which is the main concern of short-term control.

Finally, all the different cases are summarized by a flow chart in Fig. 4.9.

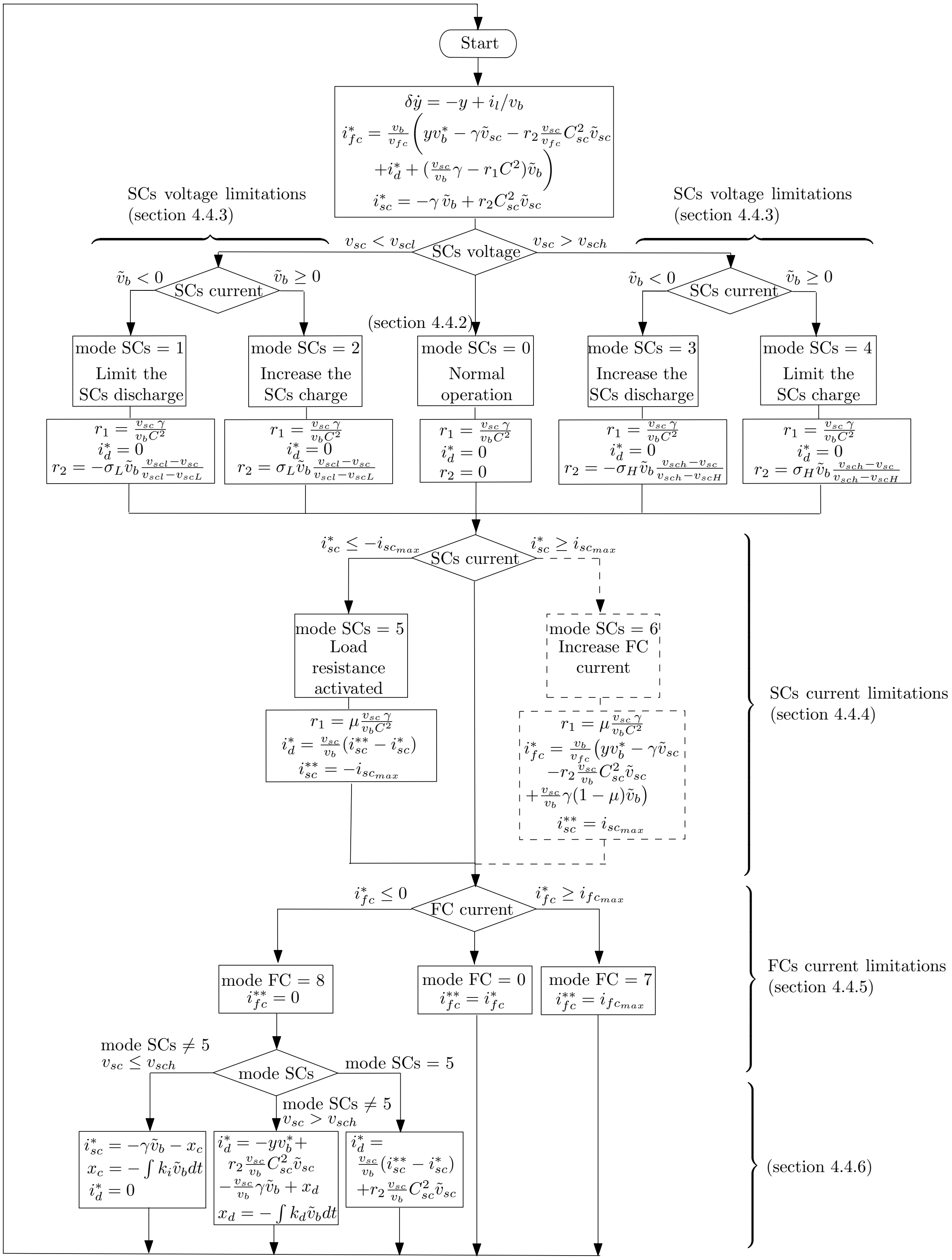

FIGURE 4.9 – Flow chart of the control law

4.4.7/ DISCRETIZATION OF THE CONTROL LAW

For the experimental validation, the controller is implemented with a real-time processor in the MicroLabBox, where the variables are sampled. The microprocessor performs these calculations once every sampling time. Therefore, the discretization of the control law is required. With a Zero-Order Hold (ZOH) device, the control values are constant during the sampling interval.

Firstly, compute the Laplace transform of (4.25) :

$$y = \frac{\frac{1}{\delta}}{s+\frac{1}{\delta}}\frac{i_l}{v_b} \tag{4.47}$$

Then, compute the Z transform with a ZOH :

$$\begin{aligned} y &= \left(1-z^{-1}\right)\mathcal{Z}\left[\frac{\frac{1}{\delta}}{s\left(s+\frac{1}{\delta}\right)}\right]\frac{i_l}{v_b} && (4.48)\\ &= \frac{1-e^{-\frac{1}{\delta}T_s}}{1-z^{-1}e^{-\frac{1}{\delta}T_s}}\frac{i_l}{v_b} && (4.49)\end{aligned}$$

so we have

$$y - z^{-1}e^{-\frac{1}{\delta}T_s}y = \left(1-e^{-\frac{1}{\delta}T_s}\right)\frac{i_l}{v_b} \tag{4.50}$$

Finally, the controller in sampled time is :

$$\begin{aligned} y[k] &= e^{-\frac{1}{\delta}T_s}y[k-1] + \left(1-e^{-\frac{1}{\delta}T_s}\right)\frac{i_l[k]}{v_b[k]}, \qquad \delta > 0 && (4.51)\\ i_{fc}^*[k] &= \frac{v_b[k]}{v_{fc}[k]}\Bigg(y[k]v_b^*[k] - \gamma\,\tilde{v}_{sc}[k] - r_2[k]\frac{v_{sc}[k]}{v_b[k]}C_{sc}^2\tilde{v}_{sc}[k] \\ &+ i_d^*[k] + \left(\frac{v_{sc}[k]}{v_b[k]}\gamma - r_1[k]C^2\right)\tilde{v}_b[k]\Bigg), \qquad \gamma > 0 && (4.52)\\ i_{sc}^*[k] &= -\gamma\,\tilde{v}_b[k] + r_2[k]C_{sc}^2\tilde{v}_{sc}[k] && (4.53)\end{aligned}$$

4.5/ SIMULATION RESULTS

The system is firstly modeled in Matlab/Simulink. The simulation results with the proposed controller are shown in this section. The simulation results are composed of three parts :

- Simulation results with the proposed controller in normal operation without limitations, which was introduced in section 4.4.2.
- Simulation results with the SCs voltage limitation that was introduced in section 4.4.3. Also, a comparison with the previous controller that was proposed in [101] is shown.
- Simulation with all limited situations as well as the operation of the dissipative load proposed in section 4.4.6.

4.5.1/ NORMAL OPERATION RESULTS

Firstly, a simulation with a scenario of a small load current cycle is proceeded, where the system and control parameters are shown in Tab. 4.3. Here, the hybrid system parameters and limitations are set according to the real parameters of the PHIL platform. The controller parameters are chosen according to the sensitivity of the test bench, where γ refers to the SCs and δ refers to the FC.

Hybrid system parameters	
DC bus capacity C	19.8×10^{-3} [F]
DC bus reference voltage v_b^*	70 [V]
SCs capacity C_{sc}	29 [F]
SCs reference voltage v_{sc}^*	45 [V]
Hybrid system limitations	
SCs voltage limitation	
v_{scL}	44 [V]
v_{scl}	44.5 [V]
v_{sch}	46 [V]
v_{scH}	46.5 [V]
SCs current limitation	
i_{scmax}	5 [A]
i_{scmin}	-5 [A]
FC current limitation	
i_{fcmax}	30 [A]
i_{scmin}	0 [A]
Controller parameters	
γ	2
δ	0.5
k_i	5
k_d	0.007
$K_{p-i_{sc}}$	6.8
$K_{i-i_{sc}}$	5760
Current sampling time	$50\,[\mu$s]
Voltage sampling time	$500\,[\mu$s]

TABLE 4.3 – Control and system parameters

Fig. 4.10 presents the details of the voltage and current values of each element : Fig. 4.10. (a) shows the curve of DC bus voltage, which varies around its reference value 70 V ; Fig. 4.10. (b) shows the load current cycle, which is designed to test the normal operation of the proposed controller ; Figs. 4.10. (c) and (d) present the fuel cell voltage and current ; in Figs. 4.10. (e) and (f), the SCs voltage and current are presented and vary within their limitations ; Fig. 4.10. (g) shows the SCs and FC operation modes while the dissipative load current is presented in Fig. 4.10. (h).

As mentioned in section 4.5.1, the DC bus voltage is managed only by the SCs, so that the transient power is provided by the SCs, and the dynamic changes on the FC current are reduced. Thanks to the term $(-\gamma\,\tilde{v}_b(t))$ in the control law of SCs reference current (see (4.27)) which represents the interconnections between elements, the FC supplies the energy in steady state while the SCs respond quickly during load power transients to stabilize the DC bus voltage (Fig. 4.10.a). The FC therefore has a smooth response, which increases its lifetime.

(a) Bus voltage v_b

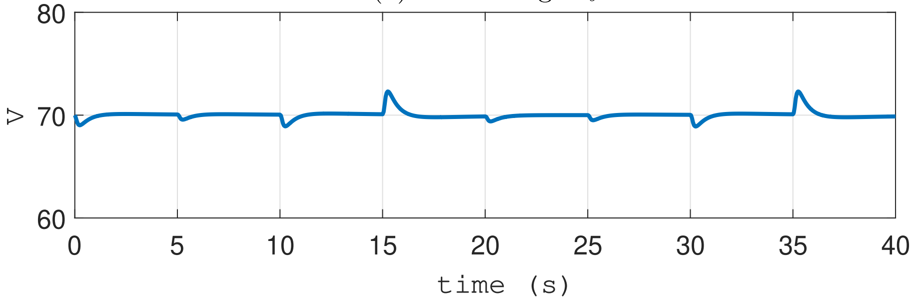

(b) Load current i_l

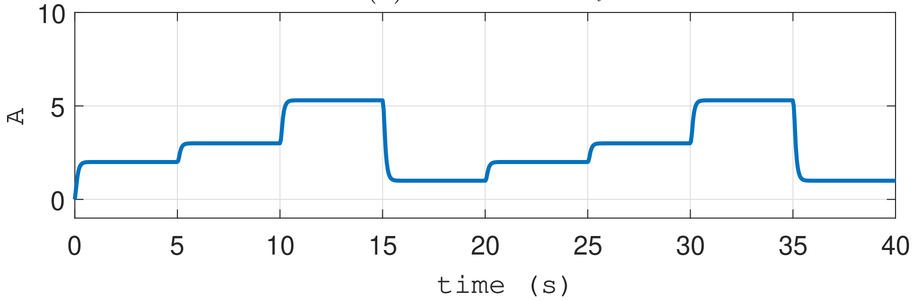

(c) Fuel cell voltage v_{fc}

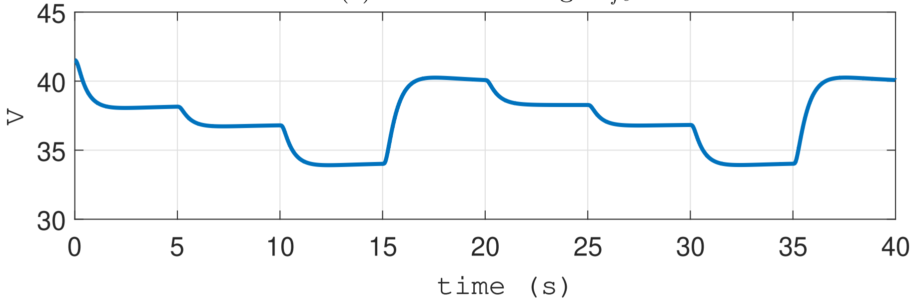

(d) Fuel cell current i_{fc}

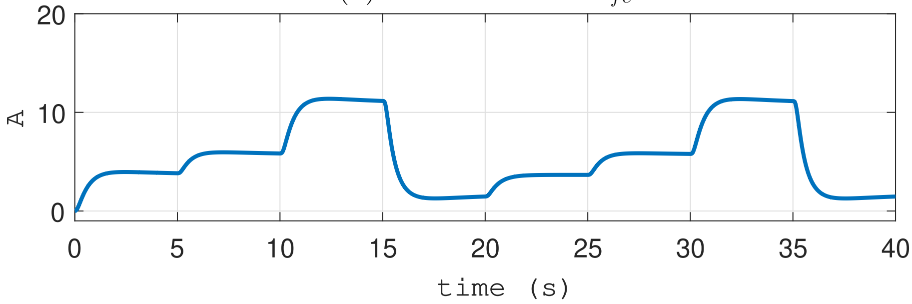

(e) SCs voltage v_{sc}

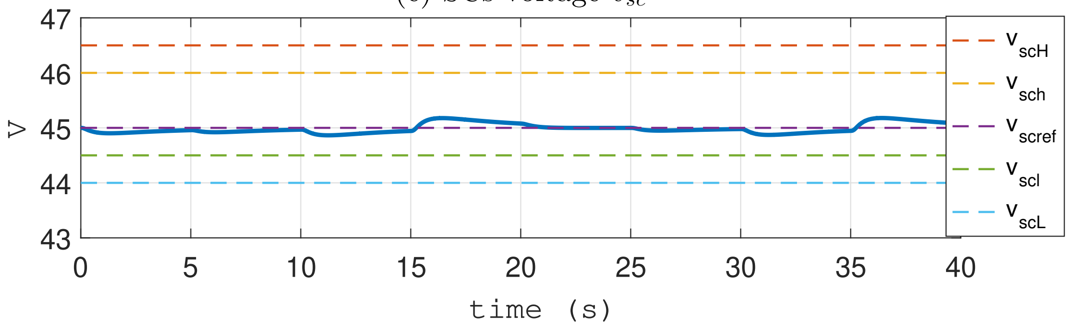

(f) SCs current i_{sc}

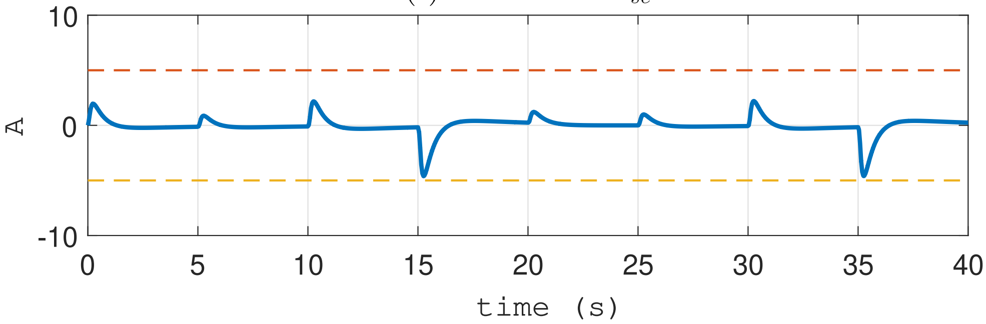

(g) SCs and FC mode

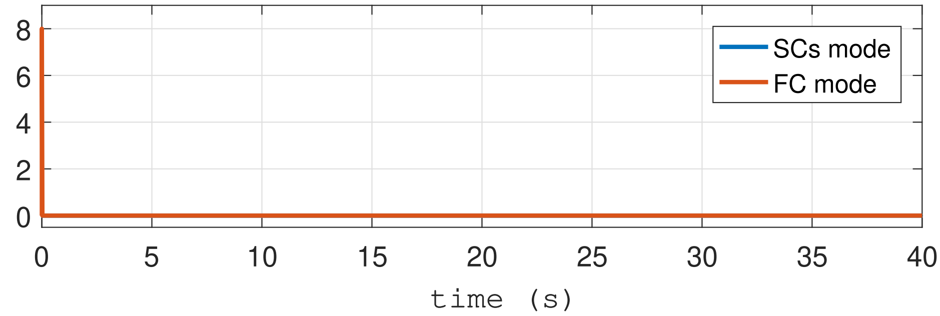

(h) Dissipative load current i_d

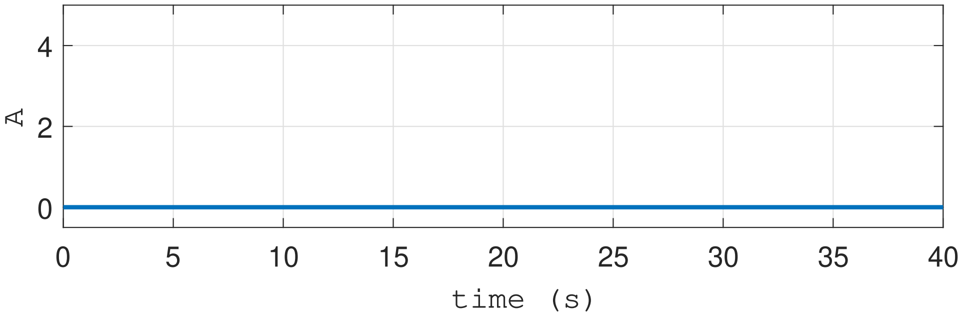

FIGURE 4.10 – Simulation results - normal operation (1)

It should be noticed that since the SCs and FC have not exceeded their limitations, the operation mode is equal to zero (without limitation) during this simulation, except for the beginning of the simulation where the FC current is limited to zero when there is no load current. Therefore, the dissipative load is not activated during this scenario.

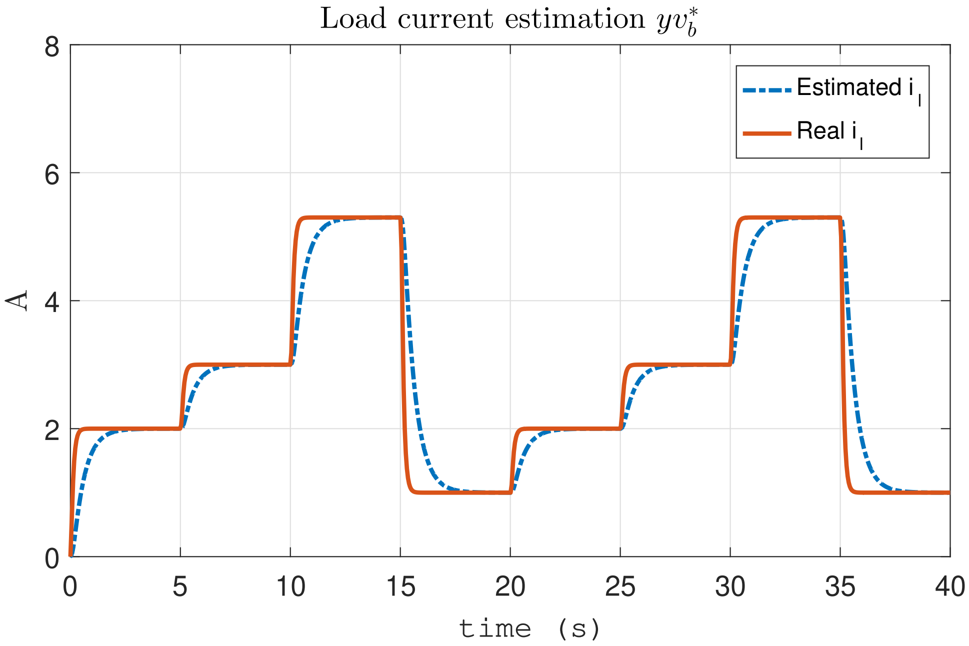

FIGURE 4.11 – Simulation results - normal operation (2)

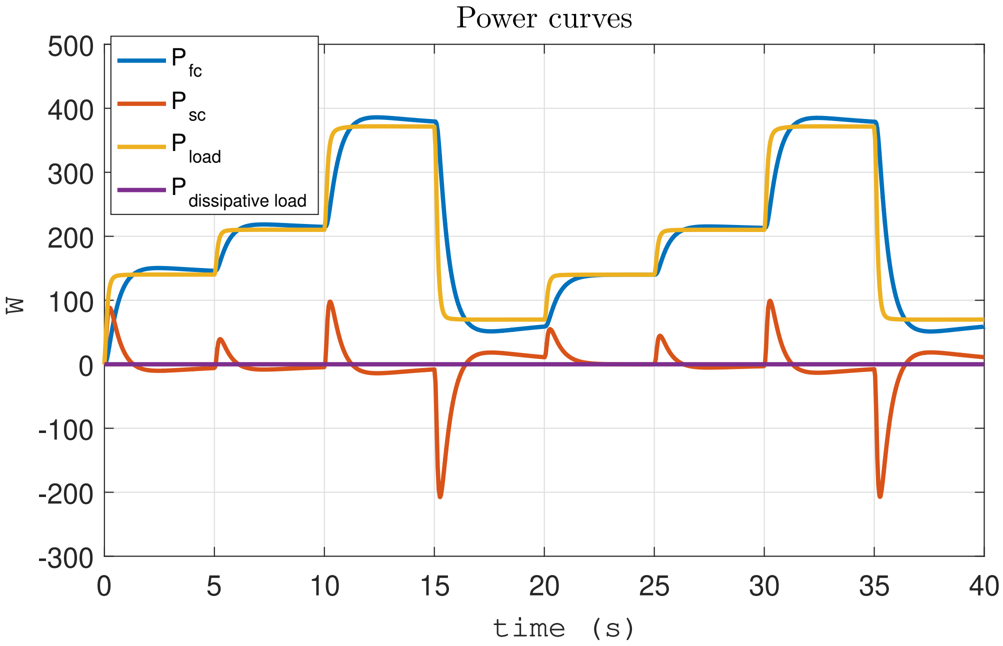

FIGURE 4.12 – Simulation results - normal operation (3)

Fig. 4.11 shows the estimation of the load current by the admittance estimator (4.28). With this estimator, the FC has a smooth reference current and recovers the SCs equilibrium point (v_{sc}^*), within the FC's transient ability. Therefore, in Fig. 4.10 (e), the SCs voltage is kept around its reference value by the FC. The tuning parameter δ is chosen as 2, which controls the sensitivity of the FC current and enables a slow response time of the FC.

Finally, the power curves are shown in Fig. 4.12. We can see clearly the difference of the dynamic response between the SCs and FC. It is significant that the SCs provide the transient power when the load current changes and the FC provides the load power during the steady state. Also, the stability of the whole system is guaranteed by the controller.

4.5.2/ SCS VOLTAGE LIMITATION AND COMPARISON

Two simulation are realized with Matlab / Simulink : one with the proposed controller and another one with the previous controller proposed in [101], in order to make a comparison. Tab. 4.4 shows the system and control parameter configuration, for both of these two controllers.

Hybrid system parameters	
DC bus capacity C	9 [mF]
DC bus reference voltage v_b^*	50 [V]
SCs capacity C_{sc}	26 [F]
SCs reference voltage v_{sc}^*	21 [V]
Hybrid system limitations	
SCs voltage limitation	
v_{scL}	20.5 [V]
v_{scl}	40.7 [V]
v_{sch}	21.3 [V]
v_{scH}	21.5 [V]
SCs current limitation	
i_{scmax}	60 [A]
i_{scmin}	-60 [A]
FC current limitation	
i_{fcmax}	45 [A]
i_{scmin}	0 [A]
Controller parameters	
γ	10
δ	2
Current sampling time	50 [μs]
Voltage sampling time	500 [μs]

TABLE 4.4 – Control and system parameters

Fig. 4.13 shows a comparison between the original control proposed in [101] (in blue) and the new one (in red) with the dynamic saturation of the SCs voltage (in red, see section 4.4.3). Here, the voltage of SCs is limited between 20.5 V and 21.5 V for the purpose of the test. Fig. 4.13 (g) shows the operation mode of SCs :

- mode SCs 0 : no limitation of SCs in charging or discharging (i.e., $v_{scl} \leq v_{sc} \leq v_{sch}$)
- mode SCs 1 : limitation of SCs discharging when the SCs voltage is low (i.e.,

$v_{scL} \leq v_{sc} < v_{scl}$, $\tilde{v}_b < 0$)

- mode SCs 2 : acceleration of SCs charging when the SCs voltage is low (i.e., $v_{scL} \leq v_{sc} < v_{scl}$, $\tilde{v}_b > 0$)
- mode SCs 3 : acceleration of SCs discharging when the SCs voltage is high to increase the convergence of v_b to v_b^*. (i.e., $v_{sch} < v_{sc} \leq v_{scH}$, $\tilde{v}_b < 0$)
- mode SCs 4 : limitation of SCs charging when the SCs voltage is high. (i.e., $v_{sch} < v_{sc} \leq v_{scH}$, $\tilde{v}_b > 0$)

The SCs current is limited when the voltage exceeds the limitation around 20 s and 30 s. In order to counteract the injection of current in the DC bus, the FC current is naturally increased based on (4.37), and consequently preserves the stability of the whole closed-loop system. Otherwise, when the mode is zero, the voltage of the SCs is between 20.5 V and 21.5 V. Therefore, r_2 is equal to zero and we retrieve the original control.

(a) Bus voltage v_b

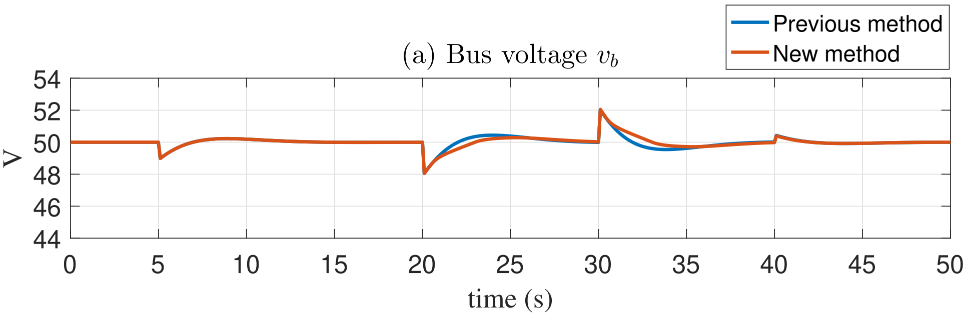

(b) Load current i_l

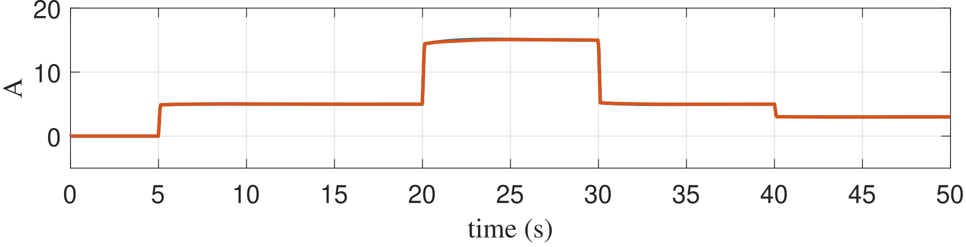

(c) Fuel cell voltage v_{fc}

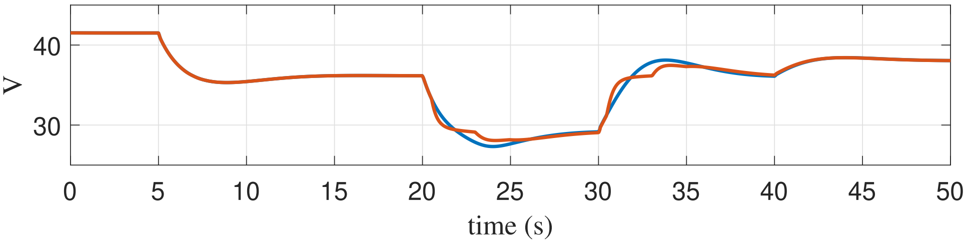

(d) Fuel cell current i_{fc}

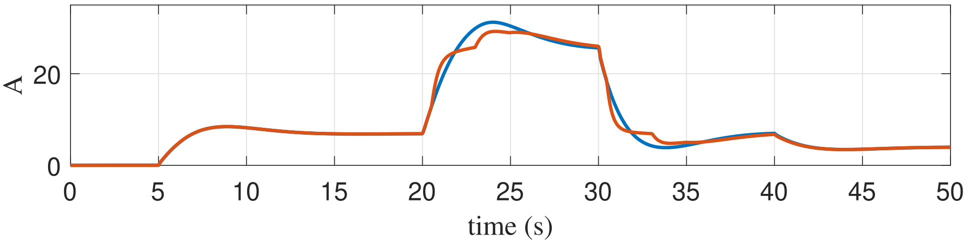

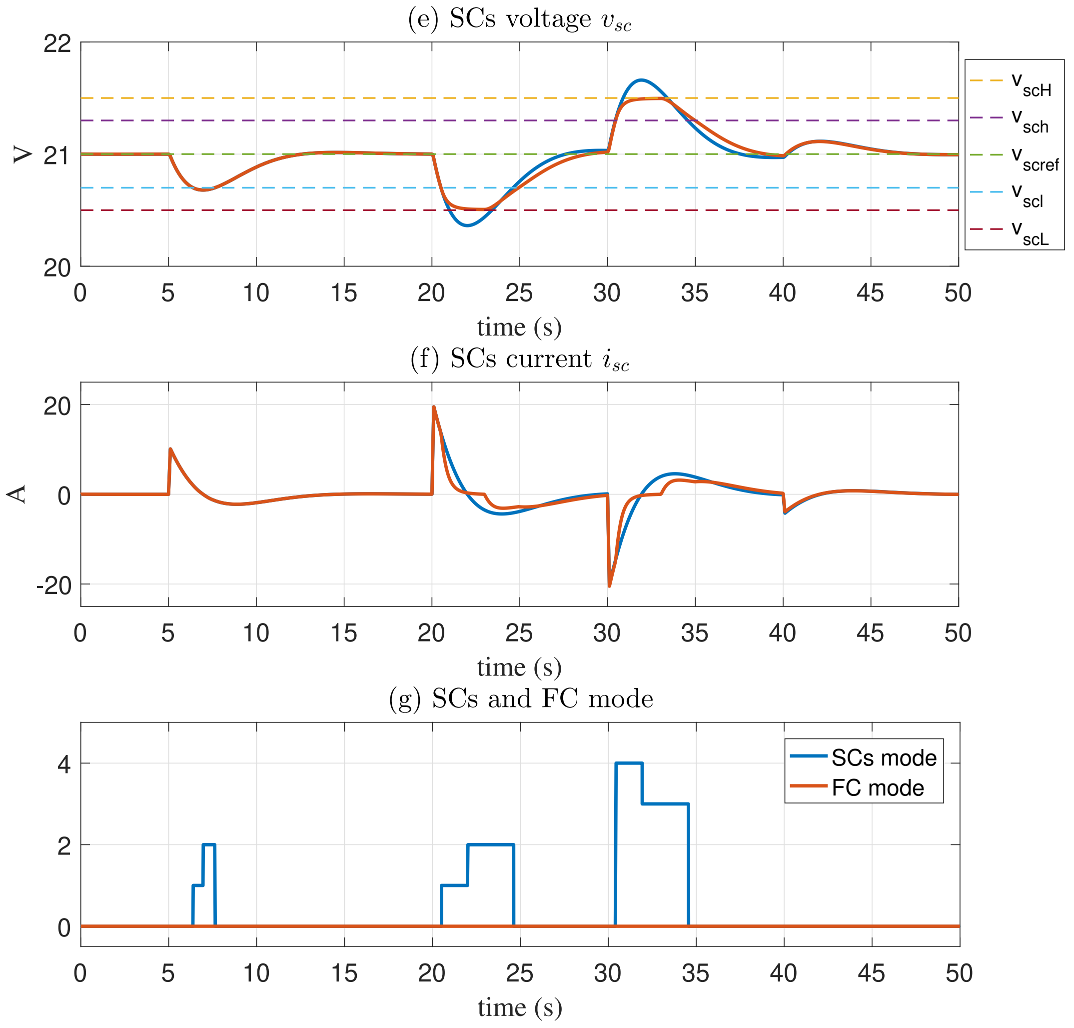

FIGURE 4.13 – Simulation results - comparison of the new and previous controllers [101]

If we look in details at Fig. 4.13 (f), firstly, between 20 s and 25 s, the SCs are discharged and the saturation function is activated to limit the discharge of the SCs when the voltage of SCs is between v_{scl} and v_{scL}. Secondly, due to the fact $\tilde{v}_b$ is positive during a few seconds, the control accelerates the charge of the SCs compared to the original control. The same comments hold for 30 s to 35 s, where the SCs are charged and the saturation function is activated to limit the charge of the SCs when the voltage of SCs is between v_{sch} and v_{scH}. Then the discharge is encouraged when the load current increases.

4.5.3/ LIMITATIONS AND DISSIPATIVE LOAD OPERATION

Another simulation is proceeded in order to test all the limited situations as well as the operation of the dissipating load, with the same configurations as in Tab. 4.3. Considering the limited current and power of the test bench, a specific load scenario has been designed in order to verify all restrained situations. In addition, the SCs voltage is limited within a specific range for this purpose. The experimental results with the same scenario are presented in the next section.

Fig. 4.14 shows the simulation results. In order to protect the FC, the upper limitation of the current is set to 80 % of the maximum value. For the first 12 s, the controller runs normally (mode SC = 0), and the SCs voltage varies around its reference value and the dissipative load is not activated.

At around 15 s, the load current increases significantly, which requires a large current from the SCs. However, the SCs voltage reaches v_{scl} (mode 1 of SCs), and the FC current is naturally increases based on (4.37) in order to counteract the injection of current in the DC bus. That is the reason why the DC bus voltage decreases but returns to the reference level quickly. From 16 s to 20 s, the power demanded by the load is greater than the maximum power of the FC, so that the FC current is limited by the saturation function, which is mode 6 of the FC. At this moment, the SCs supply the rest of the energy to ensure the whole controller stability. It is demonstrated that the controller is able to protect the element from overload while preserving the stability of the whole closed-loop system in a saturated situation. The system would not operate correctly without such an algorithm.

After that, the system current decreases and switches to generator mode, which could happen during the deceleration of a vehicle. The SCs current is limited to the minimum value at around 20 s, while the dissipating resistance load is activated (see Fig.4.29. (h)) to consume the energy that the SCs cannot absorb and stop the increase of the DC bus voltage. During the generator mode from 20 s to 23 s, the SCs are charged with a static current and make the DC bus voltage return to its reference level, thanks to the integral term in (4.44).

Another generator mode occurs during 27 s to 30 s, it follows that SCs current exceeds the limitation around 27 s (mode SC 5) and then the charging current is decreased with parameter r_2 in the control law because the SCs voltage is higher than its upper limitation v_{sch} (mode SC 4). According to section 4.4.6, the dissipative resistance load is consequently activated and helps make the DC bus voltage converge thanks to the integral term in (4.45).

The different dynamic response between the SCs and the FC is presented by the power curves in Fig. 4.15. The load and generated power are balanced by the SCs, FC and the dissipative load, according to their dynamic abilities.

(a) Bus voltage v_b

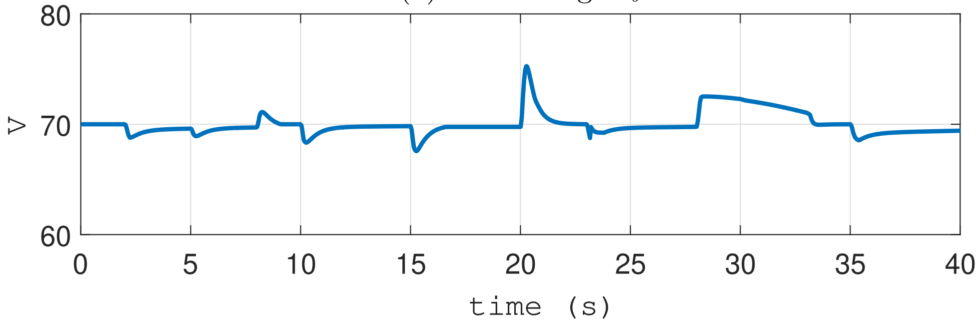

(b) Load current i_l

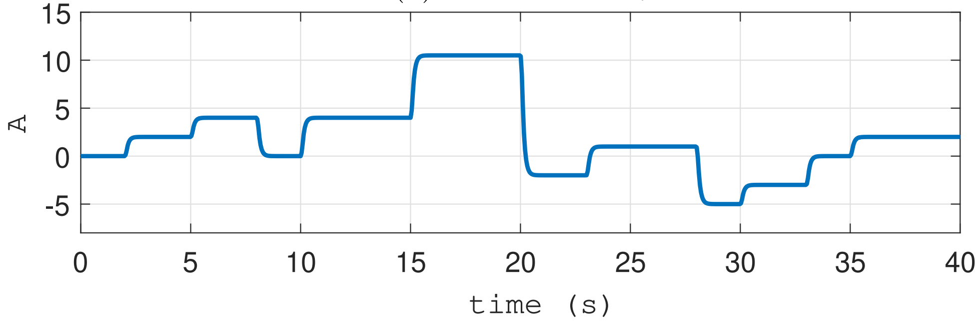

(c) Fuel cell voltage v_{fc}

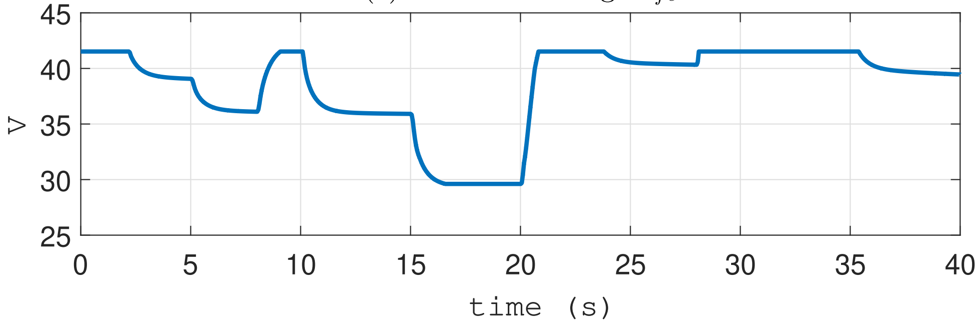

(d) Fuel cell current i_{fc}

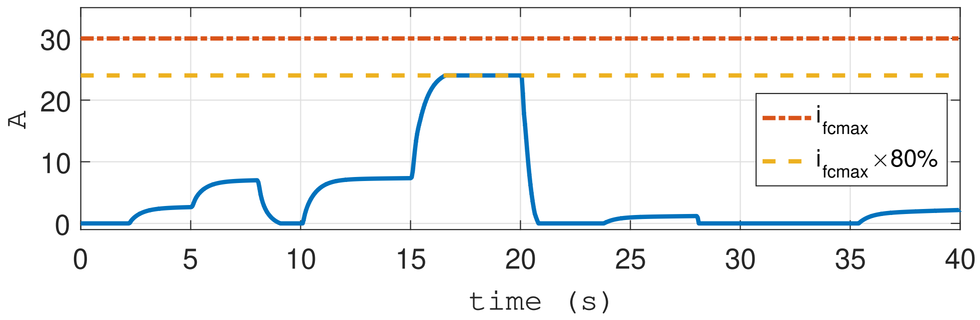

(e) SCs voltage v_{sc}

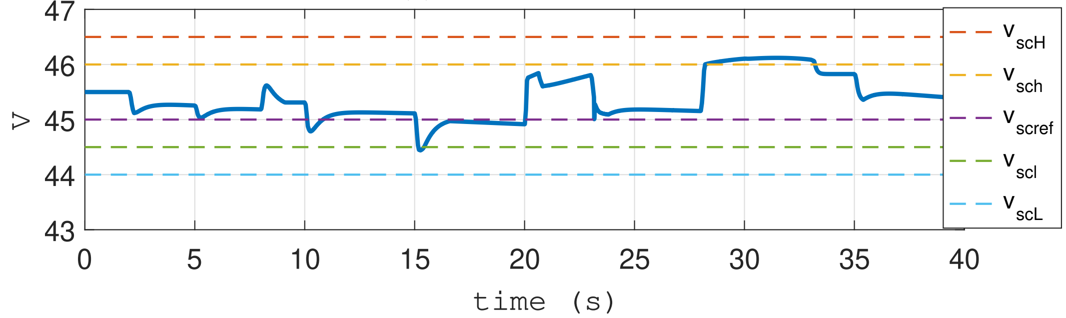

(f) SCs current i_{sc}

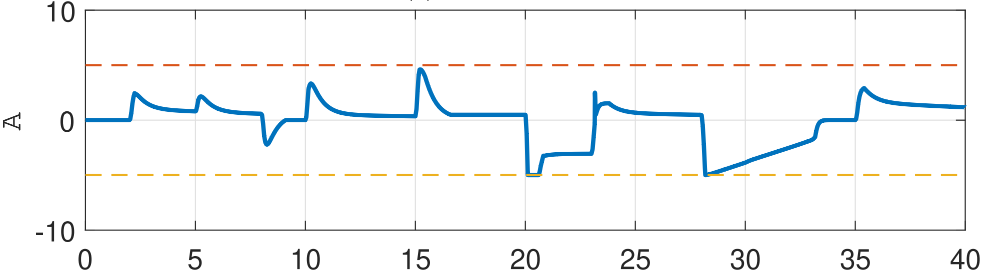

(g) SCs and FC mode

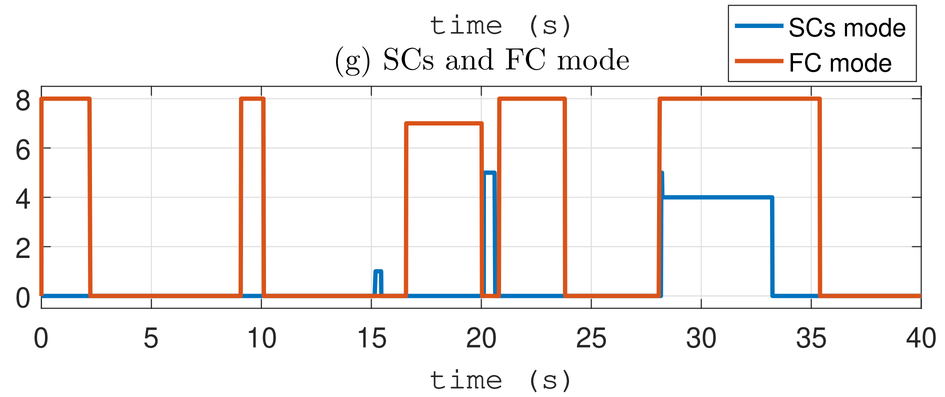

(h) Dissipative load current i_d

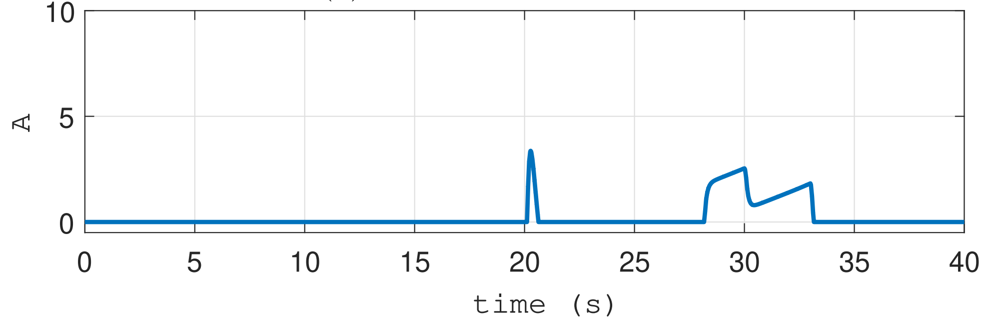

FIGURE 4.14 – Simulation results - limitation (1)

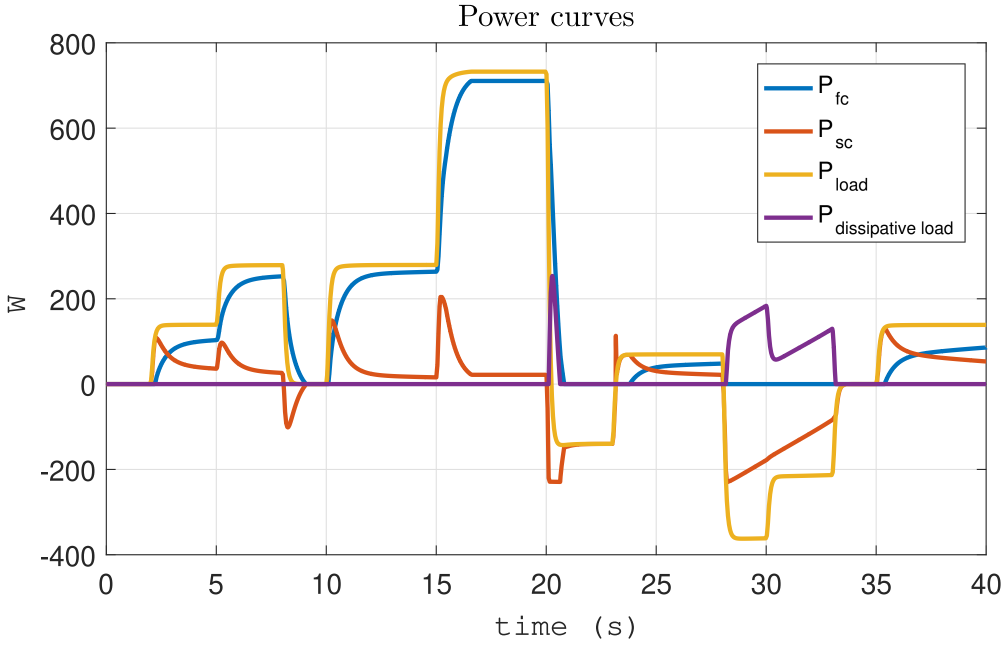

FIGURE 4.15 – Simulation results - limitation (2)

4.6/ POWER HARDWARE-IN-THE-LOOP VALIDATION

4.6.1/ TEST BENCH DESCRIPTION

The experimental validation is realized by the PHIL test bench introduced in section 3.2 of Chapter 3. The connection of the components is shown in Fig. 4.16. For the physical system, the elements used for the experiment are :

- A host PC and a MicroLabBox.
- Measurement and acquisition card and PWM generation card.
- SCs : 8 Maxwell BPAK0058-E015 type supercapacitors are installed, with 4 in series and 2 in parallel.
- An electronic load : type EA-ELR 9080-510.
- A power supply : type EA-PSI 9080-340.
- A bi-directional converter for the SCs.

For the emulated system part, the FC and its DC/DC converter models are established in Matlab / Simulink and are emulated by the power supply in the physical system. The load and dissipating resistance load current are emulated by the electronic load. Especially, the emulation of the load current is divided into two parts : the positive load current is emulated by the electronic load, while the negative load current for the generator mode is emulated by the power supply.

As introduced in Chapter 3, to realize the real-time control of the system, the real-time applications are modeled and compiled on Matlab software using the dSPACE toolbox and loaded to the MicroLabBox board, and experimental data are displayed is ControlDesk.

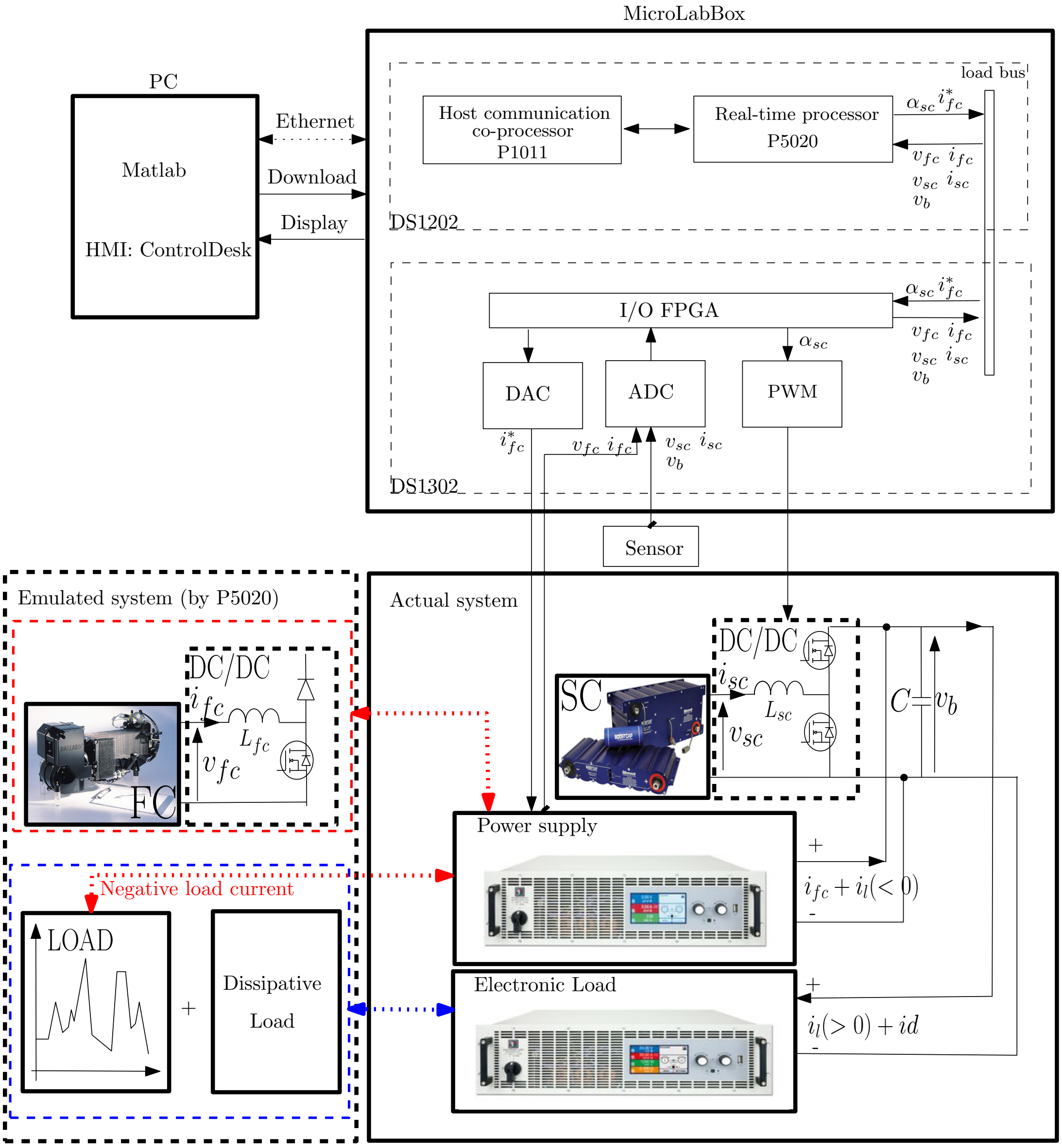

FIGURE 4.16 – Power Hardware-in-the-loop test bench structure

4.6.2/ POWER HARDWARE-IN-THE-LOOP RESULTS

A test on the PHIL platform has been done with the same load current scenario designed for the simulation in section 4.5.3. The system controller configuration is shown in Tab. 4.3. Fig. 4.17 shows a comparison of the simulation results in section 4.5.3 and the experimental results.

Comparing with the simulation results, the variations of the experimental FC voltage and current are similar (see Fig. 4.14 (c) and (d)), since the same FC model is integrated. With the real SCs, we can see a similar behavior to the simulated one. At around 15 s, the SCs current was firstly limited by the minimum current (mode 6 of SCs), then the SCs voltages reaches v_{scl}, and the discharge is limited because of the voltage limitation (mode 1 of SCs), through parameter r_2 in the control law.

(a) Bus voltage v_b

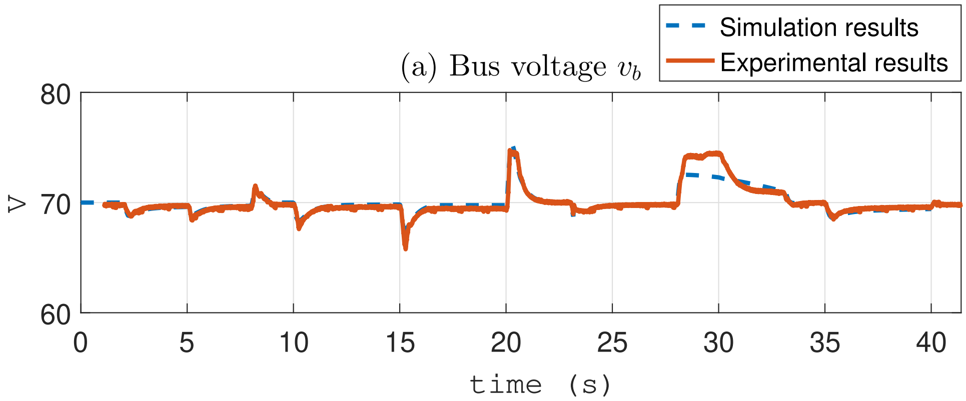

(b) Load current i_l

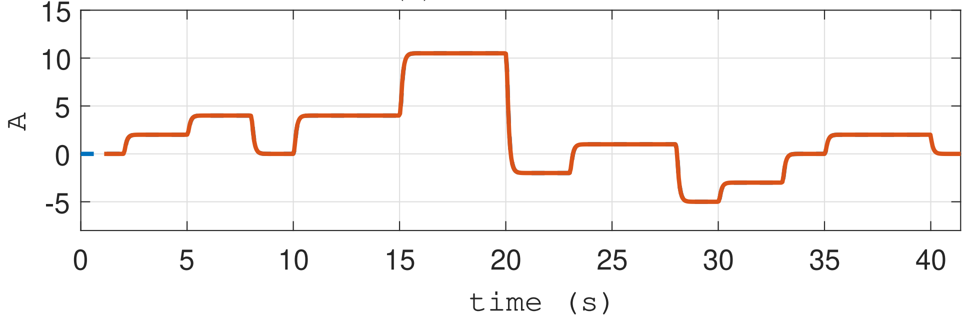

(c) Fuel cell voltage v_{fc}

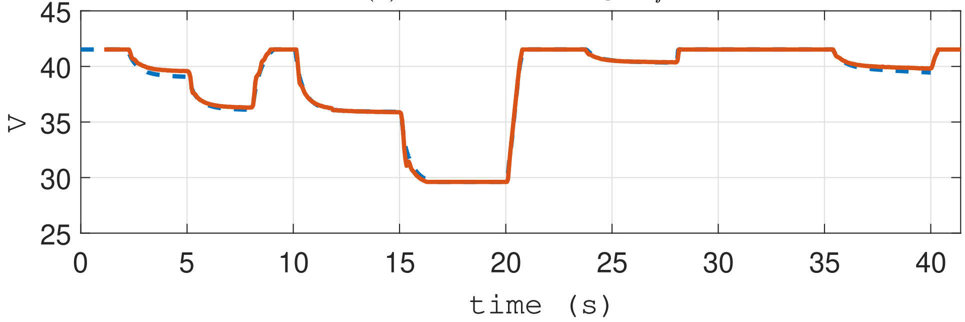

(d) Fuel cell current i_{fc}

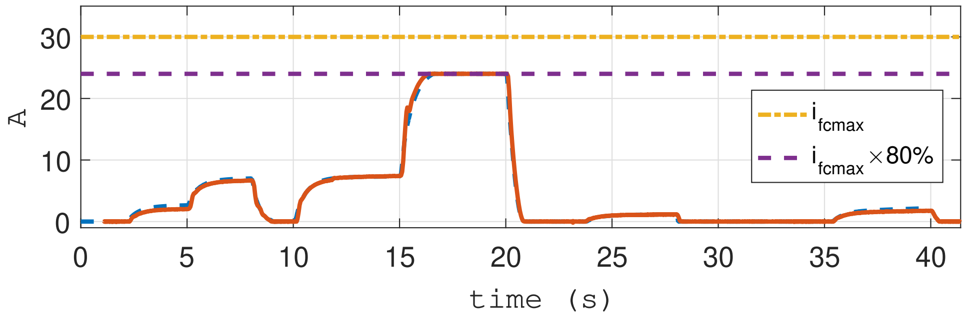

(e) SCs voltage v_{sc}

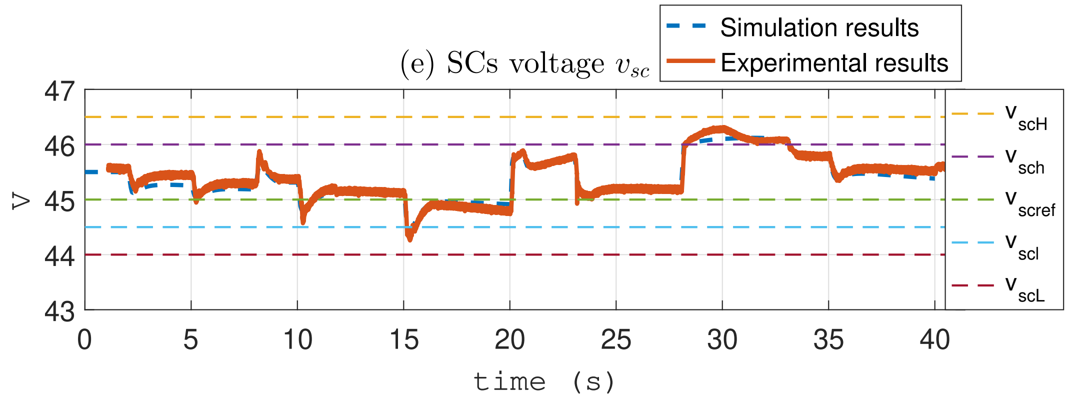

(f) SCs current i_{sc}

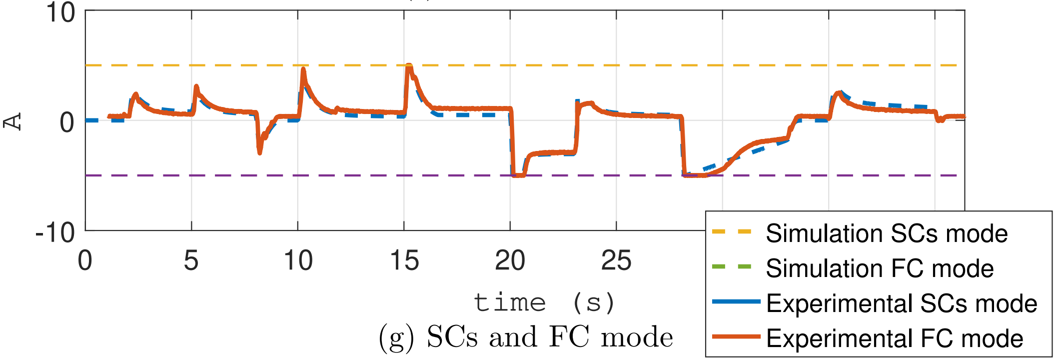

(g) SCs and FC mode

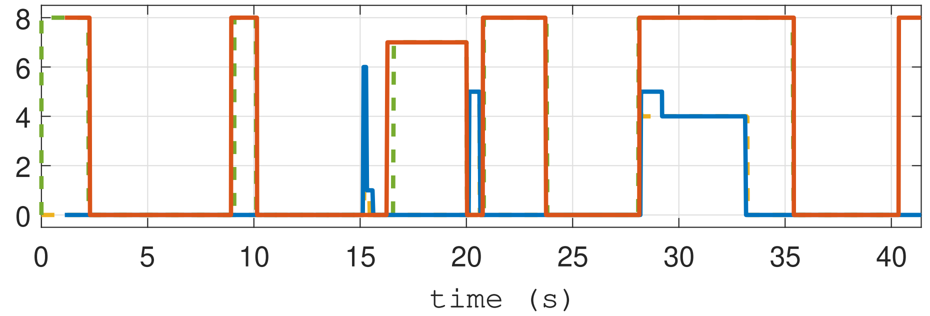

(h) Dissipative load current i_d

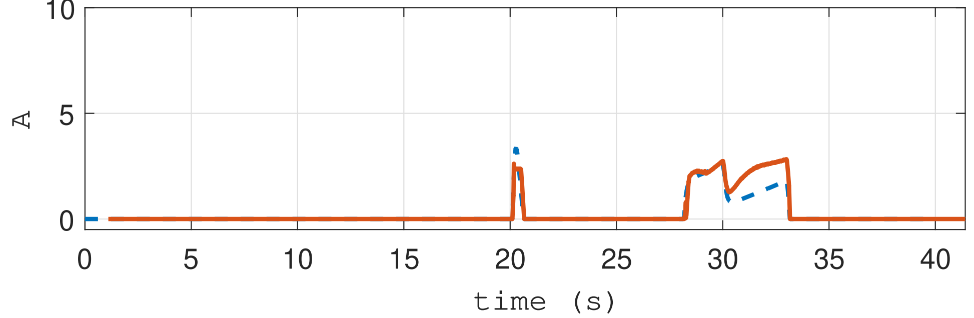

FIGURE 4.17 – PHIL results

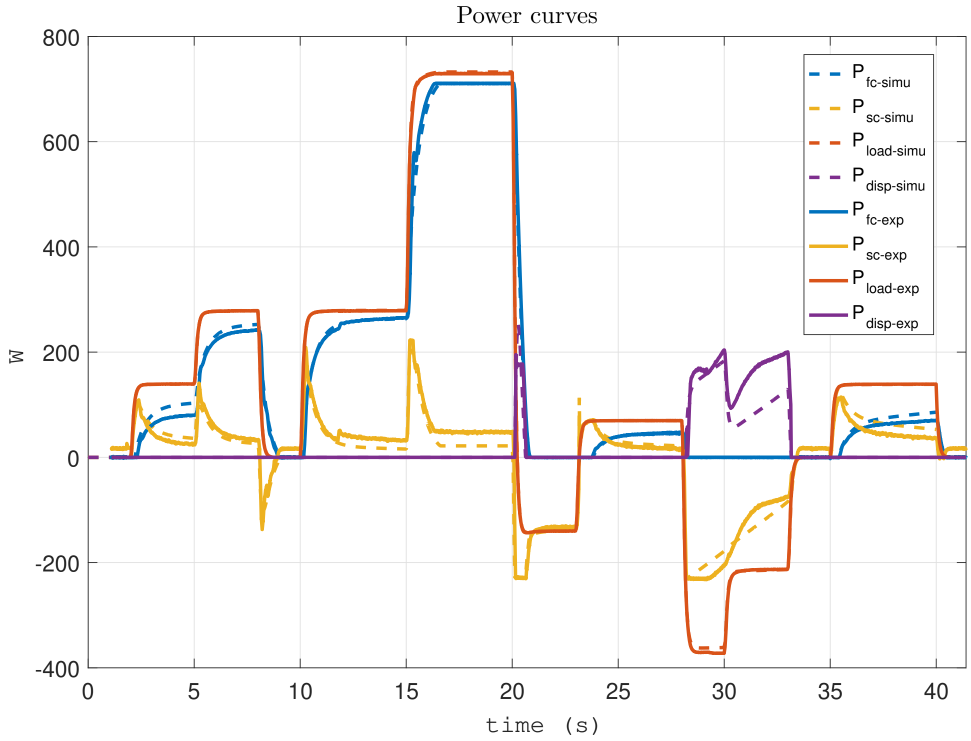

FIGURE 4.18 – PHIL results - power curves

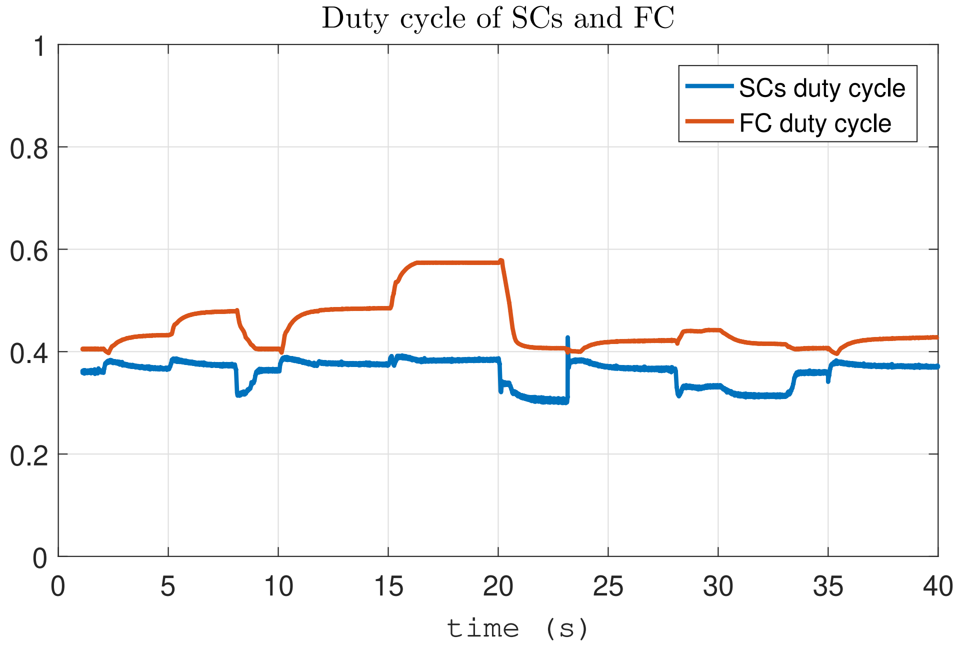

FIGURE 4.19 – PHIL results - duty cycles

Moreover, from 25 s to 35 s, the real SCs voltage in the experiment also reaches the limitation v_{sch}, which also causes a significant rise of DC bus voltage (see Fig. 4.14 (a)). The difference of the DC bus variation at around 30 s is possibly caused by the inevitable errors on the controllable electrical load and the transmission losses in the real power system. Then thanks to the integral term in (4.45), the DC bus voltage converges slowly to the reference value by the dissipative resistance load. We can also notice that during the experiment, the SCs current is a little higher than the simulated one. The reason for this difference might be due to the losses in the real power system.

The power curves of the experiment are presented in Fig. 4.18. We can see that the SCs produce more power than expected because of the losses. In addition, the duty cycle of the SCs and FC are shown in Fig. 4.19, and are not considered in the simulated system.

In order to valuate the stability of the system, the variability of the DC bus voltage around the reference value is calculated by the absolute percentage error. The mean absolute percentage error (MAPE) as well as the maximum absolute percentage error are calculated as follows :

$$MAPE_{mean} = \frac{1}{n}\sum\left|\frac{v_b - v_{bref}}{v_{bref}}\right| \tag{4.54}$$

$$MAPE_{max} = max\left(\left|\frac{v_b - v_{bref}}{v_{bref}}\right|\right) \tag{4.55}$$

The MAPE was also applied to represent the difference between the simulation and experiment results. The DC bus voltage is chosen for the comparison of the MAPE, as follows :

$$MAPE = \frac{1}{n}\sum\left|\frac{v_{bsimu} - v_{bexp}}{v_{bsimu}}\right| \tag{4.56}$$

Finally, the results are shown in Tab. 4.5. The DC bus voltage varies up to 7.5 % in the simulation results and 6.8 % in the PHIL results with an average value of 1 % around the reference voltage, so that the stability of the system is guaranteed by the proposed controller. The MAPE between the simulation and PHIL results is 0.38 %, which is small enough and we can therefore say that the experimental results correspond to the simulation results.

Simulation results	
Mean absolute percentage error	0.98 %
Maximum absolute percentage error	7.53 %
PHIL results	
Mean absolute percentage error	1.13 %
Maximum absolute percentage error	6.80 %
MAPE between simulation and PHIL on DC bus voltage	
0.38 %	

TABLE 4.5 – Comparison on DC bus values

Overall, the behavior of the real system follows the simulation results, so that the operation of the proposed controller is validated by the test.

4.7/ CONCLUSION

In this chapter, an advanced passivity-based controller was designed to manage power and energy between an hydrogen FC and SCs, which considers situations of limitations. In addition, a dissipative resistance load was also implemented into the system to protect the system from over-voltage. The proposed passivity-based controller integrates some component constraints directly into the controller equations, which ensures the stability of the whole closed-loop system. The novelty of this new IDA-PBC controller is concluded by four points :

- The SCs reference current is a function of the SCs voltage. Hence, the SCs current changes according to the voltage level of the SCs with a good choice of a tuning parameter (r_2) which enables a dynamic saturation of the SCs current.
- This parameter r_2 also exists in the control law of the FC current. Therefore the FC can compensate for the power that the SCs cannot provide when the limitation is activated.
- When the SCs voltage level is too high, the extra power can be dissipated with a controllable load during regenerative mode. These new ideas are introduced in the proposed controller based on passivity, considering the stability.
- Finally, as the limitations and dissipation are integrated directly into the control law, the stability of the closed-loop system is guaranteed.

In order to test the proposed controller, simulations were run for three scenarios and a comparison with the previous controller. Finally, the operation of the proposed algorithms was validated by the PHIL experimentation test. The experimental results showed that the integration and an efficient exploitation of the components are realized by the controller proposed in this work, while the locally asymptotic stability of the whole closed-loop system is preserved.

5

AGING-TOLERANT PASSIVITY-BASED CONTROL FOR A FC/SCS HYBRID VEHICLE

5.1/ INTRODUCTION

PEMFC systems have a limited lifetime because of multiple impairments that prevent their widespread deployment, such as operating conditions, materials aging and mechanical stresses [179]. These phenomena reduce the FC capacity for generating electric power. If the controller does not consider the aging of the FC, overloading may happen and unstable behavior can be observed.

As a consequence, prognostics and health management (PHM) of PEMFCs is mandatory for industrial applications. PHM allows extending the life of such electrochemical converters using monitoring [180], diagnostics [181], [182], prognostics [183], and corrective actions. The indicators of SoH of an FC system can be built by selecting specific features from sensors. This allows to plan preventive maintenance at the right time, and so to reduce costs. In the field of energy management, knowing the SoH and remaining life of an energy source can help improve the power and energy distribution among the different components in the system.

This chapter proposes an application of the advanced passivity-based control introduced in Chapter 4, on a commercial vehicle, combined with aging-tolerant control. Firstly, an energy management strategy is first realized by IDA-PBC. Secondly, an aging degradation model of the PEMFC proposed by Mathieu Bressel in [184] is integrated into the system. Also, an extended kalman filter based on [185, 186] provides the actual and forecast SoH of the FC in real-time in order to compute the maximum current and power that the FC can deliver. Based on the estimated information, it is guaranteed that the closed-loop power management system cannot diverge.

This chapter is divided into four sections : section 5.2 describes the hybrid model of the case study and the aging model of the PEMFC. The improvement of the proposed passivity-based controller is detailed in section 5.3. In section 5.4, an aging-tolerant controller is described and simulation results are provided in section 5.5. The experimental results based on a HIL platform that is representative of a commercial vehicle under a modified New European Driving Cycle (NEDC) are presented in section 5.6. Finally, conclusions are drawn in section 5.7.

5.2/ HYBRID SYSTEM MODEL AND CONTROL STRUCTURE

In this section, the aging model of the PEMFC as well as the vehicle model are introduced, following the same process as in Chapter 4.

5.2.1/ HYBRID SYSTEM MODEL

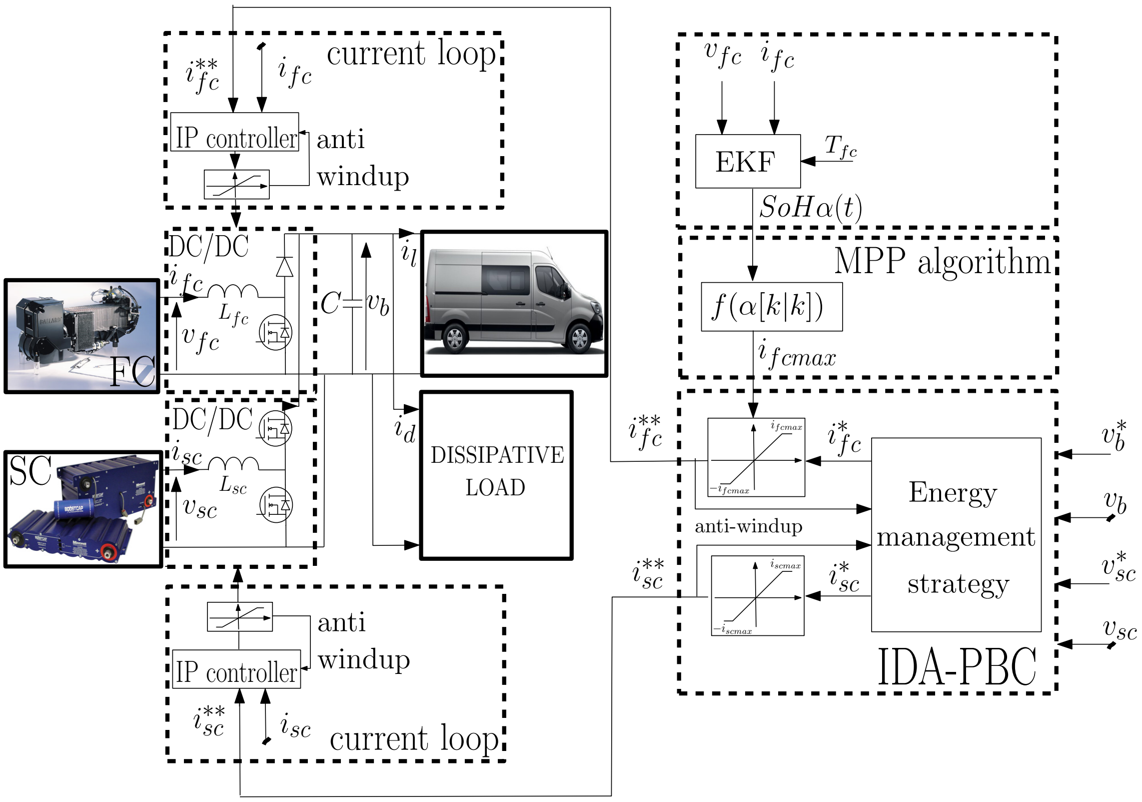

FIGURE 5.1 – System structure with aging-tolerant control

As introduced in Chapter 4, the same two-converter parallel structure of a FC/SCs system is applied in this chapter, as shown in Fig. 5.1. Differently, the load is a commercial vehicle under a widespread driving cycle. For the FC model, instead of the 5^{th} order polynomial function, a model with aging parameters is implemented. Moreover, an aging-tolerant control of the FC is associated with the IDA-PBC controller, where the SoH of the FC is estimated by an EKF algorithm in real-time. Then the FC maximum current is computed by a Maximum Power Point (MPP) algorithm, which enables the controller to know the maximum current that the FC can deliver. Therefore, combined with the proposed controller, there are two dynamic saturations :

- An implicit variable saturation function of the SCs current according to the SCs voltage level, with the choice of a tuning parameter (r_2).
- An explicit variable saturation function of the FC current according to the estimation of FC SoH.

With the same analysis as in Chapter 4, the system is firstly modeled by a 4^{th} order non-linear state space model :

$$\frac{d}{dt}v_b(t) = \frac{(1-\alpha_1(t))\,i_{fc}(t) + (1-\alpha_2(t))\,i_{sc}(t) - i_l(t) - i_d^*(t)}{C} \tag{5.1}$$

$$\frac{d}{dt}v_{sc}(t) = -\frac{i_{sc}(t)}{C_{sc}} \tag{5.2}$$

$$\frac{d}{dt}i_{fc}(t) = \frac{-(1-\alpha_1(t))\,v_b(t) + v_{fc}(t)}{L_{fc}} \tag{5.3}$$

$$\frac{d}{dt}i_{sc}(t) = \frac{-(1-\alpha_2(t))\,v_b(t) + v_{sc}(t)}{L_{sc}} \tag{5.4}$$

Then the model is reduced to the 2^{nd} order with the same hypotheses as in section 4.2.4 to design the outer loop controller as follows :

$$\frac{d}{dt}v_b(t) = \frac{1}{C}\left(\frac{v_{fc}(t)}{v_b(t)}\,i_{fc}^*(t) + \frac{v_{sc}(t)}{v_b(t)}\,i_{sc}^*(t) - i_l(t) - i_d^*(t)\right) \tag{5.5}$$

$$\frac{d}{dt}v_{sc}(t) = -\frac{i_{sc}^*(t)}{C_{sc}} \tag{5.6}$$

with $x_r(t) = [x_1, x_2]^T = [v_b, v_{sc}]^T$, control inputs $u_r = [i_{fc}^*, i_{sc}^*]^T$, and measurements $y_r = [v_b, v_{sc}]^T$ and $z_r = [i_{fc}, i_{sc}, v_{fc}]^T$.

5.2.2/ AGING MODEL OF THE PEMFC

In this research, a static model of FC is employed. It is described by the following equations [185, 186] :

$$v_{st} = n\left(E_0 - AT_{fc}\ln\left(\frac{j_{fc}}{j_0}\right) - Rj_{fc} - BT_{fc}\ln\left(1 - \frac{j_{fc}}{j_L}\right)\right) \tag{5.7}$$

$$v_{fc} = N_{fcp}\,v_{st} \tag{5.8}$$

$$i_{fc} = N_{fcs}\,i_{st} \tag{5.9}$$

This relation is used to model the polarization curve $v_{fc} = f(i_{fc})$, where v_{st} and i_{st} are the FC voltage current in the stack, n is the number of cells in one stack and N_{fcp} is the number of stacks in parallel, N_{fcs} is the number of stacks in series, E_0 represents the maximum theoretical potential, T_{fc} is the operation temperature, A and B represent the activation and concentration constants, R is the global resistance related to membranes, electrodes and connectors, j_0 is the exchange current density j_L is the limiting current density, $j_{fc} = \frac{i_{st}}{S}$ is the input current density, and S is the activation surface of the FC.

In order to study the effect of aging on the parameters value of (5.7), a 175-hour continuous experimental test was performed in [184] on an 8-cell FC stack under an automotive load profile with a surface of 220 cm^2 provided by the French Atomic Energy and Alternative Energies Commission (CEA). Fig. 5.2 shows the experimental polarization curve evolution during the long term test at $80°$C.

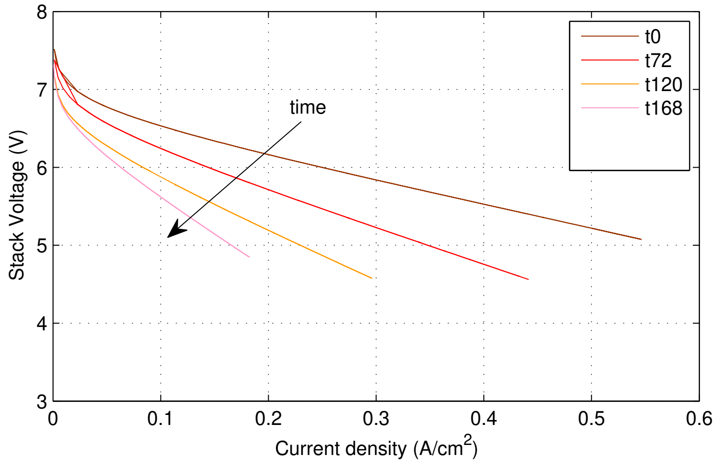

FIGURE 5.2 – Polarization curves of the FC over time [184]

Using a fitting technique, a set of model parameters were extracted from these curves. Then the deviation of some parameters with the influence of FC aging was studied in the thesis of Mathieu Bressel [187]. It was observed that only the resistance value R and the limiting current density i_L change significantly (see Fig. 5.3). Similar behaviour was found in another study [188] as well as with a 1500-hour test under a constant load [185]. A bad water management is the main factor affecting R. The value of the limiting current is decided by the apparent surface of exchange (related to the catalyst layer) [189].

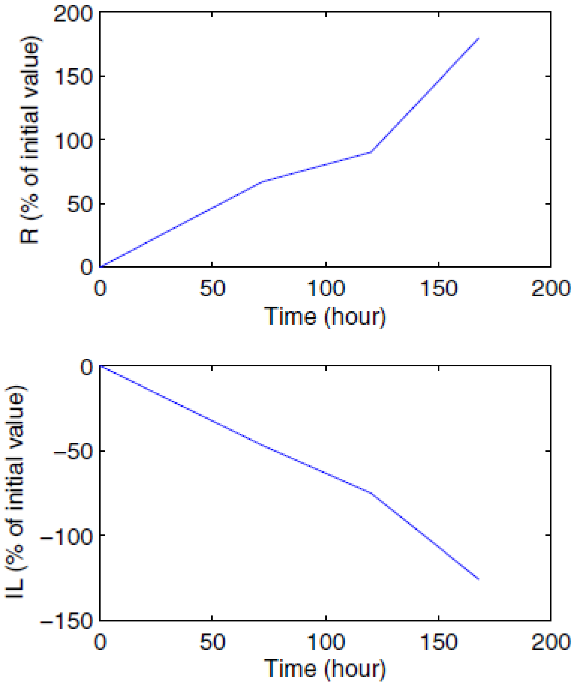

FIGURE 5.3 – Evolution of R and i_L with operation time [184]

Based on the above studies, an empirical degradation model was developed in [184] and is described as follows :

$$R(t) = R_0(1 + \alpha(t)),\ j_L(t) = j_{L0}(1 - \alpha(t)) \tag{5.10}$$

$$\alpha(t) = \int_0^t \beta(\tau)d\tau \tag{5.11}$$

where $\alpha(t)$ is the SoH indicator, $\beta(t)$ is the speed of parameters deviation, and R_0 and j_{L0} are the initial resistance and limiting current density extracted from the first polarization curve (a new FC) [185]. Finally, all data values are listed in Tab. 5.1.

Fuel cell parameters	
Number of cells n	53
Maximum FC voltage E_0	1.18120226
Activation surface S	220 cm^2
Global resistance R_0	0.001 [Ω]
Activation constant A	0.6×10^{-4}
Concentration constant B	-1.5×10^{-4}
Exchange current density j_0	9.4174×10^{-4} [A/cm^2]
Limiting current density j_{L0}	1 [A/cm^2]
Temperature T_{fc}	353.15 [K]
Number of FC stacks in series N_{fcs}	2
Number of FC stacks in parallel N_{fcp}	8

TABLE 5.1 – Fuel cell parameters

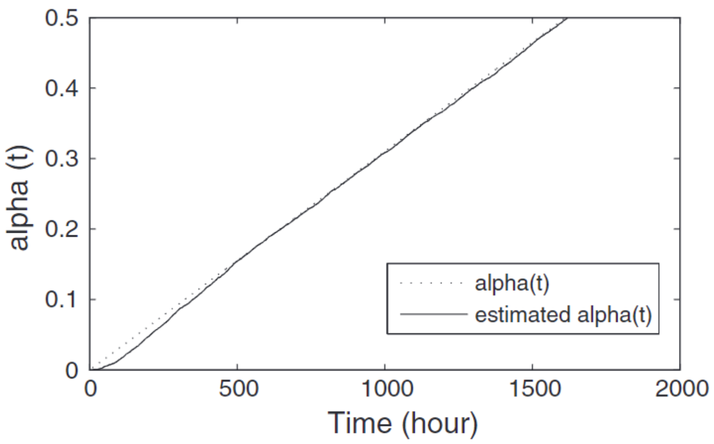

FIGURE 5.4 – Relationship between $\alpha(t)$ and FC operation duration [185]

The relationship between the working hours and the SoH $\alpha(t)$ of the experiment FC is shown in Fig. 5.4. $\alpha(t) = 0$ represents the initial condition of a new FC and $\alpha(t)$ increases with time and indicates the aging of the FC. Fig. 5.5 shows the polarization curve at 80°C for our application example with different SoH levels, where the number of cells of one FC module has been fixed to 53 with two FC modules in series and eight in parallel for the purpose of the case study. The power curves are shown in Fig. 5.6, we can see that the maximum power decreases with the aging of FC, so that it is essential to know the current of the maximum power at each moment to avoid overload. Without that knowledge, the whole hybrid closed-loop system diverges, leading to an unstable system.

This information is obtained in two steps. Firstly, the SoH is estimated by the EKF as described in [184]. Secondly, the MPP of the FC can be determined from the P-I curve of the FC. The limitation of the FC reference current is set to 80 % of the MPP (as presented in Chapter 4) and sent to the power management controller in order to protect the FC from overload. This aging-tolerant controller is detailed in section 5.4.

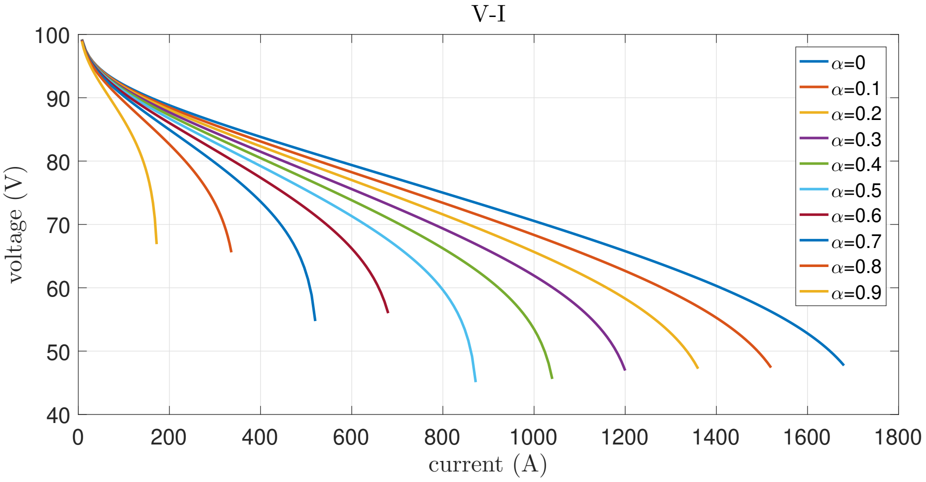

FIGURE 5.5 – V-I curves of the FC at 80°C

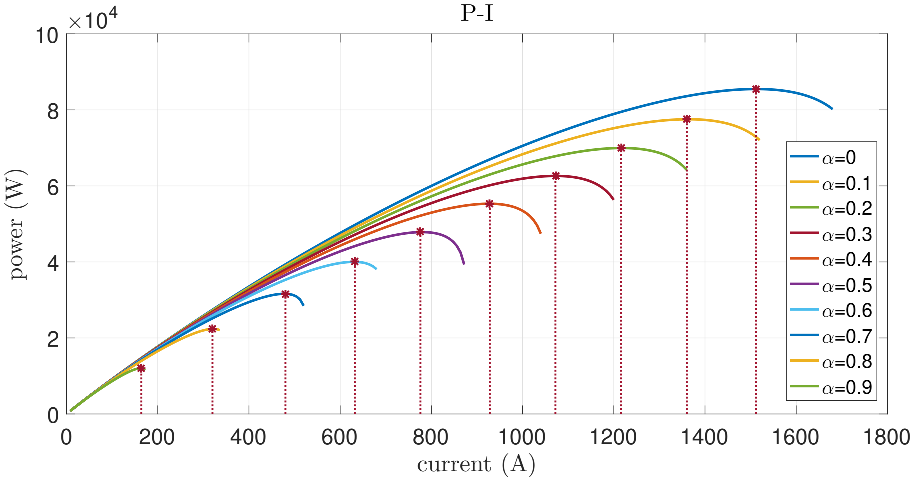

FIGURE 5.6 – Power curves through aging at 80°C

5.2.3/ VEHICLE MODELING AND LOAD CURRENT COMPUTATION

A case study based on a commercial vehicle, a Renault Master [190], is considered in this work. The load current is calculated by :

$$i_l(t) = \frac{P_l(t)}{v_b(t)} = \frac{P_{vehicle}(t)}{v_b(t)} \tag{5.12}$$

In order to compute the electrical power demanded by the vehicle, the corresponding force first needs to be calculated :

$$P_{vehicle} = F_{traction} V_{vehicle} (\eta_{traction})^k \tag{5.13}$$

with $k = 1$ if $P_{vehicle} < 0$ and $k = -1$ if $P_{vehicle} > 0$. $F_{traction}$ is the traction force, $V_{vehicle}$ is the vehicle velocity and $\eta_{traction}$ is the transmission efficiency.

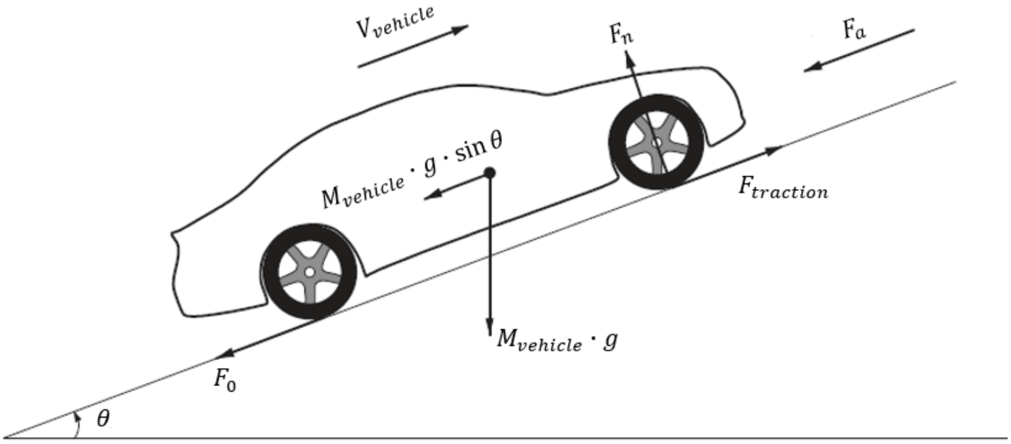

FIGURE 5.7 – Force acting on a vehicle

Fig. 5.7 shows the schematic that represents the force acting on a vehicle in motion. In this schema, θ is the angle of the slope, $M_{vehicle}$ is the mass of the vehicle, g is the gravitational acceleration, F_0 is the road slope and rolling resistant force, F_a is the aerodynamic drag. According to Newton's second law of motion, we have :

$$M_{vehicle} \frac{d}{dt} V_{vehicle} = F_{traction} - F_{res} \tag{5.14}$$

where the total amount of resistant forces F_{res} is represented by a function of the vehicle speed [190] :

$$F_{res} = F_0 + F_a + F_g \tag{5.15}$$

Here, F_g is the force caused by the gravity acting on the slope road, as shown in Fig. 5.7.

$$F_g = M_{vehicle} g sin\theta \tag{5.16}$$

The road slope and rolling resistance force F_0 can be calculated by the following equation [191] :

$$F_0 = M_{vehicle} g f_r cos\theta \tag{5.17}$$

f_r is the rolling resistance coefficient, and is decided by many variables, such as the tire material, road roughness, road material, the presence or absence of liquids on the road, etc. In most situations, f_r is considered as a linear function of the vehicle speed [192] :

$$f_r = 0.01 \left(1 + \frac{V_{vehicle}}{100}\right) \tag{5.18}$$

Usually, the aerodynamic drag resistance F_a is approximated by considering the vehicle as a prismatic body with a frontal area, which is given by :

$$F_a = \frac{1}{2}\rho C_x S_{vehicle} V_{vehicle}^2 \tag{5.19}$$

where $S_{vehicle}$ is the vehicle front area, ρ is the air density, and C_x is the vehicle aerodynamic drag coefficient that characterizes the shape of the vehicle.

In the case of a Renault Master, considering that the vehicle runs on a flat road, the vehicle parameters are chosen as shown in Tab. 5.2 [190, 193].

Vehicle parameters	
Transmission efficiency $\eta_{traction}$	0.95
Vehicle weight (without passengers) $M_{vehicle}$	1820 [kg]
Front surface $S_{vehicle}$	3.664 [m^2]
Gravitational acceleration g	9.8 [m/s]
Aerodynamic drag coefficient C_x	3.664
Air density ρ	1.225 [kg/m^3]
Road angle θ	0^o

TABLE 5.2 – Vehicle parameters

5.3/ PASSIVITY-BASED CONTROLLER

The passivity-based controller designed with the IDA-PBC methodology and introduced in sections 4.3 and 4.4 (in Chapter 4) is implemented into this system. Therefore, the control law is the same as (4.25) - (4.27), and the same configuration of r_2 :

$$\begin{aligned}
\delta\dot{y} &= -y + i_l/v_b, \qquad \delta > 0 && (5.20)\\
i_{fc}^* &= \frac{v_b}{v_{fc}}\left(y v_b^* - \gamma\tilde{v}_{sc} - r_2\frac{v_{sc}}{v_b}C_{sc}^2\tilde{v}_{sc} + i_d^* + \left(\frac{v_{sc}}{v_b}\gamma - r_1 C^2\right)\tilde{v}_b\right), \qquad \gamma > 0 && (5.21)\\
i_{sc}^* &= -\gamma\,\tilde{v}_b + r_2 C_{sc}^2\tilde{v}_{sc} && (5.22)
\end{aligned}$$

Differently, for the dissipative load operation, the integral term in i_d^* (see (4.45)) is not involved, in order to simplify the controller operation. In the situation of mode SCs ≠ 5 and mode FC = 8, the reference current of the control law is :

$$i_d^* = -y v_b^* + \gamma\tilde{v}_{sc} + r_2\frac{v_{sc}}{v_b}C_{sc}^2\tilde{v}_{sc} + \frac{v_{sc}}{v_b}\gamma\,(\mu - 1)\,\tilde{v}_b \tag{5.23}$$

When $v_{sc} > v_{sch}$, the term $(\gamma\tilde{v}_{sc} + \frac{v_{sc}}{v_b}\gamma(\mu - 1)\tilde{v}_b)$ is set to zero, in order to remove the steady state error on the DC bus voltage without the integral term, which leads μ to $(1 - \frac{v_b\tilde{v}_{sc}}{v_{sc}\tilde{v}_b})$. Then i_d^* is :

$$i_d^* = -y v_b^* + r_2\frac{v_{sc}}{v_b}C_{sc}^2\tilde{v}_{sc} \tag{5.24}$$

The benefit of this procedure is that the configuration is simplified by removing parameter k_d. Also, the SCs voltage is limited to v_{sch} instead of v_{scH} by (5.24). For practical application, it is easier to realize.

5.4/ AGING-TOLERANT CONTROL OF PEMFC

As mentioned in section 5.2.2, the FC performance tends to decrease over time. For instance, when the FC SoH is 0.5, the FC maximum current is decreased by a factor of two (see Fig. 5.5). However, if this change inside the FC is not considered in the controller, the top limit of the current saturation is still equal to the initial value. If the load demand is high, then overloading may occur and the control could diverge. Therefore, the estimation of the FC SoH should not be neglected and PHM of FCs is necessary. In this section, an aging-tolerant control of PEMFC is thus proposed, where the estimation of the SoH is realized by an EKF.

5.4.1/ GENERALITIES AND METHOD

In this section, an aging-tolerant control of PEMFC based on the previous controller is proposed, and exhibits the following properties :

- It estimates the PEMFC SoH in order to compute the maximal power and current, so that a dynamic saturation of the FC current can be designed based on a prognostic algorithm. It ensures that the FC is protected from over-current.
- It ensures the stability of the whole system based on the first property.

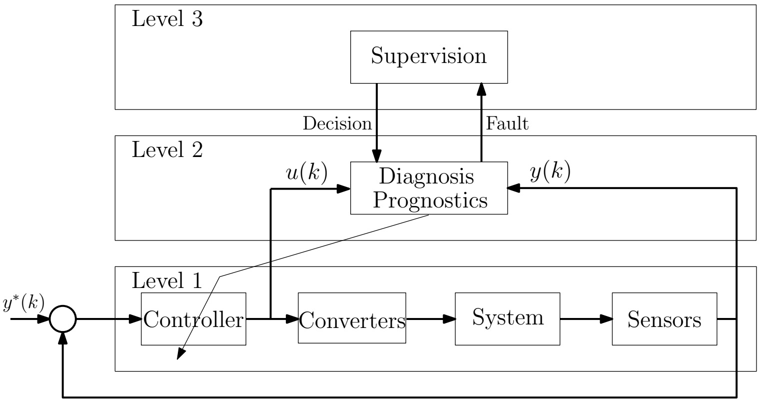

FIGURE 5.8 – General FTC scheme

In general, Fault Tolerant Control (FTC) consists of two parts [194] : an online algorithm for detection and isolation of faults that produces a signal for the supervisor when a fault is detected and isolated ; a supervisor, with the role of reconfiguration or adaptation of the input signal, can be predetermined for every fault. FTC is typically divided into a three-level scheme as proposed in [194] (see Fig. 5.8). Applied to this work, the explanation of each level is :

- Level 1 : ”Control loop”. This level includes the basic elements of the regular control loop such as the PEMFC, sensors, actuators and the controller.
- Level 2 : ”Diagnosis et prognostics”. In this work, it is the EKF which generates signals of SoH and the module of prognostics, informs the supervisor about the evolution of the PEMFC’s health. This level also plans the reconfiguration or the corrective action decided by the supervisor.
- Level 3 : ”Supervision”. It is a dynamic discrete events system. The mission of the supervisor is to isolate the failures from the fault signals as well as decide the

corrective actions to accommodate these faults. In this work, the supervision is the MPP algorithm that generates the maximum current of the FC according to the estimation of the SoH. For further work, this level can be developed and estimate the remaining useful life (RUL) of the FC, using the method proposed in [186].

The FTC architecture can be particularised as shown in Fig. 5.9 for the case of the advanced power management strategy associated with the aging-tolerant control of the FC proposed in this work.

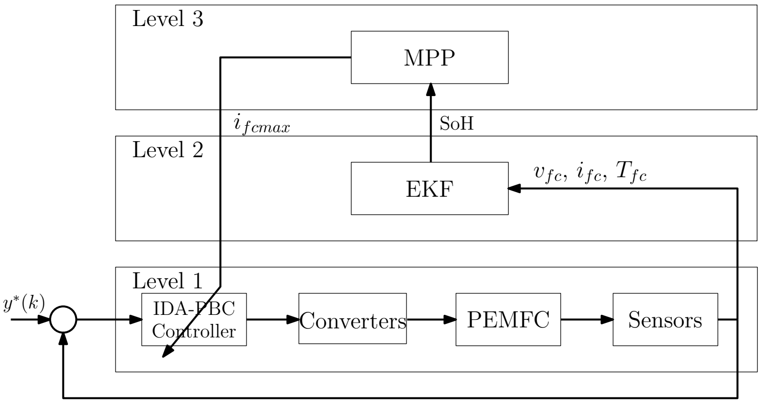

FIGURE 5.9 – FTC scheme applied to the studied system

5.4.2/ STATE-OF-HEALTH ESTIMATION

An EKF is applied in this research to estimate the global SoH α_k and the speed of degradation β_k at time t_k, as shown in Fig. 5.1, and based on the following discrete system [185, 186] :

$$x_{k|k-1} = Ax_{k-1|k-1} + w_{k-1} \tag{5.25}$$

$$y_k = g(x_{k|k-1}, u_k) + v_k \tag{5.26}$$

where the state vector of the system is $x_k = [\alpha_k \ \beta_k]^T$, u_k represents the vector of the current and temperature input, y_k is the output voltage, and w_k and v_k are the noise of process and observation that are assumed to be Gaussian with zero mean. Here, the SoH α_k is set equal to zero at the beginning (i.e., no degradation), and increases to α_{max}=0.3 at the considered End-of-Life (EoL) of the FC [185, 186]. A value of α_{max} equal to 0.3 represents a reduction of around 10% of the nominal power of the FC at 0.5 A/cm^2. At that time, the FC could continue to operate and the control can indicate that a maintenance is mandatory.

This threshold value α_{max} depends on the type of FC, FC designer or governmental rules. The US DOE target for 2020 is 5000 h of durability with cycling, with less than 10% of reduction of the nominal power at $1 - 1,5$ A/cm^2 [195]. Based on this considered value (10%) and the nominal current density, the value of α_{max} can be defined.

According to the FC aging model proposed in [185], a voltage drop ΔV is caused by the concentration, activation and ohmic losses and can be expressed as follow :

$$\Delta V = n\left(AT\ln\left(\frac{j_k}{j_0}\right) + R_0\left(1+\alpha_{k|k-1}\right)j_k + BT\ln\left(1 - \frac{j_k}{j_{L0}\left(1-\alpha_{k|k-1}\right)}\right)\right) \tag{5.27}$$

Since ΔV is not physically measurable, the state vector is estimated from the stack voltage v_{st}. Based on (5.7), $g(x_k, u_k)$ is expressed in discrete form as follows at time $t = kT_s$:

$$\begin{aligned} g(x_{k|k-1}, u_k) = n\Bigg(& E_0 - AT \ln\left(\frac{j_k}{j_0}\right) - R_0\left(1 + \alpha_{k|k-1}\right) j_k \\ & - BT \ln\left(1 - \frac{j_k}{j_{L0}\left(1 - \alpha_{k|k-1}\right)}\right)\Bigg) \end{aligned} \tag{5.28}$$

where T_s is the sampling period fixed at 0.1 s. As the speed of degradation β is unknown, we assume that β is quasi-constant on a sampling period ($\beta_{k|k-1} \simeq \beta_{k-1|k-1}$), so we have :

$$A = \begin{bmatrix} 1 & T_s \\ 0 & 1 \end{bmatrix} \tag{5.29}$$

The EKF is then as follows :

- **Initialization**

$x_{0|0} = E[x(t_0)]$

$P_{0|0} = Var[x(t_0)]$

- Prediction

$x_{k|k-1} = Ax_{k-1|k-1}$

$P_{k|k-1} = AP_{k-1|k-1}A^T + Q$

- Correction

$K_k = P_{k|k-1}H_k^T(H_kP_{k|k-1}H_k^T + R)^{-1}$, with $\mathrm{H_k} = \frac{\partial \mathrm{g(x_k,u_k)}}{\partial \mathrm{x_k}}$

$P_{k|k} = P_{k|k-1} - K_kH_kP_{k|k-1}$

$x_{k|k} = x_{k|k-1} + K_k(V_{stk} - g(x_{k|k-1}, u_k))$

where Q and R are the variance of the process and measurement noises defined in [184], v_{st} is the measured stack voltage of the FC, H_k is the observation matrix, K_k is the optimal Kalman gain.

Based on the FC current scenario of Fig. 5.10 (a), the result of the SoH estimation by the EKF is shown in Fig. 5.10 (b) and (c). In this case, we consider an accelerated aging during 8 s to 13 s, in order to test the operation of the EKF. We can notice that when the FC current is nil (or low in practical applications), the estimated parameters are not updated because the system is inobservable (see Fig. 5.10 12 s to 14 s). More details concerning the SoH estimation of the PEMFC and the unobservability can be found in [185].

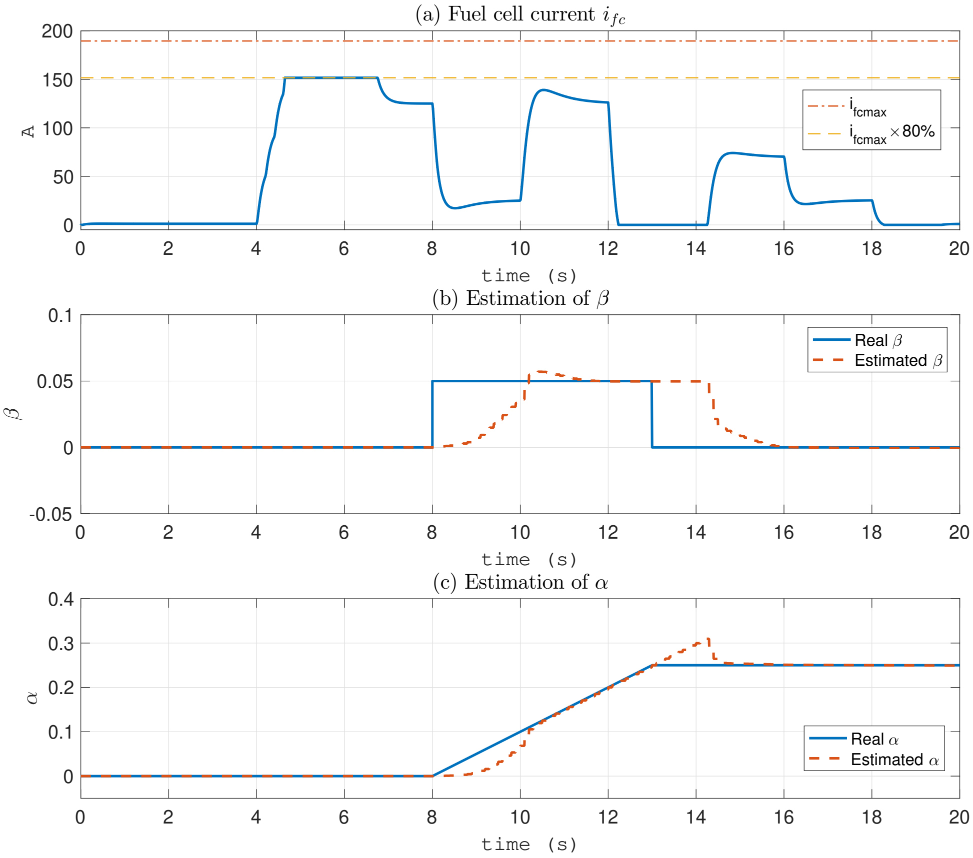

FIGURE 5.10 – Estimation of SoH with EKF

5.4.3/ MAXIMUM POWER POINT OF THE FC

With the EKF, the PEMFC SoH $\alpha_{k|k}$ and its derivative are estimated in real-time using (5.28). Then, the PEMFC power can be expressed as a function of the load current as :

$$\begin{aligned} P_{pack_k}(j_k) = n i_{st_k}\bigg(& E_0 - AT\ln\left(\frac{j_k}{j_0}\right) - R_0\left(1+\alpha_{k|k}\right) j_k \\ & - BT\ln\left(1-\frac{j_k}{j_{L0}\left(1-\alpha_{k|k}\right)}\right)\bigg) N_{fcp} N_{fcs} \end{aligned} \tag{5.30}$$

so that we are able to compute at each instant the maximal power of the fuel cell, with 2 stacks in series and 8 stacks in parallel, as shown in Fig. 5.6.

The main idea of aging-tolerant control is to realize a dynamic saturation function of the FC current, which means to find the limitation of the FC current at each time. Therefore, the next step is to compute the FC current for the maximum power. Two methods are applied to compute the maximum current of the FC in this work. The first method is a general method called iterative gradient descent, and the second one is to use a function $i_{fc_{max}} = f(\alpha)$, which is proposed specifically for this application.

ITERATIVE GRADIENT DESCENT

The general method iterative gradient descent estimates the current in order to determine the maximum power, as proposed in [186]. The steps can be listed as follows :

1. Start with an initial guess of point x_j while the counter j is set to zero.
2. Compute the gradient of the PEMFC power at this point :

$$G_j = \frac{\partial P_{pac_k}(x_j)}{\partial i_{st_k}} \tag{5.31}$$

3. The counter is incremented with a new estimate :

$$x_{j+1} = x_j - \nu G_j \tag{5.32}$$

where ν is the learning step. Steps 2 and 3 are repeated until convergence ($j < N_{max}$ or $|x_{j+1} - x_j| < \delta$), so that we can find the maximum point shown in Fig. 5.6. However, this method requires many calculations at each moment. Moreover, the performance of this algorithm depends essentially on the quality of the estimation of the SoH by the EKF.

FITTING CURVE

A specific method that simplifies the calculation is proposed by analyzing the FC model. The main idea of this method is to find the relationship between the maximum current and the SoH, with the influence of temperature. Here, the maximum current is obtained at the MPP of the FC, as indicated in Fig. 5.6.

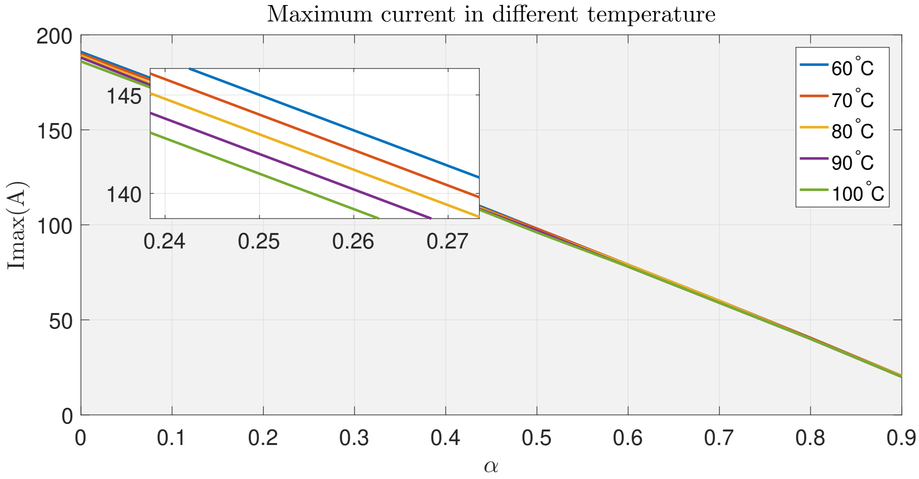

FIGURE 5.11 – Maximum current of the PEMFC under different remperatures and aging (one stack)

Firstly, the influence of the FC temperature is studied. Fig. 5.11 shows the relationship between α and the maximum current of the FC under different temperatures. The range of temperature is from $60°$C to $100°$C, which is the typical operating temperature range of a PEMFC [196]. Based on the simulation results, it can be observed that the influence of the temperature is negligible, since the differences between the curves are small enough for FTC.

Therefore, the maximum current of the FC can be calculated with $i_{fc_{max}}[k] = f(\alpha_{k|k})$, which describes the relationship between the SoH $\alpha_{k|k}$ and the maximum current. In Fig. 5.11, we can see that the curve under $80°$C (in yellow) can be considered as the average of theses curves. Using a fitting technique, the function can be fitted by the curve of the average temperature at $80°$C :

$$i_{fc_{max}}[k] = -186.1\alpha_{k|k} + 189.5 \tag{5.33}$$

According to the sizing information in section 5.2.2, the fitting function with 2 stacks in series and 8 stacks in parallel is shown in (5.34). Fig. 5.12 shows the fitted curve.

$$i_{fc_{max}}[k] = -1452.8\alpha_{k|k} + 1516 \tag{5.34}$$

In this work, the second method is applied because of its implementation simplicity. The aging-tolerant control is realized based on the EKF associated with the MPP algorithm and a dynamic saturation function of the FC reference current, as shown in Fig. 5.1.

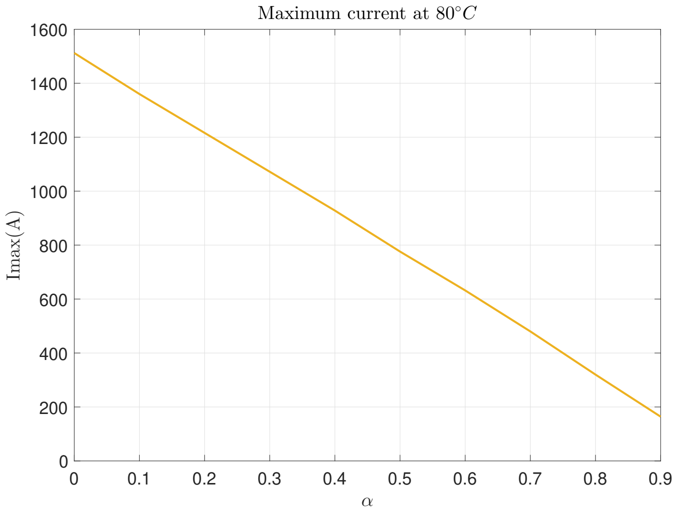

FIGURE 5.12 – Maximum current of the FC at $80°C$

5.5/ SIMULATION WITH A MODIFIED NEDC DRIVING CYCLE

5.5.1/ LOAD SCENARIO

The New European Driving Cycle (NEDC), assumed to represent the typical usage of a car in Europe, is applied in this work (see Fig. 5.13). Since the NEDC original cycle is not capable of meeting every case of limitation to test the correct operation of the proposed controller, a modified NEDC driving cycle is applied with the simulation.

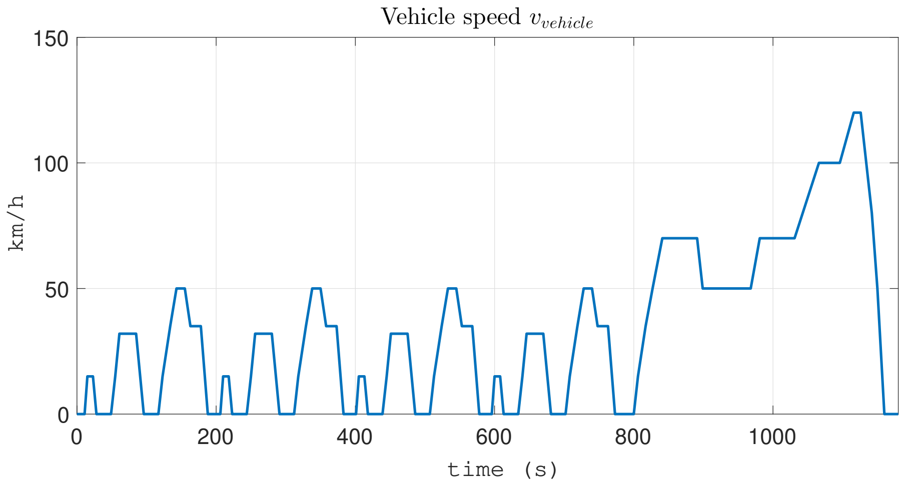

FIGURE 5.13 – NEDC driving cycle

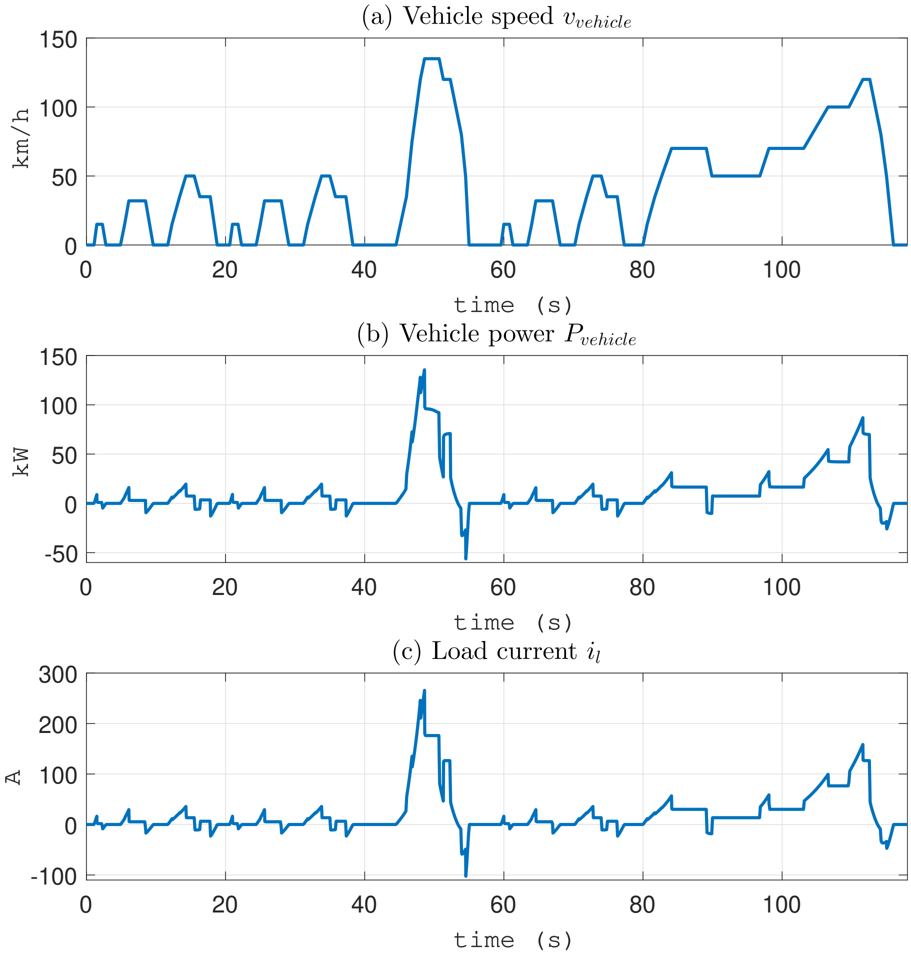

FIGURE 5.14 – Load scenario under modified NEDC driving cycle

Firstly, the duration of the driving cycle is divided by a factor of 10, in order to test the dynamic behavior of the system. As shown in Fig. 5.14 (a), the driving cycle has four repeated cycles during the first 80 s. One of these cycles is modified (between 40 s to 60 s) while the rest of the curve is unchanged. Then, with the vehicle modeled in 5.2.3, the power consumed by the vehicle under the modified NEDC driving cycle is calculated and presented in 5.14 (b). Finally, as in [193], the reference voltage of the DC bus is set to 550 V. The load current is computed by (5.12), and presented in Fig. 5.14 (c).

5.5.2/ SIMULATION WITHOUT AGING

Firstly, a simulation without the aging of FC is proceeded, with the proposed controller in Chapter 4, under the load scenario in section 5.5.1. Tab. 5.3 presents the system and controller parameters. Here, the voltage of the SCs is limited between 118 V and 128 V, and v_{scl} and v_{sch} are fixed at 119 V and 127 V. The SCs current is limited to 500 A for the first 60 seconds and then to 100 A, respectively, for the purpose of the test. Since the aging of FC is not activated, the speed of aging β is set to zero so that the SoH α is kept at 0. The FC current limitation will stay at the initial value during the simulation.

Hybrid system parameters	
DC bus capacity C	9 [mF]
DC bus reference voltage v_b^*	550 [V]
SCs capacity C_{sc}	63 [F]
SCs reference voltage v_{sc}^*	125 [V]
Hybrid system limitations	
SCs voltage limitation	
v_{scL}	118 [V]
v_{scl}	119 [V]
v_{sch}	127 [V]
v_{scH}	128 [V]
SCs current limitation	
i_{scmax}	500 [A]/100 [A]
i_{scmin}	-500 [A]/-100 [A]
FC current limitation	
i_{fcmax} with $\alpha = 0$	1516 [A]
i_{scmin}	0 [A]
Controller parameters	
γ	10
δ	0.5
Current sampling time	50 [μs]
Voltage sampling time	500 [μs]
EKF parameters	
EKF sampling time T_s	0.1 [s]
Variance of measurement noise R	10^{-3}
Covariance of process noises Q	diag(0, 3×10^{-6})
Initial matrix $P[0|0]$	diag(0, 0)

TABLE 5.3 – Control and system parameters with EKF

Fig. 5.15 presents the behavior of each element during the simulation. Figure (a) shows the curve of DC bus voltage, which varies round its reference value 550 V; figure (b) shows the load current cycle, which represents the demanded current of a commercial vehicle under the modified NEDC driving cycle; figures (c) and (d) present the FC voltage and current variations that are managed by the controller; in figure (e) and (f), the SCs voltage and current are presented and vary within their limitations; and figure (g) shows the SCs and FC operation mode while the dissipative load current is presented in figure (h).

The difference in the dynamic response between the FC and SCs can be seen clearly from the current curves in Figs. 5.15 (b) and (f) : the FC supplies the energy in steady state while the SCs respond quickly during load power transients to stabilize the DC bus voltage.

(a) Bus voltage v_b

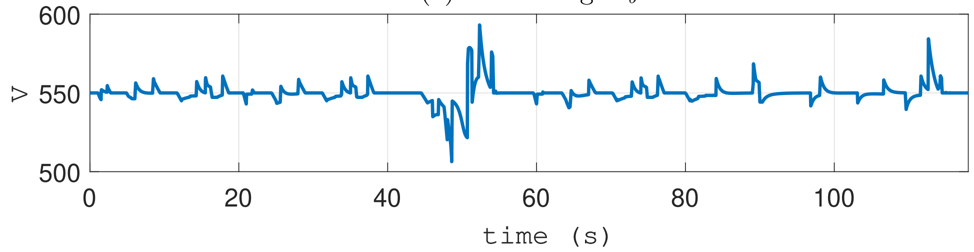

(b) Load current i_l

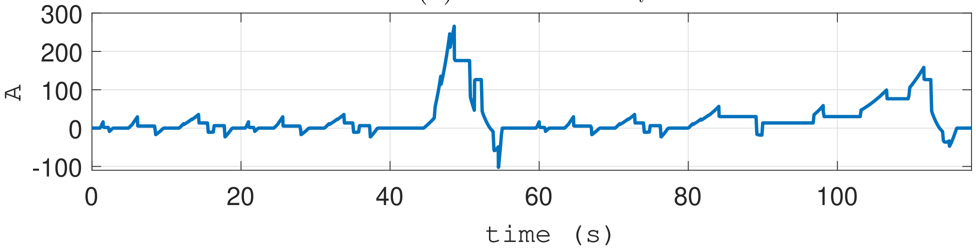

(c) Fuel cell voltage v_{fc}

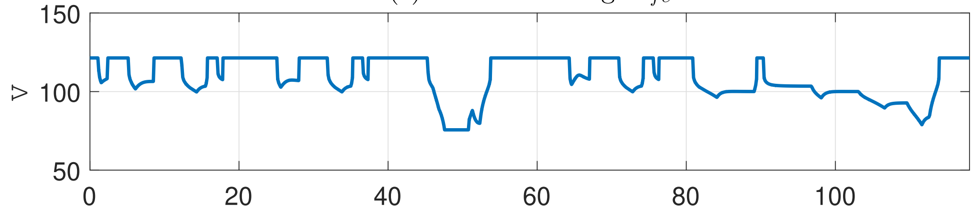

(d) Fuel cell current i_{fc}

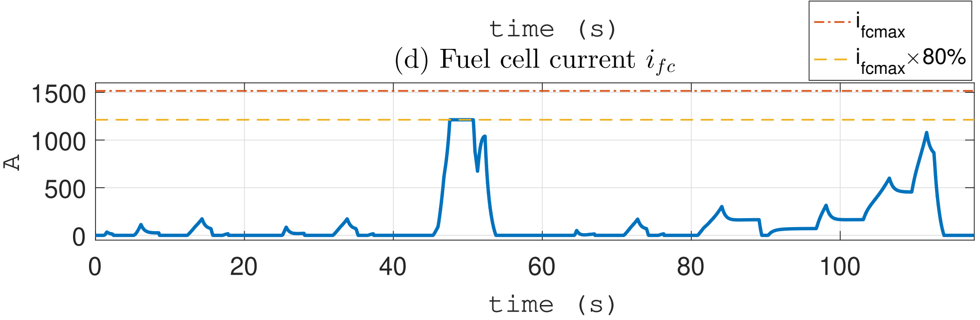

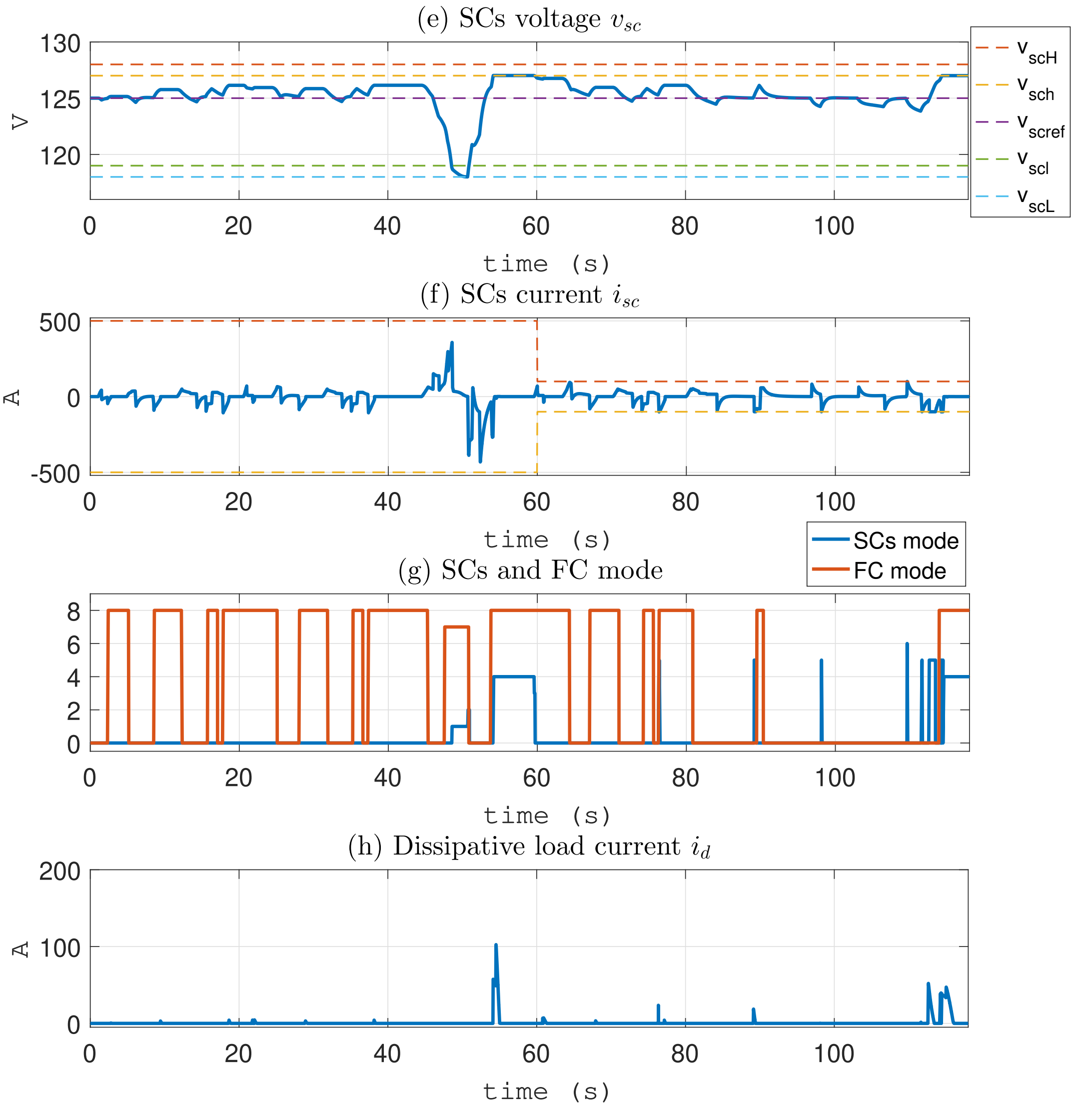

FIGURE 5.15 – Simulation without aging

With the modified NEDC driving cycle, peak demand occurs from 45 s to 50 s, the FC current is limited by the saturation function and the SCs supply the rest of the energy. It shows that when the power demanded by the load is greater than the maximum power of the FC, the FC power should be limited in order to protect the FC from overload and also ensure the whole controller stability.

Then, because of parameter r_2 in the control law, modes 1 and 2 are engaged when the SCs voltage is too low. This results in the drop on the DC bus voltage at around 50 s. After that, the vehicle speed decreases to zero, and it follows that the FC stops generating and SCs are charging from around 50 s to 55 s. Then, the SCs current is limited when the SCs voltage exceeds the limitation (mode 4) at around 55 s. During mode 4, the SCs voltage is limited at v_{sch}, according to (5.24). There is also the limitation of SCs charging current (mode 5) at 75 s, 90 s and 98 s, as well as the limitation of the discharging current (mode 6) at around 110 s.

We can also notice that when the SCs charging current is limited (mode 5), or when the FC current is limited to zero (mode 8), the dissipating resistance load is activated to consume the extra energy and protect the system (see Fig. 5.15 (h)), as presented in Chapter 4. Since the aging of the FC is not activated in this simulation, the FC works as new. Therefore, the estimated α remains at 0. That is the reason why the FC maximum current is a constant value (see Fig. 5.15 (d)).

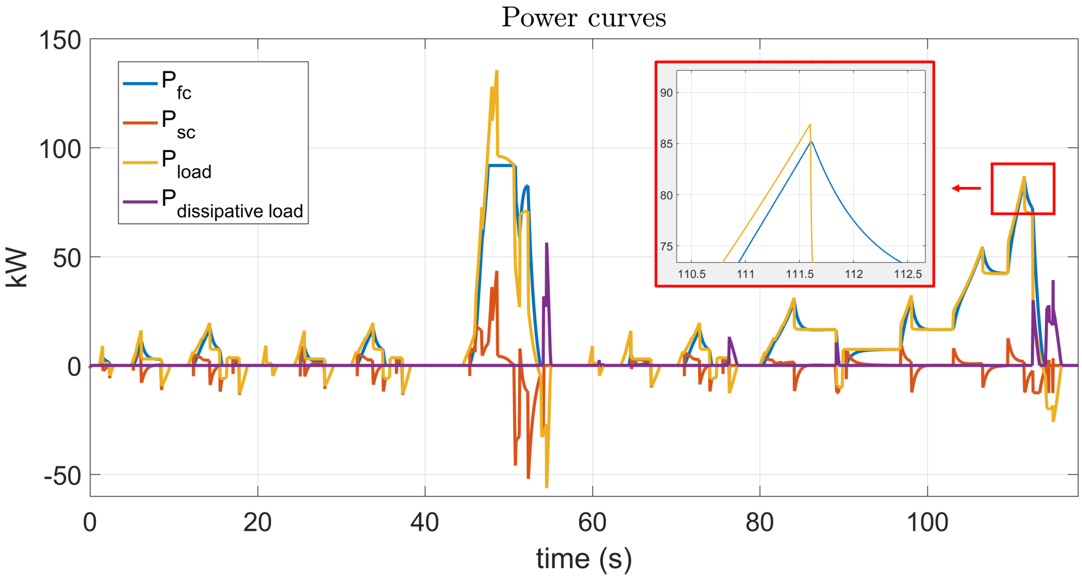

FIGURE 5.16 – Simulation without aging - power curves

Fig. 5.16 shows the power curves with a zoom on the last peak of the load power. Since the FC maximum current is stable at its initial value, the FC current is not limited at this moment. However, in reality, the degradation occurs over time, and the FC cannot deliver such a high power. If this change inside the FC system is not considered, overload may occur and the control could diverge. Therefore, a simulation considering the degradation is proceeded in the next section.

5.5.3/ SIMULATION WITH AGING

As mentioned before, the aging of the FC should not be neglected. A simulation considering the degradation is proceeded, with the same parameters shown in Tab. 5.3. As the dynamics of power management and FC degradation are very different (degradation is typically observed over hundreds of hours), in this scenario, FC aging is artificially accelerated from 60 s to 100 s. The estimation of α by the EKF is shown in Fig. 5.17. During 60 s to 70 s, α is inobservable because the FC current is zero or very small. The saturation of the FC current is updated dynamically using (5.34) based on the estimation of the SoH. In order to protect the FC system, the saturation of the FC current is set to 80 % of the MPP current.

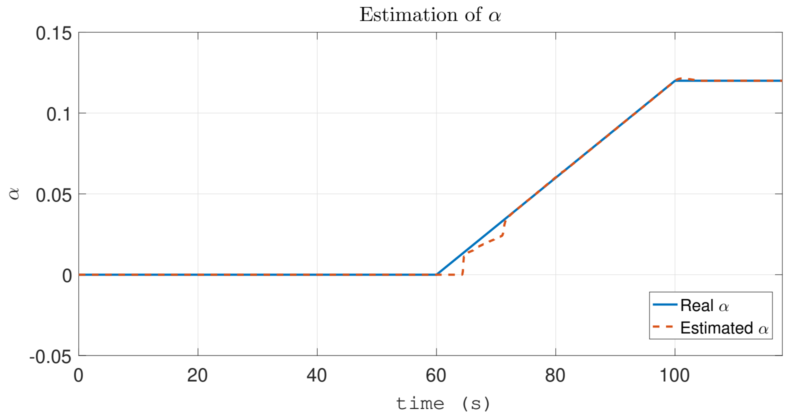

FIGURE 5.17 – Estimation of SoH

(a) Bus voltage v_b

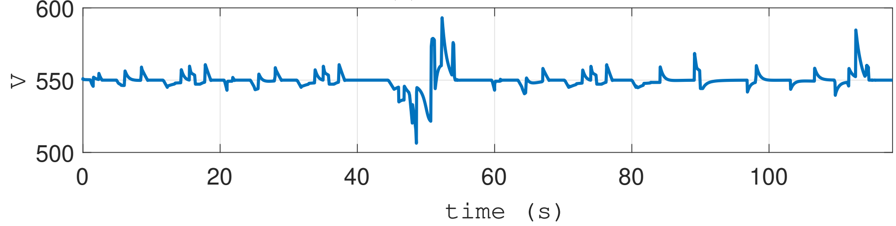

(b) Load current i_l

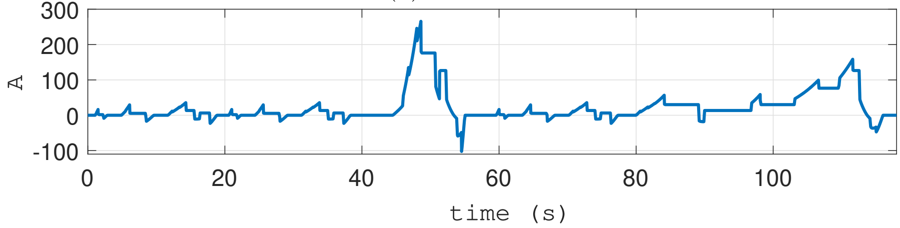

(c) Fuel cell voltage v_{fc}

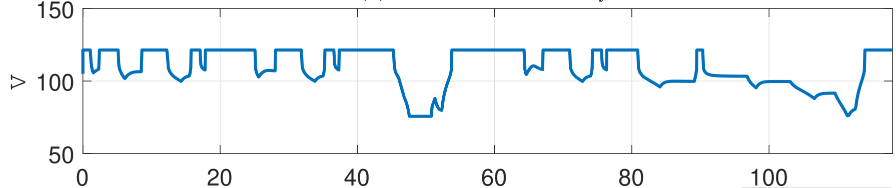

(d) Fuel cell current i_{fc}

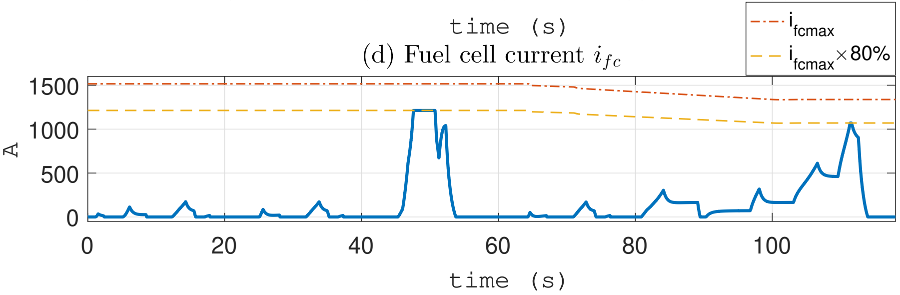

(e) SCs voltage v_{sc}

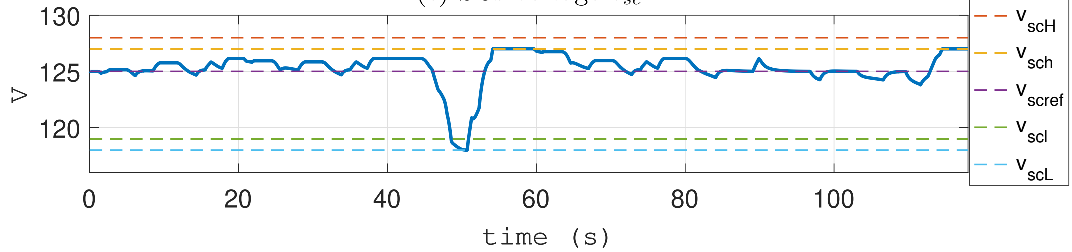

(f) SCs current i_{sc}

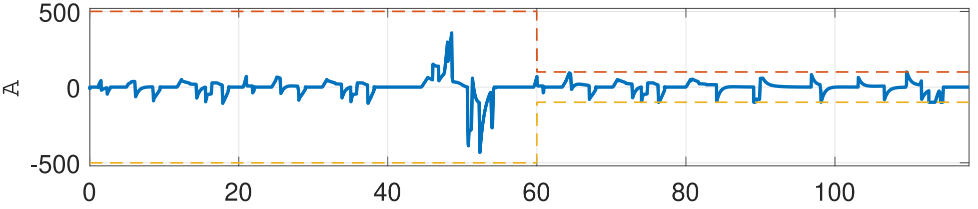

(g) SCs and FC mode

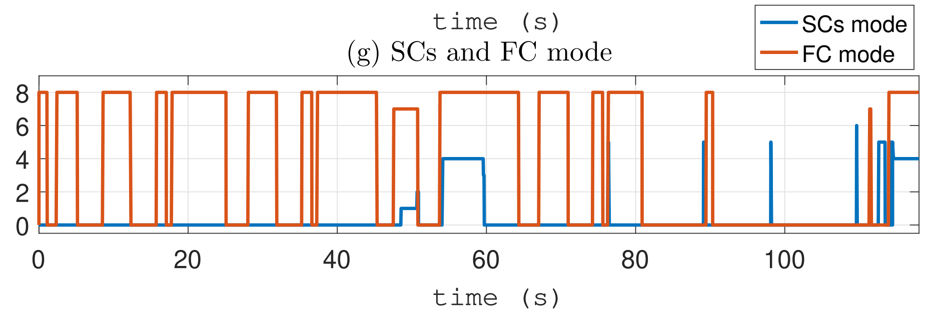

(h) Dissipative load current i_d

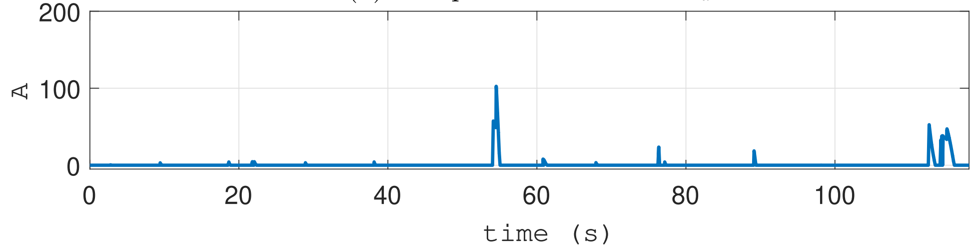

FIGURE 5.18 – Simulation with aging

Fig. 5.18 shows the voltage and current curves of each element. The dynamic saturation of the FC current can be seen in Fig. 5.18 (d). The maximum current of the FC decreases with the degradation. At around 110 s, the FC current is limited by this dynamic saturation (mode 7 in Fig. 5.18 (g)). Then the SCs current is increased automatically in order to provide enough power.

The power curves are presented in Fig. 5.19, from which the FC power is limited at around 110 s, by the dynamic saturation based on the SoH of the FC. Therefore, the maximum power of the FC is adapted in real-time, thanks to the aging-tolerant control. The system is protected from over-current. Also, since the constraints are integrated directly into the controller, the stability is guaranteed by the IDA-PBC controller.

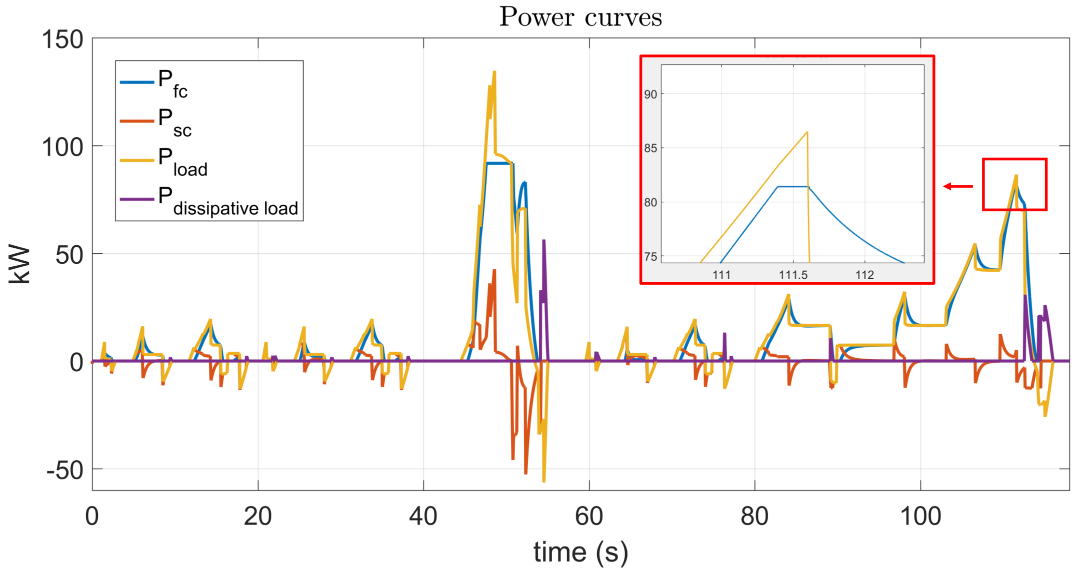

FIGURE 5.19 – Simulation with aging - power curves

5.6/ HARDWARE-IN-THE-LOOP RESULTS

To further validate the real-time operation of the proposed passivity-based control and prognostic algorithm, an implementation and experiment was conducted using the HIL platform introduced in section 3.3 of Chapter 3.

The sampling time of the EKF has been fixed at 1 s for the purpose of the validation of all the algorithms in real-time. In a real context, a sampling time equal to 1 h seems to be a sufficient value in order to capture the evolution of FC degradation [186].

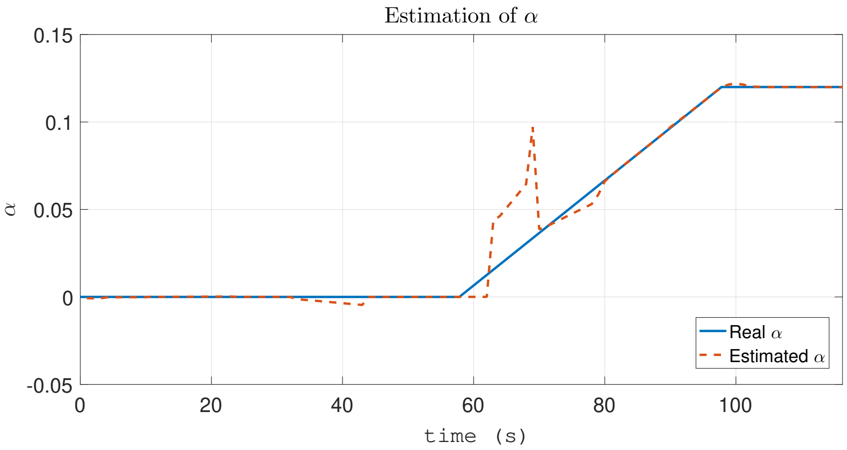

FIGURE 5.20 – HIL results - estimation of SoH

The estimation of the SoH is shown in Fig. 5.20, where the aging speed of the FC has been excessively increased for obvious practical reasons. Fig. 5.21 shows all the main data computed in the emulated system with the same scenario as in Fig. 5.18.

(a) Bus voltage v_b

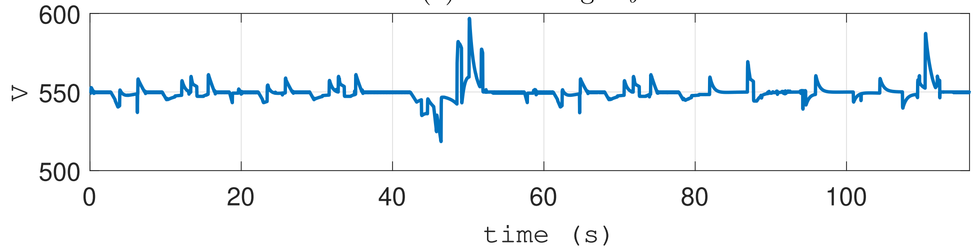

(b) Load current i_l

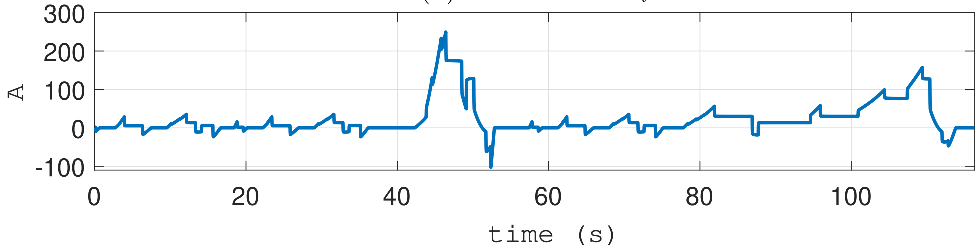

(c) Fuel cell voltage v_{fc}

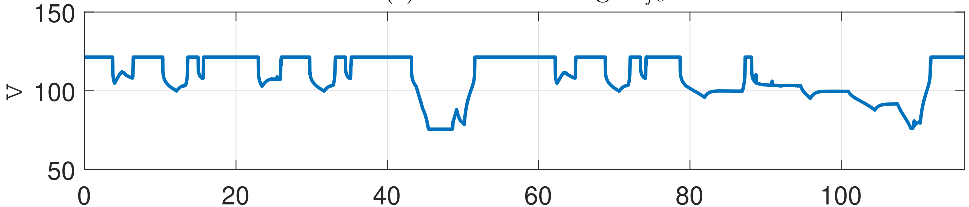

(d) Fuel cell current i_{fc}

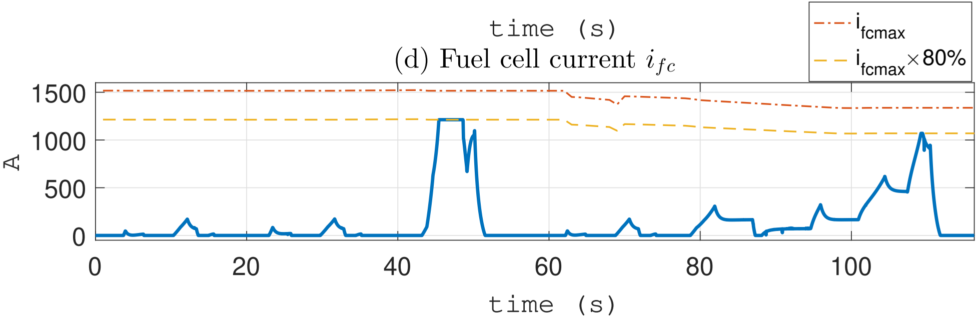

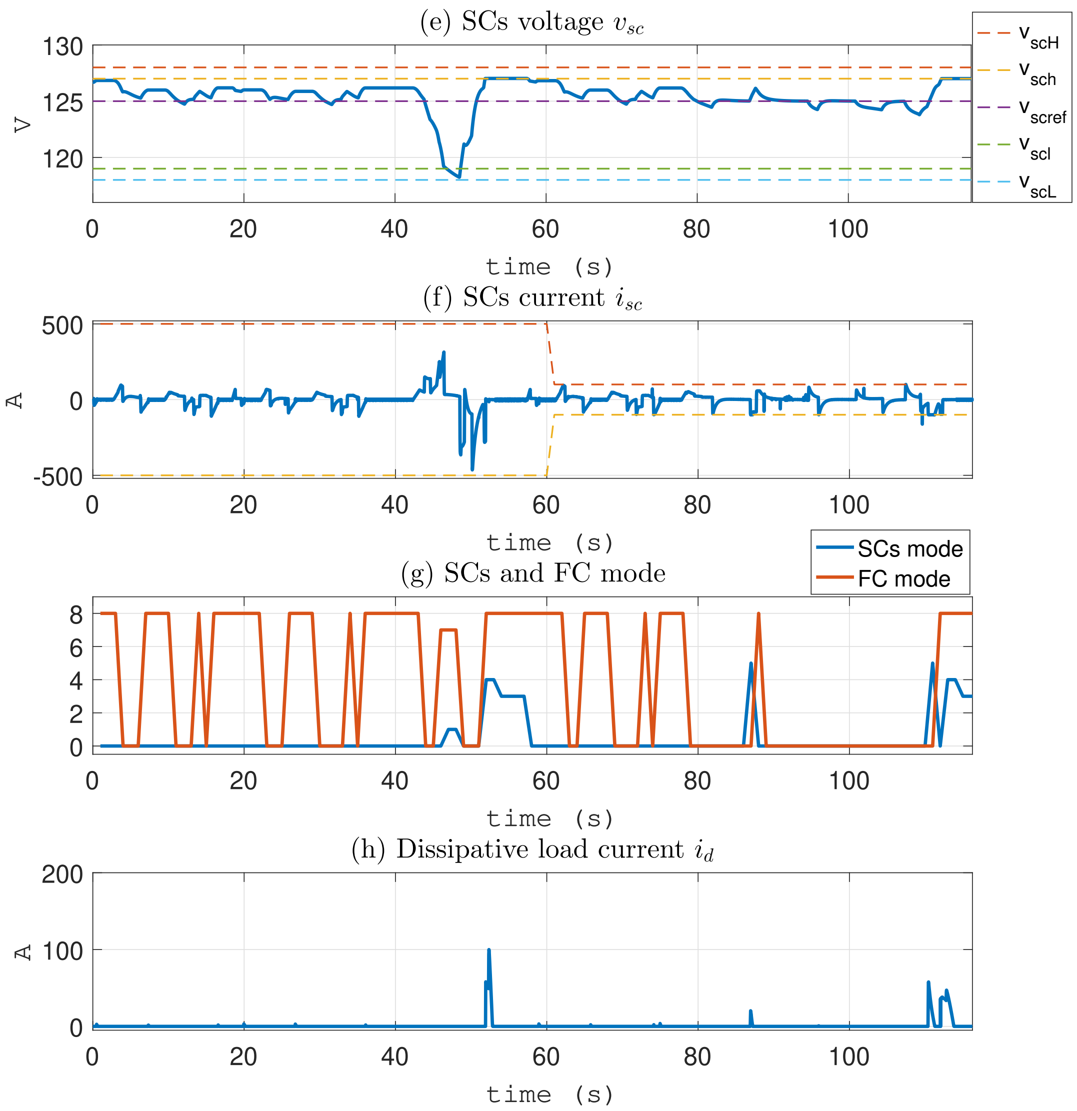

FIGURE 5.21 – HIL results

Firstly, we can notice that the HIL results are similar to the ones of the Matlab / Simulink simulation in section 5.5.3. Compared with the simulation results, some data points are missing because the acquisition step is fixed at 1 s.

Secondly, it should be mentioned that from 60 s to 80 s, the estimated α is different from the real one since the system is inobservable when the FC current is nil or low in practical applications (see Fig. 5.21 (d)). We can also observe in Fig. 5.21 (d) that the FC current is well controlled by the NIOS II microcontroller and does not exceed the maximum current fixed at 80 % of the limit FC current. It means that the speed of degradation, as well as the SoH of the emulated system, are well estimated by the EKF algorithm computed in the NIOS II microcontroller, which guarantees that the maximum FC current follows (5.34).

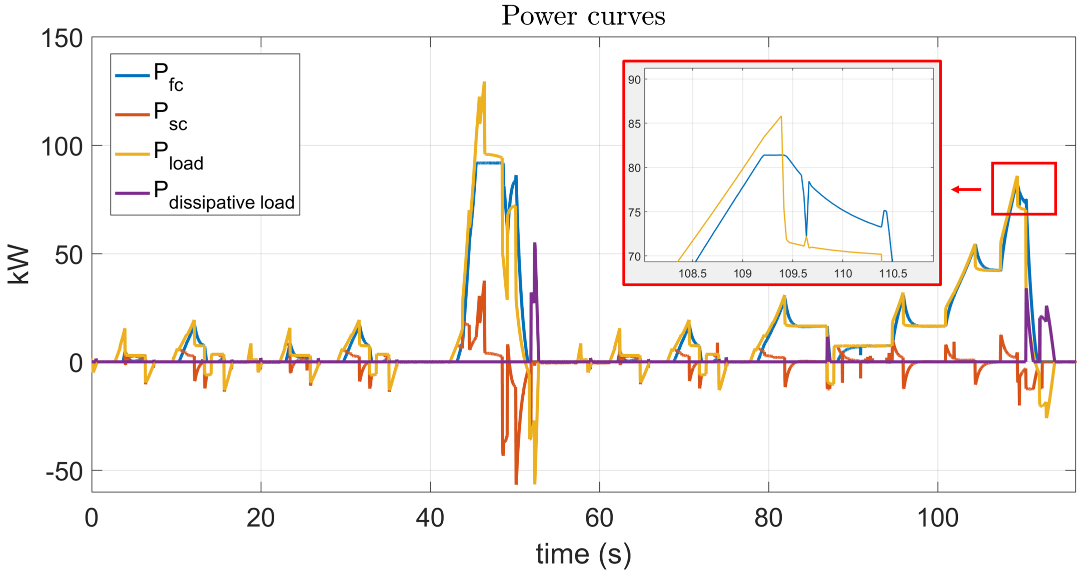

FIGURE 5.22 – HIL results - power curves

The power curves are presented in Fig. 5.22, where the FC power is limited by the controller. Fig. 5.23 shows the duty cycles of the SCs and FC. The PWM signals are generated by the ALTERA FPGA and then decoded in the DS5203 dSPACE board to retrieve the duty cycles.

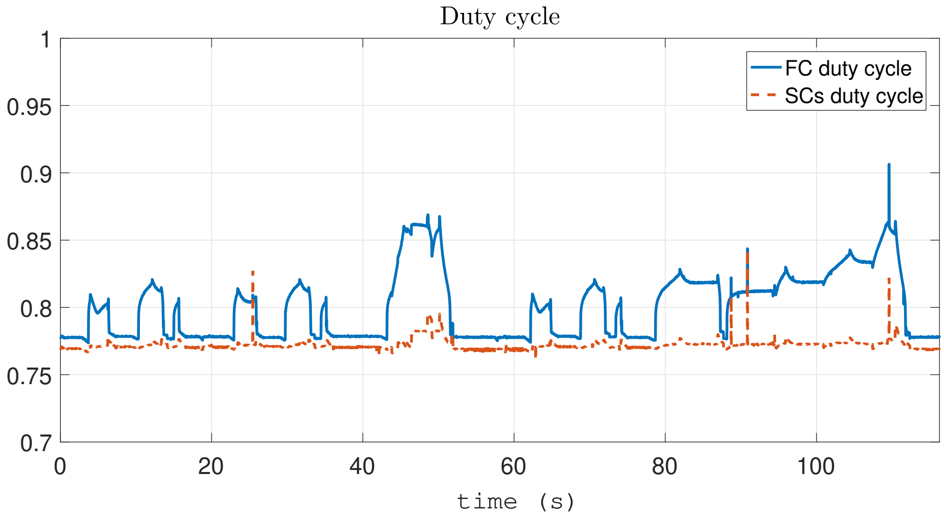

FIGURE 5.23 – HIL results - duty cycles

In a hybrid electric vehicle, the tolerance on the DC bus voltage regulation depends on converters connected to the DC bus. In general, the DC bus voltage regulation should be within 10 % of the reference value. The absolute percentage error that represents the variability on the DC bus voltage as well as the comparison between the simulation and HIL results are shown in Tab. 5.4. The DC bus voltage varies up to 8.5 % with an average value of 0.5 % around the reference voltage, which demonstrates that the stability of the system is guaranteed by the proposed controller. Between the simulation and HIL results, the mean absolute percentage error is 0.16 %, which is small enough and we can say that the experiment results correspond to the simulation result.

Simulation results	
Mean absolute percentage error	0.51 %
Maximum absolute percentage error	7.93 %
HIL results	
Mean absolute percentage error	0.50 %
Maximum absolute percentage error	8.51 %
MAPE between simulation and HIL on DC bus voltage	
0.16 %	

TABLE 5.4 – Comparison on DC bus values

5.7/ CONCLUSION

As shown in Figs. 5.2 and 5.5, the maximum FC current is time dependent and the aging of the FC is not negligible in practical applications. The lifespan of a PEMFC is still rather limited nowadays, with 2500 hours on average under transportation operating conditions, which is inferior to the prerequisites from [195, 189]. As a consequence, PHM of FCs is mandatory. This allows to plan preventive maintenance at the right time, and to reduce costs due to irreversible damages. In other words, PHM allows extending the life of such electrochemical converters using corrective actions, as proposed in this work. Moreover, the RUL of the FC can also be estimated [186]. This approach is therefore mandatory for the development of future FCVs.

Secondly, the decrease of FC maximum power over time directly impacts the power that the SCs need to provide, thereby reducing the closed-loop power management performance. It follows that the design of the components needs to be made for the long-term usage of the system.

Consequently, the power management system needs to be evaluated with a hardware-in-the-loop platform during operating conditions where the FC is aging and used before going to real experimental tests.

In summary, in this chapter, the advanced controller that manages power and energy between a hydrogen FC and SCs, was combined with an aging-tolerant control of the FC using an EKF. The proposed passivity-based control integrates some component constraints directly into the controller equations with two dynamic saturations. Simulation results showed that the controller proposed in this work ensures the integrity and an effective exploitation of the components while preserving the locally asymptotic stability of the whole closed-loop system, and also protecting the system from overloading. Then all the proposed algorithms were implemented in a soft-core NIOS II microcontroller in order to validate their operation in a real-time context before real experimentation tests.

In the next chapter, an application of the IDA-PBC controller on a microgrid-powered datacenter is presented.

6

PASSIVITY-BASED CONTROL FOR A GREEN DATACENTER

6.1/ INTRODUCTION

In this section, the IDA-PBC is applied to a microgrid, as part of the DATAZERO project. The microgrid consists of PV panels, a FC, an electrolyzer and SCs. These elements represent the hybrid power supply system of a green datacenter. Parts of this chapter were adapted from our publication [197].

In this microgrid, the PV panels are the main source, a renewable energy with zero emission. However, the PV production depends on several environmental factors, such as the weather, the temperature as well as the surrounding conditions. Therefore, PV is associated with a fuel cell and an electrolyzer, in order to mitigate the uncertainty of the renewable energy production. Also, SCs are integrated to meet the transient energy needs and to maintain the DC bus voltage around the reference value. The main objective of the controller is therefore to realize cooperation between each element automatically while ensuring the stability of the microgrid.

Unlike a short-term scheduler or dispatcher that gives the solution of Economic Dispatch (ED) to minimize the cost, the controller proposed in this work aims to solve the converters coordination problem and to ensure stability by considering the real-time condition of the system. In a real system, it would be combined with other, longer term algorithms (e.g., a day-ahead scheduler), as a part of the energy management system (EMS) in a microgrid.

The proposed real-time controller is integrated into the PHIL DC microgrid test bench introduced in Chapter 3. The objective of the test bench is to experimentally validate the correct operation of the controller on a small scale, real system.

There are four sections in this chapter : section 6.2 describes the model of the hybrid system ; then the controller design using IDA-PBC is detailed in section 6.3 ; section 6.4 presents the simulation and experiment results ; finally, the conclusions are provided in section 6.5.

6.2/ CONTROL STRUCTURE AND HYBRID SYSTEM MODEL

6.2.1/ POWER ELECTRONIC STRUCTURE

In this research, the hybrid system architecture is shown in Fig. 6.1, where all the electrical elements are connected to the DC bus through static converters. Here, the simplified hybrid system structure as well as the power management control architecture are presented.

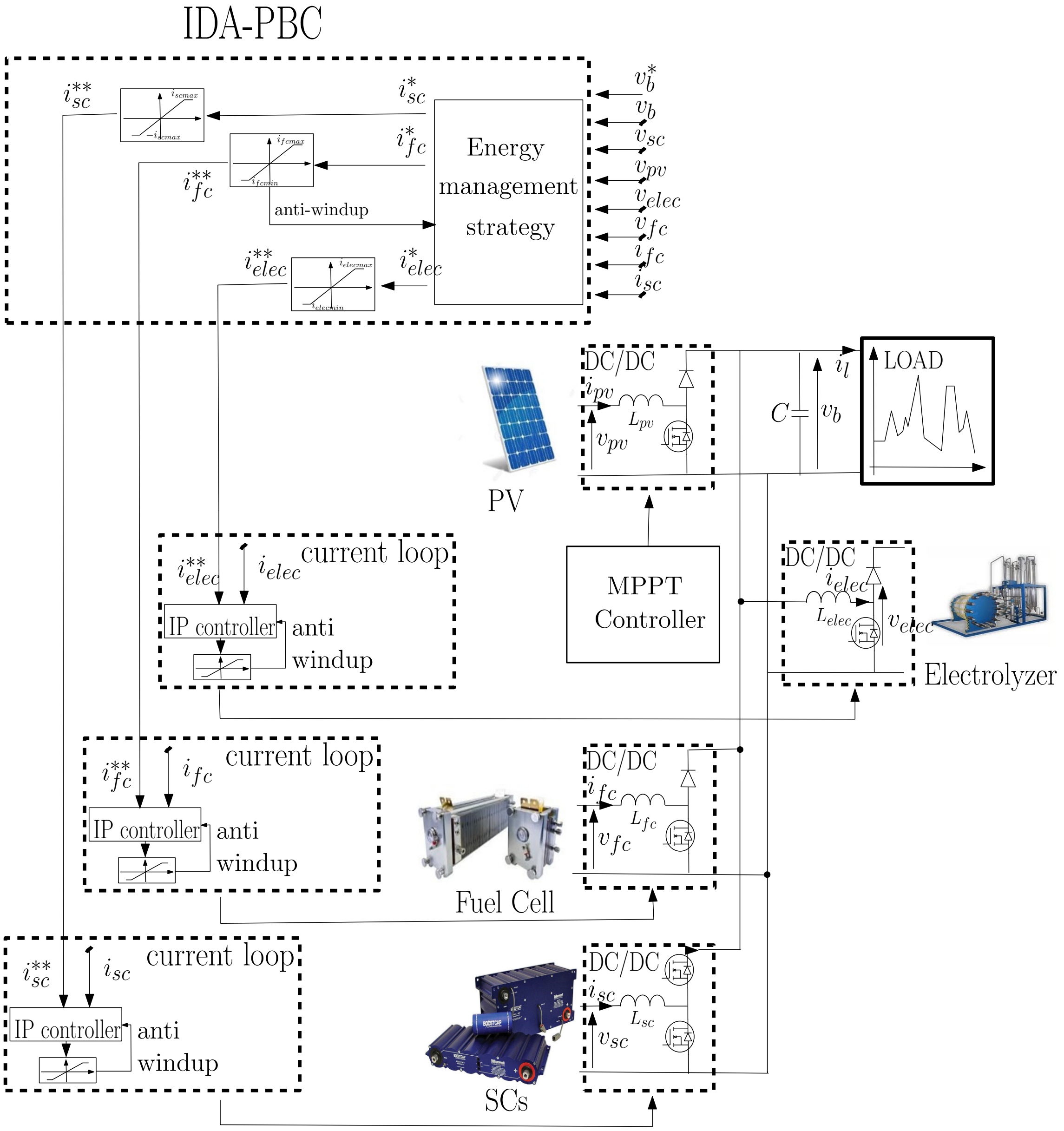

FIGURE 6.1 – System structure and control architecture

The PV panels and the FC are connected to the DC bus via two DC/DC boost converters while the electrolyzer is connected through a DC/DC buck converter. It is assumed that the PV panels are controlled by a maximum power point tracker (MPPT) controller, so that it always works on its maximum power point. A reversible boost converter is implemented for the SCs, which enables the charging and discharging of the SCs according to the load power, the PV power production and the SCs voltage level. The models of the fuel cell, SCs and theirs converters are the same as the ones introduced in sections 4.2.2 and 4.2.3 and are applied in this system.

6.2.2/ PV MODEL

The PV model proposed in [198] and [199] is used, where the I-V relationship of a solar panel is :

$$i_{pv} = E(I_{maxpv} + \Delta I_{pv})\left(1 - exp\left(\frac{v_{pv}}{b(Ef_{loss} + 1 - f_{loss})(V_{maxpv} + \Delta Vpv)} - \frac{1}{b}\right)\right) \tag{6.1}$$

E is the percentage of the solar radiance over the solar panels, which is calculated by the actual light intensity E_i and the nominal light intensity E_{iN}.

$$E = \frac{E_i}{E_{iN}} \tag{6.2}$$

I_{maxpv} is calculated by the short-circuit current I_{sc} and the exponential I-V characteristic constant b, as follows :

$$I_{maxpv} = \frac{I_{sc}}{1 - e^{\frac{1}{b}}} \tag{6.3}$$

$$b = 1 - \frac{V_{bpv}}{(Ef_{loss} + 1 - f_{loss})V_{maxpv}} \tag{6.4}$$

where V_{bpv} is the voltage when the current is $0.6321 I_{sc}$ at the nominal light intensity.

f_{loss} is the shading linear factor, which is the percentage of the voltage loss between the minimum intensity of light and the maximum intensity of light (V_{minpv} and V_{maxpv}) (6.5). V_{maxpv} is the open-circuit voltage of the solar panels array for an effective light intensity of 100 % of the maximum value ($E = 1$) while V_{minpv} represents the open-circuit voltage when the effective light intensity is less than 20 % ($E = 0.2$) over the solar panels.

$$f_{loss} = 1 - \frac{V_{minpv}}{V_{maxpv} + \Delta V_{pv}} \tag{6.5}$$

ΔI_{pv} and ΔV_{pv} represent the influence of the temperature on the current and voltage, and are calculated by the temperature coefficients TC_i and TC_v :

$$\Delta I_{pv} = TC_i(T - T_N) \tag{6.6}$$

$$\Delta V_{pv} = TC_v(T - T_N) \tag{6.7}$$

where T is the actual temperature of the PV panel and T_N is the nominal temperature.

As introduced in Chapter 3, the PV panels integrated on the test bench are the Photowatt PW1650. The modeling parameters are taken from the data sheet of this photovoltaic module, as presented in Tab. 6.1.

PV parameters	
Short-circuit current I_{sc}	5.1 [A]
Nominal light intensity E_{iN}	1000 [W/m^2]
Voltage at $0.6321 I_{sc}$ and E_{iN} V_{bpv}	37.75 [V]
Voltage at nominal radiance V_{maxpv}	43.7 [V]
Voltage at 20% of nominal radiance V_{minpv}	37.7 [V]
Nominal temperature T_N	25 [°C]
Temperature coefficient TC_i	1.46 [mA/°C]
Temperature coefficient TC_v	-158 [mA/°C]

TABLE 6.1 – PV parameters

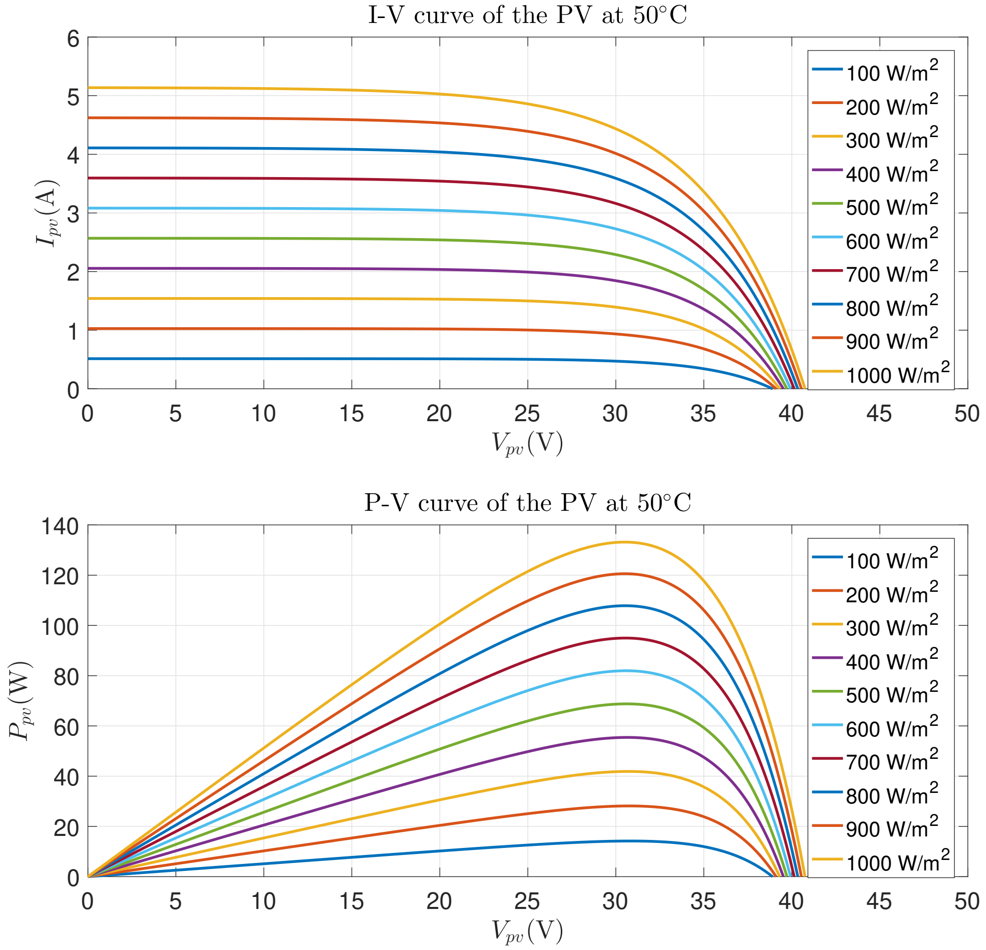

FIGURE 6.2 – Characteristics of the PV

Fig. 6.2 shows the I-V and P-V curves of the PV model at 50°C. For each solar radiance, the PV panels should always work at the MPP. On the PHIL test bench, the $P\&O$ MPPT algorithm is integrated, as introduced in Appendix A.4. In the simulation, the PV model is integrated as three lookup tables where we supposed that the PV system always operats at the MPP under each solar radiance, as shown in Fig. 6.3. For a given solar radiance, the maximum power as well as the voltage and current of this power point can be determined. The data for the lookup tables are produced by the applied PV panel model.

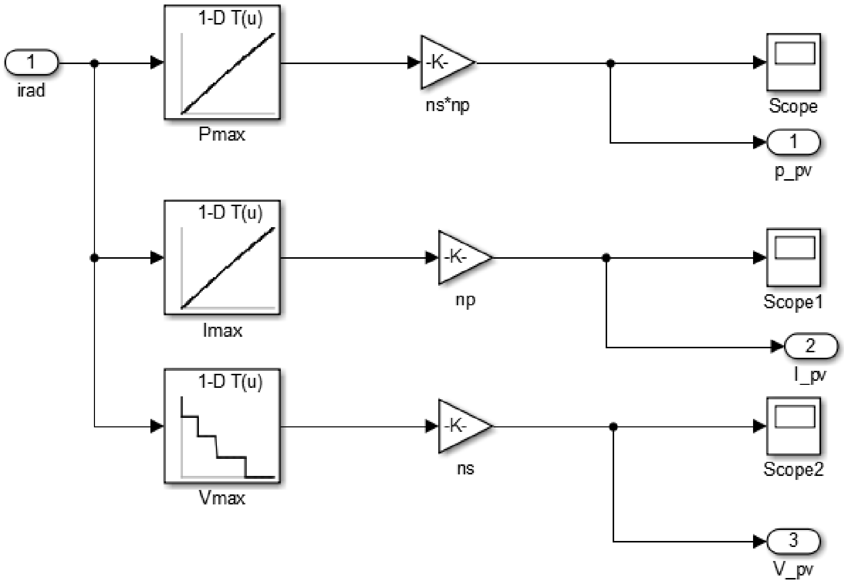

FIGURE 6.3 – Lookup tables for the PV

Finally, the PV panels are connected to the DC bus by a boost converter. The average state space model is :

$$\frac{d}{dt} i_{pv}(t) = \frac{-(1-\alpha_3(t))\, v_b(t) + v_{pv}(t)}{L_{pv}} \tag{6.8}$$

6.2.3/ ELECTROLYZER MODEL

Based on [29], a model of a PEM water electrolyzer is applied, for which the output voltage is calculated as follows :

$$v_{elec}(t) = n_{cell_s}(E^a_{rev} + E^c_{rev} + v_a(t) + v_c(t) + R_{elec}\, j_{el_{den}}(t)) \tag{6.9}$$

where a represents the anode and c represents the cathode, n_{cell_s} is the number of cells in series, E_{rev} is the reversible potential, v_a and v_c are the overpotential of each electrode, R_{elec} is the internal resistance of the cell and $j_{el_{den}}$ is the current density in A/cm^2. The current density is calculated from the electrolyzer current $i_{elec}(t)$ and the cell active surface A, as follows :

$$j_{el_{den}} = \frac{i_{elec}(t)}{A} \tag{6.10}$$

The reversible potential of both electrodes (j = a represents the anodic side and j = c represents the cathodic side) are calculated using the Nernst equation :

$$E^j_{rev} = -\frac{\Delta G_i}{n_j F} \tag{6.11}$$

$$\Delta G_j = \Delta H_j - T_k \Delta S_j \tag{6.12}$$

where ΔG_j is the variation of the total free Gibbs energy, ΔH_j and ΔS_j are the variation of enthalpy and entropy, and T_k is the temperature of the electrolyzer.

The overpotential v_j is calculated from the exchange current density i_{0j} :

$$v_j(t) = \frac{RT_k}{\alpha_j zF} ln\left(\frac{i_{el_{den}}}{i_{0j}\gamma_j}\right) \tag{6.13}$$

$$i_{0j} = zFk_{0j}T_k exp\left(-\frac{A_{0j}}{RT_k}\right) \tag{6.14}$$

R_{elec} is the total ohmic resistance of the cell, which is calculated as the sum of the ohmic losses in the membrane and in the two porous current collections as follows :

$$R_{elec} = \frac{e_m}{k} + \frac{e_a}{\sigma_a} + \frac{e_c}{\sigma_c} \tag{6.15}$$

$$k = k_{303} exp\left(1268\left(\frac{1}{303} - \frac{1}{T_k}\right)\right) \tag{6.16}$$

$$k_{303} = 0.005139\lambda - 0.326 \tag{6.17}$$

In this work, the electrolyzer stack consists of 31 cells in series and the temperature is set to $80°C$. All nomenclature and parameter values are shown in Tab. 6.2. Fig. 6.4 presents the voltage characteristic of the electrolyzer.

Based on the average model of the buck converter, the state space equation of i_{elec} is :

$$\frac{d}{dt} i_{elec}(t) = \frac{\alpha_4(t)\, v_b(t) - v_{elec}(t)}{L_{elec}} \tag{6.18}$$

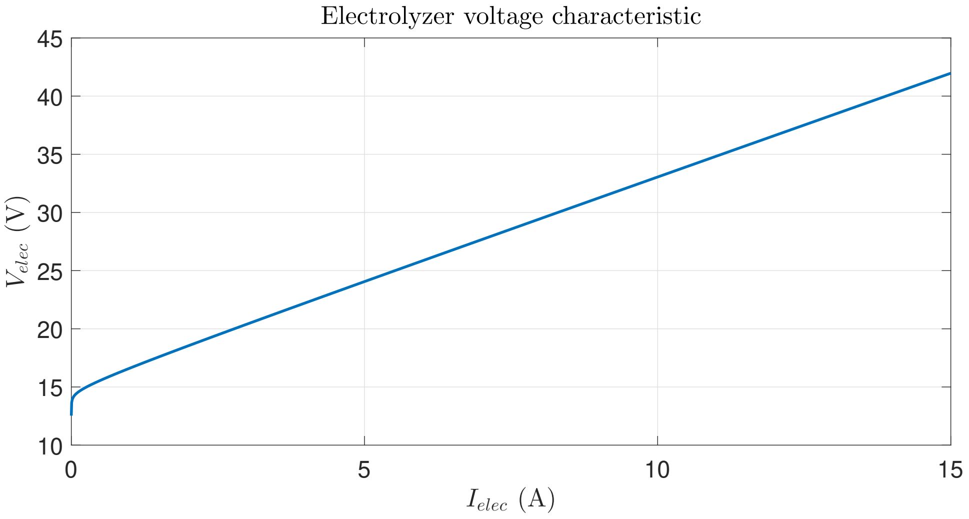

FIGURE 6.4 – V-I curve of the electrolyzer at $80°C$

Variations of enthalpy and entropy	
ΔS_a	326.36 [J/mol/K]
ΔS_c	-0.104 [J/mol/K]
ΔH_a	6229.6 [kJ/mol]
ΔH_c	-2829 [kJ/mol]
Physical constants	
n_a	-4
n_c	2
F	96485 [C/mol]
R	8.314 [J/mol/K]
z	2
Rate parameter	
k_{0a}	4.63×10^{-3} [mol/K/s/m^2]
k_{0c}	10^{-2} [mol/K/s/m^2]
Activation energy	
A_{0a}	62836 [J/mol]
A_{0c}	24359 [J/mol]
Rugosity factor	
γ_a	150
γ_c	150
Geometrical parameters	
e_m	178 [μm]
e_a	1.4 [mm]
e_c	235 [μm]
Electronic conductivity of the current collector	
σ_a	13700 [S/m]
σ_c	46 [S/m]
Number of water molecules per sulfonate site	
λ	16
Number cell in series	
n_{cell_s}	31
Cell active surface	
A	25 [cm^2]
Cell temperature	
T_k	353.15 [K]

TABLE 6.2 – Electrolyzer parameters [29]

6.2.4/ HYBRID SYSTEM MODEL

In this research, the sizing of the models parameters is based on the real equipment characteristics of the PHIL platform introduced in section 3.2 of Chapter 3. The hybrid system consists of two PV panels (330 W), one FC stack (1.2 kW), one electrolyzer stack (2.8 kW), and 8 SCs of 15 F (2 in parallel and 4 in series). On the PHIL test bench, the hydrogen system is emulated by a controllable power supply and an electronic load.

Through the above model, the nonlinear state space model of the complete system is represented by the following 6^{th} order model :

$$\begin{aligned}
\frac{d}{dt}v_b(t) &= \frac{1}{C}\Big[(1-\alpha_1(t))\, i_{fc}(t) + (1-\alpha_2(t))\, i_{sc}(t) + (1-\alpha_3(t))\, i_{pv}(t) \\
&- \alpha_4(t)\, i_{elec}(t) - i_l(t)\Big] && (6.19)\\
\frac{d}{dt}v_{sc}(t) &= -\frac{i_{sc}(t)}{C_{sc}} && (6.20)\\
\frac{d}{dt}i_{fc}(t) &= \frac{-(1-\alpha_1(t))\, v_b(t) + v_{fc}(t)}{L_{fc}} && (6.21)\\
\frac{d}{dt}i_{sc}(t) &= \frac{-(1-\alpha_2(t))\, v_b(t) + v_{sc}(t)}{L_{sc}} && (6.22)\\
\frac{d}{dt}i_{pv}(t) &= \frac{-(1-\alpha_3(t))\, v_b(t) + v_{pv}(t)}{L_{pv}} && (6.23)\\
\frac{d}{dt}i_{elec}(t) &= \frac{\alpha_4(t)\, v_b(t) - v_{elec}(t)}{L_{elec}} && (6.24)
\end{aligned}$$

with the state space vector

$$x(t) = [v_b,\, v_{sc},\, i_{fc},\, i_{sc},\, i_{pv},\, i_{elec}]^T$$

control inputs

$$u(t) = [\alpha_1,\, \alpha_2,\, \alpha_3,\, \alpha_4]^T$$

and measurements $y(t) = x(t)$, $v_{fc}(t)$ and $v_{elec}(t)$.

Here, $\alpha_1(t)$, $\alpha_2(t)$, $\alpha_3(t)$ and $\alpha_4(t)$ represent the duty cycles of the converters. Variables $v_b(t)$, $v_{sc}(t)$, $v_{fc}(t)$, $v_{pv}(t)$ and $v_{elec}(t)$ are the voltages of the DC bus, SCs, FC, PV and electrolyzer. $i_{fc}(t)$, $i_{sc}(t)$, $i_{pv}(t)$, $i_{elec}(t)$ are the current of the FC, SCs, PV and electrolyzer, and $i_l(t)$ is the DC current delivered to the load.

The control is composed of two parts : three fast inner current control loops based on IP controllers that force the current i to track the references i^*, and two slower outer voltage loops based on IDA-PBC. As mentioned in section 4.2.4, because of the difference of time scale between the voltages and the currents, we can assume that all the currents are equal to the references with the hypothesis that L_{fc}, L_{sc}, L_{pv}, and L_{elec} are small compared to the other parameters. The system can be represented by a 2^{nd} order nonlinear state space model as follows, which enables to simplify the design of the outer control loops :

$$\begin{aligned}
\frac{d}{dt}v_b(t) &= \frac{1}{C}\Big[\frac{v_{fc}(t)}{v_b(t)}\, i^*_{fc}(t) + \frac{v_{sc}(t)}{v_b(t)}\, i^*_{sc}(t) + \frac{v_{pv}(t)}{v_b(t)}\, i_{pv}(t) - \frac{v_{elec}(t)}{v_b(t)}\, i^*_{elec}(t) - i_l(t)\Big] && (6.25)\\
\frac{d}{dt}v_{sc}(t) &= -\frac{i^*_{sc}(t)}{C_{sc}} && (6.26)
\end{aligned}$$

with $x_r(t) = [x_1,\, x_2]^T = [v_b,\, v_{sc}]^T$, control inputs $u_r = [i^*_{fc},\, i^*_{sc},\, i^*_{elec}]^T$, measurements $y_r = [v_b,\, v_{sc}]^T$ and $z_r = [i_{fc},\, i_{sc},\, i_{pv},\, i_{elec},\, v_{fc},\, v_{sc},\, v_{elec},\, v_{pv}]^T$.

6.3/ CONTROLLER DESIGN USING IDA-PBC

As earlier, the objective of IDA-PBC is to assign the state point x_r to the desired equilibrium point x_r^*, and in this work, the targets are the DC bus and SCs desired voltages v_b^*

and v_{sc}^*.

$$\begin{aligned} x_r &= [x_1,\, x_2]^T = [v_b,\, v_{sc}]^T && (6.27)\\ x_r^* &= [v_b^*,\, v_{sc}^*] && (6.28)\end{aligned}$$

The energy function H_d, is chosen as follows :

$$H_d = \frac{1}{2}\,\tilde{x}_r^T\, Q\, \tilde{x}_r \tag{6.29}$$

which is a Lyapunov function, with $\tilde{x}_r = x_r - x_r^*$ and $Q = \mathrm{diag(C, C_{sc})}$.

Then the PCH system can be expressed with the error and the gradient of the desired closed-loop energy function as follows :

$$\dot{\tilde{x}}_r = [\mathcal{J} - \mathcal{R}]\nabla H_d + A(u_r, x_r, x_r^*, z_r) \tag{6.30}$$

where :

$$\mathcal{J} - \mathcal{R} = \begin{bmatrix} 0 & 0 \\ 0 & 0 \end{bmatrix}, \quad \nabla H_d = \begin{bmatrix} C\,\tilde{v}_b \\ C_{sc}\,\tilde{v}_{sc} \end{bmatrix}$$

$$A = \begin{bmatrix} \frac{1}{C}[\frac{v_{fc}(t)}{v_b(t)}\, i_{fc}^*(t) + \frac{v_{sc}(t)}{v_b(t)}\, i_{sc}^*(t) + \frac{v_{pv}(t)}{v_b(t)}\, i_{pv}(t) - \frac{v_{elec}(t)}{v_b(t)}\, i_{elec}^*(t) - i_l(t)] \\ -\frac{i_{sc}^*(t)}{C_{sc}} \end{bmatrix}$$

As mentioned in section 4.3, $\mathcal{J}_d(x)$ and $\mathcal{R}_d(x)$ can be represented as follows :

$$\mathcal{J}_d = \begin{bmatrix} 0 & J_{12} \\ -J_{12} & 0 \end{bmatrix}, \quad \mathcal{R}_d = \begin{bmatrix} r_1 & 0 \\ 0 & r_2 \end{bmatrix}$$

With the same procedure as in section 4.3, a matching equation is established between the PHC form and the IDA-PBC form, in order to solve the algebraic equation. In addition, the load current is estimated by an admittance estimator [101], where the load current i_l has been replaced by yv_b^*, i.e., the estimator multiplied by the desired voltage of the DC bus. The nonlinear control law is then determined as follows :

$$\begin{aligned} \delta\dot{y}(t) &= -y(t) + i_l(t)/v_b(t); \quad \delta > 0 && (6.31)\\ \frac{v_{fc}(t)}{v_b(t)} i_{fc}^*(t) - \frac{v_{elec}(t)}{v_b(t)}\, i_{elec}^*(t) &= y(t)v_b^* - \frac{v_{pv}(t)}{v_b(t)}\, i_{pv}(t) + C_{sc}\left(CJ_{12} - \frac{v_{sc}(t)}{v_b(t)} C_{sc} r_2\right) \tilde{v}_{sc}(t) \\ &- C\left(\frac{v_{sc(t)}}{v_b(t)} C_{sc} J_{12} + r_1 C\right) \tilde{v}_b(t) && (6.32)\\ i_{sc}^*(t) &= C_{sc}\,(CJ_{12}\,\tilde{v}_b(t) + r_2 C_{sc}\,\tilde{v}_{sc}(t)) && (6.33)\end{aligned}$$

In this work, the general non-linear controller is refined according to the following constraints :

— Firstly, in the case of normal operation, the SCs voltage is within the range of $[v_{scl}, v_{sch}]$, i.e., the SoC is within [30 %,90 %]. There is no limitation of the SCs currents, so that the inner state of the SCs can be ignored in (6.33). Therefore, the SCs reference current is not influenced by the voltage level, and r_2 is set to zero.

$$r_2 = 0 \tag{6.34}$$

— Secondly, in order to increase the lifetime of the hydrogen system, the DC bus voltage is managed only by the SCs while the FC and electrolyzer have to manage the SoC of the SCs, without a direct action of the DC bus voltage. The term with the interconnection of the DC bus voltage error $\tilde{v}_b(t)$ in (6.32) is set to zero, so we have :

$$\frac{v_{sc}}{v_b}C_{sc} + r_1 C = 0 \tag{6.35}$$

With the same idea as in section 4.4, a control parameter is implemented by setting $-C_{sc}CJ_{12} = \gamma$, with $\gamma > 0$, which leads to $r_1 = \frac{v_{sc}\gamma}{v_b C^2}$.

Based on the above analysis, the control law is now as follows using (6.34) and (6.35) :

$$\delta\dot{y}(t) = -y(t) + i_l(t)/v_b(t), \quad \delta > 0 \tag{6.36}$$

$$\frac{v_{fc}(t)}{v_b(t)}i^*_{fc}(t) - \frac{v_{elec}(t)}{v_b(t)}i^*_{elec}(t) = y(t)v^*_b - \frac{v_{pv}(t)}{v_b(t)}i_{pv}(t) - \gamma\,\tilde{v}_{sc}, \qquad \gamma > 0 \tag{6.37}$$

$$i^*_{sc}(t) = -\gamma\,\tilde{v}_b(t) \tag{6.38}$$

The FC and electrolyzer reference currents are presented in the same equation (6.37) because they are not supposed to be activated at the same time. According to the production of PV and consumption of the load, the FC or electrolyzer will be activated :

CASE WHERE $P_l > P_{pv}$

If the load power is greater than the power produced by the PV panels, the FC needs to produce the power that the PV cannot afford ; it follows that the electrolyzer is not engaged and the controller (6.37) is :

$$i^*_{elec}(t) = 0 \tag{6.39}$$

$$i^*_{fc}(t) = \frac{v_b(t)}{v_{fc}(t)}\left(y(t)v^*_b - \frac{v_{pv}(t)}{v_b(t)}i_{pv}(t) - \gamma\,\tilde{v}_{sc}(t)\right) \tag{6.40}$$

CASE WHERE $P_l < P_{pv}$

If the load power is lower than the power produced by the PV panels, it follows that the FC is stopped while the electrolyzer is engaged to produce hydrogen using the extra power. The controller (6.37) is :

$$i^*_{fc}(t) = 0 \tag{6.41}$$

$$i^*_{elec}(t) = -\frac{v_b(t)}{v_{elec}(t)}\left(y(t)v^*_b - \frac{v_{pv}(t)}{v_b(t)}i_{pv}(t) - \gamma\,\tilde{v}_{sc}(t)\right) \tag{6.42}$$

6.4/ SIMULATION AND POWER HARDWARE-IN-THE-LOOP VALIDATION

The system was first modeled using Matlab / Simulink, and then the controller was integrated into the PHIL test bench. The connection of the components is shown in Fig. 6.5. The PV panels and SCs are connected to the DC bus through their converters while the power supply and the electronic load are connected directly to the DC bus. As shown in the figure, the electronic load is used for emulating the electrolyzer with its converter and the load, and the power supply is used for emulating the fuel cell with its converter. The parameters of the test bench can be found in Tab. 3.1 of Chapter 3. Tab. 6.3 shows the system parameters and controller configurations. The controller parameters are chosen based on the sensitivity of the equipment on the PHIL test bench.

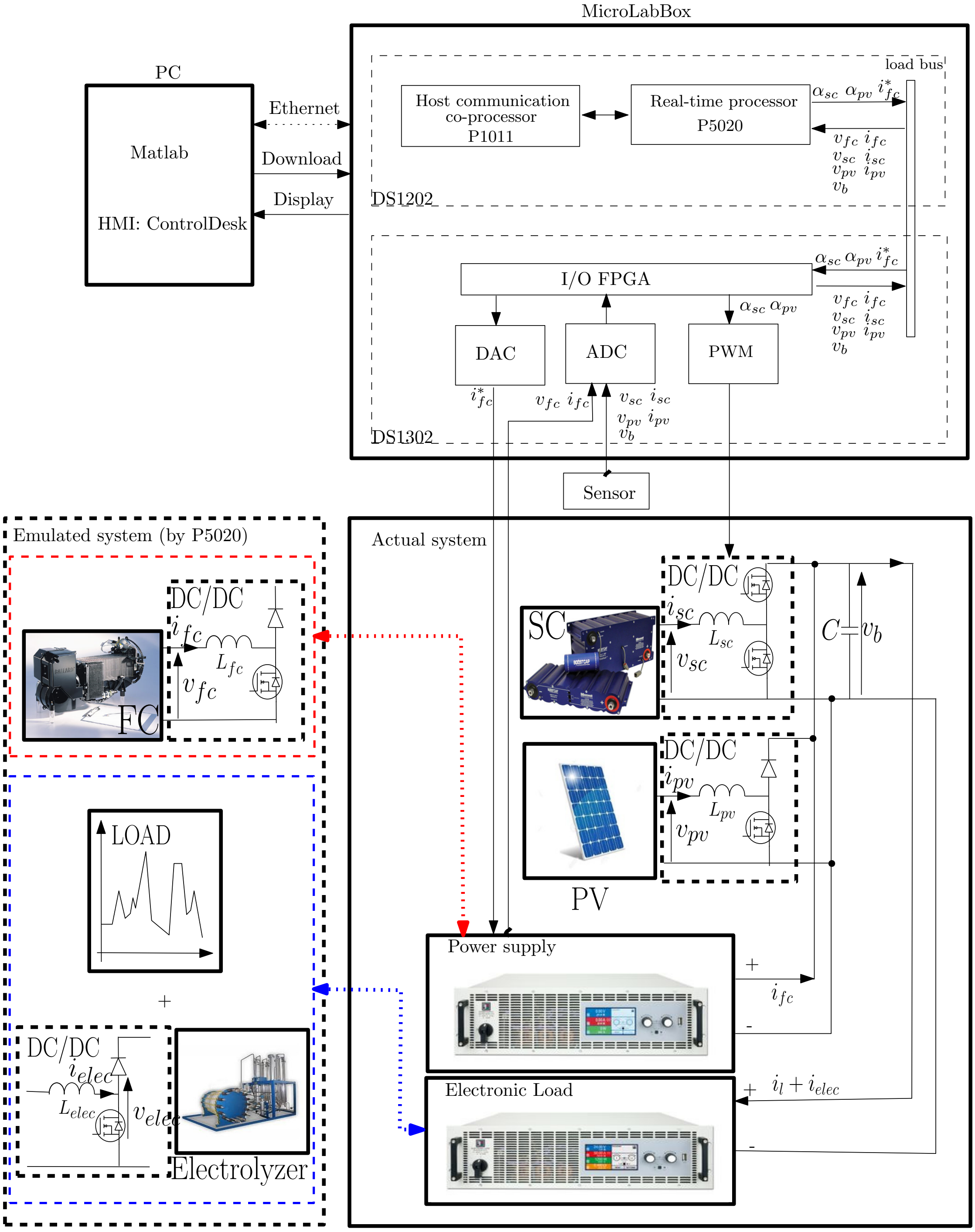

FIGURE 6.5 – Power Hardware-in-the-loop test bench structure

Hybrid system parameters	
DC bus reference voltage v_b^*	70 [V]
SCs reference voltage v_{sc}^*	45 [V]
DC bus capacity C	19.8 [mF]
SCs capacity C_{sc}	29 [F]
Controller parameters	
γ	2
δ	0.5
Current sampling time	50 [μs]
Voltage sampling time	500 [μs]

TABLE 6.3 – Controller configuration and system parameters

In the simulation, the PV output power always tracks its maximum power point, with the variation of the input solar radiance based on real data (see Fig. 6.6). A specific load cycle is applied, in order to test the operation of the controller. Then a test on the PHIL test bench is run with the same scenario. Figs. 6.7 and 6.8 show the simulation as well as the PHIL test results, where the power curves and the details of the voltage and current of each element are presented.

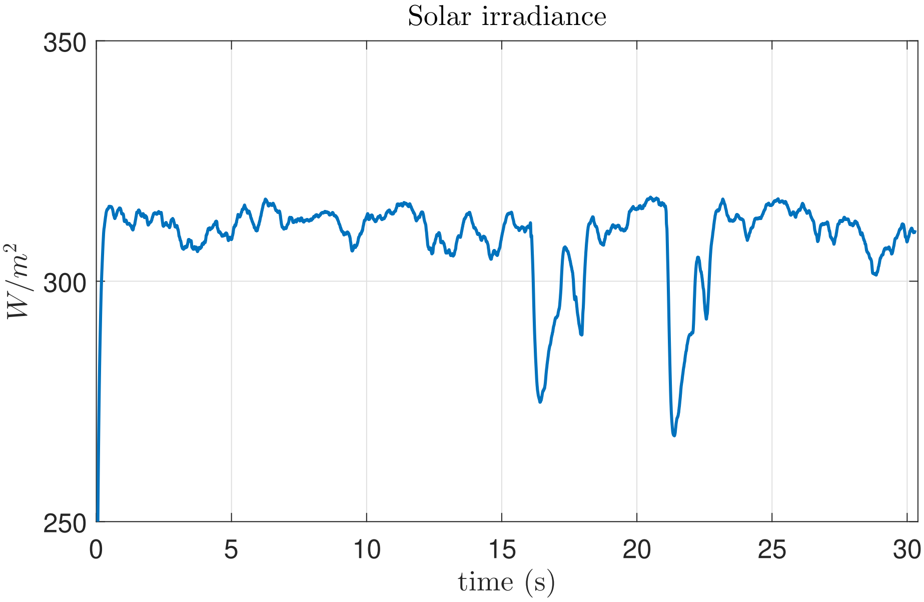

FIGURE 6.6 – Measured solar irradiance

We can notice that the hydrogen system has a smooth response while the SCs respond quickly to transient changes. On the one hand, in steady state, the FC supplies the energy that the PV cannot, while the SCs supply for transients power to stabilize the DC bus voltage (Fig. 6.7. (a)). This is obtained thanks to the interconnections between each element considered in the control law, i.e., term $\gamma \tilde{v}_b(t)$ in (6.38). This allocation between the FC and SCs helps increase the FC lifetime. On the other hand, the surplus power from PV is absorbed by the electrolyzer to produce hydrogen when the FC is stopped or when the SCs cannot absorb power due to their high voltage level, according to (6.42).

(a) Bus voltage v_b

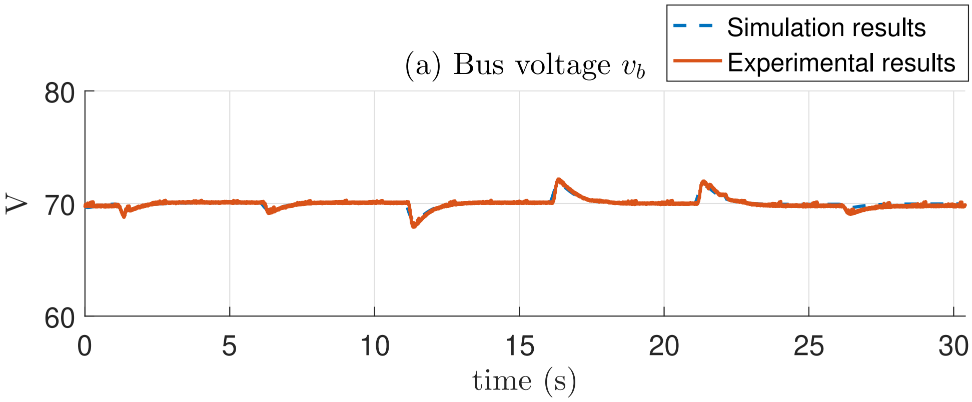

(b) Load current i_l

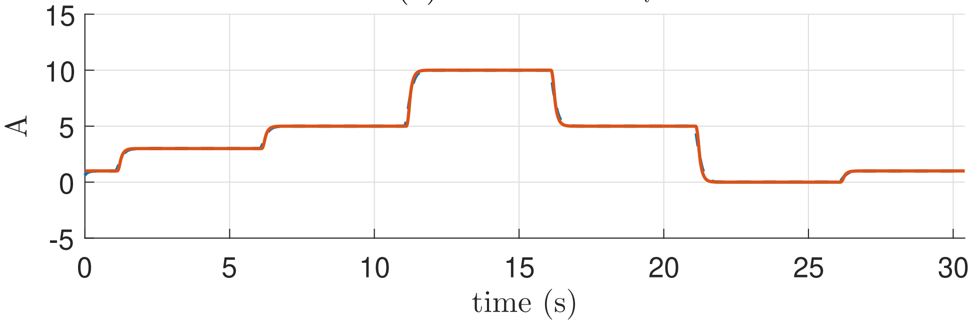

(c) PV voltage v_{pv}

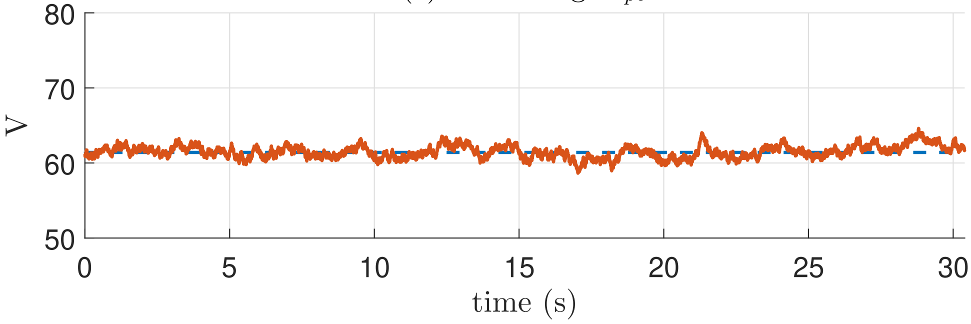

(d) PV current i_{pv}

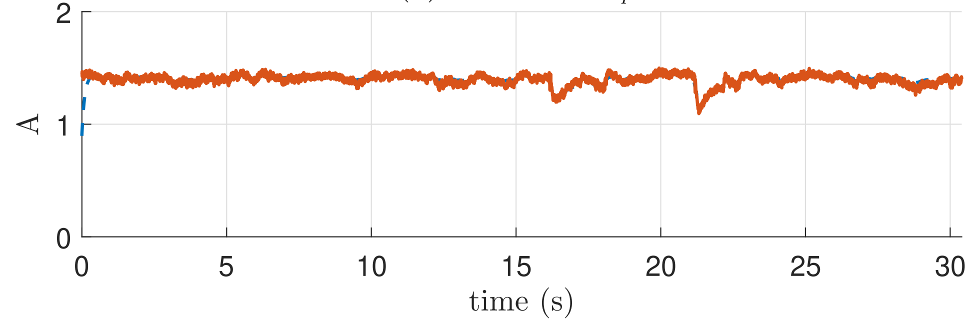

(e) Fuel cell voltage v_{fc}

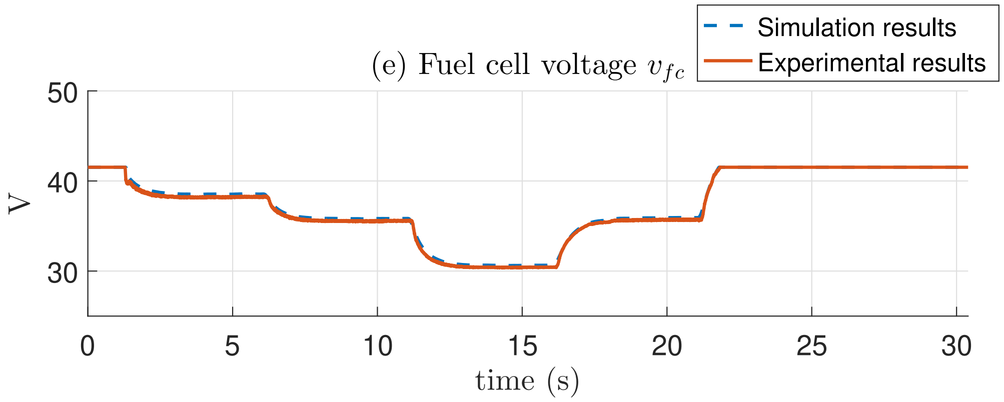

(f) Fuel cell current i_{fc}

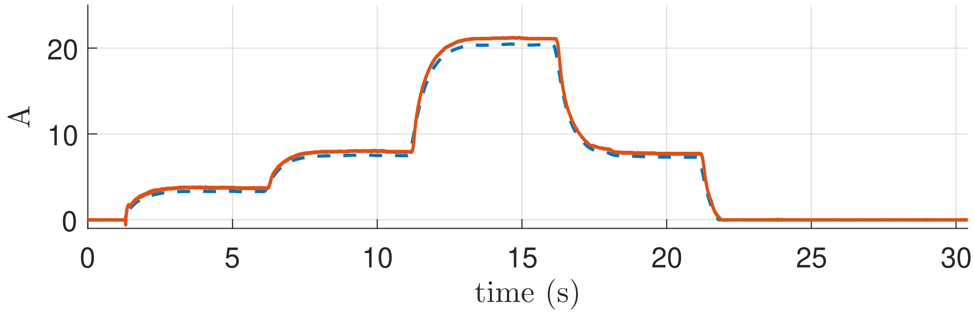

(g) Electrolyzer voltage v_{elec}

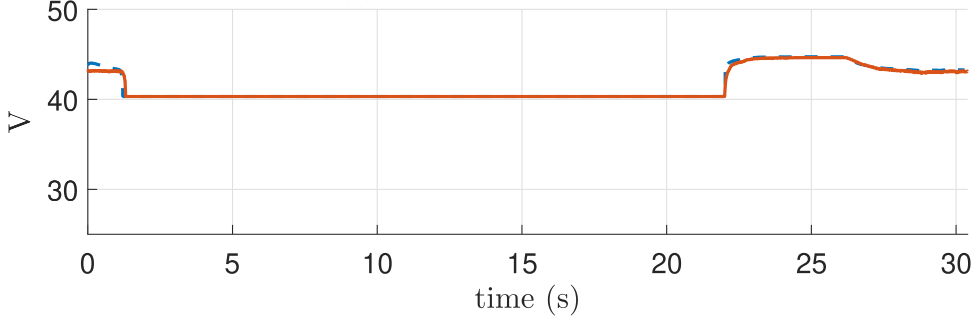

(h) Electrolyzer current i_{elec}

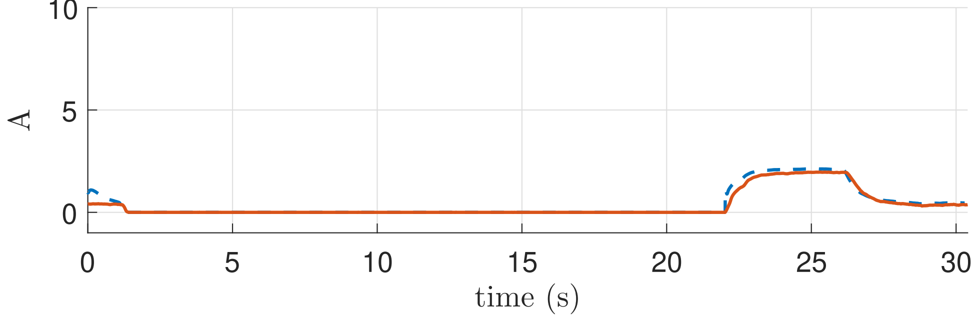

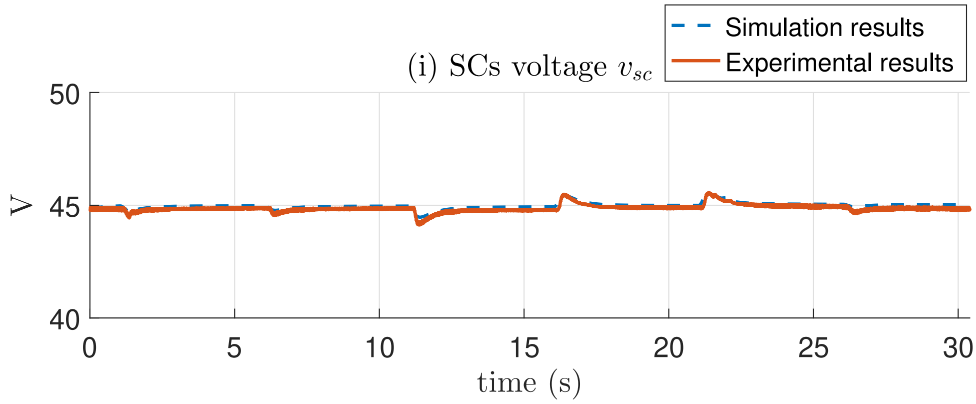
(i) SCs voltage v_{sc}

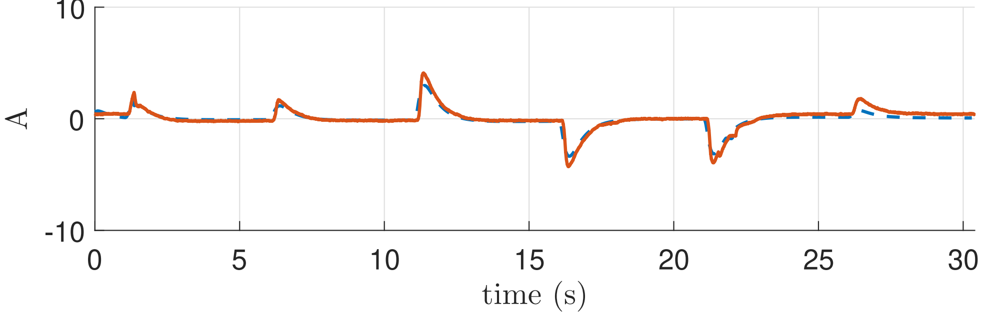
(j) SCs Current i_{sc}

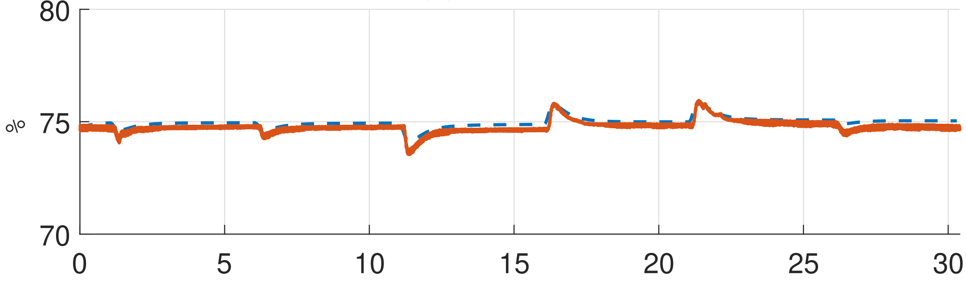
(k) SoC of SCs

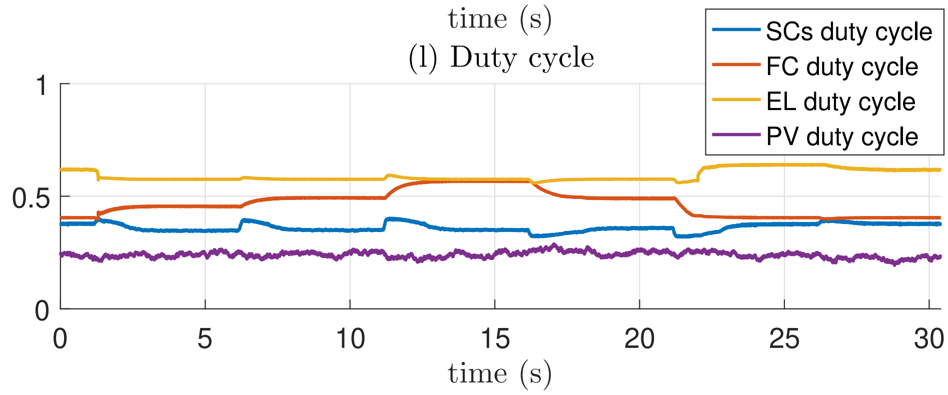
(l) Duty cycle

FIGURE 6.7 – Comparison of simulation and experiment results

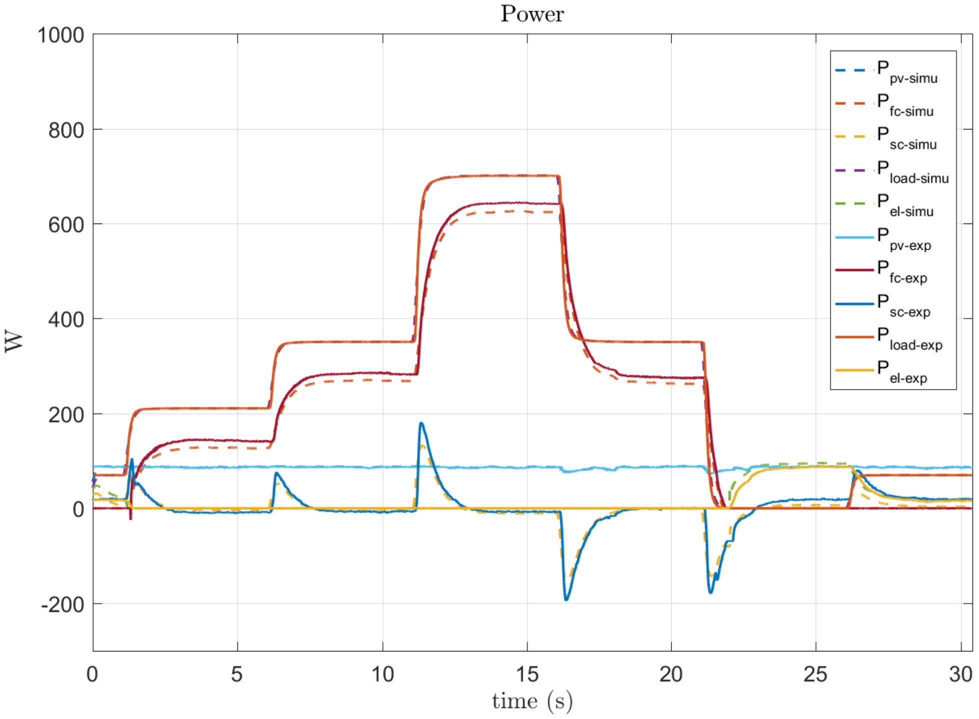

FIGURE 6.8 – Comparison of simulation and experiment results - power curves

At the beginning, the SCs voltage is at the reference level (i.e., at 45 V), and the power demand from the load begins at 0 while the PV system is generating energy. Therefore, the FC is not activated and the electrolyzer is activated until the load current increases above the PV production.

From 21 s to 26 s, the load current is zero, it follows that there is extra energy produced by the PV. Then the FC is stopped, while the SCs start charging and the electrolyzer produces hydrogen (see Fig. 6.7. (g)). Without this strategy, the DC bus voltage would increase significantly and the system would not operate correctly.

In the experimental work, the $P\&O$ method that achieves MPPT for the PV is applied. The aim of the algorithm is to maximize the power output of the PV array by modifying the duty cycle of the boost converter. Since the solar irradiance data in real-time is integrated to the simulation, the PV has the same behavior in the simulation and the experiment (see Figs. 6.7 (c) and (d)). The duty cycle determined by the current loops based on the MPPT algorithm are shown in Fig. 6.7 (l), and are not considered in the simulation since the current loops are ignored for the controller design.

The absolute percentage error that represents the variability on the DC bus voltage as well as the comparison between the simulation and PHIL results are shown in Tab. 6.4. For the PHIL results, the DC bus voltage varies up to 3.12 % with an average value of 0.39 % around the reference voltage. In general, the tolerance of the DC bus regulation in a microgrid is from 5 % to 10 % of the reference value. It is demonstrated that the stability of the microgrid is guaranteed by the proposed controller. The mean absolute percentage error between the simulation and PHIL result is 0.15 %, that has proven that the experiment results are similar to the ones obtained with the Matlab / Simulink simulation.

Simulation results	
Mean absolute percentage error	0.29 %
Maximum absolute percentage error	2.4 %
PHIL results	
Mean absolute percentage error	0.39 %
Maximum absolute percentage error	3.12 %
MAPE between simulation and PHIL on DC bus voltage	
0.15 %	

TABLE 6.4 – Comparison on DC bus values

In conclusion, the DC bus voltage and the SCs voltage are kept around the reference value, which proves that the controller realizes the stability of the whole closed-loop system as well as the different response time of each element. Finally, the experimental results have proven the feasibility of the controller.

6.5/ CONCLUSION

In this chapter, a passivity-based controller was designed for a microgrid with PV, hydrogen fuel cell, SCs and electrolyzer. The stability of the closed-loop system was proven theoretically while enabling a smooth response from the FC and a dynamic response from the SCs, with fast load demand changes, which is the main advantage of the IDA-PBC methodology. Another advantage of this controller is that it makes the configuration simple with only two parameters to set (γ and δ).

Finally, the simulation and experimental results show that the proposed controller preserves the locally asymptotic stability of the whole closed-loop system, while achieving the integrity and an optimal exploitation of the components automatically.

IV

CONCLUSION

7

GENERAL CONCLUSION

7.1/ OVERVIEW

This work focuses on the controller design for two aspects : the fuel cell hybrid electric vehicle and the microgrid. In order to ensure the smooth operation and the stability of these hybrid power systems, an advanced passivity-based control using the IDA-PBC methodology was proposed, with HIL and PHIL experimental validations.

7.1.1/ TOWARD FCHEV

The main contributions in the domain of FCHEV are summarized as follows :

1. An advanced passivity-based controller was designed to manage power and energy for a FC/SCs hybrid power system, which considers situations of limitations according to the SCs SoC. The control strategy of a dissipating resistance load that was implemented into the system was also considered into the controller, in order to protect the system from over-voltage.
2. These component constraints as well as the dissipation were integrated directly into the controller equations, which ensures the stability of the whole closed-loop system. Then, the operation of the proposed controller was validated on the PHIL platform.
3. Based on the above controller, an aging-tolerant passivity-based controller was designed by combining it with an aging estimation of the FC using an EKF. Therefore, the maximum current that the FC can deliver was calculated in real-time and was considered by the IDA-PBC controller, in order to protect the FC from overload.
4. The experimental validation of the proposed aging-tolerant passivity-based controller was realized on a HIL platform, with the application on a commercial vehicle under a modified NEDC.

7.1.2/ TOWARD MICROGRID

In the domain of microgrid, the contributions of this thesis are summarized as follows :

1. An IDA-PBC controller was designed for a green datacenter powered by a microgrid with PV, hydrogen FC, SCs and electrolyzer. The proposed controller has a good performance on the system operation, while enabling a smooth response from the

FC and a dynamic response from the SCs, with fast load demand changes. The stability of the closed-loop system was proven theoretically and was validated experimentally on the PHIL platform.

2. As a part of the DATAZERO project, the software set-up of the PHIL platform was established while a test of the communication with the remote controller was realized.

7.2/ PERSPECTIVES

7.2.1/ TOWARD FCHEV

In order to test the dynamic behavior of the system, the duration of the applied driving cycle was divided by a factor of 10, while the FC aging was also accelerated. For future work, the proposed aging-tolerant passivity-based controller could be validated under this scenario but with normal time scale and real components.

The proposed passivity-based controller focuses on the dynamic response and the stability of the hybrid power system. For industrial applications, energy efficiency and cost are essential issues, which was not considered in the PBC energy management algorithm. Therefore, optimal objectives need to be achieved in future works, such as maximization of energy efficiency and minimization of hydrogen consumption while reducing the system cost.

7.2.2/ TOWARD MICROGRID

In this work, we supposed an ideal hydrogen storage level, which is always available. The sizing and implementation of a hydrogen tank will be the next step of the research. In addition, because of the power limit on the PHIL test bench, a specific scenario of the load current was designed to test the controller's operation on the test bench with real electrical elements. For future work, a real distribution grid profile could be integrated into the system.

For the project DATAZERO, an emulator of the wind turbine needs to be implemented on the PHIL platform. A real-time model of the wind turbine will be established and will be emulated by the power supply. Also, presently, the remote control decision from the PDM is integrated into the real-time controller that is based on rule-based control. Since the passivity-based controller has a better performance on the real-time stability, a proper way for the integration of the PDM decision into the passivity-based controller needs to be figured out. This project will be continued by the DATAZERO2 project [200], which aims at improving the operation and design of cooperating datacenters operated only with renewable energies.

LIST OF PUBLICATIONS

CONFERENCES

1. Kong, S., Hilairet, M. and Roche, R., Advanced passivity-based control for a fuel cell/super-capacitor hybrid power system. IEEE Vehicle Power and Propulsion Conference (VPPC) (pp. 1-6). 2017. [201].
2. Kong, S., Hilairet, M. and Roche, R., Passivity-Based Control for a PV/Battery/Fuel Cell/Electrolyser Hybrid Power System. IEEE Milan PowerTech (pp. 1-6), 2019. [197].
3. Kong, S., Hilairet, M. and Roche, R., Commande passive d'un système d'alimentation hybride photovoltaïque/batterie/pile à combustible/électrolyseur. Conference Jeune Chercheur en Génie Électrique, 2019. [202].

JOURNAL

1. Kong, S., Bressel, M. Hilairet, M. and Roche, R., Advanced Passivity-Based, Aging-Tolerant Control for a Fuel Cell/Super-Capacitor Hybrid System. Control Engineering Practice, **under review (1^{st} revision).**

BIBLIOGRAPHY

[1] BP statistical review of world energy. [Online]. Available : https://www.bp.com/en/global/corporate/energy-economics/statistical-review-of-world-energy.html

[2] Global energy CO_2 status report 2019. [Online]. Available : https://www.iea.org/reports/global-energy-co2-status-report-2019

[3] Exponential climate action roadmap. [Online]. Available : https://exponentialroadmap.org

[4] IPCC special report on global warming of 1.5°C. [Online]. Available : https://www.ipcc.ch/sr15/

[5] Transportation sector energy consumption. [Online]. Available : https://www.eia.gov/outlooks/ieo/pdf/transportation.pdf

[6] H. S. Das, C. W. Tan, and A. Yatim, “Fuel cell hybrid electric vehicles : A review on power conditioning units and topologies,” Renewable and Sustainable Energy Reviews, vol. 76, pp. 268–291, 2017.

[7] A. S. Andrae and T. Edler, “On global electricity usage of communication technology : trends to 2030,” Challenges, vol. 6, no. 1, pp. 117–157, 2015.

[8] N. Sulaiman, M. Hannan, A. Mohamed, E. Majlan, and W. W. Daud, “A review on energy management system for fuel cell hybrid electric vehicle : Issues and challenges,” Renewable and Sustainable Energy Reviews, vol. 52, pp. 802–814, 2015.

[9] Í. Goiri, M. E. Haque, K. Le, R. Beauchea, T. D. Nguyen, J. Guitart, J. Torres, and R. Bianchini, “Matching renewable energy supply and demand in green datacenters,” Ad Hoc Networks, vol. 25, pp. 520–534, 2015.

[10] E. Oró, V. Depoorter, A. Garcia, and J. Salom, “Energy efficiency and renewable energy integration in data centres. strategies and modelling review,” Renewable and Sustainable Energy Reviews, vol. 42, pp. 429–445, 2015.

[11] Global energy transformation the remap transition pathway. [Online]. Available : https://www.irena.org/publications/2019/Apr/Global-energy-transformation-The-REmap-transition-pathway

[12] Compare fuel cell vehicles. [Online]. Available : https://www.fueleconomy.gov/feg/fcv_sbs.shtml

[13] Green data : The next step to zero-emissions datacenters. [Online]. Available : https://spectrum.ieee.org/energywise/energy/environment/green-data-the-next-step-to-zeroemissions-data-centers

[14] Google vs Microsoft vs Apple vs Facebook, the race to be 100% green. [Online]. Available : https://data-economy.com/google-vs-microsoft-vs-apple-vs-facebook-the-race-to-be-100-green/

[15] Datazero project. [Online]. Available : https://www.irit.fr/datazero/index.php/en/

[16] J.-M. Pierson, G. Baudic, S. Caux, B. Celik, G. Da Costa, L. Grange, M. Haddad, J. Lecuivre, J.-M. Nicod, L. Philippe et al., "Datazero : Datacenter with zero emission and robust management using renewable energy," IEEE Access, vol. 7, pp. 103 209–103 230, 2019.

[17] IEA. Renewables 2018. Solar Energy. [Online]. Available : https://www.iea.org/topics/renewables/solar

[18] A. Mellit, A. Massi Pavan, E. Ogliari, S. Leva, and V. Lughi, "Advanced methods for photovoltaic output power forecasting : A review," Applied Sciences, vol. 10, no. 2, p. 487, 2020.

[19] S. Sperati, S. Alessandrini, P. Pinson, and G. Kariniotakis, "The weather intelligence for renewable energies benchmarking exercise on short-term forecasting of wind and solar power generation," Energies, vol. 8, no. 9, pp. 9594–9619, 2015.

[20] S. Pelland, J. Remund, J. Kleissl, T. Oozeki, and K. De Brabandere, "Photovoltaic and solar forecasting : state of the art," IEA PVPS, Task, vol. 14, pp. 1–36, 2013.

[21] W. VanDeventer, E. Jamei, G. S. Thirunavukkarasu, M. Seyedmahmoudian, T. K. Soon, B. Horan, S. Mekhilef, and A. Stojcevski, "Short-term PV power forecasting using hybrid GASVM technique," Renewable energy, vol. 140, pp. 367–379, 2019.

[22] M. Gao, J. Li, F. Hong, and D. Long, "Day-ahead power forecasting in a large-scale photovoltaic plant based on weather classification using lstm," Energy, vol. 187, p. 115838, 2019.

[23] J. Ospina, A. Newaz, and M. O. Faruque, "Forecasting of PV plant output using hybrid wavelet-based LSTM-DNN structure model," IET Renewable Power Generation, vol. 13, no. 7, pp. 1087–1095, 2019.

[24] B. K. S. Vastav, S. Nema, P. Swarnkar, and D. Rajesh, "Automatic solar tracking system using delta plc," in 2016 International Conference on Electrical Power and Energy Systems (ICEPES). IEEE, 2016, pp. 16–21.

[25] A. Harrag and H. Bahri, "Novel neural network IC-based variable step size fuel cell MPPT controller : performance, efficiency and lifetime improvement," International Journal of Hydrogen Energy, vol. 42, no. 5, pp. 3549–3563, 2017.

[26] D. Gao, Z. Jin, J. Zhang, J. Li, and M. Ouyang, "Development and performance analysis of a hybrid fuel cell/battery bus with an axle integrated electric motor drive system," International Journal of Hydrogen Energy, vol. 41, no. 2, pp. 1161–1169, 2016.

[27] X. Huang, Z. Zhang, and J. Jiang, "Fuel cell technology for distributed generation : an overview," in 2006 IEEE international symposium on industrial electronics, vol. 2. IEEE, 2006, pp. 1613–1618.

[28] F. Barbir, "PEM electrolysis for production of hydrogen from renewable energy sources," Solar energy, vol. 78, no. 5, pp. 661–669, 2005.

[29] M. Chandesris, V. Médeau, N. Guillet, S. Chelghoum, D. Thoby, and F. Fouda-Onana, "Membrane degradation in pem water electrolyzer : Numerical modeling and experimental evidence of the influence of temperature and current density," International Journal of Hydrogen Energy, vol. 40, no. 3, pp. 1353–1366, 2015.

[30] A. Ganeshan, D. Holmes, L. Meegahapola, and B. McGrath, "Enhanced control of a hydrogen energy storage system in a microgrid," in Universities Power Engineering Conference (AUPEC), 2017 Australasian. IEEE, 2017, pp. 1–6.

[31] K. J. Reddy and S. Natarajan, “Energy sources and multi-input DC-DC converters used in hybrid electric vehicle applications–A review,” International Journal of Hydrogen Energy, vol. 43, no. 36, pp. 17 387–17 408, 2018.

[32] S. Faraji and F. N. Ani, “The development supercapacitor from activated carbon by electroless platinga review,” Renewable and Sustainable Energy Reviews, vol. 42, pp. 823–834, 2015.

[33] I. Hadjipaschalis, A. Poullikkas, and V. Efthimiou, “Overview of current and future energy storage technologies for electric power applications,” Renewable and sustainable energy reviews, vol. 13, no. 6-7, pp. 1513–1522, 2009.

[34] M. Al Sakka, J. Van Mierlo, H. Gualous, and U. Brussel, “DC/DC converters for electric vehicles,” Electric vehicles–modelling and simulations, vol. 309, 2011.

[35] M. A. Mallouh, B. Surgenor, P. Dash, and L. McInnes, “Performance evaluation and tuning of a fuzzy control strategy for a fuel cell hybrid electric auto rickshaw,” in 2012 American Control Conference (ACC). IEEE, 2012, pp. 1321–1326.

[36] C.-J. Xie, S.-H. Quan, and Q.-h. Chen, “Control strategy of hybrid power system for fuel cell electric vehicle based on neural network optimization,” in 2008 IEEE international conference on automation and logistics. IEEE, 2008, pp. 753–757.

[37] D. Xiao, W. Qi, H. Jin, and J. Fang, “Modeling and simulation for golf fuel cell electric vehicle control system,” in 2012 Spring Congress on Engineering and Technology. IEEE, 2012, pp. 1–4.

[38] S. Yu, J. Zhang, and L. Wang, “Power management strategy with regenerative braking for fuel cell hybrid electric vehicle,” in 2009 Asia-Pacific Power and Energy Engineering Conference. IEEE, 2009, pp. 1–4.

[39] A. Payman, S. Pierfederici, and F. Meibody-Tabar, “Energy management in a fuel cell/supercapacitor multisource/multiload electrical hybrid system,” IEEE Transactions on Power Electronics, vol. 24, no. 12, pp. 2681–2691, 2009.

[40] L. Wang, Z. Wang, and H. Li, “Optimized energy storage system design for a fuel cell vehicle using a novel phase shift and duty cycle control,” in 2009 IEEE Energy Conversion Congress and Exposition. IEEE, 2009, pp. 1432–1438.

[41] X. Lu, X. Miao, W. Liu, and J. Lu, “Extension control strategy of a single converter for hybrid PEMFC/battery power source,” Internatinal Journal of Applied Thermal Engineering, vol. 128, pp. 887–897, January 2018.

[42] L. Karunarathne, J. T. Economou, and K. Knowles, “Model based power and energy management system for pem fuel cell/li-ion battery driven propulsion system,” 2010.

[43] H. Alloui, M. Becherif, and K. Marouani, “Modelling and frequency separation energy management of fuel cell-battery hybrid sources system for hybrid electric vehicle,” in 21st Mediterranean Conference on Control and Automation. IEEE, 2013, pp. 646–651.

[44] S. Kelouwani, K. Agbossou, Y. Dubé, and L. Boulon, “Fuel cell plug-in hybrid electric vehicle anticipatory and real-time blended-mode energy management for battery life preservation,” Journal of Power Sources, vol. 221, pp. 406–418, 2013.

[45] A. Benrabeh, F. Khoucha, O. Herizi, M. Benbouzid, and A. Kheloui, “FC/battery power management for electric vehicle based interleaved DC-DC boost converter topology,” in 2013 15th European Conference on Power Electronics and Applications (EPE). IEEE, 2013, pp. 1–9.

[46] M. Mohammedi, O. Kraa, M. Becherif, A. Aboubou, M. Ayad, and M. Bahri, "Fuzzy logic and passivity-based controller applied to electric vehicle using fuel cell and supercapacitors hybrid source," Energy Procedia, vol. 50, pp. 619–626, 2014.

[47] G. L. Lopez, R. S. Rodriguez, V. M. Alvarado, J. Gomez-Aguilar, J. E. Mota, and C. Sandoval, "Hybrid PEMFC-supercapacitor system : Modeling and energy management in energetic macroscopic representation," Applied Energy, vol. 205, pp. 1478–1494, 2017.

[48] O. Bethoux, G. Remy, J. Riera, M. Serra, and T. Azib, "Analyses of energy management strategies for a PEMFC/UC electric vehicle," in 2012 IEEE Vehicle Power and Propulsion Conference. IEEE, 2012, pp. 956–961.

[49] P. Thounthong, S. Pierfederici, J.-P. Martin, M. Hinaje, and B. Davat, "Modeling and control of fuel cell/supercapacitor hybrid source based on differential flatness control," IEEE Transactions on Vehicular Technology, vol. 59, no. 6, pp. 2700–2710, 2010.

[50] M. Uzunoglu and M. Alam, "Modeling and analysis of an FC/UC hybrid vehicular power system using a novel-wavelet-based load sharing algorithm," IEEE Transactions on Energy Conversion, vol. 23, no. 1, pp. 263–272, 2008.

[51] D. Efstathiou, A. Petrou, P. Spanoudakis, N. Tsourveloudis, and K. Valavanis, "Recent advances on the energy management of a hybrid electric vehicle," in 2012 20th Mediterranean Conference on Control & Automation (MED). IEEE, 2012, pp. 896–901.

[52] T. Azib, O. Bethoux, C. Marchand, and E. Berthelot, "Supercapacitors for power assistance in hybrid power source with fuel cell," in Industrial Electronics, 2009. IECON'09. 35th Annual Conference of IEEE. IEEE, 2009, pp. 3747–3752.

[53] E. Tazelaar, B. Veenhuizen, J. Jagerman, and T. Faassen, "Energy management strategies for fuel cell hybrid vehicles - an overview," in 2013 World Electric Vehicle Symposium and Exhibition (EVS27). IEEE, 2013, pp. 1–12.

[54] C. Capasso and O. Veneri, "Integration between super-capacitors and ZEBRA batteries as high performance hybrid storage system for electric vehicles," Energy Procedia, vol. 105, pp. 2539–2544, 2017.

[55] J. S. Martinez, D. Hissel, M.-C. Pera, and M. Amiet, "Practical control structure and energy management of a testbed hybrid electric vehicle," IEEE Transactions on Vehicular Technology, vol. 60, no. 9, pp. 4139–4152, 2011.

[56] Q. Li, W. Chen, Y. Li, S. Liu, and J. Huang, "Energy management strategy for fuel cell/battery/ultracapacitor hybrid vehicle based on fuzzy logic," International Journal of Electrical Power & Energy Systems, vol. 43, no. 1, pp. 514–525, 2012.

[57] S. N. Motapon, L.-A. Dessaint, and K. Al-Haddad, "A comparative study of energy management schemes for a fuel-cell hybrid emergency power system of more-electric aircraft," IEEE transactions on industrial electronics, vol. 61, no. 3, pp. 1320–1334, 2013.

[58] P. Thounthong, S. Rael, and B. Davat, "Energy management of fuel cell/battery/supercapacitor hybrid power source for vehicle applications," Journal of Power Sources, vol. 193, no. 1, pp. 376–385, 2009.

[59] J. P. Torreglosa, P. Garcia, L. M. Fernandez, and F. Jurado, "Predictive control for the energy management of a fuel-cell–battery–supercapacitor tramway," IEEE Transactions on Industrial Informatics, vol. 10, no. 1, pp. 276–285, 2014.

[60] R. T. Bambang, A. S. Rohman, C. J. Dronkers, R. Ortega, A. Sasongko et al., "Energy management of fuel cell/battery/supercapacitor hybrid power sources using model predictive control," IEEE Transactions on Industrial Informatics, vol. 10, no. 4, pp. 1992–2002, 2014.

[61] M. Hannan, F. Azidin, and A. Mohamed, "Multi-sources model and control algorithm of an energy management system for light electric vehicles," Energy Conversion and Management, vol. 62, pp. 123–130, 2012.

[62] P. García, J. P. Torreglosa, L. M. Fernández, and F. Jurado, "Control strategies for high-power electric vehicles powered by hydrogen fuel cell, battery and supercapacitor," Expert Systems with Applications, vol. 40, no. 12, pp. 4791–4804, 2013.

[63] V. Paladini, T. Donateo, A. De Risi, and D. Laforgia, "Super-capacitors fuel-cell hybrid electric vehicle optimization and control strategy development," Energy conversion and management, vol. 48, no. 11, pp. 3001–3008, 2007.

[64] X. Liu, D. Diallo, and C. Marchand, "Design methodology of fuel cell electric vehicle power system," in 2008 18th International Conference on Electrical Machines. IEEE, 2008, pp. 1–6.

[65] I. Cervantes, F. J. Perez-Pinal, J. Leyva-Ramos, and A. Mendoza-Torres, "Hybrid control technique applied in a FC-SC electric vehicle platform," in 2010 IEEE Vehicle Power and Propulsion Conference. IEEE, 2010, pp. 1–5.

[66] A. Chauhan and R. Saini, "A review on integrated renewable energy system based power generation for stand-alone applications : Configurations, storage options, sizing methodologies and control," Renewable and Sustainable Energy Reviews, vol. 38, pp. 99–120, 2014.

[67] M. S. Mahmoud, M. S. U. Rahman, and M.-S. Fouad, "Review of microgrid architectures–a system of systems perspective," IET Renewable Power Generation, vol. 9, no. 8, pp. 1064–1078, 2015.

[68] A. Gholami, F. Aminifar, and M. Shahidehpour, "Front lines against the darkness : Enhancing the resilience of the electricity grid through microgrid facilities," IEEE Electrification Magazine, vol. 4, no. 1, pp. 18–24, 2016.

[69] M. Castañeda, L. Fernández, H. Sánchez, A. Cano, and F. Jurado, "Sizing methods for stand-alone hybrid systems based on renewable energies and hydrogen," in 2012 16th IEEE Mediterranean Electrotechnical Conference. IEEE, 2012, pp. 832–835.

[70] S. El Alimi, T. Maatallah, and S. B. Nasrallah, "Break-even analysis and optimization of a stand-alone hybrid system with battery storage for residential load consumptiona case study," Renewable and Sustainable Energy Reviews, vol. 37, pp. 408–423, 2014.

[71] A. Maleki and A. Askarzadeh, "Comparative study of artificial intelligence techniques for sizing of a hydrogen-based stand-alone photovoltaic/wind hybrid system," international journal of hydrogen energy, vol. 39, no. 19, pp. 9973–9984, 2014.

[72] E. Eriksson and E. M. Gray, "Optimization and integration of hybrid renewable energy hydrogen fuel cell energy systems–a critical review," Applied Energy, vol. 202, pp. 348–364, 2017.

[73] M. Starke, L. M. Tolbert, and B. Ozpineci, "AC vs. DC distribution : A loss comparison," in 2008 IEEE/PES Transmission and Distribution Conference and Exposition. IEEE, 2008, pp. 1–7.

[74] A. Askarzadeh and L. dos Santos Coelho, “A novel framework for optimization of a grid independent hybrid renewable energy system : A case study of iran,” Solar Energy, vol. 112, pp. 383–396, 2015.

[75] I. Baniasad Askari, L. Baniasad Askari, M. Kaykhah, and H. Baniasad Askari, “Optimisation and techno-economic feasibility analysis of hybrid (photovoltaic/wind/fuel cell) energy systems in kerman, iran ; considering the effects of electrical load and energy storage technology,” International Journal of Sustainable Energy, vol. 33, no. 3, pp. 635–649, 2014.

[76] H. Belmili, M. Haddadi, S. Bacha, M. F. Almi, and B. Bendib, “Sizing stand-alone photovoltaic–wind hybrid system : Techno-economic analysis and optimization,” Renewable and Sustainable Energy Reviews, vol. 30, pp. 821–832, 2014.

[77] H. Zahboune, F. Kadda, S. Zouggar, E. Ziani, J. Klemes, P. Varbanov, and Y. Zarhloule, “The new electricity system cascade analysis method for optimal sizing of an autonomous hybrid PV/wind energy system with battery storage,” in 2014 5th International Renewable Energy Congress (IREC). IEEE, 2014, pp. 1–6.

[78] B. Zhao, X. Zhang, P. Li, K. Wang, M. Xue, and C. Wang, “Optimal sizing, operating strategy and operational experience of a stand-alone microgrid on dongfushan island,” Applied Energy, vol. 113, pp. 1656–1666, 2014.

[79] A. H. Mamaghani, S. A. A. Escandon, B. Najafi, A. Shirazi, and F. Rinaldi, “Techno-economic feasibility of photovoltaic, wind, diesel and hybrid electrification systems for off-grid rural electrification in colombia,” Renewable Energy, vol. 97, pp. 293–305, 2016.

[80] Z. Jian, Z. He, J. Jia, and Y. Xie, “A review of control strategies for DC micro-grid,” in 2013 Fourth International Conference on Intelligent Control and Information Processing (ICICIP). IEEE, 2013, pp. 666–671.

[81] M. Barnes, J. Kondoh, H. Asano, J. Oyarzabal, G. Ventakaramanan, R. Lasseter, N. Hatziargyriou, and T. Green, “Real-world microgrids-an overview,” in 2007 IEEE International Conference on System of Systems Engineering. IEEE, 2007, pp. 1–8.

[82] P. Thounthong, P. Tricoli, and B. Davat, “Performance investigation of linear and nonlinear controls for a fuel cell/supercapacitor hybrid power plant,” International Journal of Electrical Power & Energy Systems, vol. 54, pp. 454–464, 2014.

[83] J. Peng, H. He, and R. Xiong, “Rule based energy management strategy for a series–parallel plug-in hybrid electric bus optimized by dynamic programming,” Applied Energy, vol. 185, pp. 1633–1643, 2017.

[84] I. Tegani, A. Aboubou, M. Ayad, R. Saadi, M. Becherif, M. Bahri, M. Benaouadj, and O. Kraa, “Experimental validation of differential flatness-based control applied to stand alone using photovoltaic/fuel cell/battery hybrid power sources,” International Journal of Hydrogen Energy, vol. 42, no. 2, pp. 1510–1517, 2017.

[85] B. Wang, J. Xu, R.-J. Wai, and B. Cao, “Adaptive sliding-mode with hysteresis control strategy for simple multimode hybrid energy storage system in electric vehicles,” IEEE Transactions on Industrial Electronics, vol. 64, no. 2, pp. 1404–1414, 2016.

[86] A. Tofighi and M. Kalantar, “Power management of PV/battery hybrid power source via passivity-based control,” Renewable Energy, vol. 36, no. 9, pp. 2440–2450, 2011.

[87] K. H. Ang, G. Chong, and Y. Li, “PID control system analysis, design, and technology,” IEEE transactions on control systems technology, vol. 13, no. 4, pp. 559–576, 2005.

[88] A. Tani, M. B. Camara, B. Dakyo, and Y. Azzouz, “DC/DC and DC/AC converters control for hybrid electric vehicles energy management-ultracapacitors and fuel cell,” IEEE Transactions on Industrial Informatics, vol. 9, no. 2, pp. 686–696, 2012.

[89] H.-w. He, Y.-q. Zhang, and F. Wan, “Control strategies design for a fuel cell hybrid electric vehicle,” in 2008 IEEE Vehicle Power and Propulsion Conference. IEEE, 2008, pp. 1–6.

[90] C. Sandoval, V. M. Alvarado, J.-C. Carmona, G. L. Lopez, and J. Gomez-Aguilar, “Energy management control strategy to improve the FC/SC dynamic behavior on hybrid electric vehicles : A frequency based distribution,” Renewable energy, vol. 105, pp. 407–418, 2017.

[91] A. Fadel and B. Zhou, “An experimental and analytical comparison study of power management methodologies of fuel cell–battery hybrid vehicles,” Journal of Power Sources, vol. 196, no. 6, pp. 3271–3279, 2011.

[92] P. Thounthong, S. Rael, and B. Davat, “Analysis of supercapacitor as second source based on fuel cell power generation,” IEEE Transactions on Energy Conversion, vol. 24, no. 1, pp. 247–255, 2009.

[93] E. F. Camacho and C. Bordons, “Introduction to model predictive control,” in Model Predictive Control. Springer, 2007, pp. 1–11.

[94] Control of constrained hybrid systems - MPC. [Online]. Available : https://people.ee.ethz.ch/~cohysys/control.html

[95] Q. Chen, L. Gao, R. A. Dougal, and S. Quan, “Multiple model predictive control for a hybrid proton exchange membrane fuel cell system,” Journal of Power Sources, vol. 191, no. 2, pp. 473–482, 2009.

[96] A. Arce, J. Alejandro, and C. Bordons, “MPC for battery/fuel cell hybrid vehicles including fuel cell dynamics and battery performance improvement,” Journal of process control, vol. 19, no. 8, pp. 1289–1304, 2009.

[97] T.-T. Nguyen, H.-J. Yoo, and H.-M. Kim, “Applying model predictive control to smes system in microgrids for eddy current losses reduction,” IEEE Transactions on Applied Superconductivity, vol. 26, no. 4, pp. 1–5, 2016.

[98] S. Mariéthoz, O. Bethoux, and M. Hilairet, “A distributed model predictive control scheme for reducing consumption of hybrid fuel cell systems,” in IECON 2012-38th Annual Conference on IEEE Industrial Electronics Society. IEEE, 2012, pp. 868–873.

[99] S. Zhang, R. Xiong, and F. Sun, “Model predictive control for power management in a plug-in hybrid electric vehicle with a hybrid energy storage system,” Applied Energy, vol. 185, pp. 1654–1662, 2017.

[100] B. Wang, L. Xian, U. Manandhar, J. Ye, X. Zhang, H. B. Gooi, and A. Ukil, “Hybrid energy storage system using bidirectional single-inductor multiple-port converter with model predictive control in DC microgrids,” Electric Power Systems Research, vol. 173, pp. 38–47, 2019.

[101] M. Hilairet, M. Ghanes, O. Béthoux, V. Tanasa, J. Barbot, and D. Normand-Cyrot, “A passivity-based controller for coordination of converters in a fuel cell system,” Control engineering practice, vol. 21, no. 8, pp. 1097–1109, 2013.

[102] I. Lachhab and L. Krichen, “An improved energy management strategy for FC/UC hybrid electric vehicles propelled by motor-wheels,” International journal of hydrogen energy, vol. 39, no. 1, pp. 571–581, 2014.

[103] S. Ahmadi and S. Bathaee, “Multi-objective genetic optimization of the fuel cell hybrid vehicle supervisory system : Fuzzy logic and operating mode control strategies,” International Journal of Hydrogen Energy, vol. 40, no. 36, pp. 12 512–12 521, 2015.

[104] B. Cezar and A. Onea, “A rule-based energy management strategy for parallel hybrid vehicles with supercapacitors,” in 15th International Conference on System Theory, Control and Computing. IEEE, 2011, pp. 1–6.

[105] Y. Wang, Z. Sun, and Z. Chen, “Development of energy management system based on a rule-based power distribution strategy for hybrid power sources,” Energy, vol. 175, pp. 1055–1066, 2019.

[106] G. T. Samson, T. M. Undeland, O. Ulleberg, and P. J. Vie, “Optimal load sharing strategy in a hybrid power system based on PV/fuel cell/battery/supercapacitor,” in Clean Electrical Power, 2009 International Conference on. IEEE, 2009, pp. 141–146.

[107] J.-q. Li, Z. Fu, and X. Jin, “Rule based energy management strategy for a battery/ultra-capacitor hybrid energy storage system optimized by pseudospectral method,” Energy Procedia, vol. 105, pp. 2705–2711, 2017.

[108] Y. Gao and M. Ehsani, “Design and control methodology of plug-in hybrid electric vehicles,” IEEE Transactions on Industrial Electronics, vol. 57, no. 2, pp. 633–640, 2009.

[109] O. Cord et al., Genetic fuzzy systems : evolutionary tuning and learning of fuzzy knowledge bases. World Scientific, 2001, vol. 19.

[110] N. Bizon, “Nonlinear control of fuel cell hybrid power sources : Part I - voltage control,” Applied energy, vol. 88, no. 7, pp. 2559–2573, 2011.

[111] S. G. Li, S. Sharkh, F. C. Walsh, and C.-N. Zhang, “Energy and battery management of a plug-in series hybrid electric vehicle using fuzzy logic,” IEEE Transactions on Vehicular Technology, vol. 60, no. 8, pp. 3571–3585, 2011.

[112] M. Kisacikoglu, M. Uzunoglu, and M. Alam, “Load sharing using fuzzy logic control in a fuel cell/ultracapacitor hybrid vehicle,” International journal of hydrogen energy, vol. 34, no. 3, pp. 1497–1507, 2009.

[113] M. B. Y. Reddy and M. R. Babu, “Fuzzy control based hybrid grid connected hybrid PV/PEMFC/Battery distributed generation system,” 2019.

[114] Y. L. Murphey, Z. Chen, L. Kiliaris, and M. A. Masrur, “Intelligent power management in a vehicular system with multiple power sources,” Journal of Power Sources, vol. 196, no. 2, pp. 835–846, 2011.

[115] S. Caux, W. Hankache, M. Fadel, and D. Hissel, “On-line fuzzy energy management for hybrid fuel cell systems,” International journal of hydrogen energy, vol. 35, no. 5, pp. 2134–2143, 2010.

[116] J. S. Martínez, J. Mulot, F. Harel, D. Hissel, M.-C. Pera, R. I. John, and M. Amiet, “Experimental validation of a type-2 fuzzy logic controller for energy management in hybrid electrical vehicles,” Engineering Applications of Artificial Intelligence, vol. 26, no. 7, pp. 1772–1779, 2013.

[117] X. Yuan, Z. Chen, Y. Yuan, and Y. Huang, “Design of fuzzy sliding mode controller for hydraulic turbine regulating system via input state feedback linearization method,” Energy, vol. 93, pp. 173–187, 2015.

[118] S. Laghrouche, F. Plestan, and A. Glumineau, “Higher order sliding mode control based on integral sliding mode,” Automatica, vol. 43, no. 3, pp. 531–537, 2007.

[119] X. Liu, “Contribution to adaptative sliding mode, fault tolerant control and control allocation of wind turbine system,” Ph.D. dissertation, 2016.

[120] O. Kraa, H. Ghodbane, R. Saadi, M. Ayad, M. Becherif, A. Aboubou, and M. Bahri, “Energy management of fuel cell/supercapacitor hybrid source based on linear and sliding mode control,” Energy Procedia, vol. 74, pp. 1258–1264, 2015.

[121] Z. Song, J. Hou, H. Hofmann, J. Li, and M. Ouyang, “Sliding-mode and lyapunov function-based control for battery/supercapacitor hybrid energy storage system used in electric vehicles,” Energy, vol. 122, pp. 601–612, 2017.

[122] J. Liu, S. Laghrouche, and M. Wack, “Observer-based higher order sliding mode control of power factor in three-phase AC/DC converter for hybrid electric vehicle applications,” International Journal of Control, vol. 87, no. 6, pp. 1117–1130, 2014.

[123] J. Liu, Y. Zhao, B. Geng, and B. Xiao, “Adaptive second order sliding mode control of a fuel cell hybrid system for electric vehicle applications,” Journal of Mathematical Problems in Engineering, 2015.

[124] J. J. Moré, P. F. Puleston, C. Kunusch, and M. A. Fantova, “Development and implementation of a supervisor strategy and sliding mode control setup for fuel-cell-based hybrid generation systems,” IEEE Transactions on Energy Conversion, vol. 30, no. 1, pp. 218–225, 2015.

[125] R. S. Ashok, Y. Shtessel, and M. Ghanes, “Sliding mode control of hydrogen fuel cell and ultracapacitor based electric power system : Electric vehicle application,” IFAC Proceedings of 20th IFAC World Congress, vol. 50, no. 1, pp. 14 794–14 799, 2016.

[126] D. Zambrano-Prada, O. López-Santos, and L. Martínez-Salamero, “Dynamic power sharing strategy for hybrid energy storage system based on sliding mode control,” in IECON 2019-45th Annual Conference of the IEEE Industrial Electronics Society, vol. 1. IEEE, 2019, pp. 3888–3893.

[127] S. Laghrouche, J. Liu, F. S. Ahmed, M. Harmouche, and M. Wack, “Adaptive second-order sliding mode observer-based fault reconstruction for PEM fuel cell air-feed system,” IEEE Transactions on Control Systems Technology, vol. 23, no. 3, pp. 1098–1109, 2014.

[128] R. J. Talj, D. Hissel, R. Ortega, M. Becherif, and M. Hilairet, “Experimental validation of a pem fuel-cell reduced-order model and a moto-compressor higher order sliding-mode control,” IEEE Transactions on Industrial Electronics, vol. 57, no. 6, pp. 1906–1913, 2009.

[129] R. Talj, M. Hilairet, and R. Ortega, “Second order sliding mode control of the moto-compressor of a PEM fuel cell air feeding system, with experimental validation,” in 2009 35th Annual Conference of IEEE Industrial Electronics. IEEE, 2009, pp. 2790–2795.

[130] R. Talj, D. Hissel, R. Ortega, M. Becherif, and M. Hilairet, “A reduced-order model and a higher-order sliding-mode control of the air supply system of a proton-exchange-membrane fuel cell with experimental validation," in 2009 8th International Symposium on Advanced Electromechanical Motion Systems & Electric Drives Joint Symposium. IEEE, 2009, pp. 1–6.

[131] J. Liu, S. Laghrouche, M. Harmouche, and M. Wack, "Adaptive-gain second-order sliding mode observer design for switching power converters," Control Engineering Practice, vol. 30, pp. 124–131, 2014.

[132] X. Rain, M. Hilairet, and R. Talj, "Second order sliding mode current controller for the switched reluctance machine," in IECON 2010-36th Annual Conference on IEEE Industrial Electronics Society. IEEE, 2010, pp. 3301–3306.

[133] W. Thammasiriroj, V. Chunkag, M. Phattanasak, S. Pierfederici, B. Davat, and P. Thounthong, "Nonlinear model based single-loop control of interleaved converters for a hybrid source system," ECTI Transactions on Electrical Engineering, Electronics, and Communications, vol. 15, no. 1, pp. 19–31, 2017.

[134] M. Soheil-Hamedani, M. Zandi, R. Gavagsaz-Ghoachani, B. Nahid-Mobarakeh, and S. Pierfederici, "Flatness-based control method : A review of its applications to power systems," in 2016 7th Power Electronics and Drive Systems Technologies Conference (PEDSTC). IEEE, 2016, pp. 547–552.

[135] M. Phattanasak, W. Thammasiriroj, R. Gavagsaz-Ghoachani, M. Zandi, J. Martin, S. Pierfederici, and B. Nahid-Mobarakeh, "Hybrid power source FC/SC with single-loop control approach : Reference trajectories generation," IEEE Vehicle Power and Propulsion Conference (VPPC), 2017.

[136] M. Joševski and D. Abel, "Flatness-based model predictive control for the fuel optimization of hybrid electric vehicles," IFAC-PapersOnLine, vol. 48, no. 23, pp. 464–470, 2015.

[137] T. Allag and T. Das, "Robust control of solid oxide fuel cell ultracapacitor hybrid system," IEEE Transactions on Control Systems Technology, vol. 20, no. 1, 2012.

[138] H. Jafarnejadsani, J. Pieper, and J. Ehlers, "Adaptive control of a variable-speed variable-pitch wind turbine using radial-basis function neural network," IEEE transactions on control systems technology, vol. 21, no. 6, pp. 2264–2272, 2013.

[139] S. Mane, M. Mejari, F. Kazi, and N. Singh, "Improving lifetime of fuel cell in hybrid energy management system by lure lyapunov-based control formulation," IEEE Transactions on Industrial Electronics, vol. 64, no. 8, 2017.

[140] H. El Fadil, F. Giri, J. M. Guerrero, and A. Tahri, "Modeling and nonlinear control of a fuel cell/supercapacitor hybrid energy storage system for electric vehicles," IEEE Transactions on Vehicular Technology, vol. 63, no. 7, pp. 3011–3018, 2014.

[141] S. B. Siad, A. Malkawi, G. Damm, L. Lopes, and L. G. Dol, "Nonlinear control of a dc microgrid for the integration of distributed generation based on different time scales," International Journal of Electrical Power & Energy Systems, vol. 111, pp. 93–100, 2019.

[142] T. Allag and T. Das, "Robust control of solid oxide fuel cell ultracapacitor hybrid system," IEEE transactions on control systems technology, vol. 20, no. 1, pp. 1–10, 2011.

[143] C. Song, B. Wu, J. Zhao, and P. Li, "An integrated state space partition and optimal control method of multi-model for nonlinear systems based on hybrid systems," Journal of Process Control, vol. 25, pp. 59–69, 2015.

[144] Q. Li, W. Chen, Y. Wang, J. Jia, and M. Han, “Nonlinear robust control of proton exchange membrane fuel cell by state feedback exact linearization,” Journal of Power Sources, vol. 194, no. 1, pp. 338–348, 2009.

[145] M. Wieczorek and M. Lewandowski, “A mathematical representation of an energy management strategy for hybrid energy storage system in electric vehicle and real time optimization using a genetic algorithm,” International Journal of Applied Energy, vol. 192, pp. 222–233, 2017.

[146] R. Ortega, A. Van Der Schaft, B. Maschke, and G. Escobar, “Interconnection and damping assignment passivity-based control of port-controlled hamiltonian systems,” Automatica, vol. 38, no. 4, pp. 585–596, 2002.

[147] A. Loria, “Passivity in control systems,” C.N.R.S, UMR 5228, Laboratoire d’Automatique de Grenoble.

[148] C. Cecati, A. Dell’Aquila, M. Liserre, and V. G. Monopoli, “A passivity-based multilevel active rectifier with adaptive compensation for traction applications,” IEEE Transactions on Industry Applications, vol. 39, no. 5, pp. 1404–1413, 2003.

[149] R. Ortega, J. A. L. Perez, P. J. Nicklasson, and H. J. Sira-Ramirez, Passivity-based control of Euler-Lagrange systems : mechanical, electrical and electromechanical applications. Springer Science & Business Media, 2013.

[150] S. Mane, F. Kazi, and N. Singh, “Fuel cell and ultra-capacitor based hybrid energy control using IDA-PBC methodology,” in Industrial Instrumentation and Control (ICIC), 2015 International Conference on. IEEE, 2015, pp. 879–884.

[151] R. Ortega and E. Garca-Canseco, “Interconnection and damping assignment passivity-based control : A survey,” European Journal of control, vol. 10, no. 5, pp. 432–450, 2004.

[152] A. Benmouna, M. Becherif, D. Depernet, and M. A. Ebrahim, “Novel energy management technique for hybrid electric vehicle via interconnection and damping assignment passivity based control,” Renewable Energy, vol. 119, pp. 116–128, 2018.

[153] B. Amrouche, T. O. Cherif, M. Ghanes, and K. Iffouzar, “A passivity-based controller for coordination of converters in a fuel cell system used in hybrid electric vehicle propelled by two seven phase induction motor,” International Journal of Hydrogen Energy, vol. 42, no. 42, pp. 26 362–26 376, 2017.

[154] R. Logesh et al., “Resources, configurations, and soft computing techniques for power management and control of PV/wind hybrid system,” Renewable and Sustainable Energy Reviews, vol. 69, pp. 129–143, 2017.

[155] L. Croci, A. Martinez, P. Coirault, G. Champenois, and J.-P. Gaubert, “Passivity-based control of photovoltaic-wind hybrid system with euler-lagrange modeling,” in IECON 2012-38th Annual Conference on IEEE Industrial Electronics Society. IEEE, 2012, pp. 1126–1131.

[156] M. Becherif, M. Ayad, A. Henni, and A. Aboubou, “Hybridization of solar panel and batteries for street lighting by passivity based control,” in 2010 IEEE International Energy Conference. IEEE, 2010, pp. 664–669.

[157] A. Tofighi and M. Kalantar, “Interconnection and damping assignment and euler-lagrange passivity-based control of photovoltaic/battery hybrid power source for stand-alone applications,” Journal of Zhejiang University Science C, vol. 12, no. 9, p. 774, 2011.

[158] N. Khefifi, A. Houari, M. Ait-Ahmed, M. Machmoum, and M. Ghanes, "Robust ida-pbc based load voltage controller for power quality enhancement of standalone microgrids," in IECON 2018-44th Annual Conference of the IEEE Industrial Electronics Society. IEEE, 2018, pp. 249–254.

[159] X. Lin and Y. Lei, "Coordinated control strategies for SMES-battery hybrid energy storage systems," IEEE Access, vol. 5, pp. 23 452–23 465, 2017.

[160] W. Gil-González, O. Montoya, A. Garcés, and G. Espinosa-Pérez, "IDA-passivity-based control for superconducting magnetic energy storage with PWM-CSC," in 2017 Ninth Annual IEEE Green Technologies Conference (GreenTech). IEEE, 2017, pp. 89–95.

[161] F. Yang, B. Sheng, and Y. Fu, "Energy management for fuel cell-supercapacitor hybrid system using passivity-based controller with multi-equilibrium states," in Industrial Electronics Society, IECON 2015-41st Annual Conference of the IEEE. IEEE, 2015, pp. 000 511–000 516.

[162] M. Ayad, M. Becherif, A. Henni, A. Aboubou, M. Wack, and S. Laghrouche, "Passivity-based control applied to DC hybrid power source using fuel cell and supercapacitors," Energy Conversion and Management, vol. 51, no. 7, pp. 1468–1475, 2010.

[163] S. Wang, B. Li, Z. Xu, X. Zhao, and D. Xu, "A precise stability criterion for power hardware-in-the-loop simulation system," in 2019 10th International Conference on Power Electronics and ECCE Asia (ICPE 2019-ECCE Asia). IEEE, 2019, pp. 3265–3270.

[164] D. Shi, X. Dai, X. Zhang, and Q. Quan, "A practical performance evaluation method for electric multicopters," IEEE/ASME Transactions on Mechatronics, vol. 22, no. 3, pp. 1337–1348, 2017.

[165] X. Dai, C. Ke, Q. Quan, and K.-Y. Cai, "Simulation credibility assessment methodology with FPGA-based hardware-in-the-loop platform," arXiv preprint arXiv :1907.03981, 2019.

[166] M. Mahmood, M. Azam, K.-u.-N. Fatima, M. Sarwar, M. Abubakar, and B. Hussain, "Design and implementation of an automatic synchronizing and protection relay through power-hardware-in-the-loop (PHIL) simulation," arXiv preprint arXiv :1907.00339, 2019.

[167] P. V. Barrios, A. Burstein, and P. Nguyen, "Feasibility and performance assessment of commercial PV inverters operating with droop control for providing voltage supports services," in 2019 IEEE PES Innovative Smart Grid Technologies Europe. IEEE Press, 2019.

[168] P. Kotsampopoulos, A. Kapetanaki, G. Messinis, V. Kleftakis, and N. Hatziargyriou, "A power-hardware-in-the-loop facility for microgrids," Int. J. Distrib. Energy Resour. Technol. Sci. Publishers, vol. 9, no. 1, pp. 89–104, 2013.

[169] L. F. Osborne, J. Brummond, R. Hart, M. Zarean, S. M. Conger et al., "Clarus : Concept of operations," United States. Federal Highway Administration, Tech. Rep., 2005.

[170] D. Paire, "Dimensionnement et gestion d'énergie de systèmes d'entraînements électriques hybrides : application à un ascenseur avec récupération d'énergie," Ph.D. dissertation, 2010.

[171] H. Cherragui, M. Hilairet, and S. Giurgea, "Hardware-in-the-loop simulation of a boost converter with the Xilinx system generator from Matlab/Simulink," in IECON 2015-41st Annual Conference of the IEEE Industrial Electronics Society. IEEE, 2015, pp. 001 837–001 842.

[172] G. F. Lauss, M. O. Faruque, K. Schoder, C. Dufour, A. Viehweider, and J. Langston, "Characteristics and design of power hardware-in-the-loop simulations for electrical power systems," IEEE Transactions on Industrial Electronics, vol. 63, no. 1, pp. 406–417, 2015.

[173] M. V. G. Babu and R. S. Naik, "Comparitive analysis of PI, IP, PID and fuzzy controllers for speed control of dc motor," in International Research Journal of Engineering and Technology (IRJET), 2017.

[174] ActiveMQ website. [Online]. Available : https://activemq.apache.org/

[175] M. Hilairet, O. Bethoux, M. Ghanes, V. Tanasa, J.-P. Barbot, and M.-D. Normand-Cyrot, "Experimental validation of a sampled-data passivity-based controller for coordination of converters in a fuel cell system," IEEE Transactions on Industrial Electronics, vol. 62, no. 8, pp. 5187–5194, 2015.

[176] P. Thounthong, S. Raël, and B. Davat, "Control strategy of fuel cell and supercapacitors association for a distributed generation system," IEEE Transactions on Industrial Electronics, vol. 54, no. 6, pp. 3225–3233, 2007.

[177] H. Peng and A. G. Stefanopoulou, "Control-oriented modeling and analysis for automotive fuel cell systems," Journal of dynamic systems, measurement, and control, vol. 126, pp. 14–25, 2004.

[178] A. Donaire and S. Junco, "On the addition of integral action to port-controlled hamiltonian systems," Automatica, vol. 45, no. 8, pp. 1910–1916, 2009.

[179] D. Zhou, Y. Wu, F. Gao, E. Breaz, A. Ravey, and A. Miraoui, "Degradation prediction of pem fuel cell stack based on multiphysical aging model with particle filter approach," IEEE Transactions on Industry Applications, vol. 53, no. 4, pp. 4041–4052, 2017.

[180] S. Yin, X. Li, H. Gao, and O. Kaynak, "Data-based techniques focused on modern industry : An overview," IEEE Transactions on Industrial Electronics, vol. 62, no. 1, pp. 657–667, 2015.

[181] Z. Li, R. Outbib, S. Giurgea, and D. Hissel, "Diagnosis for PEMFC systems : a data-driven approach with the capabilities of online adaptation and novel fault detection," IEEE Transactions on Industrial Electronics, vol. 62, no. 8, pp. 5164–5174, 2015.

[182] S. Yin, S. X. Ding, X. Xie, and H. Luo, "A review on basic data-driven approaches for industrial process monitoring," IEEE Transactions on Industrial Electronics, vol. 61, no. 11, pp. 6418–6428, 2014.

[183] K. Javed, R. Gouriveau, N. Zerhouni, and P. Nectoux, "Enabling health monitoring approach based on vibration data for accurate prognostics," IEEE Transactions on Industrial Electronics, vol. 62, no. 1, pp. 647–656, 2015.

[184] M. Bressel, M. Hilairet, D. Hissel, and B. O. Bouamama, "Fuel cell remaining useful life prediction and uncertainty quantification under an automotive profile," in IECON 2016-42nd Annual Conference of the IEEE Industrial Electronics Society. IEEE, 2016, pp. 5477–5482.

[185] ——, "Extended kalman filter for prognostic of proton exchange membrane fuel cell," Applied Energy, vol. 164, pp. 220–227, 2016.

[186] ——, “Remaining useful life prediction and uncertainty quantification of proton exchange membrane fuel cell under variable load,” IEEE Transactions on Industrial Electronics, vol. 63, no. 4, pp. 2569–2577, 2016.

[187] M. Bressel, “Modélisation graphique pour le pronostic robuste de pile à combustible à membrane echangeuse de proton,” Ph.D. dissertation, 2016.

[188] M. Jouin, R. Gouriveau, D. Hissel, M.-C. Péra, and N. Zerhouni, “Degradations analysis and aging modeling for health assessment and prognostics of PEMFC,” Reliability Engineering & System Safety, vol. 148, pp. 78–95, 2016.

[189] W. Schmittinger and A. Vahidi, “A review of the main parameters influencing long-term performance and durability of PEM fuel cells,” Journal of power sources, vol. 180, no. 1, pp. 1–14, 2008.

[190] O. Veneri, C. Capasso, and S. Patalano, “Experimental study on the performance of a ZEBRA battery based propulsion system for urban commercial vehicles,” Applied Energy, vol. 185, pp. 2005–2018, 2017.

[191] D. Makarchuk, J. Kreicbergs, A. Grislis, and M. Gailis, “Analysis of energies and speed profiles of driving cycles for fuel consumption measurements,” in 14th International Scientific Conference Engineering for Rural Development, Latvia, 2015.

[192] M. Ehsani, Y. Gao, S. Longo, and K. Ebrahimi, Modern electric, hybrid electric, and fuel cell vehicles. CRC press, 2018.

[193] O. Veneri, C. Capasso, and S. Patalano, “Experimental investigation into the effectiveness of a super-capacitor based hybrid energy storage system for urban commercial vehicles,” Applied Energy, vol. 227, pp. 312–323, 2018.

[194] M. Blanke, M. Staroswiecki, and N. E. Wu, “Concepts and methods in fault-tolerant control,” in American Control Conference, 2001. Proceedings of the 2001, vol. 4. IEEE, 2001, pp. 2606–2620.

[195] U. of Energy. DOE technical targets for polymer electrolyte membrane fuel cell components. [Online]. Available : https://www.energy.gov/eere/fuelcells/doe-technical-targets-polymer-electrolyte-membrane-fuel-cell-components

[196] C.-Y. Wen and G.-W. Huang, “Application of a thermally conductive pyrolytic graphite sheet to thermal management of a PEM fuel cell,” Journal of Power Sources, vol. 178, no. 1, pp. 132–140, 2008.

[197] S. Kong, M. Hilairet, and R. Roche, “Passivity-based control for a PV/battery/fuel cell/electrolyser hybrid power system,” in 2019 IEEE Milan PowerTech. IEEE, 2019, pp. 1–6.

[198] F. Peng et al., “A novel method to estimate the maximum power for a photovoltaic inverter system,” in 2004 IEEE 35th Annual Power Electronics Specialists Conference (IEEE Cat. No. 04CH37551), vol. 3. IEEE, 2004, pp. 2065–2069.

[199] E. I. Ortiz-Rivera and F. Z. Peng, “Analytical model for a photovoltaic module using the electrical characteristics provided by the manufacturer data sheet,” in 2005 IEEE 36th Power Electronics Specialists Conference. IEEE, 2005, pp. 2087–2091.

[200] Datazero2 project. [Online]. Available : https://www.irit.fr/datazero/index.php/en/datazero2

[201] S. Kong, M. Hilairet, and R. Roche, “Advanced passivity-based control for a fuel cell/super-capacitor hybrid power system,” in 2017 IEEE Vehicle Power and Propulsion Conference (VPPC). IEEE, 2017, pp. 1–6.

[202] ——, “Commande passive d’un systeme d’alimentation hybride photovoltaïque/batterie/pile à combustible/électrolyseur.”

[203] R. Gules, J. D. P. Pacheco, H. L. Hey, and J. Imhoff, “A maximum power point tracking system with parallel connection for PV stand-alone applications,” IEEE transactions on industrial electronics, vol. 55, no. 7, pp. 2674–2683, 2008.

LIST OF FIGURES

LIST OF TABLES

V

APPENDIX

A

MODELS IN MATLAB/SIMULINK OF THE PHIL TEST BENCH

A.1/ OVERVIEW

In this subsection, the Simulink model is introduced. The whole model can be seen in Fig. A.1, and consists of :

- Parameter settings and measurements acquisition,
- Start phase initialization and protection : state machine, over-voltage protection, DC bus voltage control, setting of electrical load and power source,
- Display switch for the HMI,
- Short-term controller : IDA-PBC controller and rule-based controller,
- Current loops with IP controller,
- MPPT controller of the PV plant,
- Emulator model of hydrogen system,
- PWM and I-V setting,
- Ethernet connection.

The most important models are presented in details in the following parts.

A.2/ STATE MACHINE

A state machine is implemented into the system to enable an automatic start and stop of the PHIL test-bench. It consists of ten states from 0 to 9, which are defined as follows :

- State 0 : This is the initial state of the system, where the whole system is stopped. During this state, the start procedure can be activated by clicking on button ”start” on the HMI in ControlDesk shown in Fig. B.1 ; if this happens, skip to state 1.
- State 1 : During this state, the DC bus will be charged by the power supply until the DC bus voltage reaches the reference value, then skip to state 2.
- State 2 : After waiting for 10 s to stabilize the DC bus voltage, skip to state 3.
- State 3 : Charge SCs and the battery with a constant current using the power supply until the SoC arrives at the reference value, then skip to state 4.
- State 4 : Allow SCs to stabilize v_{bus} by the DC bus voltage controller and skip to state 5.
- State 5 : At this state, the system is ready to run a test. During this state, we can :

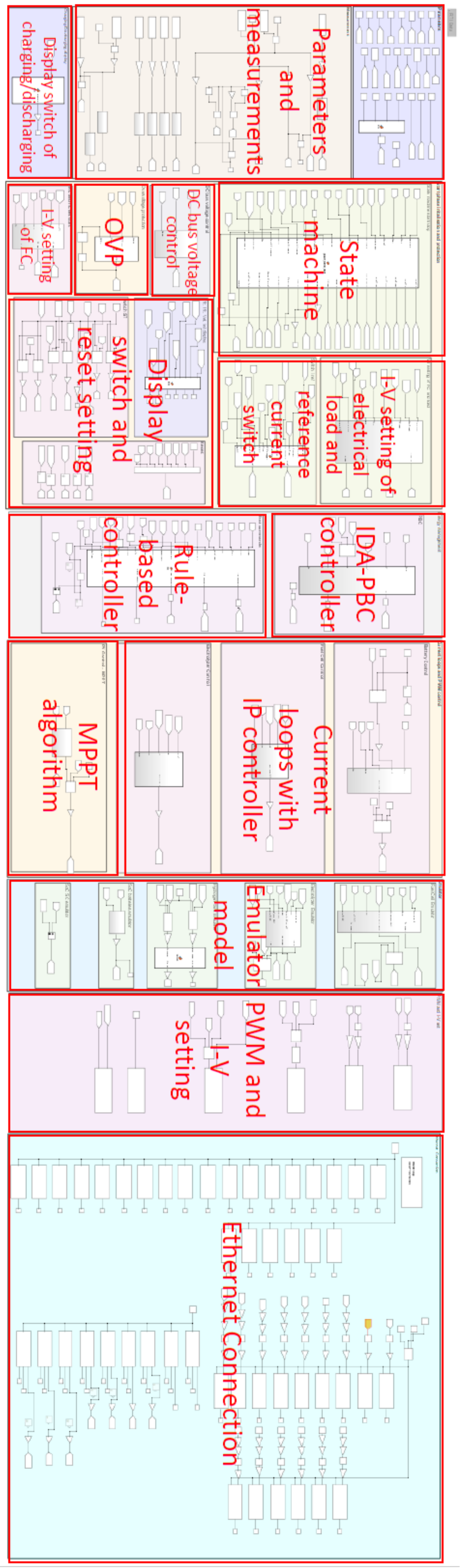

FIGURE A.1 – The entire Simulink model

activate the PV as well as the MPPT algorithm (detailed in section A.4) ; enable manual control ; enable the load cycle ; enable the real-time controller. Then the system can be stopped by clicking the stop button on the HMI, in which case the system skips to state 6.

- State 6 : The stop procedure is activated, and the state machine will : stop the load cycle, stop the MPPT, stop the controller, forbid the SCs to stabilize v_{bus} while allowing the power supply to stabilize v_{bus} and skip to state 7.
- State 7 : Discharge the SCs with a constant current using the load while charging the batteries to their reference SoC using the power supply, then skip to state 8.
- State 8 : After waiting for 10 s to stabilize the SCs voltage, skip to state 9.
- State 9 : Discharge the DC bus with the resistance until the DC bus voltage is lower than 1 V, then return to state 0.

* In case of emergency stop, skip to state 6 immediately.

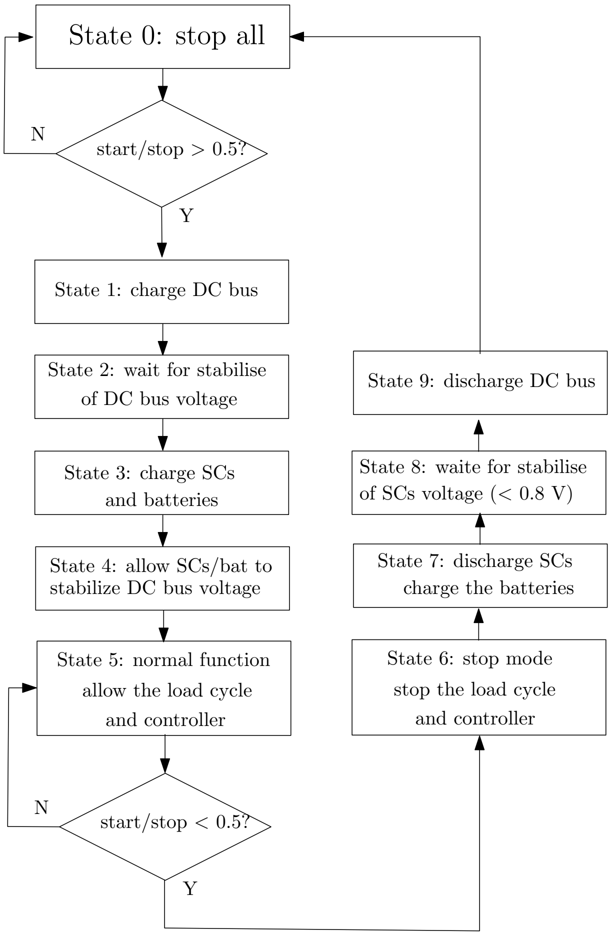

FIGURE A.2 – State scheduling and system behavior

The application of the state machine for the FC/SC system is presented in Fig. A.2, which shows the state scheduling and system behavior from state 0 to state 9. For the start/stop value, 1 is for starting and 0 is for stopping. So that if start/stop = 1, the system state is in the case of start/stop > 0.5 and the start procedure is activated ; and in the contrary, the stop procedure is activated if start/stop < 0.5.

In the Simulink model of the state machine, the on/off switch for each element as well as the controller are the outputs of this program. The configuration changes via the HMI (e.g., start/stop button, emergency stop button and control enable button, etc.) as well as the voltage measurements, SoC measurements and over-voltage protection are considered into the state machine program as input values. Also, a waiting time for stabilization which is used at states 2 and 8, is realized by the integrator.

A.3/ EMULATOR OF HYDROGEN SYSTEM

The model of the HESS is implemented in Matlab / Simulink using the dSPACE toolbox, which includes an FC model, an EL model and a hydrogen tank model. These models are compiled and loaded to the MicroLabBox and using the dSPACE compiler in Matlab. This enables the FC to be emulated using a power source while the EL can be emulated by the electric load.

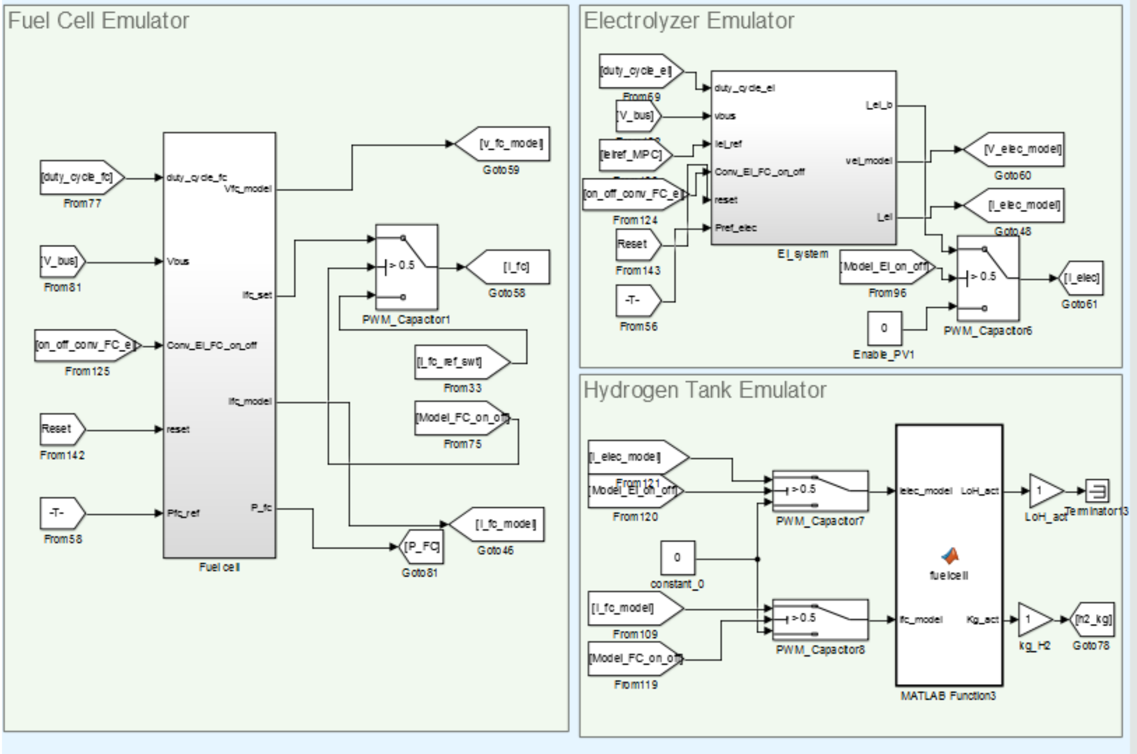

FIGURE A.3 – Hydrogen system emulator in Simulink

The model of the fuel cell is presented in section 4.2.2, while the EL model is introduced in section 6.2.3. Here, the mass of stored hydrogen at step k is calculated as follows :

$$n_{H_2}[k] = \frac{i_{elec}[k] - i_{fc}[k]}{2F} \tag{A.1}$$

$$m_{H_2}[k] = m_{H_2}[k-1] + n_{H_2}[k]M \tag{A.2}$$

where n_{h2} is the hydrogen molar flow rate in mol/s, m_{H_2} is the mass of hydrogen in kg, F is the Faraday constant of 96485 A/mol, M is the molar mass of dihydrogen molecule, which is 2.02 kg/mol.

A.4/ MPPT ALGORITHM

The aim of the MPPT algorithm is to maximize the power output of the PV array by modifying the duty cycle of the boost converter. Therefore, in this work, we chose to use the simple perturbation and observation ($P\&O$) method that achieves maximum power point tracking [203]. The principle of $P\&O$ is presented in Fig. A.4.

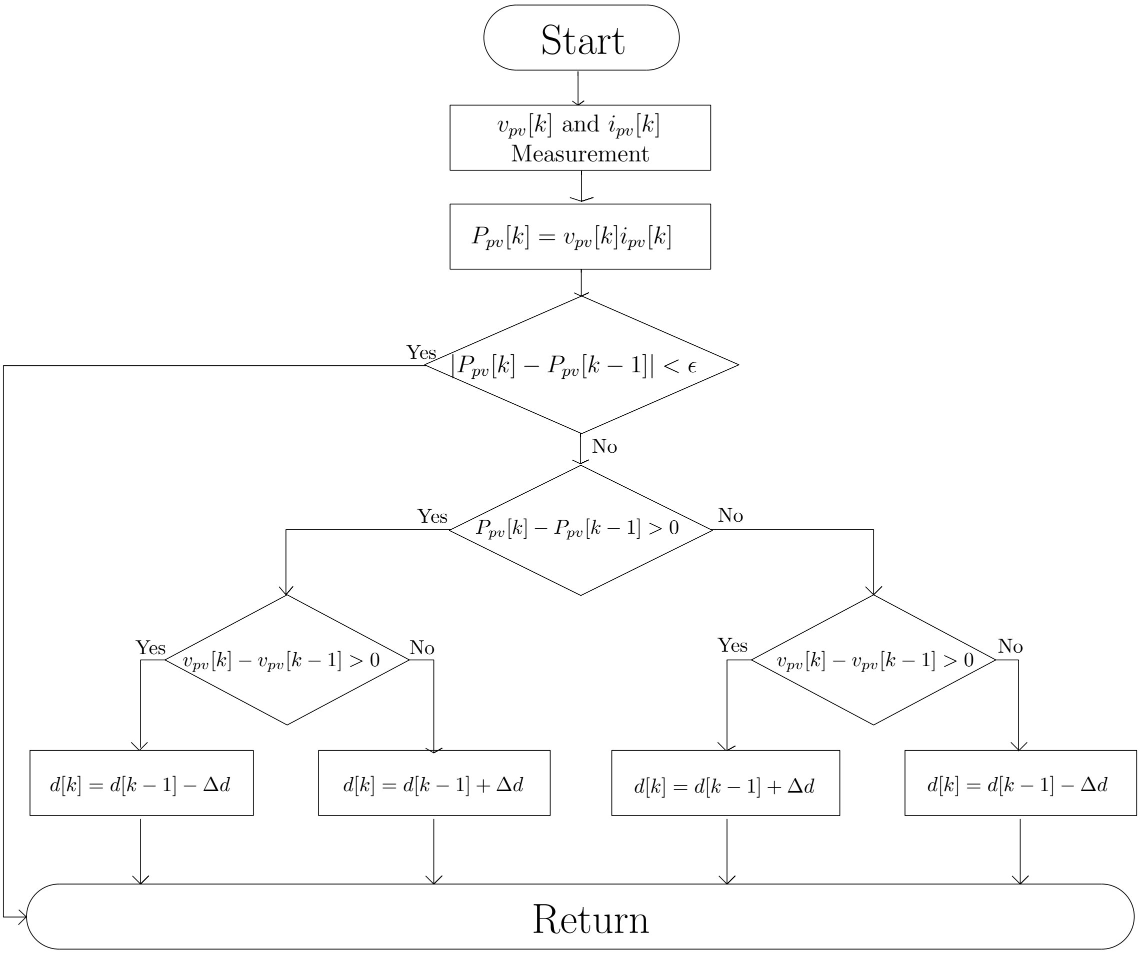

FIGURE A.4 – $P\&O$ method for MPPT algorithm of the boost converter.

The control algorithm measures the current and voltage values and determines the power output of the PV array at each time interval. After that, the measured power amount is compared with the previously measured power value. After that, the previous PV voltage is compared with the actual PV voltage, and the duty cycle is changed accordingly to maximize the power output of the PV array. In this system, the MPPT sampling time is set to 1 ms while the duty cycle interval Δd is set to 0.001.

B

HMI OF THE PHIL TEST BENCH

Fig. B.1 shows the HMI of the microgrid test bench. The following applications are realized through this HMI :

- Indication of the elements' state, which is labeled as zone number 1 in Fig. B.1. Through these signals with different colors, the signs of charging/discharging, on/off duty cycle of the PWM control, over-voltage protection, emergency stop as well as the output signals of the state machine are displayed clearly.
- Display of the measurements (current, voltage) as well as the system parameters by digital blocks.
- Through zone number 2, the option of the system start/stop as well as the controller enable/disable options can be changed in real time. In the case of emergency, the system can be stopped immediately by the emergency stop button. These are realized by the state machine that is detailed in Appendix A.
- The emulator model of the FC and the electrolyzer can be activated through the "Control" blocks.
- Changing the parameters such as DC bus reference voltage, and gain of the IP controller (see Appendix A) in real time.
- Manual control of the current or duty cycle for the test (zone number 3 in Fig. B.1).
- Switch of the PV MPPT or manual control.
- Display of the emulators information from the Simulink model : voltage and current of fuel cell and electrolyzer models, as well as the weight of hydrogen storage.
- Enable/disable the TCP connection and display of the information from the remote controller PDM (zone number 4).
- Plot the curves in real time. At the bottom of the HMI, we can see :
  - Power curves display : the power of the load, FC, batteries, SCs PV, electrolyzer
  - State display : the state number of the state machine (see below)
  - Voltage curves display : the voltage of the DC bus, load, FC, batteries, SCs PV, electrolyzer
  - SoC display : the batteries and the SCs state of charge
  - Current curves display : the current of the load, FC, batteries, SCs PV, electrolyzer
  - Duty cycle display : the duty cycle of the batteries, SCs and PV current loops
  - Current setting display : current setting for the power supply and the electric load (the emulators)
- Save and export the experimental data to the Matlab workspace.

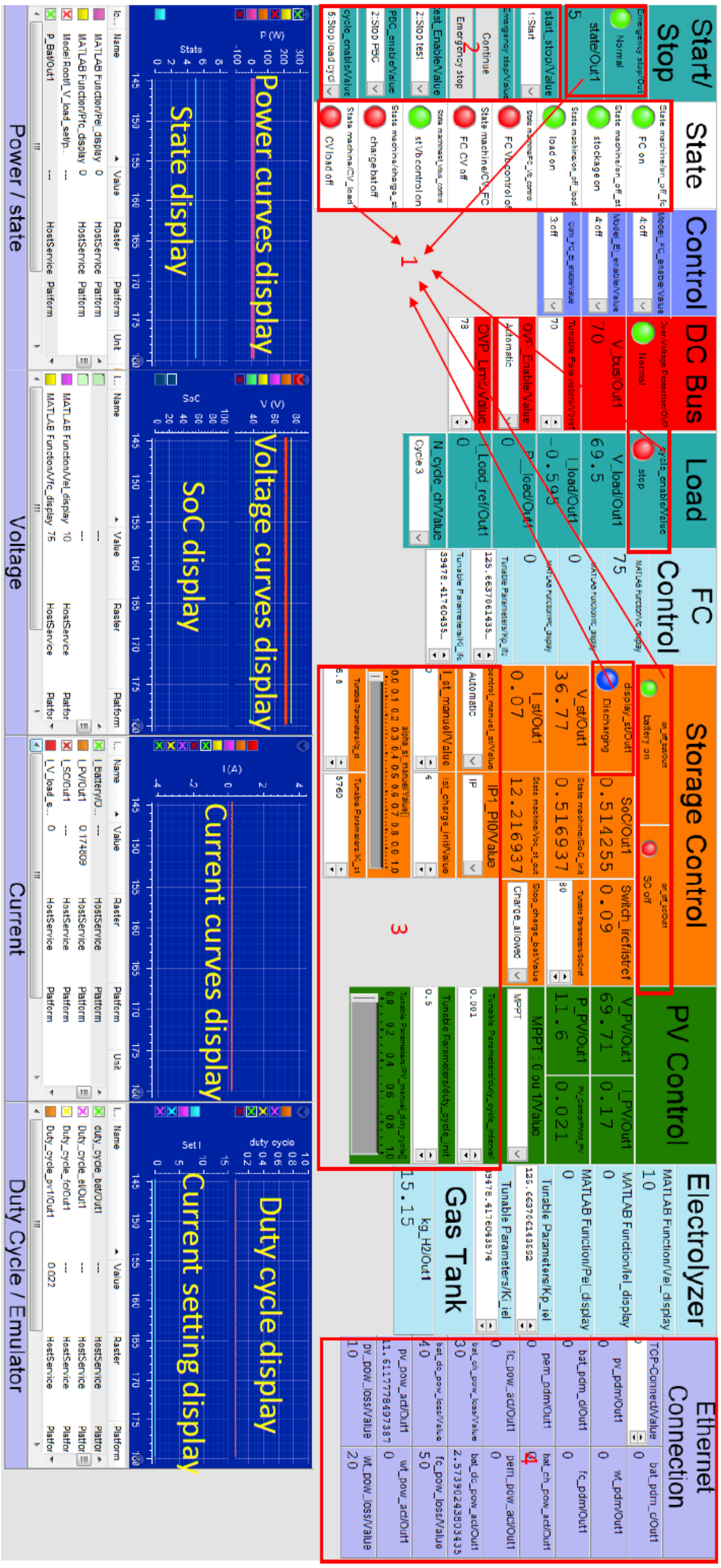

FIGURE B.1 – HMI in ControlDesk

C

HMI AND INTEL/ALTERA FPGA MONITOR PROGRAM OF THE HIL TEST BENCH

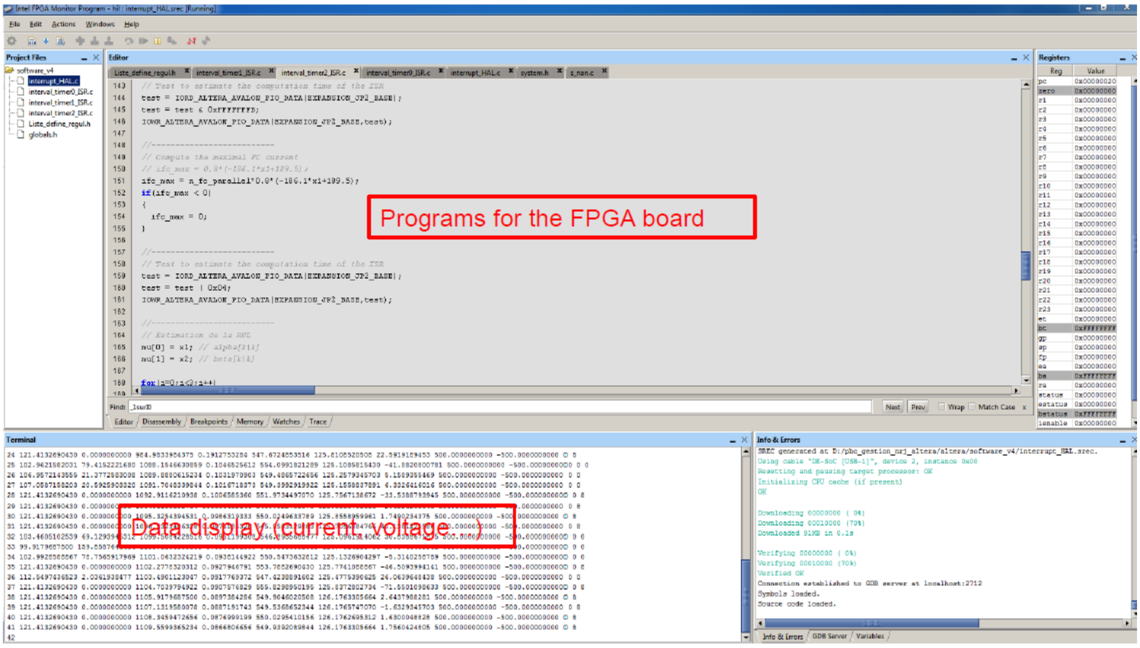

```
// Test to estimate the computation time of the ISR
test = IORD_ALTERA_AVALON_PIO_DATA(EXPANSION_JP2_BASE);
test = test & 0xFFFFFFFB;
IOWR_ALTERA_AVALON_PIO_DATA(EXPANSION_JP2_BASE,test);

//------------------------
// Compute the maximal FC current
// ifc_max = 0.9*(-186.1*x1+189.5);
ifc_max = n_fc_parallel*0.9*(-186.1*x1+189.5);
if(ifc_max < 0)
{
  ifc_max = 0;
}

//------------------------
// Test to estimate the computation time of the ISR
test = IORD_ALTERA_AVALON_PIO_DATA(EXPANSION_JP2_BASE);
test = test | 0x04;
IOWR_ALTERA_AVALON_PIO_DATA(EXPANSION_JP2_BASE,test);

//------------------------
// Estimation de la RUL
mu[0] = x1; // alpha[k|k]
mu[1] = x2; // beta[k|k]

for(i=0;i<3;i++)
```

Programs for the FPGA board

Data display (current, voltage...)

```
SREC generated at D:/pbc_gestion_nrj_altera/altera/software_v4/interrupt_HAL.srec.
Using cable "DE-SoC [USB-1]", device 2, instance 0x00
Resetting and pausing target processor: OK
Initializing CPU cache (if present)
OK

Downloading 00000000 ( 0%)
Downloading 00010000 (70%)
Downloaded 91KB in 0.1s

Verifying 00000000 ( 0%)
Verifying 00010000 (70%)
Verified OK
Connection established to GDB server at localhost:2712
Symbols loaded.
Source code loaded.
```

FIGURE C.1 – Information in INTEL/ALTERA FPGA Monitor Program

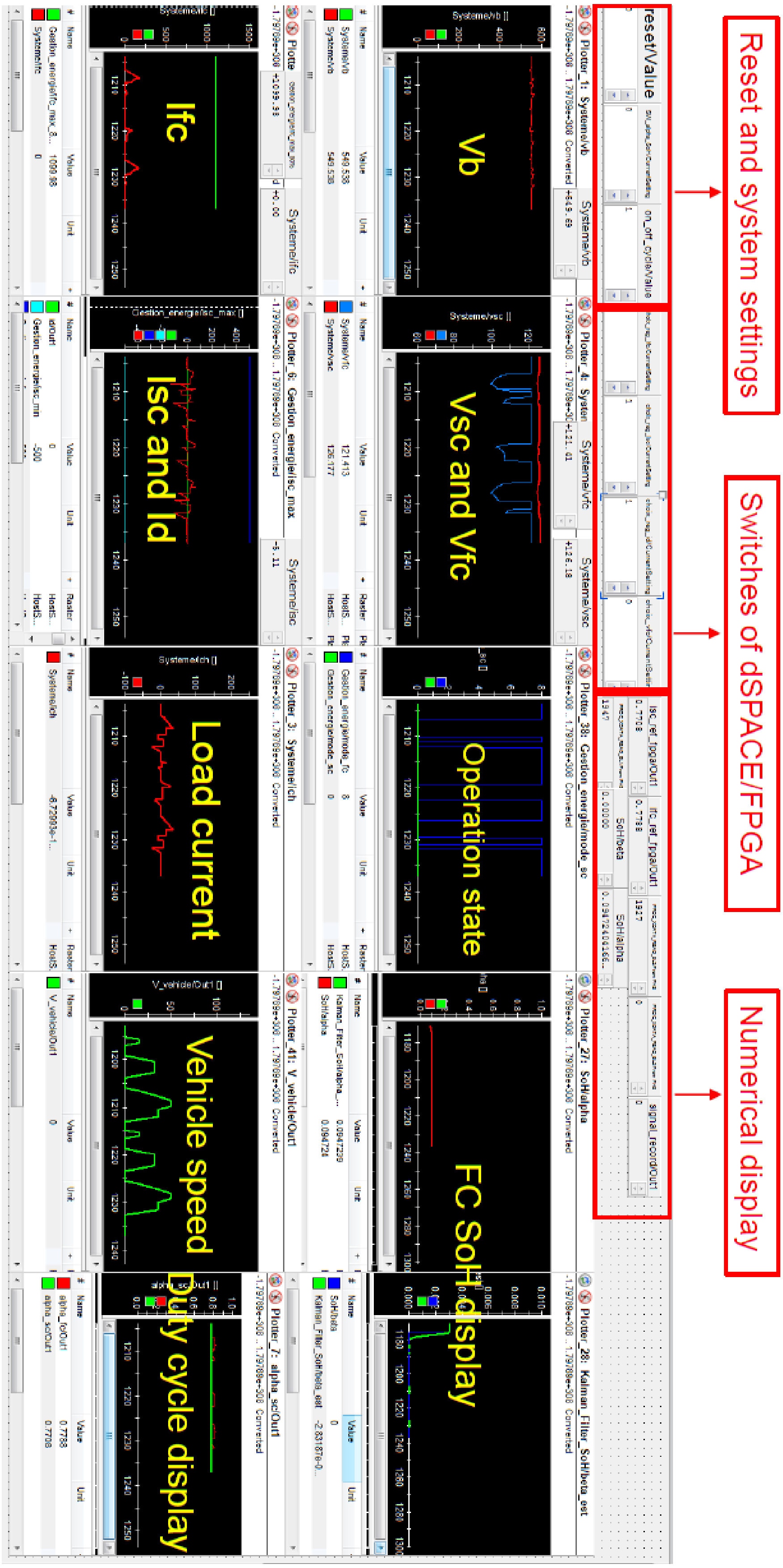

FIGURE C.2 – HMI of HIL platform - Emulated data

Document réalisé avec LaTeX et :
le style LaTeX pour Thèse de Doctorat créé par S. Galland — http://www.multiagent.fr/ThesisStyle
la collection de paquets `tex-upmethodology` — http://www.arakhne.org/tex-upmethodology/